

Fused Silica Precision Shell Integrating (PSI) Navigation-Grade Micro Gyroscopes

by
Sajal Sagar Singh

A dissertation submitted in partial fulfillment
of the requirements for the degree of
Doctor of Philosophy
(Electrical and Computer Engineering)
in The University of Michigan
2020

Doctoral Committee:

Professor Khalil Najafi, Chair
Dr. Jae Yoong Cho
Professor Yogesh Gianchandani
Professor Noel Perkins
Professor Emeritus Kensall D Wise

Sajal Singh

sajals@umich.edu

ORCID iD: 0000-0003-0578-920X

©Sajal Singh 2020

Part of this thesis is written while staying at home due to the COVID-19 pandemic. While I am safely staying at home, there are many who are risking their life to perform essential jobs for us. This thesis is dedicated to all the frontline workers, doctors, medical personnels, grocery staffs, delivery persons, bus drivers and many other who are providing us essential services and taking care of us during this time of global pandemic. To all of you,
and
to Dr. Abdul Kalam, to Irrfan Khan.

ACKNOWLEDGEMENTS

I feel incredibly fortunate to have gotten a chance to pursue my PhD under Prof. Khalil Najafi's guidance. The way he shaped my research path, giving me immense freedom, letting me make my own mistakes and learn from them and at the same time making sure I move in the right direction is something which made my PhD journey thoroughly enjoyable. I am very grateful to him for keeping my morale high during my lows and challenging me to achieve better during my highs. I am also indebted to him for giving me an overall professional experience beyond my research in form of several opportunities to attend conferences, DARPA meetings and helping me build my professional network. Finally, I thank him for his trust and encouragement. I don't remember going in his office and not coming out more encouraged and I have always appreciated his optimism.

I also feel fortunate to have Prof. Ken Wise, Prof. Yogesh Gianchandani, Prof. Noel Perkins and Dr. Jae Cho in my doctoral committee and I thank them for their valuable feedback and guidance. Special thanks to Prof. Gianchandani for his support and taking interest in my research progress and always checking on me.

It was a real pleasure to work alongside Dr. Jae Cho and I have learnt a lot from our discussions on several topics related to gyroscopes. His multidimensional knowledge and hardwork has inspired me throughout my PhD research. I also thank Mr. Robert Gordenker for his help in keeping all my equipment running. With Robert

around, I always had the confidence that my research would not get stalled. Thank you to Trasa Burkhardt for taking care of all the organizational work of our group which enabled me to focus on my research.

I would also like to thank my friends within Najafi group. Dr. Tal Nagourney for his mentorship when I first joined the group. I had a really nice time working with him in the cleanroom and discussing a variety of topics. I thank Dr. Ali Darvishian for being my 3 am friend and always being very helpful and kind to me. I will always cherish our late night discussions on life and our cultures. I thank Dr. Jong-Kwan Woo for all his testing support and discussions on circuits side of gyroscopes. I collectively thank all my friends in Najafi group, Dr. Amin Sandoughsaz, Dr. Yi Yuan, Dr. Stacey Tang, Dr. Donguk Yang, Dr. Guohong He and soon to be Drs. Chris, Benoush, Ester and Farzad.

Part of the fabrication of PSI gyroscopes was done at the Lurie Nanofabrication Facility (LNF) and I thank all the staff members who made sure that all the equipment were up and running. Special thanks to Dr. Pilar Herrera-Fierro for all her help over the past years.

My PhD journey was enjoyable thanks to my friends. Thanks to Ranit, Tarun, Gunjan, Harsh, Tansheet, Deepti, Mayur, Neha, Neeharika, Pallav, Ramprasad, Daniel, Saurabh, Subhajit, Suyash, Rohith and Ester. I would like to specially thank Mayur and Neha Birla for being like my family in Ann Arbor and always being there for me. Special thanks to my wonderful friend Mahshid for being such a great friend and taking me to different fun events to make sure I spend enough time outside labs! I also thank Farzad and Mahshid for their help when my parents visited Ann Arbor. Finally I would like to thank my parents, Shashi Singh and Rakesh Singh for giving me immense freedom and support. I owe them a lot for all the sacrifices they

made and hardships they faced to make my journey from a small town of Munger to Michigan possible. I worked hard four years for my PhD but they worked hard four decades to make this possible. I thank my father for inspiring me to pursue science. During the course of my undergraduate and graduate studies there were several scientific achievements including the detection of gravitational wave, ISRO successfully sending *Mangalyan* to the orbit of Mars in its first attempt, EHT obtainig the first ever image of a black hole, SpaceX demonstrating reusable rockets etc. Such breakthroughs continued to inspire and motivate me to pursue science. At the same time, some failures like 737 Max's crashes, ISRO narrowly missing the landing of *Chandrayaan* on the lunar surface, Boeing's Starliners failure to dock ISS etc. also highlighted that there is so much to learn.

TABLE OF CONTENTS

DEDICATION	ii
ACKNOWLEDGEMENTS	iii
LIST OF FIGURES	ix
LIST OF TABLES	xvi
ABSTRACT	xvii
CHAPTER	
I. Introduction	1
1.1 Overview	1
1.2 Inertial Sensors for Navigation	2
1.3 Accelerometer	4
1.3.1 Piezoelectric Accelerometer	5
1.3.2 Piezoresistive Accelerometer	5
1.3.3 Capacitive Accelerometer	5
1.3.4 Vibrating Beam Accelerometer	6
1.4 Gyroscopes	6
1.4.1 Optical Gyroscopes	6
1.4.2 Cold Atom Interferometer Gyroscopes	7
1.4.3 Vibratory Gyroscopes	8
1.5 Vibratory μ -Shell Gyroscopes	12
1.5.1 Thin Film μ -Shell Gyroscopes	14
1.5.2 Molded μ -Shell Gyroscopes	15
1.5.3 Working Principle	17
1.5.4 Transduction Mechanism	19
1.5.5 Rate Gyroscopes (RG)	21
1.5.6 Rate-Integrating Gyroscopes (RIG)	23
1.5.7 Sensor Parameters	24
1.6 Errors in Inertial Sensors	27
1.6.1 Scale Factor Error	28
1.6.2 Bias Error	29
1.6.3 Angle Random Walk	31
1.6.4 Shock and Vibration Sensitivity	35
1.7 Research Objective and Contributions	36
1.8 Organization	39
II. Precision Shell Integrating Resonator – Design and Fabrication	40
2.1 Introduction to PSI Resonators	40

2.2	Nomenclature	41
2.3	Fabrication of PSI Resonator	43
2.4	Energy Dissipation Mechanism	44
2.4.1	Thermoelastic Damping	45
2.4.2	Anchor or Support Loss	48
2.4.3	Viscous Loss	50
2.4.4	Surface Loss	51
2.5	Using Patterned Substrate to Tune Thickness	51
2.6	Fabrication of Patterned Substrate	54
2.7	Blowtorch Molding	55
2.7.1	Propane-Oxygen Flame	56
2.7.2	Mold	57
2.8	Singulation	58
2.8.1	Laser Cutting	59
2.8.2	Lapping and CMP	60
2.8.3	Hydrofluoric Acid Release	63
2.9	PSI Resonators	65
2.10	H-NX type PSI	66
2.11	H-TN type PSI	67
2.12	S-XX (Solid Stem) type PSI	71
2.13	Open-PSI Resonators	75
2.14	Imperfections	82
2.14.1	Height Imperfection	83
2.14.2	Circularity Imperfection	83
2.14.3	Mass Imperfection	84
2.14.4	Anchor Misalignment	86
2.14.5	Surface Imperfection	87
2.15	Conclusion	87
III. Precision Shell Integrating Resonator – Test and Characterization		89
3.1	Overview	89
3.2	Optical Test Setup	90
3.3	Test Results of $n=2$ Modes	92
3.3.1	Singulation using Lap/CMP Method	93
3.3.2	Singulation using HFA Method	101
3.4	Test Results of $n=3$ Modes	104
3.5	Test Results for Open Shell Resonators	107
3.6	Repeatability and Uniformity	110
3.7	Fused Silica Annealing and Material Characterization	112
3.7.1	Uncoated FS Resonators	114
3.7.2	Pt-Coated FS Resonators	118
3.8	Shock Testing	120
3.9	Long Term Testing	122
3.9.1	Fatigue Testing	122
3.9.2	Frequency and Δf Drift	124
3.10	Metal Coating	126
3.11	Conclusion	132
IV. Precision Shell Integrating Gyroscope		134
4.1	Gyroscope Architectures	134
4.2	Test Setup and Measurement Technique	136
4.3	Surface Electrode Architecture	137

4.3.1	Fabrication of Electrodes	138
4.3.2	Assembly Process	139
4.3.3	Gyroscope Testing	140
4.4	Side Electrode Architecture	143
4.4.1	Fabrication of Electrodes	143
4.4.2	Assembly Process	144
4.4.3	Gyroscope Testing	144
4.5	Shell-in-Shell (<i>SiS</i>) Architecture	146
4.5.1	Design and Fabrication	148
4.5.2	Numerical Analysis	152
4.5.3	Testing and Evaluation	155
V. Conclusions and Future Work		158
5.1	Summary	158
5.2	Conclusions	158
5.2.1	High-performance Resonators with Tailored Stiffness/Mass	159
5.2.2	3D Structures with Discrete Open Windows	161
5.2.3	Hydrofluoric Acid Based Singulation Method	162
5.2.4	Integration of Resonators to make PSI Gyroscopes	162
5.3	Future Works	164
BIBLIOGRAPHY		165

LIST OF FIGURES

Figure

1.1	Schematic representation showing (a) vehicle navigating using GPS signal to go from point A to B. (b) However, a false signal can trick the current location and can alter the path of the vehicle.	3
1.2	An IMU located on an airplane’s body consists of accelerometers in each direction to measure displacement (x,y,z) and velocity (u,v,w). Gyroscopes measure the angular velocity ($\Omega_x, \Omega_y, \Omega_z$).	4
1.3	Working principle of optical gyroscopes relying on phase change due to path length difference under rotation of two laser moving in opposite direction.. . . .	7
1.4	Modes of a tuning fork. (a) in-plane mode where the tines vibrate in its plane and (b) out-of-plane where the tines oscillate in direction perpendicular to its in-plane motion.	9
1.5	Tuning fork gyroscopes from (a) Draper Labs [17], (b) quad mass gyro with the drive and sense modes motion of the four masses [18], (c) tuning fork gyro from Systron Donner with the control architecture [12].	10
1.6	Ring resonator gyroscopes fabricated at The University of Michigan using (a) electroplated Nickel [20], (b) Single Crystal Silicon [21] and (c) Polysilicon [22]. . .	11
1.7	Disc resonator gyroscopes (a) fabricated using Silicon [29], (b) with amplitude amplifiable dual mass architecture [31], (c) made from Silicon Carbide [32]. . . .	12
1.8	Hemispherical Resonator Gyroscope containing fused silica shell resonator and electrodes manufactured by (a) Northrop Grumman in USA [38] and (b) SAFRAN in France [39].	14
1.9	Fabrication scheme for manufacturing shell resonators by depositing a thin-film material on a pre-etched mold. Some thin-film resonators.	15
1.10	Working principle of optical gyroscopes relying on phase change due to path length difference under rotation of two laser moving in opposite direction.. . . .	16
1.11	Glass blowing process and some resonators fabricated using this approach at UC Irvine and Southeast University, China.	17
1.12	Modeshapes in wineglass type resonators. When a perfectly symmetric wineglass as shown in (a) is stuck at the rim, the rim vibrates. (b) The $n=2$ wineglass mode is in the shape of ellipse and has two nodal diameter, the dots shows the position of maximum displacement or anti-nodes in first cycle of vibration and dashed lines shows the second cycle of vibration. Similarly (c) the $n=3$ mode of vibration has three nodal diameter and is in the shape of a star.	18
1.13	(a) The shell is driven in its ‘drive mode’, (b) under rotation the Coriolis force acts on the shell and (c) transfers energy into the second mode where the motion is sensed and the rate of rotation is determined.	19
1.14	Electrode configuration in shell resonator gyroscopes. The electrodes can be placed either at the bottom to sense out-of-plane motion or can be placed at the side to sense in-plane motion.	20
1.15	Schematic representation of open-loop mode operation. The gyroscope is electrostatically driven in one of its mode, under rotation, the amplitude build-up in the sense mode is sensed by the surrounding electrodes.	22

1.16	Schematic representation of closed-loop mode operation. The gyroscope is electrostatically driven in one of its mode, under rotation, the amplitude build-up in the sense mode is suppressed by applying a voltage by the surrounding electrodes.	23
1.17	(a) When a wineglass is excited at its $n=2$ resonant frequency, (b) the rim (as seen from the top) starts oscillating in an elliptical pattern. (c) Now when the wineglass is rotated by an angle of 90 degree from its stem, (d) the reference point (shown in red dot) moves 90 degree but the pattern of vibration lags by 27 degree.	24
1.18	A sensor's input-output curve. Slope of the plot is called the scale factor or sensitivity and the intercept on y-axis (at zero input) is called as bias.	26
1.19	Measured ring-down of a resonator. Ring-down time is calculated by measuring the time taken for the amplitude (or velocity) to decay to $1/e$.	30
1.20	Allan variation plot of a gyroscope showing different dominant noise sources at different sampling time. ARW is read by reading the y-axis value at $t=1$ second and BI is determined by reading the lowest value on the plot.	31
1.21	Variation of $\frac{\Delta f}{f}$ on ARW. Large frequency mismatch limits the sensor noise even if Q is large.	33
2.1	Different types of PSI resonators where selective regions are locally thin either in a continuous form or in form of discrete windows. PSI can be fabricated with either a hollow stem or a solid stem.	41
2.2	Resemblance of a PSI resonator structure with that of a human body. PSI resonators are named as X-YZ where X denotes the stem type, H or S for hollow or solid anchor. The next letter determines the thickness of the joint, and the third letter determines the thickness of rim. The letter in parenthesis is used to denote each region. Human body cartoon: www.dreamstime.com .	42
2.3	Different types of PSI resonators with thicknesses of different regions. PSI resonators can have a solid or hollow stem. Approximate thickness in micrometers are shown within parenthesis.	43
2.4	Key components and steps to fabricate PSI resonator using blowtorch molding.	44
2.5	Design and fabrication steps to make high quality PSI resonator.	44
2.6	A vibrating beam undergoes alternating compression and expansion cycles causing temperature gradient across the beam.	46
2.7	Material properties and simulated Q_{TED} for different materials. Figure reproduced from [72].	47
2.8	Effect of material properties on Q_{TED} . As α , k , E , ν increases, Q_{TED} decreases. Similarly, as CSP or ρ is increased, Q_{TED} increases. [72].	47
2.9	Modeshape of a wineglass resonating in $n=2$ and $n=3$ modes. Maximum displacement occurs at the rim while the apex of the dome does not move.	49
2.10	Tuning sidewall thickness using patterned substrate. (a) When the substrate is flat, the thickness of the shell gradually reduces. This can be altered by using (b) a patterned substrate with features. CT scans of the two shells shows normalized thickness.	52
2.11	3D structure fabricated using two substrates, (left) an un-patterned FS and (right) patterned FS to define thin window near the center. Reflow initiates at the thinned region of patterned substrate. This leads to a thicker rim (t_2) as compared to that of unpatterned substrate (t_1) i.e. $t_2 > t_1$ which leads to $f_2 > f_1$, where f is the resonant frequency.	53
2.12	(a) SEM image of wafer coated with evaporated Cr/Au of 50/500 nm thickness. Grain size is 60 nm (b) Schematic and photograph of a substrate with etched features. Imperfections in patterned substrates during lithography and etching. (c) Poor adhesion caused lifting of the photoresist and metal layers, (d) severe undercutting around the edges, (e) a perfect pattern with well-defined and sharp features.	56

2.13	Flame positions during blowtorch molding. The flame is turned on and brought slowly towards the mold. The temperature of the FS substrate is increased, and 3D shell is molded. The flame then retracts back. The entire process takes less than a minute.	57
2.14	Effect of thermal conductivity of mold on profile of shell resonator. (a) Very small k would increase the temperature causing uncontrolled molding leading to a cylindrical shaped shell, (b) an optimum value of k would cause the substrate to deform and hang in the mold, (c) high value of k would cause rapid cooling causing the shell to locally harden before it is completely molded [83].	58
2.15	Different shapes and aspect ratio shells can be fabricated using different mold and patterned substrates.	59
2.16	After the substrate is blowtorched, the molded structure is taken out of the mold. The molded shell has a desired 3D part and a non-desired 2D part. The 3D part should be singulated from the structure.	60
2.17	The method of singulating shells using lapping/polishing method. (a) A molded is (b) coated with sacrificial protective metal and (c)-(d) set into a thick silicon wafer using thermoplastic. (e)-(f) The flat portion of the shell is lapped, and the rims are polished using CMP. Finally, the thermoplastic is dissolved, and metal is wet etched to release the shells.	61
2.18	Non-idealities during lapping and polishing (a) an unpolished rim has a rugged surface which can be smoothed by (b) polishing after lapping. (c) Due to unoptimized parameter or mounting, the shells can be broken completely or (d) get chipped at the edges. Chipping of rim has not shown to degrade Q significantly.	62
2.19	Process steps for HFA releasing of shells. (a)-(c) Shells are filled in with Crystalbond and (d) dipped in HFA acid to (e) etch the flat part and release the shell.	64
2.20	Photograph of shells released using lap/CMP and HFA etching. SEM image showing the rough region near the rim.	65
2.21	10 kHz H-NT PSI shells are fabricated using (a) 550 μm thick flat FS substrate which when (b) blowtorched gives the (c) 3D shaped resonator. (d) CT scan showing the thickness profile.	66
2.22	Two approaches to fabricate H-TN PSI by (a) etching a thin region and (b) etching to make a thick disc at the center. FEM simulation is used to optimize the dimensions of the patterns to obtain the desired profile and thickness.	68
2.23	Fabricated H-TN shells. Rim thickness in both cases is 200 μm and the shoulder thickness is 50 μm . In the shell on the left, the sidewall thickness is thick and then becomes thin whereas on the right it gradually thins as it reaches the shoulder where it becomes thick.	69
2.24	PSI resonators with mass imbalance. (a) imbalance is also at the rim while (b) imbalance is mostly away from the rim. Mass imbalance at the rim affects frequency mismatch much more than it being away from the rim.	69
2.25	Simulation model to calculate $n=2$ frequency mismatch due to imbalanced mass distribution. Mass imbalance at the rim causes 3 times more frequency mismatch as compared to similar mass imbalance away from the rim.	70
2.26	By varying the radius of central pattern on patterned substrate the height of the thick shoulder can be controlled.	71
2.27	Fabrication process of S-TM type PSI structure. (a) Finite element model is used to optimize the dimension of features on patterned substrate. (b) The central disc forms the thick top shoulder, the outer annulus defines the thick rim, (c) photograph of a fabricated patterned substrate atop a dome type mold. To fabricate the shell, (d) first a FS rod is inserted, and the substrate is torched on the mold. (e) Optical photograph of a torched shell. After molding, (f) the shell is singulated and (g) mounted on a silicon substrate for testing.	72

2.28	SEM image of S-TM PSI resonator. The shoulder region is 450 μm thick and it gradually thins down to nearly 175 μm at the rim. It can be seen that the FS rod gets seamlessly welded to the substrate.	73
2.29	Fabrication process of S-TT PSI structure. (a) Finite element model is used to optimize the dimension of features on patterned substrate. (b) The central disc forms the thick top shoulder, the outer annulus defines the thick rim, (c) photograph of a fabricated patterned substrate atop a dome type mold. To fabricate the shell, (d) first a FS rod is inserted, and the substrate is torched on the mold. (e) Optical photograph of a torched shell. After molding, (f) the shell is singulated and (g) mounted on a silicon substrate for testing.	74
2.30	SEM image showing (a) a fabricated S-TT PSI resonator showing thick shoulder and thick rim, (b) cross section of the resonator, the rim is 300 μm and shoulder is 400 μm (the stem broke off during cross sectioning. (c) Another resonator showing seamless welding of the substrate to the FS rod.	75
2.31	Fabrication process of S-TT type PSI structure. (a) Mold like those for H-XX type PSI is used but the stem is removed, and a slot is machined. (b) FS rod is placed in the slot and the patterned substrate is molded. (c) The substrate deforms forming the thick rim and thick shoulder fusing to the solid stem. (d) Photograph of a singulated PSI device.	75
2.32	(a) Schematic showing shells with open windows at different locations and (b) fabricated shells with discrete thin windows symmetrically defined on the outside of the shell. These thin windows can be through etched to make open windows. . .	76
2.33	(a) Layout of patterned substrate to make 3D shells with eight discrete thin/open regions. The dimensions w_s and l_w can be tuned to obtain desired aspect ratio of windows on the shell. (b) Flat 550 μm FS wafer is patterned and etched in HF to obtain the desired etch depth. The thick and the thin part after etching is 350 μm and 150 μm , respectively.	77
2.34	Fabrication flow to make shells using (a) patterned substrate which is (b)-(c) blowtorch molded to make shells with thin windows on its surface as shown in (d) photograph of a fabricated and singulated shell. (e) SEM images shows closeup of the etched window on the shell.	78
2.35	(a) SEM of a shell with thinned region, clearly highlighting the region, in the shape of a window, where the flat FS was first thinned, then deformed using blow torching. (b) CT scan image of a shell with thin windows. Cross-sectional view of thin region (shown on left) and thick spring (shown on right) is shown. (c) Variation of thickness along the height, h , of the shell is plotted for both spring and window.	79
2.36	Shells with different aspect ratio of thin windows fabricated by changing dimensions of etched features on the patterned substrate.	80
2.37	(a) Process of through-etching thin windows by protecting the inside with Crystalbond 509 and dipping in HFA bath for timed etching.(b) Photos of a singulated shell where the thinned regions were further etched in HF to create the open windows. This etch can be timed to define the area of the open window. . . .	81
2.38	(a) Selective conductive coating on shell reduces loss and increases Q. (b) Shell fabricated with open window is used as a stencil mask to selectively coat metal on another shell.	82
2.39	Different types of imperfections in shell resonators. These can be mitigated by process optimization.	83
2.40	Effect of imperfection in height and circularity on Q_{anchor} , Q_{TED} , f and Δf of shell resonator. Figures from Dr. B. Shiari, Univ. of Michigan and reported in [83].	85
2.41	(a) Microscope image of a singulated shell taken on Olympus LEXT showing misalignment of anchor wrt shell. (b) Numerical results showing Q_{anchor} with misalignment, δ . Simulation results are from Dr. A. Darvishian.	86

3.1	Fundamental of laser Doppler velocimetry to measure velocity of moving sample by measuring phase change. Photograph from PolyTec [101].	90
3.2	Schematic diagram showing the test setup and modeshape of a PSI resonator.	91
3.3	Measured ring-down time of three different PSI resonators.	94
3.4	SEM image of S-TT PSI resonator showing (a) thick region at the shoulder and rim region. (b) sidewall profile showing thickness variation.	94
3.5	Variation of measured Q for several types of PSI resonators. It is seen that as Δf increases, devices's Q decreases.	95
3.6	Reported ring-down times for 3D shells fabricated using different techniques with different materials and sizes through projects funded by DARPA's Microscale Rate Integrating Gyroscope (MRIG) program [44]-[56], [13], [63]-[68], [84], [86], [91], [96], [112]-[116].	96
3.7	Measured ring-down time for Michigan's fused-silica shell resonators vs. time. The shells are either 5mm or 10mm in diameter operating at 5-10kHz, and are either bare, or coated with a thin metal layer [86], [87]-[89], [109]-[115].	97
3.8	$Q \cdot \tau$ product for different micro-resonators reported in literature along with the ones developed at The University of Michigan. C: Coated with metal, UC: Uncoated. 98	
3.9	(a) Two main causes of Δf includes thickness variation and acircularity. Thickness variation can be reduced by improving temperature distribution around the rim by using (b) a dithering stage which can dither the resonator during torching to improve temperature uniformity. (c) Dithering improved thickness variation however did not affect Δf (shown against each device).	100
3.10	Measured Δf from resonators fabricated from three different molds and processed in five different batches. Resonators fabricated from same molds exhibited similar Δf range irrespective of the processing batch.	101
3.11	Photograph of PSI resonators singulated using lap/polish method and HFA method. SEM image shows the rough region at the rim caused due to HFA penetration through micro-voids at the wax-FS junction.	102
3.12	Measured ring-down time plot for a H-NN type PSI resonator exhibiting more than 500 seconds ring-down time constant. This resonator is released using HFA method of singulation.	102
3.13	(a) Measured ring-down time of nine HF-released devices and comparison with 22 shells released using lap/polish method. (b) To compare Δf , eight shells are blowtorched using the same mold under identical conditions. Four of them are singulated using HFA method and the other four are singulated using lap/polish method. Δf from both the method is comparable indicating that HFA method is not detrimental to Δf	103
3.14	(a) Variation of numerically calculated Δf in $n=2$ and $n=3$ wineglass modes for cases where imperfection is near the rim and away from the rim as shown in Figure 2.25. (b) Experimental data for five devices.	106
3.15	Comparison of measured Q in $n=2$ and $n=3$ wineglass modes for five devices. Although high-Q have been measured in $n=2$ mode for other devices, this plot shows that $n=3$ mode exhibits high-Q irrespective of what $n=2$ mode Q is. Measured resonant characteristics are tabulated.	106
3.16	Performance improvement in $n=2$ and $n=3$ modes for shells with different sized windows before and after etching off the windows. Bars in blue corresponds to performance before windows are etched and red bars represent Q after etching off the windows.	110
3.17	Variation of $n=2$ wineglass frequency in the two modes for several shell resonators fabricated at The University of Michigan. Devices are fabricated in several batches over several years and are normalized to the average frequency of the batch. Variation of frequency is within $\pm 10\%$. Some data is from [83].	111

3.18	Variation of Q from different batches. Each Q is normalized by Q_{max} from that batch. The data presented shows relative values of Q with respect to the highest Q from that batch. It is seen that in initial years, spread of Q was more scattered. However, with improvement in fabrication process, the spread became more tight and closer to the maximum value. This means more devices exhibited Q close to Q_{max} from the batch. For this graph, 150+ devices each with $Q > 1$ Million was chosen.	112
3.19	Improvement in Q for four modes of two resonators after annealing at 450 °C. More than 1.5 times improvement in Q is measured after subjecting to annealing for 8 hours in forming gas.	115
3.20	Improvement in Q for four modes of two resonators after annealing at 850 °C. More than 1.5 times improvement in Q is measured after subjecting to annealing for 8 hours in Argon gas. This improvement is in addition to 1.5x improvement after 450 °C annealing indicating high temperature annealing improves Q beyond what low temperature does.	116
3.21	Effect of exposure to different environment on quality factor of fused silica resonator. Quality factor is the average of three devices and two modes of each device and is normalized.	117
3.22	Effect of exposure to different environment on quality factor of fused silica resonator coated with ALD Platinum. Quality factor is the average of two devices and two modes of each device and is normalized.	119
3.23	Numerical simulation showing displacement of H-TN and S-TT type PSI resonators under 20000g vertical and lateral shock. H-TN PSI experiences larger displacement due to thinner regions at shoulder and rim than S-TT PSI. The maximum stress is 0.24 GPa which is an order of magnitude smaller than the tensile stress of FS. Shock testing setup to impart shock upto 6000g.	121
3.24	Measured Q over a span of one month for four devices under continued resonance. Device 1 and 2 are singulated using lap/CMP method and Device 3 and 4 are singulated using HFA method.	123
3.25	Performance of all four devices increased in the last set of measurement after cleaning and annealing. Performance exceeded the initial Q because of longer annealing.	125
3.26	Variation of $n=2$ wineglass frequencies measured over 2500 Million cycles of resonance. Maximum frequency drift measured is ~ 0.5 Hz.	126
3.27	Variation of $n=2$ wineglass Δf measured over a month of continued resonance. Δf drifts by ~ 0.06 Hz which is within the measurement uncertainty.	127
3.28	Effect of different metals on Q of PSI resonators. Four different combinations of metals are used, and the Q is measured before and after deposition of metal. For sputtered metals, deposition is only on one side but ALD deposition is conformally on both inside and outside of shell.	131
4.1	Gyroscope architectures showing surface electrodes where electrodes are placed beneath the rim to measure out-of-plane displacement and side electrodes where electrodes are placed beside the rim to measure in-plane displacement. Advantages and disadvantages of each architecture is tabulated.	136
4.2	Measurement technique to measure resonant characteristics.	136
4.3	PSI Gyroscope with surface electrode architecture. (a) Schematic representation and (b) photograph of a fabricated and assembled PSI gyroscope wire bonded inside LTCC package.	138
4.4	Fabrication flow to make surface electrode substrates and photograph of wafer with electrode substrates	139
4.5	Assembly process. (a) Solder preform and spacers are placed beneath the anchor and rim respectively, (b) temperature is ramped up to 400 °C while applying pressure on the shell, (c) temperature is cooled down and the spacers are removed.	140

4.6	(a) SEM image showing resonator, electrode and the capacitive gap. (b) Measured capacitance (in pF) at all sixteen electrodes for a gyroscope with surface electrodes.	141
4.7	(a) The bonding pads are wire bonded to pins of the LTCC package and mounted on a PC Board with an ASIC. (b) Measured ring-down time plot of one mode.	142
4.8	ADEV plot exhibiting 0.006 deg/rt-hr ARW and 0.027 deg/hr BI and table containing device characteristics.	142
4.9	Schematic diagram and photographs of PSI gyro on a quarter and finger for scale.	143
4.10	Cross sectional view of PSI gyro integrated on electrode substrate and photograph of vacuum packaged PSI gyros.	144
4.11	(a) Control and readout system for operating PSI gyro in force rebalance mode and (b) measured ring-down time of one of the $n=2$ wineglass modes after reducing frequency split to <100 mHz.	145
4.12	Measured ADEV plot generated at room temperature showing navigation-grade ARW and BI. Other resonant characteristics are tabulated.	146
4.13	Comparison of ARW and BI of reported gyroscopes.	147
4.14	Schematic diagram and photograph of fabricated SiS device.	148
4.15	Design of molds to make resonator shell and electrode shell.	148
4.16	(a) A mold with angled sidewall is used to blow a flat fused silica substrate to (b) make the resonator shell which is then (c) lapped/polished to release and cleaned and coated with metal on both sides.	149
4.17	(a) Fused silica substrate is patterned to define 16 thin trenches. (b) It is then torched to make electrode shell and (c) filled inside with Crystalbond and etched in HF acid to etch off the thin trenches. (d) The device is then coated with metal.	150
4.18	Fabrication flow of resonator and electrode shells. They are then integrated together to form SiS device.	151
4.19	(a) Photograph of an assembled SiS device after removing the spacers and (b) photograph of a partially broken SiS device showing the profile of resonator and electrode.	152
4.20	(a) Simulation model with straight electrodes and curved electrodes, (b) variation of capacitance change and frequency tuning as a function of electrode height for both electrode configuration.	153
4.21	Effect of gap non-uniformity on capacitance and frequency tuning for curved electrode. As the non-uniformity increases, capacitance and tuning reduce and becomes comparable to that of straight electrode.	154
4.22	Causes of variation in capacitive gap due to thickness or profile variation.	155
4.23	Testing method of SiS device. The attachments are done using Crystalbond and shell bias is applied through the anchor.	156
4.24	Measured FFT of SiS #1 device showing a frequency mismatch of 1.3 Hz and Q of 0.2 Million.	156
4.25	Measured FFT and ring-down plot of SiS #2 device showing a frequency mismatch of 5.8 Hz and Q of 0.4 Million.	157

LIST OF TABLES

Table

2.1	Measured $n=2$ and $n=3$ wineglass frequency from six devices, 3 each using patterned and unpatterned substrate.	54
3.1	Device Performance and Process Parameters of Lap/CMP, Laser and Chemical Singulation Techniques.	104
3.2	Comparison of device parameters affecting noise in the $n=2$ and $n=3$ wineglass modes.	105
3.3	Measured resonant characteristics of devices before and after opening windows. . .	108
3.4	Measured resonant characteristics of devices before and after 450 °C annealing. . .	114
3.5	Measured resonant characteristics of devices before and after 850 °C annealing. . .	115
3.6	Summary of metal layers investigate in the past and their effect on Q [83]. Al_2O_3 is deposited through ALD and other metals are sputter coated.	130
4.1	Measured resonant characteristics of three PSI gyros with surface Electrodes. . . .	141

Abstract

This thesis is aimed at the development of low-cost, vacuum-packaged navigation-grade microelectromechanical system (MEMS) Coriolis vibratory gyroscopes (CVG) using 3-dimensional fused-silica (FS) shell resonators, called Precision Shell Integrating (PSI) gyroscope. PSI gyroscopes consist of 3D shells (dia=10mm, height=5mm) that resemble a wine glass. CVGs are used for measuring rotation angle and rate to aid navigation in GPS-denied environments. While MEMS gyroscopes dramatically reduce cost and size, they struggle to achieve performance comparable to their macro-counterparts. This thesis focuses on making small size/cost and high-performance gyroscopes by understanding bottlenecks in performance and mitigating them through innovative design and fabrication technologies. To improve performance, previous research focused on obtaining high quality factor (Q) from the resonator. In this thesis, navigation-grade performance is achieved by simultaneous improvement in resonator parameters like Q , ring-down time τ , effective mass, frequency, frequency mismatch Δf , and transduction parameters like signal-to-noise ratio, and capacitance, all of which combine to enhance resolution and accuracy.

Improvements in resonant parameters is achieved by making resonators by blowtorching a FS substrate with etched features. This allows fabrication of 3D shells with distributed stiffness/mass (by tailoring thickness in range of 10–450 μm at different locations) exhibiting high- Q (>12.5 Million) and long- τ (>500s) with small Δf (<2Hz) and large modal mass ($\approx 12\text{mg}$) and frequency (5–10 kHz). High- Q , long- τ and small Δf is obtained by making symmetric structures with superior surface quality enabled through efficient torching, cleaning and annealing. Modal mass is increased by increasing rim thickness. Similarly, large thickness at anchor transition regions (shoulder) increases shock survivability. Increasing the thickness of both the rim and shoulder from 150 μm to 300 μm leads to 2x increase in modal mass and 13x decrease in shock-induced displacement.

Shells with discrete and mm-scale open windows are also designed and fabricated for the first time. This is done by two-step etching of the substrate before molding and shells after molding. Open windows on shells can increase Q by reducing thermoelastic and anchor loss. Besides, this technology can be used to define discrete electrodes on a curved surface of a molded shell which is otherwise

not practical through conventional lithography. It can also be used to fabricate 3D shadow mask for selective metal coating on resonators. A low-cost and fast approach to singulate 3D resonators from their molded substrate using selective hydrofluoric acid etching of the flat substrate. This technology increases throughput and reduces cost by >25x as compared to other conventional processes, without compromising performance.

PSI gyroscopes are fabricated by assembling resonators on electrode substrates. Two architectures, one where electrodes are placed beneath the rim (surface electrodes) and other where electrodes are placed at the side of rim (side electrode) is explored. Unprecedented angle random walk of 160 $\mu\text{deg}/\text{rt-hr}$ and bias instability of <1 mdeg/hr is measured from PSI gyroscope with side electrodes without any temperature compensation. This is not only the best reported performance ever from a MEMS gyroscope, it compares favorably with some of the commercial state-of-the art macro-scale gyroscopes. Furthermore, a novel gyroscope architecture which involves integrating PSI resonators with a custom-designed curved electrode substrate is developed. Curved electrodes which nearly follow the resonator's profile are fabricated. This architecture could potentially increase capacitance by >5x as compared to side electrodes due to its conformal overlap. Curved electrodes improve resolution, frequency tuning, and temperature sensitivity.

CHAPTER I

Introduction

1.1 Overview

Research presented in this thesis is aimed at achieving navigation-grade performance in terms of very low noise and high accuracy from a micro-scale vibratory gyroscope. Vibratory gyroscope along with accelerometers make up a backup navigation system and can be effectively used to navigate in GPS-denied environment. These sensors therefore find applications in navigation of autonomous cars, defense vehicles, drones etc. To obtain precise angular information high-performance gyroscopes are needed. Existing vibratory gyroscopes are high precision but are bulky, power hungry and expensive. Miniaturized vibratory gyroscopes on the other hand offer attractive features like low cost, small size and can enable low cost solution for high-precision navigation. However, development of such high-performance gyroscopes at small scale has not yet been a reality. This is due to several challenges associated with miniaturization. This thesis is aimed at overcoming those challenges and developing navigation-grade miniaturized vibratory gyroscope called Precision Shell Integrating or PSI gyroscope. PSI gyros consists of a hemispherical shell resonator of diameter 10 mm and height ~ 5 mm. The total chip size is 12 mm x 12 mm x 5.5 mm and vacuum packaged complete device is 16 mm x 16 mm x 10 mm. Design,

fabrication and successful testing of such gyroscopes are presented, and challenges associated with each of them is discussed and methods of mitigation is developed to obtain reliable and repeatable results. This chapter begins with an introduction of inertial sensors and their application in navigation. Different accelerometers and gyroscopes are discussed. Following this, shell resonator gyroscopes and their working principles and sources of errors are discussed. Parameters which determine the performance of such gyroscopes are identified and in subsequent chapters key learning and findings are discussed.

1.2 Inertial Sensors for Navigation

GPS navigation is commonly used in many applications including defense, drones, autonomous vehicles, and robotics [1, 2]. However, absolute dependence on GPS is unreliable due to its limited reachability and susceptibility to external interference [3]. For example, autonomous vehicles could suddenly stop or lose its path leading to potential collision if they loses the navigation signal from the GPS in a tunnel. Similarly, a jammer or even a simple and cheap device can be used to spoof GPS signal which would trick the vehicle into believing false information. For example, consider a UAV navigating in air. Once the flight plan is loaded remotely onto the UAV with a destination point B, the UAV identifies its current location with the help of GPS signals as shown in Figure 1.1(a). It is supposed to go from point A to B and the autopilot wants to continue its trajectory as per the location information obtained from “true” GPS signal. Now the GPS signal is spoofed through a false signal to make the vehicle believe that it is at a wrong location and that it must turn right to get back to its intended path A–B. The autopilot would respond and turn right to get back to its desired path to B. Although, in reality the vehicle is

being tricked into an undesirable situation as shown in Figure 1.1(b). This could be catastrophic and severely compromises security. Therefore, for navigation of such autonomous vehicles one can't rely entirely on GPS. To make navigation more secure and reliable, inertial navigation system (INS)—consisting of inertial sensors, are used for navigation in conjunction with GPS [4].

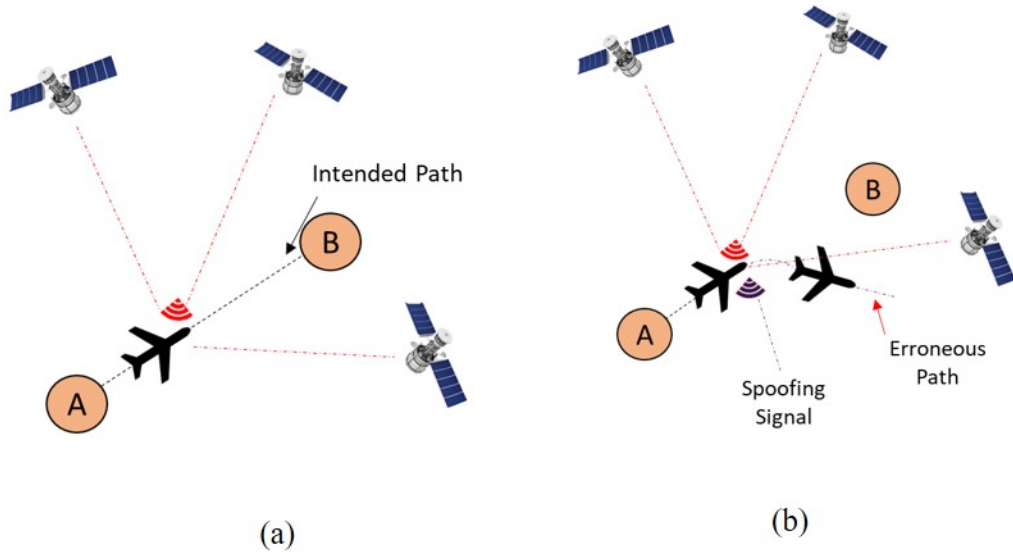


Figure 1.1: Schematic representation showing (a) vehicle navigating using GPS signal to go from point A to B. (b) However, a false signal can trick the current location and can alter the path of the vehicle.

The INS take the initial position, velocity and, orientation information from an external source (e.g. GPS, pre-existing maps, fixed objects) and computes the updated position, velocity and, orientation by integrating the data from its motion sensors. Thereafter, it can continue to navigate without any help from any external reference which makes it immune to jamming. This however is accompanied by errors which is described in 1.6. This method of navigation by using distance and direction information which could come from an inertial measurement unit (IMU) is called dead reckoning. An IMU mainly consist of three accelerometers and three gyroscopes in each direction (x, y and z) to measure acceleration (or velocity or position) or rate

(or angle) of rotation respectively as shown in Figure 1.2(b) [5]. Sometime three magnetometers are also added to measure the magnitude and direction of magnetic field or to measure geographic move (e.g. move east or west). Accelerometers measure the force (or acceleration) which helps in determining velocity and position. Gyroscopes measure the rotation rate and angle of rotation. Both linear and angular motion information are vital to precisely calculate the attitude and position of an aerial body.

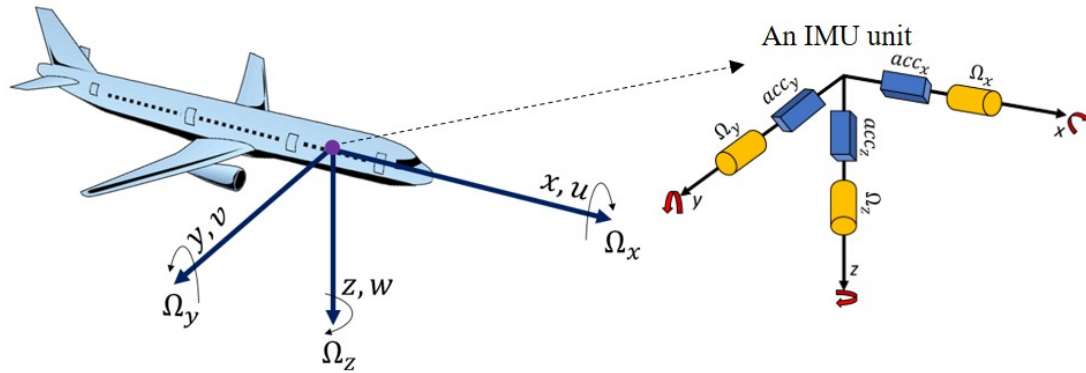


Figure 1.2: An IMU located on an airplane's body consists of accelerometers in each direction to measure displacement (x,y,z) and velocity (u,v,w) . Gyroscopes measure the angular velocity $(\Omega_x, \Omega_y, \Omega_z)$.

1.3 Accelerometer

Accelerometers are used to measure acceleration by virtue of measuring the force experienced by a movable body attached to an extensible (or deformable) spring. When the accelerometer case (located in a moving body) experiences an acceleration, the proof mass inside the case, moves in direction opposite to the applied acceleration. The distance it moves is proportional to the magnitude of the acceleration as per Newton's second law as shown below,

$$F_{ext} = m \cdot a = k \cdot x_{proofmass} \quad (1.1)$$

$$x_{proofmass} \propto a \quad (1.2)$$

The displacement $x_{proofmass}$, is basically what needs to be measured in some way or the other to get the value of applied acceleration. There are several types of accelerometer and each has their own technique to measure displacement of the proof mass, $x_{proofmass}$. Some of them are explained briefly below,

1.3.1 Piezoelectric Accelerometer

These types of accelerometers have the proof mass mounted on a piezoelectric material. When the device experiences an acceleration, the proof mass tends to move and presses against the piezoelectric block which in turns generate an electronic voltage. The voltage output can be calibrated and measured to estimate the displacement of proof mass and in turn the applied acceleration [6, 7].

1.3.2 Piezoresistive Accelerometer

These types of accelerometers have piezoresistors embedded in the spring beams which connects the movable proof mass. Under an applied acceleration, the motion of the proof mass results in either tension or compression in the springs which leads to a change in resistance of the piezoresistors. This change in resistance can be calibrated to measure the motion of the proof mass and in turn calculate the applied acceleration [8, 9].

1.3.3 Capacitive Accelerometer

These types of accelerometers have a fixed electrode at a small gap away from the movable proof mass forming a parallel plate capacitor. In response to external acceleration, the proof mass moves and either change the gap between two plates or the overlapping area causing a change in capacitance. This change is a function of the displacement of the proof mass which can be used to calculate the acceleration [10, 11].

1.3.4 Vibrating Beam Accelerometer

Vibrating-Beam or Resonant accelerometers comprises of a proof mass with attached resonant sensors (resonating beam) and elastic beam springs. Under acceleration, the proof mass experiences an inertial force which gets transmitted axially either in form of tension or compression to the resonant sensors. The additional inertial forces act on the stiffness of the beams increasing the resonant frequency in case of tensile force and decreasing the resonant frequency in case of compressive force. This change in frequency of the resonant sensors is a measure of the inertial forces the proof mass experiences which can be used to estimate the applied acceleration [12].

1.4 Gyroscopes

Gyroscopes are used to measure the angular rate of rotation and the angle of rotation. There are mainly two broad categories of gyroscope—optical and vibratory. Other types of gyroscopes also exist including spinning mass, cold atom interferometry, nuclear magnetic resonance etc. The operating principles of a few are briefly described below,

1.4.1 Optical Gyroscopes

Optical gyroscopes work on the principle of Sagnac effect. There are mainly two types of optical gyroscopes—Ring laser gyroscopes (RLG), where light travels in a resonant cavity and fiber-optic gyroscope (FOG) where light travels in a fiber optic. In an inertial frame of reference, light travels at a constant speed in a given medium. If a coherent light beam is split and sent in two opposite direction in a circular non-rotating waveguide (through mirrors placed in resonant cavities in case of RLS and through fiber optic in FOG), the path length is the same for the two light beams and

they meet in-phase. However, when the frame is rotated perpendicular to the plane, one beam sees a longer path while the other sees a shorter path leading to a change in path length which leads to a phase change. This is the principle of Sagnac effect and is shown schematically in Figure 1.3. The phase change contains information related to the rotation speed [13].

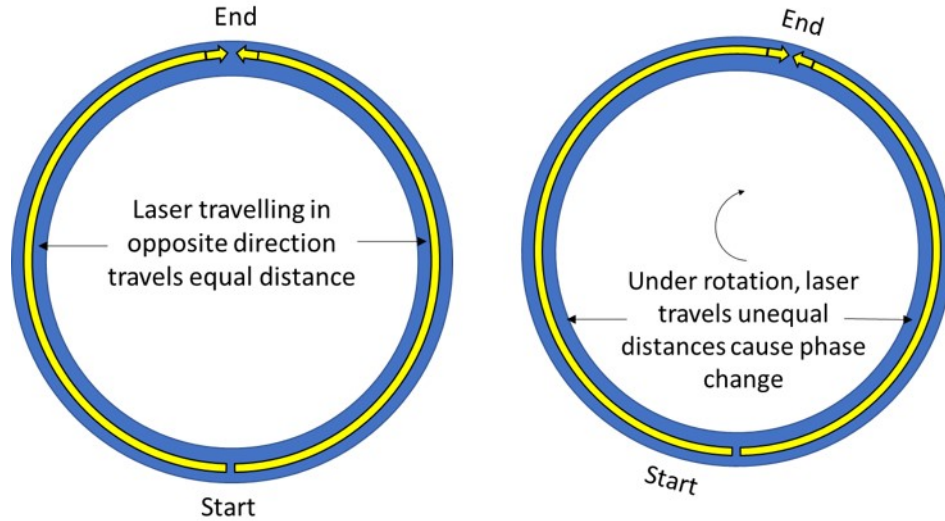


Figure 1.3: Working principle of optical gyroscopes relying on phase change due to path length difference under rotation of two laser moving in opposite direction..

1.4.2 Cold Atom Interferometer Gyroscopes

Atom interferometry is similar to that of light interferometry in a sense that matter (atoms) have wave properties just like that of light. So, a beam of atoms sent out in opposite direction on a rotating frame would combine with an interference pattern containing information related to the rotation rate. Atom interferometry is beneficial over light interferometry as it tends to be more sensitive owing to its short de Broglie wavelengths, and could create a larger phase shift for smaller rotation rate. Cold atom interferometry operates at very low temperature so as to achieve the required velocity or wavelength control of the atom source. In many of atom interference experiments, the role of light and matter is reversed. Like in atom interferometry,

the beam splitters and mirrors are lasers (light) while the emitting source is atoms (matter).

1.4.3 Vibratory Gyroscopes

These types of gyroscope are also known as the Coriolis vibratory gyroscopes (CVGs) as they operate on the principle of Coriolis effect. They consist of a vibrating mass which can be a string, beam, a pair of beams, tuning forks, disc, ring, cylinder, hemisphere etc. anchored at some place. The vibrating mass of these gyroscopes are driven into resonance and under rotation the Coriolis force acts perpendicular to both the velocity of motion and direction of rotation. This causes the vibrating pattern to precess around the sensor frame. The magnitude of force is proportional to the rate of rotation.

Tuning Fork Gyroscopes

Tuning fork gyroscopes (TFG) are perhaps the simplest vibratory gyroscopes. The first TFG fabricated in early 1950s used large metallic forks [14]. The working principle of these gyroscopes can be understood by taking an example of a tuning fork consisting of two tines with square cross section and a stem as shown in Figure 1.4.

Square cross section ensures that the fork has same frequencies in the x and y directions. The tines are driven into resonance in one axis (x-axis shown by red arrows in Figure 1.4(a)) so as to vibrate the tines in-plane moving back and forth. Next, the tuning fork is given a rotation about its stem. It is known that under rotation Coriolis force is applied in the direction perpendicular to both velocity and rotation axis. Due to Coriolis force, each tine experiences a force in the out-of-plane direction. This force causes the tines to start vibrating in its out-of-plane mode

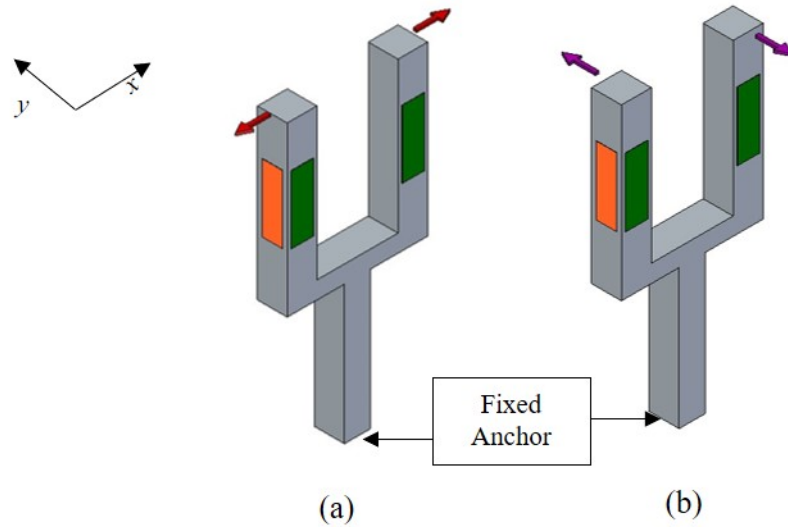


Figure 1.4: Modes of a tuning fork. (a) in-plane mode where the tines vibrate in its plane and (b) out-of-plane where the tines oscillate in direction perpendicular to its in-plane motion.

(shown by violet arrows in Figure 1.4(b)) which can be sensed and measured. The earliest tuning forks however posed many barriers to achieving high performance because of imperfections in their manufacturing, poor material properties, and poor temperature behavior.

Efforts at miniaturizing gyroscopes started in 1970s when a quartz-based TFG with reasonable performance was first demonstrated [15, 16]. It was not until late 1980s that micro electromechanical systems (MEMS) technologies were first attempted and applied by Draper Lab to build a micromachined gyroscope [17]. Their gyroscope consisted of a proof mass supported by several springs. The proof mass was driven into resonance using comb-drive type actuator fabricated monolithically alongside the mass. Under rotation, the proof mass would move up and down and the vibrational motion is captured capacitively by electrodes placed underneath. Since, then many more MEMS tuning fork gyros have been reported based on different versions of vibrating tuning forks. One of them is quad mass gyroscope (QMG) reported in [18]. Here, four resonating masses are used instead of two as in conventional tuning

forks. The four masses move out-of-phase and minimizes reaction forces and moment on the anchor reducing the flow of useful vibrational energy through the substrate. Using the QMG architecture, authors in [18] reported ARW of 0.015 deg/rt-hr and BI of 0.09 deg/hr.

Although the performance of early MEMS gyroscopes in terms of noise and bias stability were not great, advances in technology, device structures, process control, transducer architectures, vacuum packaging, and readout/control electronics have enabled MEMS gyroscopes to provide performance that rivals larger and more expensive optical/mechanical gyroscopes. The most advanced of tuning fork gyros that has been commercially available for many years is from Honeywell which recently reported a near-navigation-grade ARW of 0.006 deg/rt-hr and BI of 0.02 deg/hr [19]. Systron Donner also recently reported near navigation-grade ARW of 0.001 deg/rt-hr and BI of 0.005 deg/hr from their quartz tuning fork gyro [12]. Some tuning fork gyroscope architectures are shown in Figure 1.5.

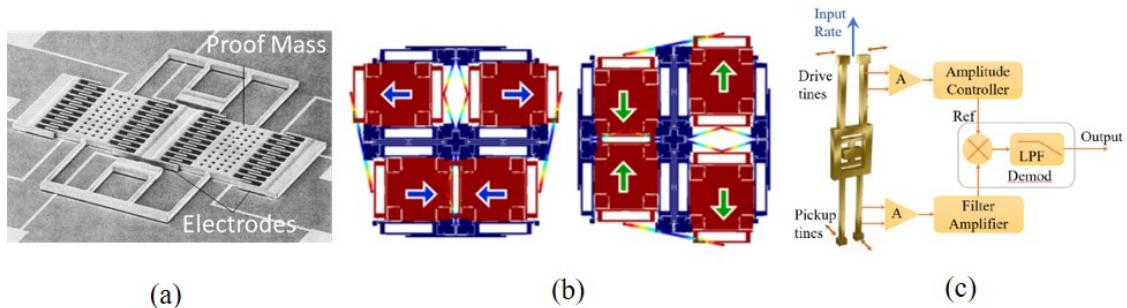


Figure 1.5: Tuning fork gyroscopes from (a) Draper Labs [17], (b) quad mass gyro with the drive and sense modes motion of the four masses [18], (c) tuning fork gyro from Systron Donner with the control architecture [12].

Ring Resonator Gyroscopes (RRG)

Ring type resonators anchored using a central stem have also been used as gyroscopes since mid-1990s. The degenerate modeshape of ring resonators makes them

attractive for use as a gyroscope. These gyroscopes operate in their degenerate wineglass modes usually $n=2$ and $n=3$ wineglass modes. Electrodes are monolithically fabricated surrounding the resonator with small capacitive gap. The resonator is driven in its wineglass modes and the drive amplitude is maintained. Under rotation, the vibrational energy is transferred to its second mode and the motion is sensed by surrounding electrodes. The first ever micromachined ring gyroscope was reported by University of Michigan using electroplated Nickel [20]. Later in 2000s, ring gyroscopes fabricated from single crystal silicon [21] and polysilicon [22] were reported. Some of ring resonator gyroscopes are shown in Figure 1.6. Since then, a lot of research has been conducted and several ring gyroscopes have been reported with improved fabrication and performance some of them for high shock environment application [23]-[27]. Ring gyroscopes have smaller angular gain and small modal mass due to the limited height of the ring possible from microfabrication.

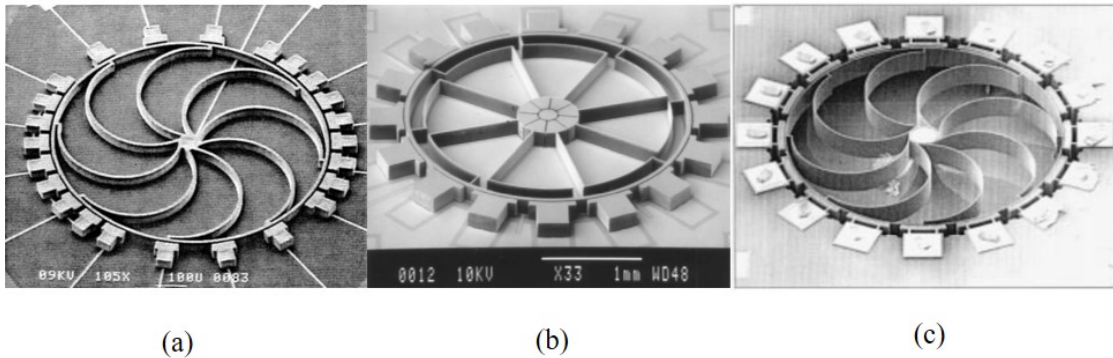


Figure 1.6: Ring resonator gyroscopes fabricated at The University of Michigan using (a) electroplated Nickel [20], (b) Single Crystal Silicon [21] and (c) Polysilicon [22].

Disc Resonator Gyroscopes (DRG)

Disc resonator gyroscopes like ring resonator also operate in their flexural wineglass modes. DRGs differ from RRG in terms of their structure which is a solid disc instead of a ring. Several designs of DRG including solid disc, perforated disc, disc

with several rings, etc. have been reported [28]-[33]. Boeing’s DRG made from silicon micromachining have achieved one of the best performances with ARW of 0.0021 deg/rt-hr and BI of 0.012 deg/hr [28]. More recently, a group from China reported a silicon DRG with ARW of 0.01 deg/rt-hr and BI of 0.04 deg/hr [29]. Another version of DRG with dual mass, inner-mass for drive and outer-mass for sense is proposed to dynamically amplify the amplitude of vibration. This design has achieved ARW of 0.048 deg/rt-hr and BI of 0.6 deg/hr [30, 31]. Some of the DRGs are shown in Figure 1.7. DRGs operating in high frequency $n=3$ wineglass fabricated from DRIE of Silicon Carbide has also been reported and have achieved ARW of 0.06 deg/rt-hr and BI of 0.85 deg/hr [32]. More details on the working principle of wineglass gyroscopes including ring, disc and shell gyros will be discussed in the next section. This thesis is focused on vibratory gyroscopes henceforth, the term “gyroscope” or

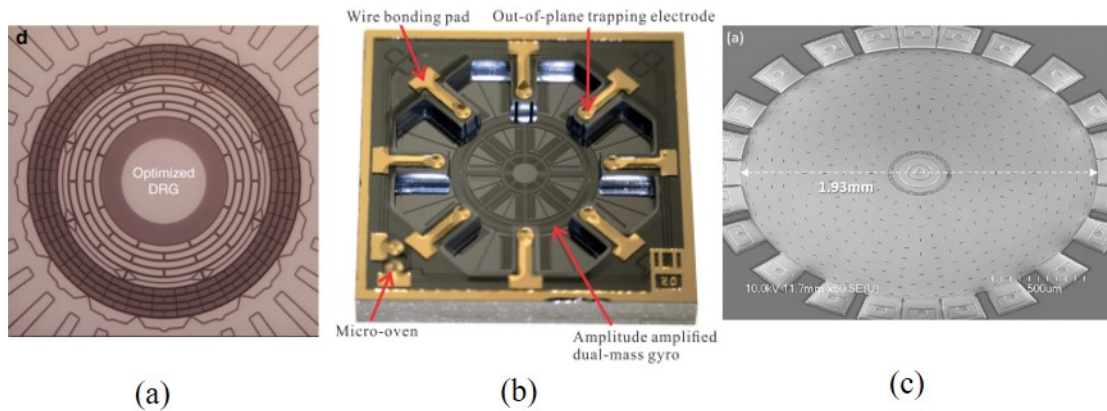


Figure 1.7: Disc resonator gyroscopes (a) fabricated using Silicon [29], (b) with amplitude amplifiable dual mass architecture [31], (c) made from Silicon Carbide [32].

“gyro” would refer to “vibratory gyroscope” unless specified otherwise.

1.5 Vibratory μ -Shell Gyroscopes

Different designs of gyroscopes have been discussed until now. Almost all of them have failed to exhibit high Q, long ring-down time, large effective mass, and

large capacitance at reasonably low frequency all of which are important to achieve navigation-grade performance. Most of these resonators are fabricated from Silicon and are limited by thermoelastic damping (discussed in Chapter II) therefore Q more than a couple of million is hard to achieve. Due to low Q and high frequency, the ring-down time is also small except QMG which has achieved long ring down time (5 minutes) at very low frequency (1.6 kHz). Also, due to their small height (due by fabrication limitation), their modal mass and drive/sense capacitance is small. Therefore, to reach navigation-grade performance 3D structures are more attractive to exploit its large aspect ratio to improve capacitance. Also, new materials like fused silica with innovative designs needs to be explored. At the MEMS scale, micromachining of fused silica is challenging however at the macro scale these can be mechanically machined. Hemispherical Resonator Gyroscopes or HRGs are state-of-the-art gyroscopes which have demonstrated navigation-grade resolution (or very low noise) and can measure the rate of rotation as small as five orders of magnitude smaller than the rotation rate of the earth. HRG technology is commercialized by Northrop Grumman in United States [34]-[38] and by SAFRAN in France [39]-[43] by the name of CrystalTM. Figure 1.8 shows photographs of HRG by Northrop Grumman and SAFRAN. HRGs, because of their large size can be machined out from a fused silica block. They have excellent symmetry and unique design which leads to high Q of more than ten million, very low ARW ($< 1 \times 10^{-4}$ deg/rt-hr) and BI (< 0.001 deg/hr) making them ultra-precise but also ultra-expensive. One HRG typically costs more than 100k USD. They are made using precision trimming of a fused silica block into a hemispherical shell and precision polishing which takes about 3 months. Though they are high performance gyroscopes, their large sizes, high costs and power requirements limit their use in many applications. Therefore,



Figure 1.8: Hemispherical Resonator Gyroscopes containing fused silica shell resonator and electrodes manufactured by (a) Northrop Grumman in USA [38] and (b) SAFRAN in France [39].

miniaturization of shell resonators gained a lot of interest in late 2000s. Several shell gyroscopes made from materials like oxide, diamond, nitride, metals etc. have been reported. Broadly, micro shell resonators can be classified in two categories based on their method of fabrication, (i) thin-film type and (ii) molded type. Micro shell gyroscopes are explained in the next section.

1.5.1 Thin Film μ -Shell Gyroscopes

Thin film type shell gyroscopes are fabricated by depositing a thin film of either oxide, diamond, nitride etc. on a pre-etched hemispherical mold (fabricated by isotropic etching) followed by complete etching of mold to release hemispherical shells [44]-[55]. Figure 1.9 shows the fabrication process and photographs of resonators fabricated by depositing thin films on a sacrificial mold.

Sometime, resonators integrated with electrodes are also fabricated using similar approach. A hemispherical mold is first etched out using isotropic wet etching and electrodes are deposited and defined lithographically. Then, a sacrificial layer is deposited whose thickness depends on the desired capacitive gap. Finally, device layer (diamond, nitride, oxide etc.) is deposited following which the sacrificial layer is etched off to make a resonator and surrounding electrodes separated by a small

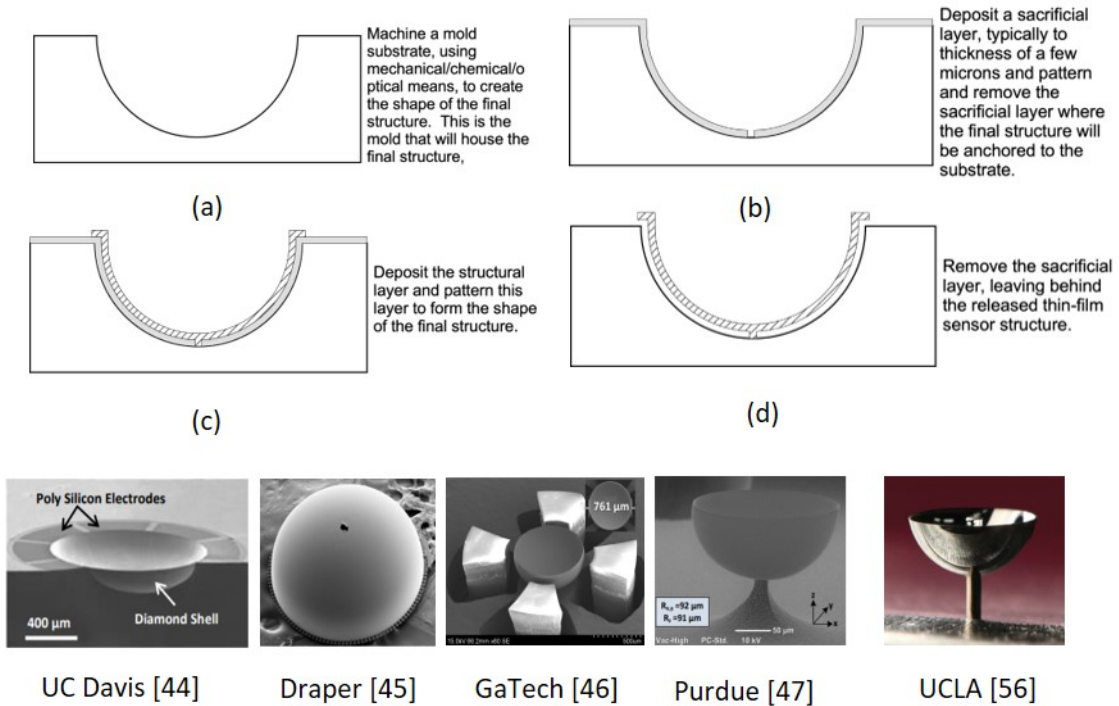


Figure 1.9: Fabrication scheme for manufacturing shell resonators by depositing a thin-film material on a pre-etched mold. Some thin-film resonators.

gap. Figure 1.10 shows the fabrication process and integrated resonators fabricated using this approach. This allows for fabrication of very small, uniform gap and at the same time leads to conformal overlap due to curved nature of the electrodes as shown in Figure 1.10(c). A variation of this process employs blow molding of a thin sheet of Platinum-bimetallic glass (Pt-BMG) at $275\text{ }^{\circ}\text{C}$ instead of deposition on a pre-etched mold [56]. However, all resonators fabricated using this approach have failed to achieve high Q ($Q \ll 1$ Million), due to a combination of damping mechanisms. Moreover, because of limited aspect ratio, intrinsic capacitance is small even though the electrodes are conformal.

1.5.2 Molded μ -Shell Gyroscopes

Most of the shells fabricated using deposition of thin films suffered in Q due to material losses. To obtain high- Q , high quality, low loss material like fused silica

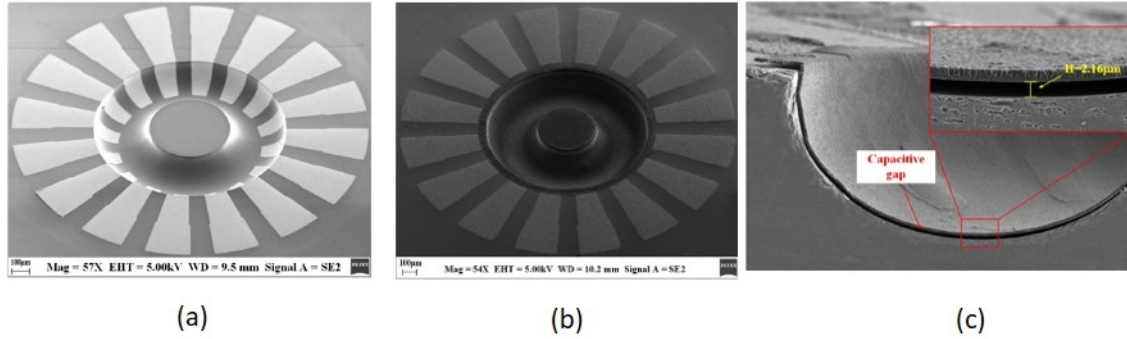


Figure 1.10: Working principle of optical gyroscopes relying on phase change due to path length difference under rotation of two laser moving in opposite direction..

is required. However, microfabrication of fused silica to make 3D structures is not possible. Therefore, specialized fabrication needs to be developed. One method is using molding technique to make high-aspect ratio 3D shells. Mainly two types of molding including glass blowing and blowtorch molding have been demonstrated to fabricate very high Q resonators ($Q > 10$ Million). However, in this approach, the resonators and electrodes are fabricated separately and then integrated together with a small capacitive gap [58]-[62], although in some cases they can also be monolithically fabricated [63, 64]. The process of glassblowing starts by plasma assisted bonding of two fused quartz wafer of different thickness. The thickness of the device layer determines the thickness of the shell and therefore the operating frequency. It is usually between $80\text{--}170\ \mu\text{m}$ thick but the substrate layer is much thicker as shown in Figure 1.11. In different configurations either the device layer or the substrate layer is etched and then the two wafers are bonded to each other so that the etched region is at a predefined pressure. At high temperature, this trapped air expands giving a 3D shape in the form of shell [60, 61],[63]-[67]. Another method of fabricating 3D shells does not need any bonding of substrates. Here a reversed pressure difference is created which causes the substrate to “blow down” at high temperature [68]. Blowtorch molding is explained in detail in Chapter II.

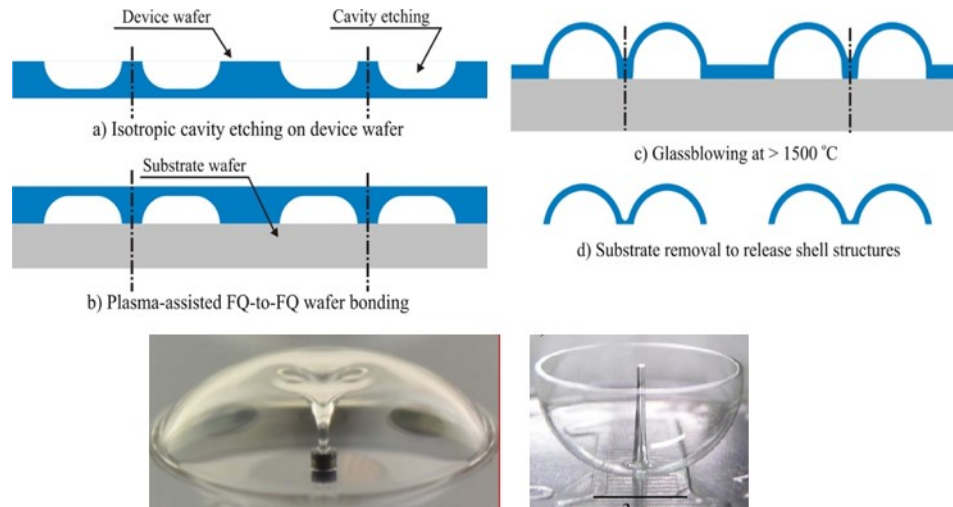


Figure 1.11: Glass blowing process and some resonators fabricated using this approach at UC Irvine and Southeast University, China.

1.5.3 Working Principle

Most CVGs comprise of a resonating mechanical structure and relies on the Coriolis force generated in the rotating frame of reference to sense the rate of rotation. A gyroscope with a cylindrically symmetric mechanical resonator such as a wineglass has identical frequencies for flexural modes, so called the wine-glass modes (WG). For example, consider a wineglass as shown in Figure 1.12. Now when the rim of the wineglass is stuck with a finger, the rim starts to resonate in its resonant mode shapes. The $n=2$ WG modes (i.e. WG modes whose displacement pattern have two nodal diameters), have two elliptical displacement patterns each offset at an angle of 45 degree to each other as shown in Figure 1.12(b). Similarly, the $n=3$ WG modes (i.e. WG modes whose displacement patterns have three nodal diameters), have three-sided star shaped displacement pattern separated at an angle of 30 degrees to each other as shown in Figure 1.12(c). Similarly, there are higher order modes which are usually not used for gyroscopic application due to their high frequencies. Consider a resonator deforming in one of its degenerate mode. Now the entire sys-

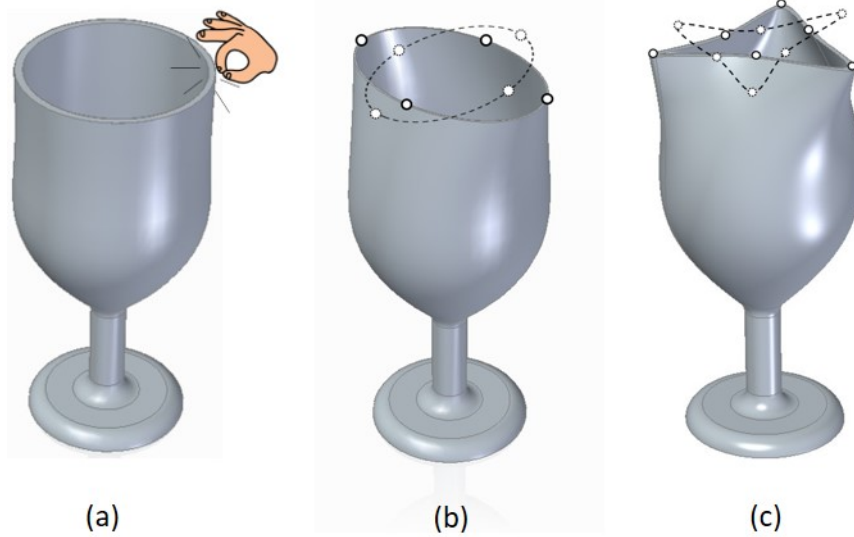


Figure 1.12: Modeshapes in wineglass type resonators. When a perfectly symmetric wineglass as shown in (a) is stuck at the rim, the rim vibrates. (b) The $n=2$ wineglass mode is in the shape of ellipse and has two nodal diameter, the dots shows the position of maximum displacement or anti-nodes in first cycle of vibration and dashed lines shows the second cycle of vibration. Similarly (c) the $n=3$ mode of vibration has three nodal diameter and is in the shape of a star.

tem is rotated about its axis of symmetry. Under rotation, the Coriolis force acts perpendicular to the direction of motion (\vec{v}) and the rotation axis ($\vec{\Omega}$) and is given by,

$$\vec{F}_{Coriolis} = 2kM\vec{v} \times \vec{\Omega} \quad (1.3)$$

To operate it as a gyroscope the shell is driven by one of the many transduction schemes which are discussed in the next section. They are driven in one of its resonant mode called *drive mode*. At this stage vibrational amplitude and energy is maximum in this mode as shown in Figure 1.13(a) where energy is maximum in mode 1. Under rotation, the Coriolis force (\vec{F}_C) acts perpendicular to the initial direction of motion and the direction of rotation axis at different part of the shell is shown in Figure 1.13(b). Due to this force, energy starts to transfer from this mode to the second mode called *sense mode* as shown in Figure 1.13(c). The Coriolis force as

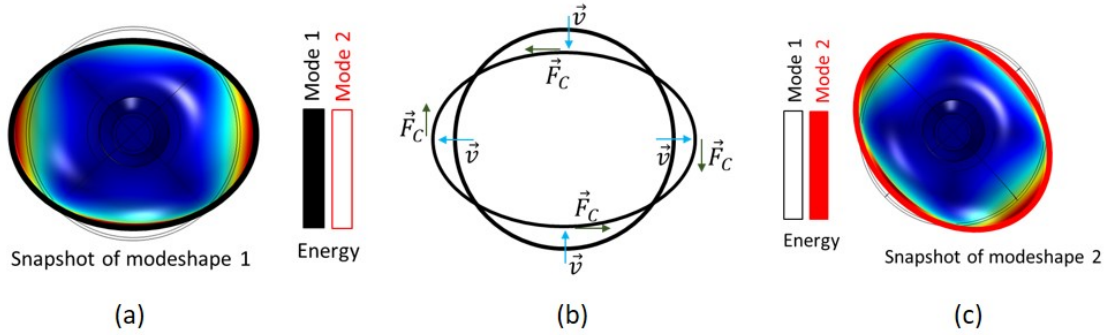


Figure 1.13: (a) The shell is driven in its ‘drive mode’, (b) under rotation the Coriolis force acts on the shell and (c) transfers energy into the second mode where the motion is sensed and the rate of rotation is determined.

given by Equation 3 causes amplitude to rise in the sense mode which is proportional to the rate of rotation. To ensure maximum vibrational amplitude in the sensing mode, it is essential for both the modes to have closely matched frequencies. This is because Coriolis force which is responsible for driving the sense mode motion is at the drive mode frequency. When the drive and sense modes have same frequency, Coriolis force will lead the sense mode to resonance. Resonance in sense mode would mean larger sense amplitude improving sensitivity. In the next subsection, different methods of driving and sensing a gyroscope is discussed.

1.5.4 Transduction Mechanism

Gyroscopes can be driven and sensed by different transduction mechanisms. Popular among them are electrostatic and optical methods. This section briefly describes both these techniques,

Electrostatic Transduction

Electrostatic transduction is one of the most popular transduction mechanisms used in MEMS sensors and actuators. This technique employs the use of parallel plates to form a capacitor where one plate is fixed (electrodes) while the other plate

is movable (shell resonator). These two plates are separated by a small capacitive gap which can be between $10\text{--}50\ \mu\text{m}$. In PSI gyroscopes the electrodes can be placed so as to measure the in-plane motion or out-of-plane motion. In this thesis, they are referred to as ‘side electrode configuration’ and ‘surface electrode configuration’, respectively as shown in Figure 1.14. Chapter IV will discuss the design and fabrication of electrodes as well as assembly process of the gyros.

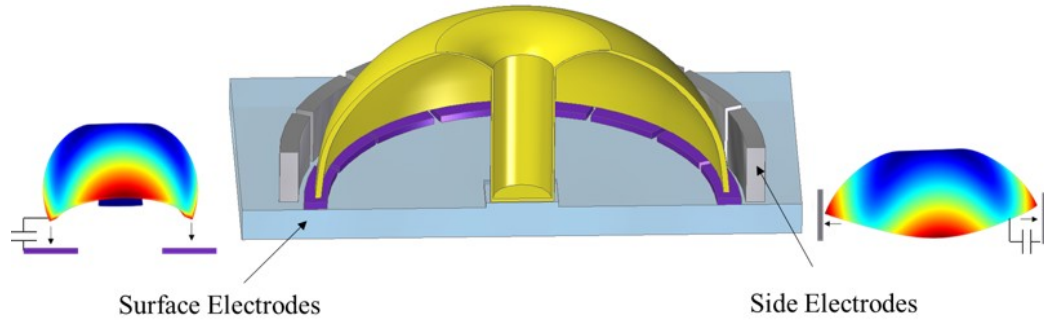


Figure 1.14: Electrode configuration in shell resonator gyroscopes. The electrodes can be placed either at the bottom to sense out-of-plane motion or can be placed at the side to sense in-plane motion.

The shell is DC biased to a fixed voltage. The surrounding electrodes at 0 degree is used to drive the shell in resonance and maintain a fixed drive amplitude using closed-loop operation. Under rotation, energy transfer takes place from the drive mode to the sense mode as shown in Figure 1.13. Depending on the mode of operation, an amplitude buildup in the sense mode is either allowed (open-loop mode) or suppressed by opposing force from the sense electrodes (closed-loop mode). Either way, the surrounding electrode located at 45 degree to drive electrode (in case of $n=2$ mode of operation) or 30 degree (in case of $n=3$ mode of operation) participates to determine sense motion by either measuring the change in capacitance due to resonator motion or by determining the voltage (force) needed to nullify this motion. Determination of capacitance or force quantifies the amplitude of the resonator which is used to measure rate of rotation as explained in Section 1.5.3.

Opto-Electro Transduction

Another popular transduction mechanism is optical sensing. In this technique, the resonator is driven at resonance just like electrostatic driving, however, the sensing is done optically through laser interferometry. The details of optical transduction can be found in [69].

Depending on the application, these gyroscopes can be operated either as rate gyroscopes (RG) or rate-integrating gyroscopes (RIG) also known as the Whole-angle mode. In the next subsections, the operating principles for both RG and RIG and their associated characteristics are discussed.

1.5.5 Rate Gyroscopes (RG)

Rate Gyroscopes are used to measure rotation rate. There are two major sensing mechanisms in this mode of operation namely the open-loop mode and the closed loop mode (also called as force-rebalance mode). In open-loop mode a gyroscope is driven at a fixed amplitude in its drive mode. Under rotation, the Coriolis force causes the amplitude to build in the sense mode. The ratio of the vibrational amplitudes in the two modes is given by,

$$\frac{u_{sense}}{u_{drive}} = 2Q \frac{\Omega_z}{\omega} \quad (1.4)$$

where, u is the corresponding amplitude, Q is the mechanical quality factor, ω is the resonance frequency of the two modes and Ω_z is the rotation rate. Figure 1.15 shows the idea of open-loop mode of operation. The amplitude in the sense mode can be measured through measurement of change in capacitance to determine the rotation rate. As can be seen from Equation 1.4, the sense mode amplitude (u_{sense}) is directly proportional to Q and inversely proportion to frequency. This is

because when the device has a high Q , it is less prone to random vibrations and thermomechanical noise.

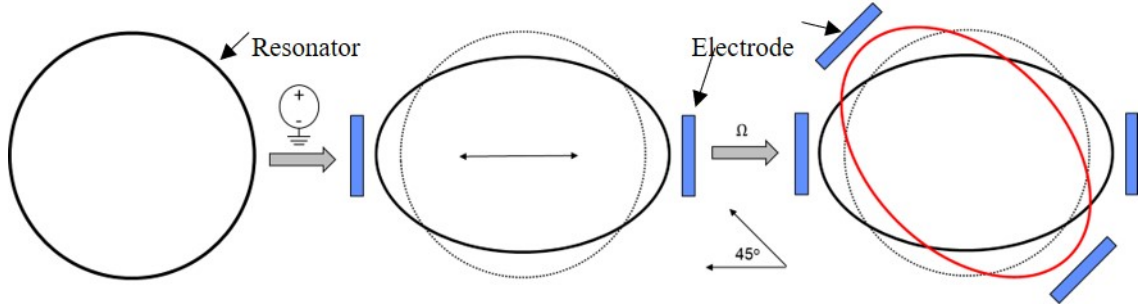


Figure 1.15: Schematic representation of open-loop mode operation. The gyroscope is electrostatically driven in one of its mode, under rotation, the amplitude build-up in the sense mode is sensed by the surrounding electrodes.

Also, small frequency enables large deflections due to low stiffness. Therefore, high- Q and low frequency device is crucial to increase the scale factor of gyroscope in open-loop RG mode. This mode of operation relies on the amplitude build-up in the sense mode which takes time. As a result, the response to rotation-rate is not instantaneous which limits the gyroscope bandwidth. This is overcome by operating the gyroscope in close-loop mode. In close-loop mode, also known as the force-rebalance mode, the gyroscope is driven to a fixed amplitude in the drive mode just as the open-loop mode. However, instead of allowing the amplitude build-up in the sense mode as is done in open-loop mode, a counter force is applied in the sense direction to nullify the Coriolis force and inhibit any motion of the resonator. Figure 1.16 shows the idea of closed-loop mode of operation.

The rotation rate can then be calculated using the relation,

$$\frac{f_{sense}}{f_{drive}} = 2Q \frac{\Omega_z}{\omega} \quad (1.5)$$

where, f is the applied force in the drive and sense mode. Like RG mode, the sense mode force is proportional to Q and inversely proportional to frequency. As

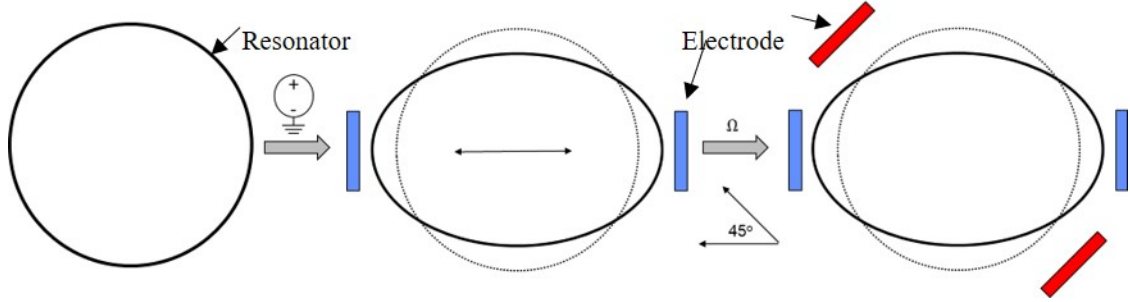


Figure 1.16: Schematic representation of closed-loop mode operation. The gyroscope is electrostatically driven in one of its mode, under rotation, the amplitude build-up in the sense mode is suppressed by applying a voltage by the surrounding electrodes.

a result, high-Q and low frequency devices are necessary to increase the scale factor of gyroscope. Since there is no amplitude buildup in the sense mode, the response to rotation rate is quicker and the bandwidth is increased. However, the feedback electronics induces noise in the system.

1.5.6 Rate-Integrating Gyroscopes (RIG)

RIGs are used to measure the angle of rotation. In this mode of operation vibration is induced and the sensor frame is rotated. While the sensor frame follows the input rotation, the vibration pattern however lags behind. The vibration pattern shifts its axis of vibration because of the Coriolis force and lags behind the "true" angle by a precession angle θ_{gyro} relative to the true rotation angle or rotation angle of the sensor frame, θ_{true} . The ratio of the two angles is defined as angular gain, A_g .

$$A_g = \frac{\theta_{gyro}}{\theta_{true}} \quad (1.6)$$

A_g depends on the geometric parameters of a resonator and is therefore stable with temperature variations over lifetime of sensor. Its value is 1 for an ideal tuning fork type gyroscope although due to inevitable non-idealities, $A_g < 1$. For a shell gyro A_g is ~ 0.3 . This means when a gyro is rotated by 90° the vibration pattern

lags by $\sim 27^\circ$ as shown in Figure 1.17. Once angular gain is known, rotated angle can be determined using the relation,

$$\theta_{true} = \frac{\theta_{gyro}}{A_g} \quad (1.7)$$

Angular gain is an important parameter determining the device performance in whole angle operation mode and is therefore a measure of scale factor in this mode. Figure 1.17 illustrates the operating principle of a wineglass resonator in the RIG mode.

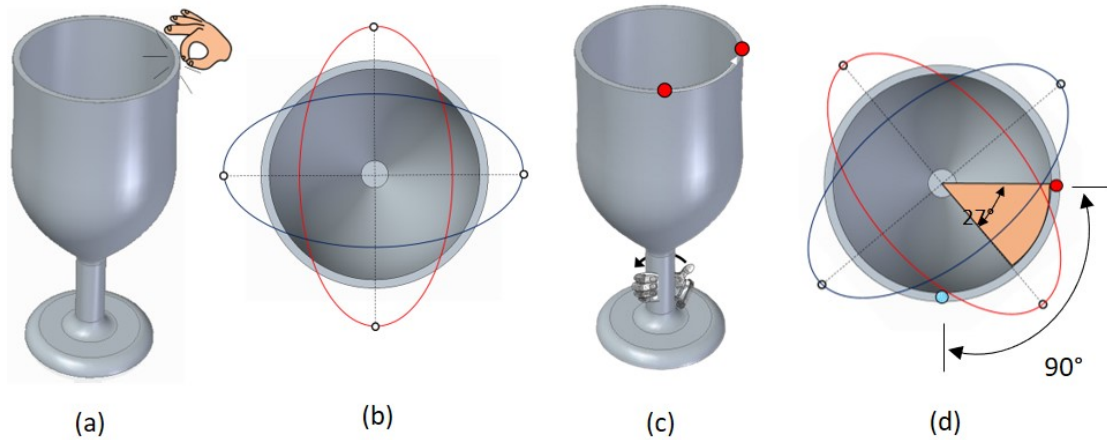


Figure 1.17: (a) When a wineglass is excited at its $n=2$ resonant frequency, (b) the rim (as seen from the top) starts oscillating in an elliptical pattern. (c) Now when the wineglass is rotated by an angle of 90 degree from its stem, (d) the reference point (shown in red dot) moves 90 degree but the pattern of vibration lags by 27 degree.

In the next section, sources of error and their mitigation strategies are discussed.

1.5.7 Sensor Parameters

Performance of an inertial sensors is characterized by several parameters including sensitivity, resolution, and accuracy.

Sensitivity

Sensitivity is defined as the change in output signal per change in input signal. For example, if a gyroscope when subjected to a rotation rate of 1 deg/hr (X) generates an output signal of 1 mV (Y), then the sensitivity is defined as Y/X which in this case would be 1 mV/deg/hr. In other words, sensitivity is the slope of the input-output plot as shown in Figure 1.18. Sensitivity in gyro community is usually called scale-factor. A large value of scale factor means larger slope on the input-output graph. This would mean for a small change in input, there would produce a large output signal which is desirable because large signals are easier to measure.

Resolution

Resolution is the smallest rotation signal which the sensor can reliably measure. This number is primarily determined by the noise from the sensor. The source of noise could be the mechanical resonator, the electronics or both. For example, consider a gyroscope sensor with a noise of 1 deg/hr. Now, if this gyroscope is rotated at the rate of 0.5 deg/hr, the rotation signal would be indistinguishable from the noise. Therefore, the resolution or minimum detectable signal of this sensor is 1 deg/hr. The earth rotates 360 degree in about 24 hours, so the rotation rate of earth is ~ 15 deg/hr. A high performing gyroscope have very fine resolution (or very low noise) meaning they can measure even minute changes in rotation angle or rate of rotation. Noise is characterized by Angle random walk or ARW of a gyroscope and it determines the resolution for a gyroscope. The larger HRGs for instance have a noise of $< 1 \times 10^{-4}$ deg/hr which means it can measure rotation as small as five orders of magnitude smaller than the rotation of earth.

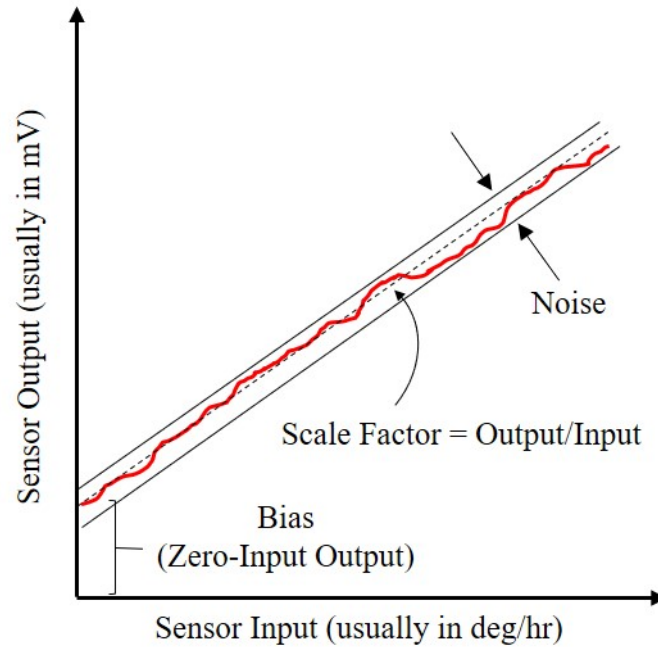


Figure 1.18: A sensor's input-output curve. Slope of the plot is called the scale factor or sensitivity and the intercept on y-axis (at zero input) is called as bias.

Accuracy

Accuracy is deviation of the measured signal from the actual signal. To understand accuracy, it is necessary to talk about bias instability first. Consider an idle gyroscope with zero rotation. In this case, there ideally should not be any output signal. However, almost all sensors experience some output even when the input is zero and this is called zero-input output or bias. Bias can be determined by the input-output graph of Figure 1.18 by reading the intercept on the y-axis which is the output at zero input. To understand this, let us consider a gyroscope with sensitivity of 1 mV/deg/hr. Consider this gyro has a bias (or offset) which is fixed at 1 deg/hr. Now when the gyro is given a rotation of 1 deg/hr, the gyro output would be 2 mV (1 mV due to actual rotation and 1 mV due to bias offset). If we know the bias offset, we can calibrate and subtract 1 mV from the output to get actual output

data. This measured signal (1 mV) is then accurate as it corresponds to the actual rotation (1 deg/hr). Now consider another case where the bias offset is not constant, and it fluctuates between say 1–2 deg/hr. In this case, if we subtract 1 mV from the output signal as before then we may end up with a wrong value as the voltage corresponding to bias offset could be anything between 1–2 mV. In such cases, the accuracy of the sensor is compromised. Therefore, one would want to minimize the bias drift as much as possible. The bias drift is interchangeably referred to as Bias Stability or Bias Instability (BI) which is the instability (drift) of bias.

The range of the values of ARW and BI determine the grade of gyroscope. ARW better than 1×10^{-3} deg/rt-hr and BI better than 0.01 deg/hr is called navigation grade performance. ARW and BI will be discussed in the next section.

1.6 Errors in Inertial Sensors

As described earlier, dead reckoning using inertial sensors requires integrating the sensor outputs. This leads to an accumulation of error over time leading to incorrect final position. To effectively use dead reckoning, the sources of errors needs to be understood and mitigated. This section discusses the major errors pertaining to gyroscopes and their sources which leads to a deterioration in sensor performance. Errors in gyroscopes can be in the form of bias, random noise, nonlinearity, scale factor errors, vibration-induced errors etc. Errors in gyroscopes or any inertial sensors are categorized into systematic errors and random errors. As the name suggests systematic errors have a fixed value for each sensor while random errors usually have a range. Systematic errors further have four components, a fixed value error, a temperature-dependent error, a run-to-run variation and an in-run variation.

- *Fixed value error* - This error type has a fixed value for each sensor which can

be offset using the control architecture.

- *Temperature-dependent error* – These originate due to variations in surrounding temperatures. Error in signal due to temperature can also be calibrated and offset using the circuitry. If this error is not compensated for, the signal shows variation when the sensor starts and is still warming up to its normal operational temperature and when temperature fluctuates.
- *Run-to-run variation* – The run-to-run variation as the name suggests is the variation in sensor output every time the sensor is activated. This is different each time the sensor is used but is constant over a run. This type of error cannot be compensated by the IMU circuitry but needs to be taken care of by the INS alignment or integration algorithms.
- *In-run variation* – In-run variation is the variation in sensor output during a run either naturally or during a sudden event such as shock. Over time, the sensors' output slowly drifts leading to erroneous output. This error cannot be calibrated by the IMU or INS algorithms, but it needs to be corrected using reference data from other navigation sensors.

1.6.1 Scale Factor Error

Scale factor errors are characterized by an incorrect or non-linear input-output plot. This can take place if the vibration amplitude (or change in capacitance) is different than it should be. This erroneous change in capacitance could either be due to non-uniform or varying capacitive gap from fabrication imperfection or from CTE mismatch between the resonator and electrode material, respectively. Scale factor drift is a major cause of error responsible for non-accurate sensor output. These errors can significantly reduced by ensuring a uniform capacitive gap around

the sensor, making the sensor and electrode of the same material, using differential sensing by placing electrodes both inside and outside of the resonator so when one gap increases, the other would decrease leading to a constant final amplitude of vibration. Finally, the temperature can be constantly measured, and the voltages can be adjusted through a closed loop system to maintain constant scale factor.

1.6.2 Bias Error

Bias or the zero-rate output is the sensor output when the input is zero and is given in $^{\circ}/\text{hr}$. All gyroscopes exhibit a constant bias i.e. it exhibits a finite output even when there is zero input. Bias are of two types static bias and dynamic bias. Static bias, also known as fixed bias, turn-on bias, or bias repeatability is fixed during a run but could vary between runs and therefore they comprise the run-to-run error. Dynamic bias, also known as in-run bias variation or bias instability (BI) constitutes the random error. BI can be attributed to imperfections in resonator, temperature fluctuations, stresses etc. At stable temperature with isolation from environmental vibrations, BI is dominated by the damping asymmetry which is the difference of inverse of ring-down time constants of the two modes as given in Equation 1.8.

$$BI \propto \Delta \frac{1}{\tau} \quad (1.8)$$

Ring-down time constant (τ) is defined as the time taken for the resonator amplitude to decay to $1/e$ of its initial amplitude as shown in Figure 1.19.

A perfectly balanced and symmetric resonator would have the two modes with same frequency and τ . This means that the stiffness and damping axes are essentially aligned. In such cases, the vibrating pattern can freely precess in response to rotation. However, due to fabrication imperfections, the two modes split up with a separate

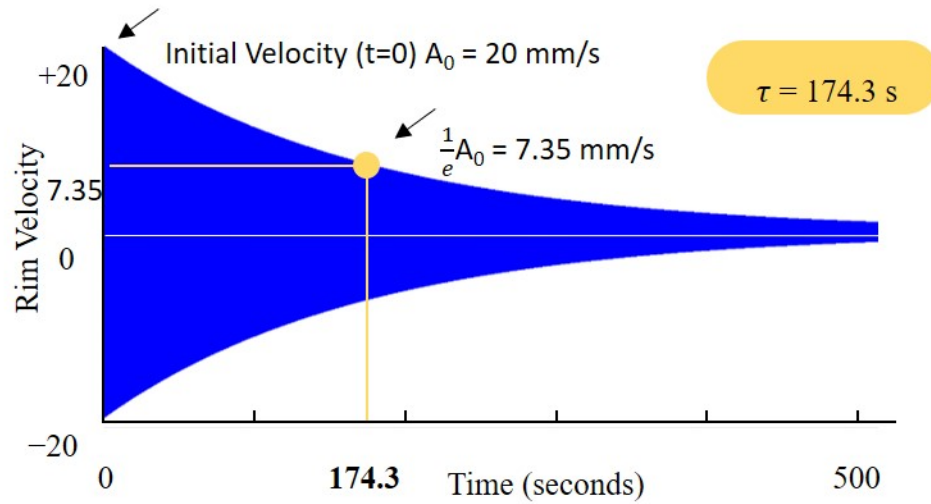


Figure 1.19: Measured ring-down of a resonator. Ring-down time is calculated by measuring the time taken for the amplitude (or velocity) to decay to $1/e$.

frequency and τ for each mode. Besides, τ also shifts (not necessarily in the same way) due to changes in temperature and vacuum pressure. These imperfections lead to fixing of the principle axes. Besides, the stiffness and damping axes are no longer aligned. In such cases, an erroneous force will be generated due to the anisotropic damping to change the orientation of the antinode of the standing wave. This force is not distinguishable from the Coriolis force and will create bias drift. Long ring down time constant would mean lower damping mismatch, $\Delta \frac{1}{\tau}$, leading to a lower BI. ARW and BI (discussed next) and several other random drifts are characterized through the Allan variance plot. An Allan variance plot is generated by obtaining output data for a long time from a stationary gyroscope. ARW is determined by reading the value corresponding to integration time = 1 second and slope = $-1/2$. BI is determined by reading the lowest value on an Allan variation plot which is the lowest noise floor as shown in Figure 1.20.

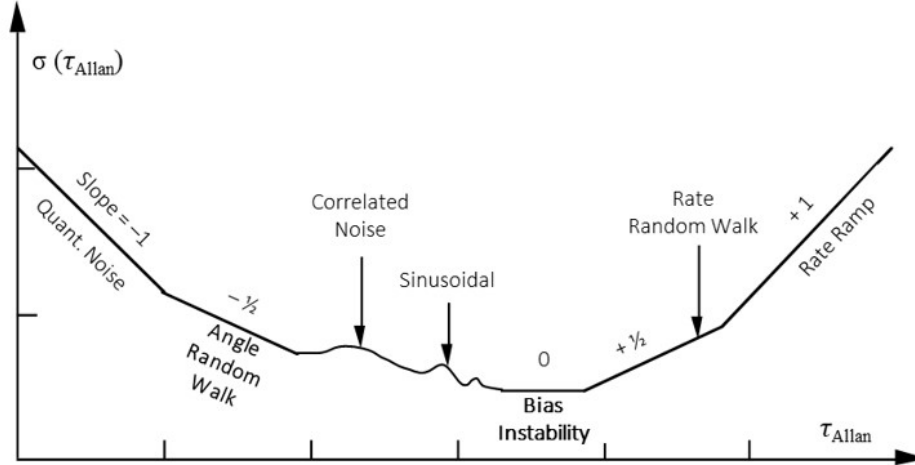


Figure 1.20: Allan variation plot of a gyroscope showing different dominant noise sources at different sampling time. ARW is read by reading the y-axis value at $t=1$ second and BI is determined by reading the lowest value on the plot.

1.6.3 Angle Random Walk

Angle Random Walk or ARW is the error in measured angle either due to thermo-mechanical Brownian noise (mechanical ARW) or due to the associated circuitry (electrical ARW). It is usually given in $^{\circ}/\sqrt{h}$ and corresponds to the value with $-1/2$ slope on the Allan variance plot. ARW determines the resolution that the gyroscope can reliably measure. For a mode matched gyroscope (with identical drive and sense mode) with high Q , ARW is dominated by the mechanical noise and it given by Equation 1.9 [70, 71].

$$ARW_{mech} = \frac{1}{2A_g q_{drive}} \sqrt{\frac{k_B T Q}{M_{eff} \omega_o}} \sqrt{\left(1 - \left(\frac{\omega}{\omega_o}\right)^2\right)^2 + \left(\frac{\omega}{Q \omega_o}\right)^2} rad/s \quad (1.9)$$

To have a high-performing gyroscope, a) the scale factor (sensitivity) should be increased and b) both the noise and the bias instability should be reduced. For this, the resonator of a gyroscope must have a) close mode matching ($\omega_{drive} = \omega_{sense}$), high Q , high frequency, large effective mass (M_{eff}) and a large driving amplitude (q_{drive}). Besides, they should be tolerant to harsh environment particularly high

shock and temperature variations. In the subsequent paragraphs, improvement in each parameter for a shell resonator is discussed to achieve low ARW and BI.

- *Mode Matching* - The sensing scheme can be either by sensing change in amplitude (AM) or by change in frequency (FM). In AM gyroscopes, the amplitude of vibration (in case of open-loop mode) or the voltage (force) required to suppress the amplitude buildup (in closed-loop mode) in the sense mode is proportional to the angular rate of rotation as discussed earlier. As a result, to enhance the sensitivity it is extremely critical to have the two modes closely matched (in the range of few tens of mHz) to get the benefit of large deflection at resonance. For example, in the case of a tuning fork gyro discussed in Section 1.4.3, consider the tines are vibrating in the x-direction (driving mode) and under rotation the tines start vibrating in y-direction (sense mode) due to Coriolis force. The Coriolis force (in the sense direction) has the frequency of drive mode. If there is a frequency mismatch between drive and sense modes, the sense mode will not respond to rotation and the vibration pattern will essentially be fixed in the x-direction. This is because the Coriolis force would be unable to excite the sense mode into resonance because its frequency is no more at the frequency of Coriolis force. Therefore, it is important to have a mode matched device ideally with zero frequency mismatch. However due to unavoidable manufacturing imperfections, the resonators often experience a finite frequency mismatch (>10 Hz). This mismatch can be reduced by either physical trimming or adding mass to tune mass and stiffness or they can be electrically tuned by electrostatic softening. All these techniques have their own limitations. While physical trimming can match large frequency mismatch but can reliably be done only on large devices like the HRGs. On the other hand, electrostatic tuning cannot match a

large frequency split due to limitation on applied voltages and gaps. As a result, at micro scale, the best bet is to fabricate an intrinsically low frequency mismatch resonator and then fine tune electrostatically. Figure 1.21 shows the effect of $\frac{\Delta f}{f}$ on ARW for different Q . It can be seen that increasing Q can be counter productive if Δf is large.

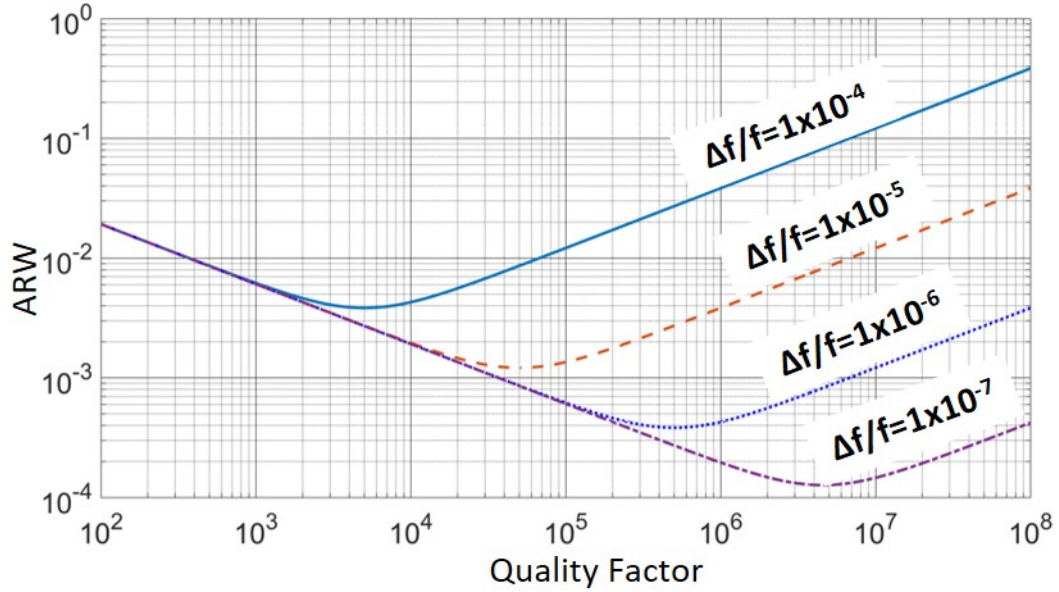


Figure 1.21: Variation of $\frac{\Delta f}{f}$ on ARW. Large frequency mismatch limits the sensor noise even if Q is large.

- *Quality Factor* – The next important requirement from the resonator for high performance gyroscope is high-quality factor or Q . Q is defined as the capability of a resonator to contain the vibrational energy. A high- Q resonator would dissipate energy slower than that of a low- Q resonator. Q is given by $Q = \pi \cdot \tau \cdot f$, where f is the operating frequency and τ is the ring-down time constant. Ring-down time constant as described in the previous section is the time taken by the amplitude of vibration to decay to $1/e$ of its initial value. A high Q device would exhibit long ring-down time constant (meaning it will dissipate the energy at a slow rate) and vice versa. To have high Q resonators, it is critical to study the

dissipation mechanisms and address the mitigation method in the design of the device. Section 2.4 discusses the causes of energy dissipation in shell resonators.

- *Frequency of Operation* – As can be seen from Equation 1.6.3, the operating frequency is root-inversely proportional to noise. Therefore, a higher operating frequency is desirable for gyroscope. For navigation grade gyroscope, long τ (> 100 second), large driving amplitude ($q > 1\mu m$) and large scale-factor (> 100 mV/dps) are also important alongside high Q [28, 70]. All these parameters depend on operating frequency, f . First, τ and f have inverse relation for constant Q ($Q = \pi \cdot \tau \cdot f$). As a result, high frequency operation would reduce τ . Second, a high frequency device, because of large stiffness would lead to lower drive amplitude, q , at a fixed voltage. Third, scale-factor is proportional to both q and τ for fixed voltage and gap. Finally, extent of frequency mismatch tuning would be smaller for high frequency devices as compared to low frequency devices at constant voltage because of large stiffness. It is therefore clear that although increasing f improves ARW, it is actually detrimental to the overall sensor performance. Therefore, frequency of operation should be placed between 5–20 kHz—much higher than environmental frequency floor and low enough to ensure large deformation and long τ .
- *Modal Mass* – Modal mass of the resonator is defined as the mass of the resonator which moves at resonance. Modal mass (or effective mass) like frequency has a root-inverse proportionality to angle random walk as can be seen in Equation 1.6.3. Therefore to obtain low noise the resonator should have a large modal mass. This can also be thought intuitively as a bulky resonator is less likely to be affected by random thermomechanical motion as compared to a light-weight

resonator. Modal mass can be increased by either increasing the thickness of the rim or by increasing the size and/or height of the resonator. While increasing rim thickness directly influences operating frequency, increasing size and height can achieve large modal mass without affecting f and are therefore more desirable. In this thesis, the resonators are designed to have radius = 5 mm, height 5mm, rim thickness 200–300 μm which provides large modal mass (8–10 mg) at desired $n=2$ wineglass frequency (5–12 kHz).

1.6.4 Shock and Vibration Sensitivity

A navigation grade gyroscope mainly finds its application in defense and military vehicles which experiences shock as high as several thousands of g . Therefore, along with high performance, these gyroscopes should also be tolerant to very high shock and be insensitive to vibrations from the environment. For a 3-dimensional shell resonator, both these parameters are dictated by the magnitude of parasitic mode frequencies, $f_{parasitic}$ (tilting and vertical modes) as well as their placement with reference to the operating $n=2$ mode frequencies, $f_{n=2}$, of the gyroscope. Under an event of shock, the resonator experiences displacement leading to stress accumulation (σ_{shock}). When $\sigma_{shock} > \sigma_{MaxTensile}$, the structure experiences damage. Shock survivability is therefore dictated by the lowest $f_{parasitic}$ as the resonator is most flexible in that mode. When the acceleration frequency is outside the parasitic mode bandwidth, the magnitude of deflection, d , under an acceleration magnitude, a , caused due to shock is:

$$d \propto \frac{a}{f_{parasitic\ lowest}^2} \quad (1.10)$$

and when the acceleration frequency is within the parasitic mode bandwidth,

magnitude of deflection is:

$$d \propto aQf_{parasitic\ lowest} \frac{a}{f_{parasitic\ lowest}^2} \quad (1.11)$$

Therefore, to have very high shock survivability, it is critical to a) select material with high $\sigma_{Max.Tensile}$ and b) design the resonator to have low parasitic deflection. The shell resonator in this work is made of fused silica which has a $\sigma_{Max.Tensile}$ 2GPa. To ensure low parasitic deflection, the sidewall profile is tuned. Interference from environmental vibrations is another cause of drift in performance of gyroscope. Vibration sensitivity is also influenced by $f_{parasitic\ lowest}$ as well as $f_{parasitic}$ lying in the bandwidth of the gyroscope from $f_{n=2}$. Deflection in $f_{parasitic\ lowest}$ mode due to vibrations changes the capacitive gap between the electrode and resonator and therefore mismatches the otherwise matched $f_{n=2}$ modes. At the same time any $f_{parasitic}$ in the gyroscope bandwidth from $f_{n=2}$ affects sensitivity as Coriolis forces would excite these modes. Therefore, to have vibrations insensitivity, the mechanical resonator should have a large $f_{parasitic\ lowest}/f_{n=2}$ and $f_{parasitic}$ should be located outside the bandwidth of the gyroscope from $f_{n=2}$. To incorporate all the features as discussed above to have a low cost miniaturized (10 mm diameter) high-performance gyroscope, this thesis is focused on design, fabrication and testing of high performance (very low ARW and BI) shell resonator gyroscope, called PSI Gyroscopes with low intrinsic frequency mismatch, very high Q, large modal mass and high shock tolerance for application in gun-launched munitions.

1.7 Research Objective and Contributions

Development of miniaturized high-performance gyroscopes have been an area of research from past many years. Several groups around the world including at The

University of Michigan have been actively researching on developing miniaturized gyroscopes with high precision. Still several challenges have not been mitigated and questions are unanswered which has been limiting successful development of such sensors. This thesis is aimed at successful mitigation of those challenges to develop navigation-grade micro-gyroscopes and advancing the understanding of scientific community through lessons learnt during the course of this research. A high performance CVG is largely dependent on the performance of its mechanical resonator. The parameters which define the performance of a resonator include, high-Q, low frequency mismatch, high shock resistance and long ring-down time constant. Additionally, to increase the scalability of these micro-gyroscopes, the fabrication process needs to be both scalable and cost affordable. This research is aimed at tackling each of the above-mentioned parameter focusing on:

- Understanding material and structural sources of damping and frequency mismatch and optimize design and fabrication methods to fabricate fused silica 3D shells using blowtorch molding to obtain >12 million quality factor and < 2 Hz frequency mismatch for application in navigation-grade micro gyroscopes and other resonant sensors and actuators. These results are repeatable and consistent.
- Development of a new 3D shell design and fabrication technologies to selectively tune mass and stiffness by locally varying thickness to either make certain regions thick/thin or have open windows on the surface of shells. Such tuned 3D shells with thick/thin regions on surface of shells have quality factor > 7 Million and < 2 Hz frequency mismatch. These are important for low noise and high shock tolerant sensors and actuators. 3D structures with open windows find application for use as 3D shadow mask and as a resonator with very low anchor

loss.

- Development of a novel technology to release 3D shells for use as a resonator using HF acid. This technology reduces cost by more than 25 times and reduces fabrication time by half alongside getting high quality factor and low frequency mismatch. This technology also enables mass fabrication without any sophisticated tools or expensive consumables.
- Development of Precision Shell Integrating gyroscopes by assembling resonators with surrounding electrodes. Gyros with electrodes on the side and bottom for in-plane and out-of-plane transduction is developed. Very low noise ARW (0.16 mdeg/rt-hr) and BI (1.4 mdeg/hr) is measured from the developed gyro. Besides, an unprecedented gyroscope configuration with curved electrodes made from fused silica is fabricated. This innovative gyroscope configuration with curved electrodes could provide large overlap area with curved resonator leading to improved sensitivity and improved frequency tuning. Additionally, temperature sensitivity is minimized due to same material resonator and electrode.

The outcome of this thesis will be fabrication of resonators with $Q > 12$ Million, long ring-down time > 8 minutes and low intrinsic frequency mismatch < 2 Hz. Gyros with different electrode configurations will be designed, fabricated and tested to obtain ARW of 0.16 mdeg/rt-hr and BI of 1.4 mdeg/hr. Additionally, technologies to fabricate resonators with tailored stiffness and mass distribution will be developed. A new shell design with selective discontinuities through locally thin/thick/open regions on surface of shells with application in several domains will be developed. New technologies will be developed to increase throughput and reduce manufacturing cost of gyros. Test results of a class of resonators and gyroscopes will be presented

and discussed.

1.8 Organization

This thesis is divided into four chapters. Chapter I provides an introduction of gyroscopes and discusses important parameters and their effects on the performance of gyroscopes. Chapter II introduces the PSI resonators and discusses motivation for fabricating resonators with tuned sidewall along with a discussion on their design and fabrication. Each component of fabrication process is discussed and the rate determining step limiting throughput and dominating cost of manufacturing is identified. A new low-cost singulation method is then developed and implemented to significantly reduce manufacturing time and cost. Three kinds of PSI resonators are discussed in detail. Besides, a new concept of open shell-shell with open windows and the usefulness of this design is discussed and results are presented. Chapter III discusses the resonance testing results of PSI resonators. Furthermore, effect of annealing and material characterization of fused silica is presented and discussed. Results on shock and fatigue testings are presented. Finally, effect of four different metal layers on Q is studied. Chapter IV discusses the various electrode configurations and presents gyroscope testing results from each electrode configuration. Additionally, a new curved electrode configuration design and fabrication technology is presented. Chapter V summarizes the work.

CHAPTER II

Precision Shell Integrating Resonator – Design and Fabrication

2.1 Introduction to PSI Resonators

Precision Shell Integrating resonators or PSI resonator is a class of fused silica shell resonators with distinct features mentioned below,

- Material – Fused Silica
- Radius = 5 mm
- Height 5 mm
- Rim Thickness 150–350 μm
- Stem Feature – Hollow or Solid
- Sidewall Profile – User-defined
- Other Feature – Ability to locally tune stiffness and mass

PSI resonators are designed to allow its usage in different applications, for example, where high-Q at small or large operating frequencies are needed or applications where very high shock tolerance ($>20,000\text{g}$) is priority, or when open windows is desired on the surface to provide access inside the shell etc. This chapter is focused on

design guidelines and development of fabrication technologies to fabricate different kinds of PSI resonators. Figure 2.1 shows schematic designs of three types of PSI resonators where stiffness and mass are tailored by varying the thickness at selective locations. They can be hemi-toroidal with either hollow or solid stem or can be hemispherical with no stem.

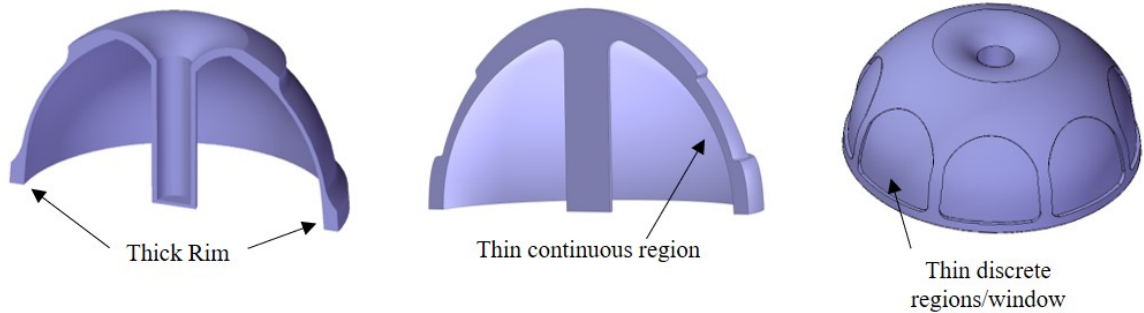


Figure 2.1: Different types of PSI resonators where selective regions are locally thin either in a continuous form or in form of discrete windows. PSI can be fabricated with either a hollow stem or a solid stem.

Using the design guidelines and fabrication methods developed in this work and explained later in this chapter, it is possible to fabricate a variety of shell resonators with engineered surface topology. Each design could be used for application-specific-resonator-application. Since PSI encompasses several designs of resonators, a nomenclature based on shell's shape is first developed. Next, a discussion on energy damping mechanisms to study effect of different parameters on Q is carried out. This is followed by a discussion on each component of fabrication including, substrate fabrication, blowtorch molding, singulation technique etc. Three different kinds of PSI resonators are discussed. Finally, open-shell type PSI resonator is discussed.

2.2 Nomenclature

Design of a PSI resonator is similar to that of a human body as shown in Figure 2.2. They have a body or anchor region (either hollow or solid) which holds the

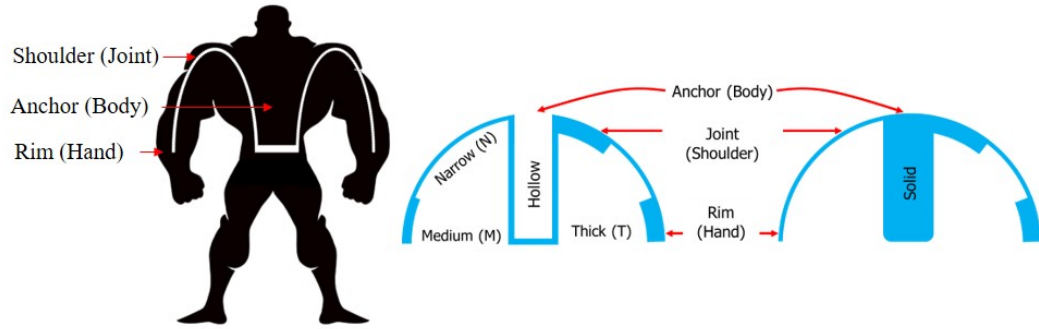


Figure 2.2: Resemblance of a PSI resonator structure with that of a human body. PSI resonators are named as X-YZ where X denotes the stem type, H or S for hollow or solid anchor. The next letter determines the thickness of the joint, and the third letter determines the thickness of rim. The letter in parenthesis is used to denote each region. Human body cartoon: www.dreamstime.com.

entire structure together, a shoulder or joint region and a hand or rim region. As in a human body, the hands are free to move and is connected to the body through shoulders, similarly, PSI resonators have a free rim (which vibrates) and is connected to the anchor through a shoulder. Each of these regions can have different variations as will be discussed later. The nomenclature of different types of PSI resonator is determined by the relative thickness of shoulder and rim and the characteristic of the anchor. The nomenclature is of the type X-YZ. Figure 2.2 shows two sub class of PSI resonators, one with a hollow stem and another with a solid stem. The first letter in the nomenclature determines whether the resonator has a hollow anchor, ‘H’, or a solid anchor, ‘S’. The relative thickness of the joint or shoulder (anchor transition region) determines the next letter of the nomenclature which can either be ‘N’ (normal), ‘M’ (medium) or ‘T’ (thick). Similarly, the third letter determines the relative thickness of the rim or hand and can also be either a ‘N’, ‘M’, or ‘T’. It is to be noted that the thicknesses are relative to each other. Different PSI resonators with the nature and thickness of their joint and rim are shown in Figure 2.3. Devices beginning with ‘H-’ have a hollow stem and those with ‘S-’ have a solid stem as shown

in Figure 2.2. Devices following the nomenclature X-YT i.e. ending with ‘T’ will have thick rim and large modal mass while devices following the nomenclature X-TY i.e. having a thick shoulder will have minimum shock induced vertical displacement. Fabrication of such resonators with tuned thicknesses will be described in the next section.

	FEATURES OF DIFFERENT PSI DESIGNS											
	S-NT	H-NT	S-NM	H-NM	S-MT	H-MT	S-MM	H-MM	S-TT	H-TT	S-TM	H-TM
Anchor [Body]	S	H	S	H	S	H	S	H	S	H	S	H
Joint [Shoulder] (in μm)	N (~60)	N (~60)	N (~20)	N (~20)	M (~100)	M (~100)	M (~40)	M (~40)	T (~300)	T (~300)	T (~300)	T (~300)
Rim [Hand] (in μm)	T (>300)	T (>300)	M (~200)	M (~200)	T (>300)	T (>300)	M (~200)	M (~200)	T (>300)	T (>300)	M (~200)	M (~200)

Figure 2.3: Different types of PSI resonators with thicknesses of different regions. PSI resonators can have a solid or hollow stem. Approximate thickness in micrometers are shown within parenthesis.

2.3 Fabrication of PSI Resonator

Unlike the macro-scale resonators which can be precisely machined, miniaturized resonators cannot be mechanically machined due to its complex curvature and thickness as small as few tens of microns. At the same time, fabrication of 3D structures of fused silica is not possible using conventional silicon micromachining. Therefore, specialized techniques need to be developed to fabricate PSI shells. At the same time, the fabrication technique should be low cost, repeatable, fast and scalable to enable volume production. Glass blowing as discussed in Chapter I is one such technique. In this thesis, an in-house developed vacuum blowtorch molding technique is used to make 3D shells with superior quality. Blowtorch molding enables the fabrication of shells with different aspect ratios, thicknesses and shapes. At the same time, it takes

about 10–30 seconds to mold the shell and has the capability to be incorporated at the wafer level. Figure 2.4 shows key components of blowtorch molding process to make PSI resonator.

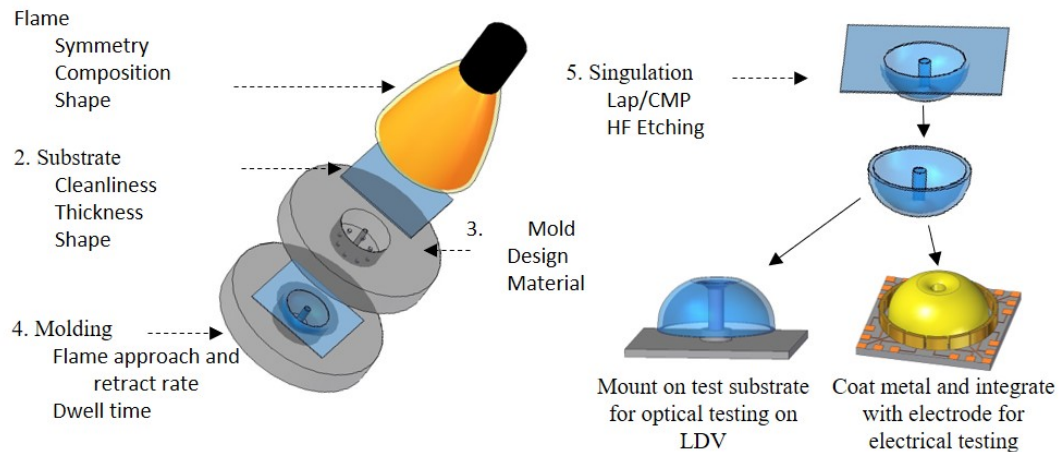


Figure 2.4: Key components and steps to fabricate PSI resonator using blowtorch molding.

The fabrication of PSI resonators is done in two main steps, design step and fabrication step, with each step having several sub-steps as shown in Figure 2.5. In the next few sections and sub-sections each of these will be discussed.

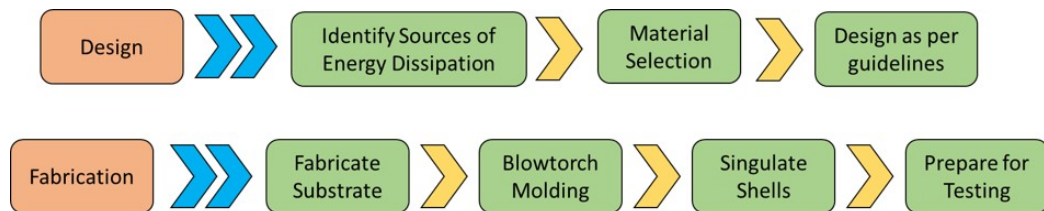


Figure 2.5: Design and fabrication steps to make high quality PSI resonator.

2.4 Energy Dissipation Mechanism

As explained in Chapter I, several parameters like Q , mass, frequency, drive amplitude etc. determine the overall performance of gyroscope. Amongst these, obtaining mass comparable to those of macro-gyroscopes is difficult at the MEMS scale. While small mass is beneficial for MEMS gyros because force ($f = m.a$) experienced during

shock is small making these tolerant to high shock however it is disadvantageous as it limits their energy storing capability. Thus, obtaining high Q at the small scale becomes challenging. Therefore, it is important to research and understand each source of damping and mitigate them through design changes and improvements in fabrication methodology to decrease energy dissipation. Quality factor is mainly dependent on, (i) material property, (ii) design and (iii) environment of operation. Based on these, several sources of damping can cause vibrational energy to escape from the resonator. Sources of damping including loss due to local temperature variations on the surface of resonator (thermoelastic damping or TED), loss due to defects in material, loss through anchor (anchor or support loss), loss due to surface quality, loss due to friction caused by air molecules (viscous damping) etc. could contribute in determining the final Q of resonator. This section discusses major damping mechanisms and the mitigation methodology to obtain high Q from PSI resonators.

2.4.1 Thermoelastic Damping

Thermoelastic damping or TED depends on both material and design of the device. During vibration a resonator moves causing regions on the surface of shell to elongate or contract. For example, a vibrating beam as shown in Figure 2.6 undergoes expansion on its top surface and compression on its bottom surface in the first half cycle and vice versa in the second half of the cycle. This local expansion and contraction lead to changes in local temperature causing a temperature gradient across the surface as shown in Figure 2.6.

As the resonator oscillates, there is a coupling of mechanical strain and temperature field which causes such temperature gradients to form periodically. Vibrational energy is therefore used to maintain thermal equilibrium. This process is however

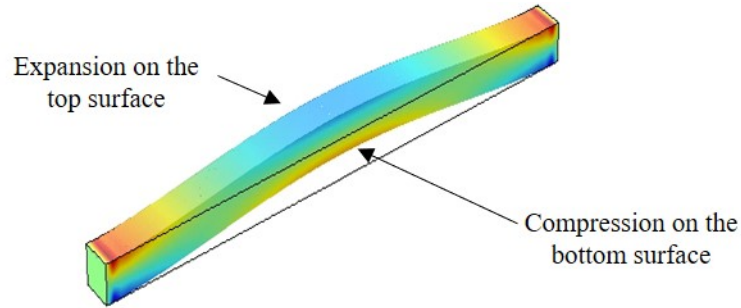


Figure 2.6: A vibrating beam undergoes alternating compression and expansion cycles causing temperature gradient across the beam.

irreversible and therefore causes loss of vibrational energy in each cycle causing thermoelastic damping or TED. To reduce TED, formation of temperature gradients could be minimized. This can be done through material selection and design changes. To study the effect of material properties on TED, a finite element simulation is done for a shell resonator made of different candidate materials in [72]. Figure 2.7 shows key material properties of candidate materials and their numerically calculated Q_{TED} . It can be seen that Fused Silica and Zerodur stands out from the rest in terms of Q_{TED} and its value is more than 70 million and 46 billion respectively. Of course, these numbers are for a perfectly symmetric structure with perfect material but in reality, imperfections in both structure and material is inevitable which affects Q_{TED} . The effect on imperfections will be discussed in Section 2.14. Figure 2.8 shows variation of Q_{TED} with different material properties with respect to FS and it can be deduced that material with low thermal conductivity (k) and low coefficient of thermal expansion (α) can exhibit very high Q_{TED} .

Several studies have also been done to understand the effect of geometry on Q_{TED} . [73] developed an analytical model to study the effect of boundary conditions and shapes on Q_{TED} for plates. Similarly [74] placed slots in the path of temperature gradient and studied its effect on Q_{TED} . Similar study was done by [75] recently to

Material*	E (GPa)	ν	ρ (kg/m ³)	k (W/(m·K))	α (10 ⁻⁶ ×1/K)	C_{SP} (J/(kg·K))	Q (FEM)	Q (Analytical model)
SiO ₂	70	0.17	2200	1.4	0.5	730	7.5e7	7.9e7
Zerodur	90.3	0.24	2530	1.46	0.02**	820	4.6e10	5.9e10
Al ₂ O ₃	400	0.22	3965	35	6.5	730	1.7e4	1.8e4
SiC(6H)	748	0.45	3216	490	4.3	690	8.2e3	6.5e3
Si ₃ N ₄	250	0.23	3100	20	2.3	700	1.8e5	2.0e5
Borosilicate	63	0.2	2230	1.13	3.3	754	2.0e6	2.5e6
GaAs	85.9	0.31	5316	33	5.7	550	5.2e4	5.2e4
Ge	103	0.26	5323	58	5.9	310	2.1e4	1.5e4
InSb	409	0.35	5770	18	5.4	200	5.7e3	6.8e3
C[100]	1050	0.1	3515	990	0.8	520	3.3e5	1.8e5
Si(c)	170	0.28	2329	130	2.6	700	6.7e4	4.7e4

Figure 2.7: Material properties and simulated Q_{TED} for different materials. Figure reproduced from [72].

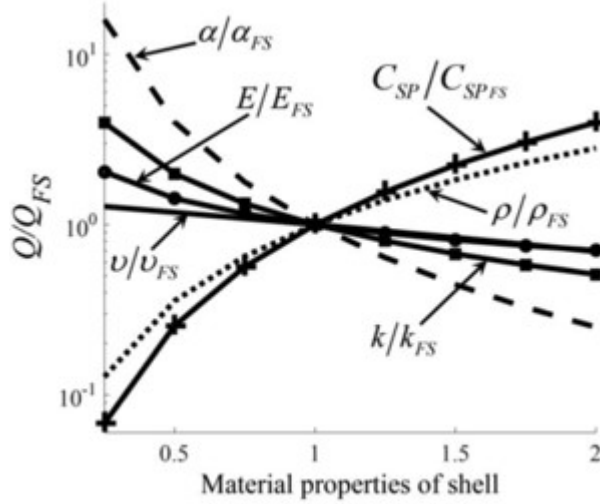


Figure 2.8: Effect of material properties on Q_{TED} . As α , k , E , ν increases, Q_{TED} decreases. Similarly, as C_{SP} or ρ is increased, Q_{TED} increases. [72].

tune Q_{TED} in disc resonators. To understand the dependence of resonator design on Q_{TED} , let us consider a model from Zener to calculate TED of a simple beam developed in [76, 77]. For a cantilever beam, Q_{TED} can be estimated using the analytical formula given by,

$$Q_{TED} = \left[\frac{\rho C_{sp}}{E \alpha^2 T_0} \right] \cdot \left[\frac{\omega_M^2 + \omega_T^2}{\omega_M \cdot \omega_M} \right] \quad (2.1)$$

Where the symbols have their usual meaning and ω_M is the mechanical frequency and ω_T is the thermal frequency which has an inverse relation to thermal transport time of the heat flow across the flexing beam. The terms in first bracket are ma-

terial related meaning they are determined by properties of the material used and temperature of operation. The terms in second bracket also depend on the physical dimensions of the beam. Now, to maximize Q_{TED} , both material term and design terms should have their maximum values. If the ω_M and ω_T of the resonator matches, the second brackets attains its minimum value of 2 therefore reaching the lower limit of Q provided the material term is constant. This can also be understood intuitively as when the mechanical relaxation time matches its thermal transport time, there is a strong thermomechanical coupling and maximum energy is dissipated in each cycle of vibration reducing Q. Therefore, it is desirable to have mismatched ω_M and ω_T . If $\omega_M \gg \omega_T$, the mechanical deformation time is much smaller such that heat transport struggles to happen dissipating a small amount of energy. Vice versa when $\omega_M \ll \omega_T$, the deformation time is quite large so that resonator essentially remains at thermal equilibrium again dissipating small amount of energy. To calculate Q_{TED} for a shell resonator [72] developed a simple analytical model and compared the results with those from COMSOL simulations and excellent agreement was met. Q_{TED} for PSI resonator is on the order of several tens of million.

2.4.2 Anchor or Support Loss

Anchor or support loss as the name suggests is the loss of vibrational energy from the resonating rim through anchor into the substrate. This kind of loss is dominant in any resonator and can be minimized through smart design. One of the most common way to reduce support loss is to fix the resonator at one its nodal point. The effect of anchoring can be easily felt using a simple tuning fork. If a tuning fork is hit against a hard surface holding the bottom of the stem (nodal point for a tuning fork), one could hear the singing of the tines. Now, if the time fork is hit but this time it is held from one of its tines, there would be almost no singing. This is

because in the latter case, the energy is quickly lost from the tine to the hand. For a wineglass type resonator (shell, cylinder, disc, ring etc.) resonating in its $n=2$ or $n=3$ wineglass, one of the nodal points is at the apex of the dome as shown in Figure 2.9 therefore the shells are anchored at the central region.

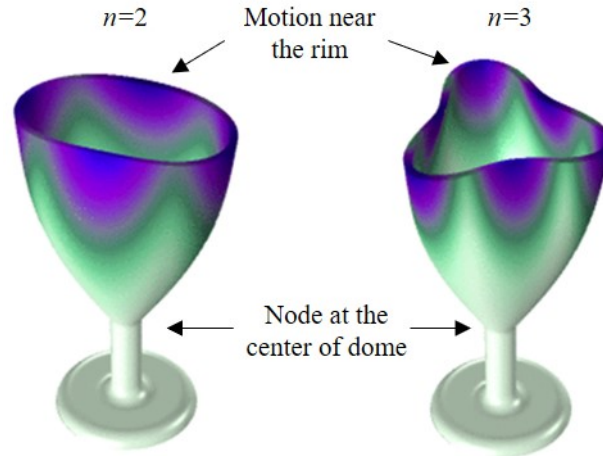


Figure 2.9: Modeshape of a wineglass resonating in $n=2$ and $n=3$ modes. Maximum displacement occurs at the rim while the apex of the dome does not move.

Other methods to reduce anchor loss is to decouple the resonating rim from the anchor point. For a shell resonator this can be done by increasing the height of the device. There have been several studies to study anchor loss in resonators. [78] studied the effect of creating trenches on the mounting substrates near the anchor point and numerically observed an improvement in Q_{anchor} by virtue of energy reflection. [79] studied the effect of anchor dimension and observed that Q_{anchor} increased as the anchoring area is reduced. [80] on the other hand created slots around the anchor on the resonator and numerically observed an improvement in Q_{anchor} which they attributed to stress isolation at the anchor. Besides, the symmetry of the structure plays a vital role in determining Q_{anchor} . Asymmetries including those from misalignment of anchor with respect to the shell's body, mass imbalance, acircularity, height asymmetries etc. have shown to affect Q_{anchor} to different extent. Effect of

all these parameters have been numerically studied and summarized in [81, 82]. For a perfectly symmetric shell with provisions made to ensure none of the dissipated energy is reflected back to the resonator, numerical simulations have shown Q_{anchor} to be on the order of several hundreds million. Even with asymmetries, Q_{anchor} is hundred million.

2.4.3 Viscous Loss

Viscous or fluidic damping is the loss of mechanical energy from the resonator to the ambient environment through the surrounding medium. Depending on the pressure around the resonator, the air medium can be classified as continuum or free molecular flow regime. This is often characterized by a non-dimensional number called Knudsen number which is the ratio of the mean free path of air molecule to the characteristic diameter or the feature. At pressure nearing those of atmosphere, the air molecules are so close to each other that they interact with each other. This is the continuum regime. In such cases, viscous damping exclusively becomes the dominant loss mechanism for MEMS resonators. Therefore, they are often operated at reduced pressure such that the mean free path increases and the interaction among gas particles becomes less important than those with the resonator surface. In such case the vibrating resonator imparts its momentum to colliding air molecules. This way the mechanical energy is transferred from the resonator to the surrounding medium. While there is no accurate model to exactly predict fluidic damping in shell resonators, however, it has been experimentally observed that Q starts to saturate at pressure < 1 mTorr. All testing of PSI resonator in this thesis is carried out at < 10 μ Torr pressure ensuring very large mean free path (on the order of several meter) and therefore leads to very small fluid-structure interaction.

2.4.4 Surface Loss

Surface losses can be of several types and are associated with defects or impurities present on the surface of a resonator. Such defect could scatter vibrational energy causing damping. Besides, any foreign particle could also dissipate energy for the same reason. Therefore, improving the surface quality to ensure it is free of any kind of organic residue, particles, defect etc. is critical to reduce damping due to surface effects. A number of steps are taken in this regard to ensure superior surface quality of the fabricated shells. The initial substrate used to make the shells are properly cleaned to get rid of any organic residue. Besides, the fabrication method, which is discussed later in this chapter, imparts ultra-smooth surface finish with roughness < 0.2 nm. At the same time, the fabrication process is improved to ensure that the resonator surface is free of any unwanted residue or particles.

2.5 Using Patterned Substrate to Tune Thickness

One key component for the fabrication of PSI resonators is the initial substrate. The thickness, shape, design and cleanliness of the substrate determine the overall shape, size and surface quality of the shell resonator. 10 mm diameter FS PSI resonators are fabricated from 23x23 mm FS squares diced from a high purity Corning 7860 OA grade FS wafer. Figure 2.10 shows two scenarios where a flat initial substrate and a patterned initial substrate is used. The patterns on the substrate is used to locally define the thickness of the shell resonator. For example, in Figure 2.10(a), the flat substrate deforms during torching and the side wall profile gradually thins as it moves down.

This can be seen in the schematic design as well as the CT scan of one of PSI shell fabricated from a flat substrate. The scenario on the right (Figure 2.10(b)) is

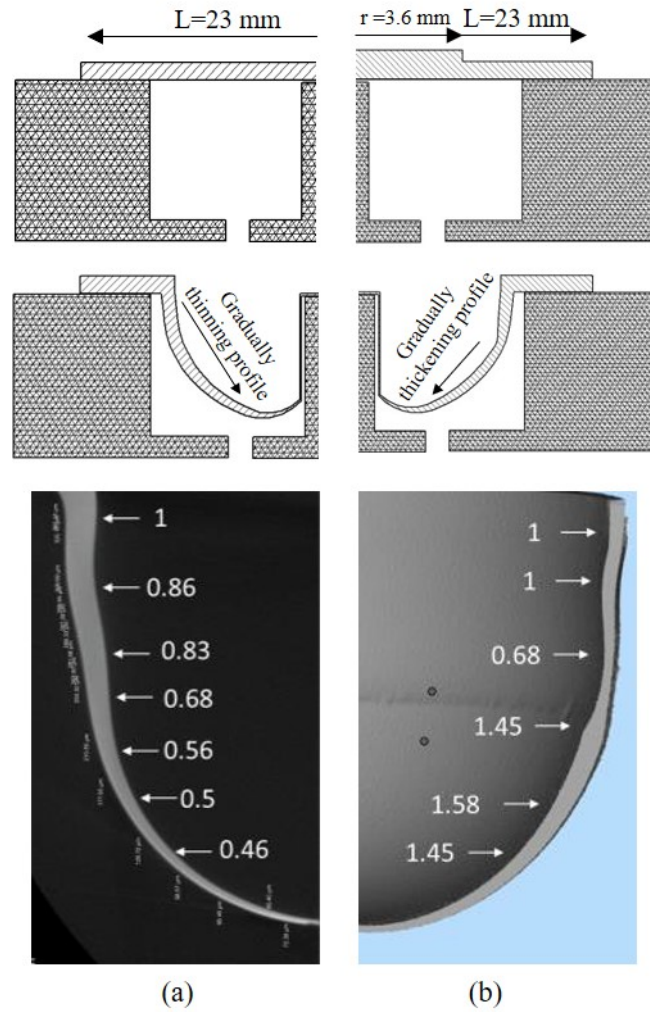


Figure 2.10: Tuning sidewall thickness using patterned substrate. (a) When the substrate is flat, the thickness of the shell gradually reduces. This can be altered by using (b) a patterned substrate with features. CT scans of the two shells shows normalized thickness.

when the substrate is patterned and etched to define a thick disc of radius 3.6 mm at the center. When this substrate is deformed, the thick disc falls roughly midway of the shell changing the thickness profile. With this approach, thickness profile can be locally tuned. This selective tuning of thickness is useful in many ways for example a thick shoulder can increase vertical stiffness and therefore reduce displacement in an event of shock. Shocks will be discussed in more detail in Chapter III. Another advantage of tuning thickness is to modify the resonant characteristics of the res-

onator. To obtain low noise performance from a vibratory gyroscope, the mechanical resonator must have large effective mass and frequency between 5–20 kHz to enable large deformation in response to rotation. Effective mass can be increased by increasing the thickness of the resonating part which is the free rim. However, increasing rim thickness proportionally increases frequency which is not desirable. Patterning the substrate to selectively thin specific part would modify the reflow pattern and reduce the stiffness and therefore frequency while increasing the effective mass.

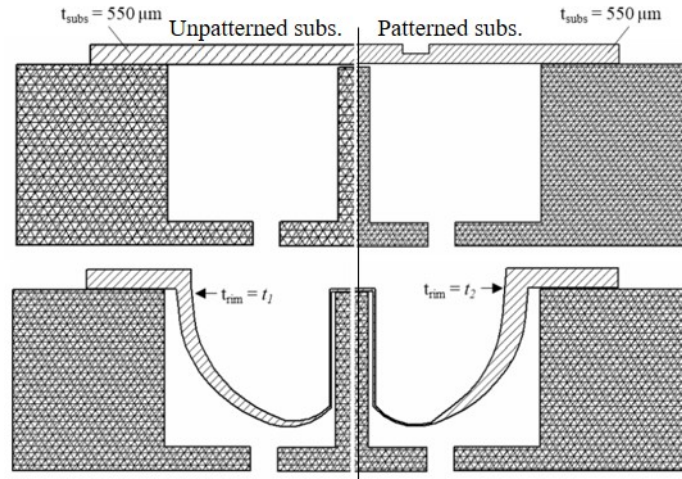


Figure 2.11: 3D structure fabricated using two substrates, (left) an un-patterned FS and (right) patterned FS to define thin window near the center. Reflow initiates at the thinned region of patterned substrate. This leads to a thicker rim (t_2) as compared to that of unpatterned substrate (t_1) i.e. $t_2 > t_1$ which leads to $f_2 > f_1$, where f is the resonant frequency.

Formation of thin regions can also be conversely used to increase frequency by modifying the reflow pattern through thin window placed at different locations. For example, the patterned substrate as shown in Figure 2.11 has etched circular trench placed away from the rim. During torching, reflow initiates at these thin regions and the formed shell has modified rim thickness and profile as compared to those made from flat unpatterned substrate as shown in the same figure. The altered rim thickness modifies frequency and modal mass. Table 2.1 tabulates $n=2$ and $n=3$

wineglass frequencies of shells made from 550 μm thick un-patterned and patterned substrates as shown in Figure 2.11.

Table 2.1: Measured $n=2$ and $n=3$ wineglass frequency from six devices, 3 each using patterned and unpatterned substrate.

Unpatterned Substrate		Patterned Substrate	
$n=2$ WG freq.	$n=3$ WG freq.	$n=2$ WG freq.	$n=3$ WG freq.
10.23	27.96	16.29	43.03
10.16	27.88	14.47	38.92
11.26	31.24	16.30	43.00

2.6 Fabrication of Patterned Substrate

Using the patterned substrate one can fabricate shell with any user-defined sidewall thickness profile with large local thickness variation. This thickness variation on a PSI shell can be as large as hundreds of microns. This means that the initial patterned substrates need to have steps which is hundreds of microns. Therefore, deep etching of fused silica is required. Wet etching is chosen over dry etching due to the following reason,

- Ease of fabrication in terms of cost and time
- Batch fabrication
- The angled profile of wet etched pattern leads to a gradual change in thickness profile on the shell which eliminates any sharp corners and reduces stress concentration.

To deep etch fused silica, a combination of metal and photoresist mask is used. The wafer is first coated with a 50/500 nm bilayer of Cr/Au. The metal coated wafer is then spin coated with AZ 9260 photoresist at 3000 rpm to coat 7 microns of photoresist. The wafer is soft baked at 115 $^{\circ}\text{C}$ for 120 seconds and exposed under a UV light for 40 second. Then, the wafer is developed in 3:1 solution of DI and

AZ400K. Post development, the wafer is put on a hotplate at 130 °C for 30 minutes to hard bake the photoresist. The hard bake further crosslinks the photoresist. The exposed metals are etched off and the wafer is etched in 49% HF at room temperature at an etch rate of $\sim 1 \mu\text{m}/\text{min}$ with 1:1.2 ratio of vertical to lateral etch. The lateral etch is compensated for in the mask design. The etching is done in steps of 30 minutes after which the wafer is thoroughly rinsed in DI water to remove any trapped Fluoride ion and the etch depth is measured to monitor the etch rate. After the desired etch depth is reached, the photoresist is stripped in hot Nanostrip and the metal masks are stripped in their respective etchants. The wafer is then diced in squares of 23 mm sides and the diced substrates are cleaned in Acetone and IPA in an ultrasonic bath followed by a Piranha clean for 20 minutes. The Piranha clean step gets rid of any residue from the blue tape used for dicing. Figure 2.12(a) shows the fabrication flow to make the patterned substrate. The lithography step is very important as any pinholes, cracks on photoresist or adhesion issue could be detrimental to the patterned substrate. Figure 2.12(b-c) shows a patterned substrate where HF penetrated through the pinhole and caused pits on the wafer and a severely undercut pattern. Such imperfections could induce mass imbalance on the final shell which can affect both Q as well as frequency mismatch of the resonator.

2.7 Blowtorch Molding

Blowtorch molding uses a custom machined graphite mold, a fuel-oxygen blowtorch and vacuum lines. Both material and design of the molds are critical for efficient thermal control. Key components of blowtorch molding are shown in Figure 2.4 (1–4). High quality fused silica substrate of 200–500 μm thickness is placed on top of the mold and vacuum is applied inside the mold to create a pressure difference

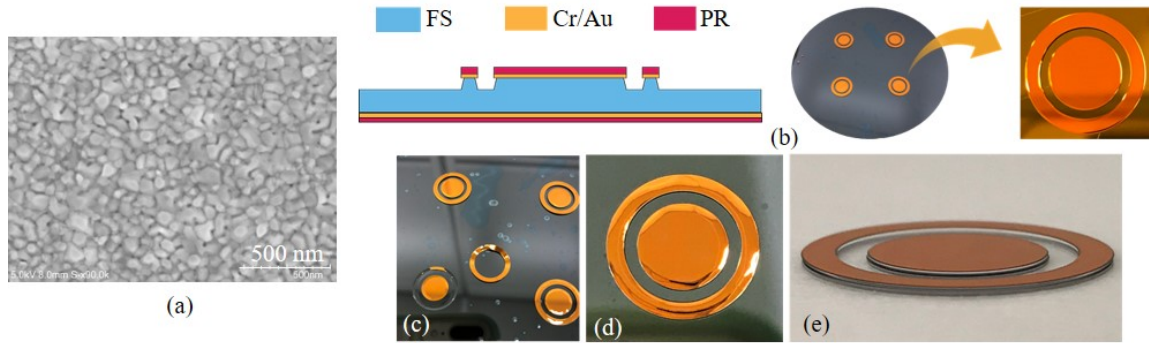


Figure 2.12: (a) SEM image of wafer coated with evaporated Cr/Au of 50/500 nm thickness. Grain size is 60 nm (b) Schematic and photograph of a substrate with etched features. Imperfections in patterned substrates during lithography and etching. (c) Poor adhesion caused lifting of the photoresist and metal layers, (d) severe undercutting around the edges, (e) a perfect pattern with well-defined and sharp features.

across the FS substrate. The blowtorch flame is carefully brought down to heat the substrate above its softening point. The temperature of the substrate increases from room temperature to beyond 1600 °C. This ramp rate needs to be optimized to obtain the optimal shape as well as good surface quality. Once the substrate softens, the pressure difference causes the shell to reflow inside the mold and the flame then retracts as shown in Figure 2.13. The reflowed FS touches the mold only on the top and the curved surface just hangs in without having any contact with the surface of mold imparting excellent surface quality. The shape of the resonator is determined by a number of parameters, including mold dimensions, torch temperature, pressure difference and mold design. The molding process completes in 10–30 seconds depending on the thickness of the substrate. Blowtorching stretches the substrate several mm out of the plane. Such extreme deformation thins the substrate by as much as 90%. This stretching imparts superior surface quality with surface roughness $< 2 \text{ \AA}$.

2.7.1 Propane-Oxygen Flame

Maintaining optimum temperature profile and symmetry during molding is important for the shape and quality of the resonator. For example, an asymmetric

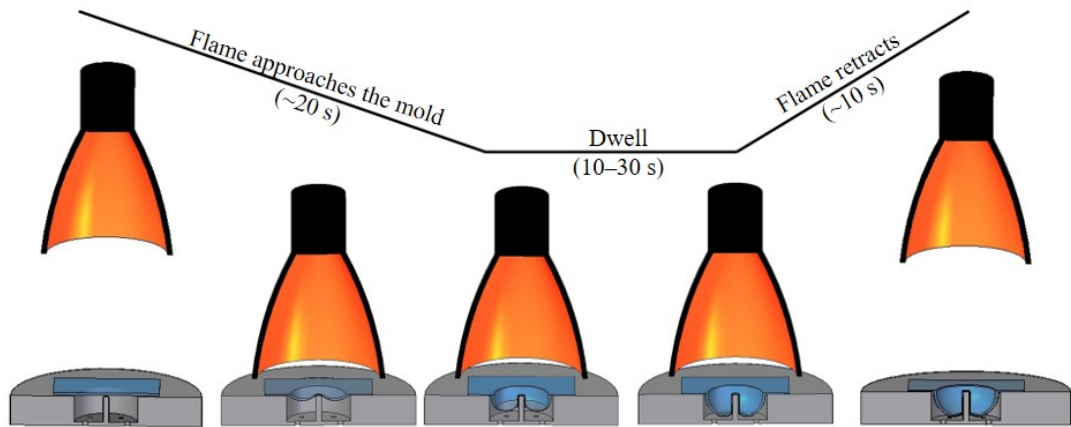


Figure 2.13: Flame positions during blowtorch molding. The flame is turned on and brought slowly towards the mold. The temperature of the FS substrate is increased, and 3D shell is molded. The flame then retracts back. The entire process takes less than a minute.

flame can cause temperature variations which could lead to structural asymmetry in the shells. Besides, to obtain ultra-smooth surface, the shell should not touch the mold except at a few locations. Therefore, it is desirable that the shell hangs in the mold and do not conform to its cylindrical shape. All these can be enabled by optimizing the fuel ratio, flame shape through flame tip, approach rate of the flame while molding, alignment of flame to substrate etc.

2.7.2 Mold

Both material and design of mold dictate the repeatability and quality of the shell. Since the blowtorching process heats the mold up to nearly two thousand degrees Celsius temperature in a matter of few tens of second, the material of the mold should be able to sustain such extreme temperature cycles. It should also have the optimum thermal conductivity to maintain the temperature during molding. Figure 2.14 shows the effect of thermal conductivity on the shape of the final resonator. If the thermal conductivity of the mold is very small, it would get extremely hot and would lead to uncontrolled molding and the substrate would conform to the shape

of the mold. If thermal conductivity is too high, it would dissipate heat quickly causing regions of the shell to locally harden before it is completely molded. To avoid both these extremes, material with intermediate thermal conductivity should be used to provide the desired shape. In addition, it is also necessary to choose a material which is low cost and easily machinable. Graphite is an excellent candidate because of its optimum thermal conductivity, low cost, ease of machining, ability to sustain extreme thermal cycles and is therefore used to make PSI resonators.

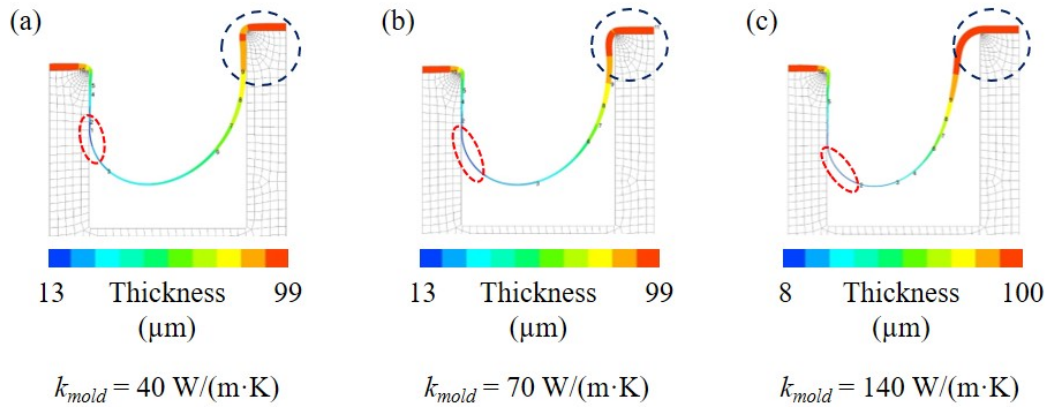


Figure 2.14: Effect of thermal conductivity of mold on profile of shell resonator. (a) Very small k would increase the temperature causing uncontrolled molding leading to a cylindrical shaped shell, (b) an optimum value of k would cause the substrate to deform and hang in the mold, (c) high value of k would cause rapid cooling causing the shell to locally harden before it is completely molded [83].

The shape and aspect ratio of the shell depends on the substrate and the mold design. Using different design of molds, different shapes of resonator have been fabricated as shown in Figure 2.15. By varying the sidewall curvature of mold and using different patterned substrates, different shapes of shells with different anchor scheme is possible [84].

2.8 Singulation

A molded resonator has a useful 3D part and a flat and undesired 2D part which needs to be removed as shown in Figure 2.16. This can be done in mainly three ways

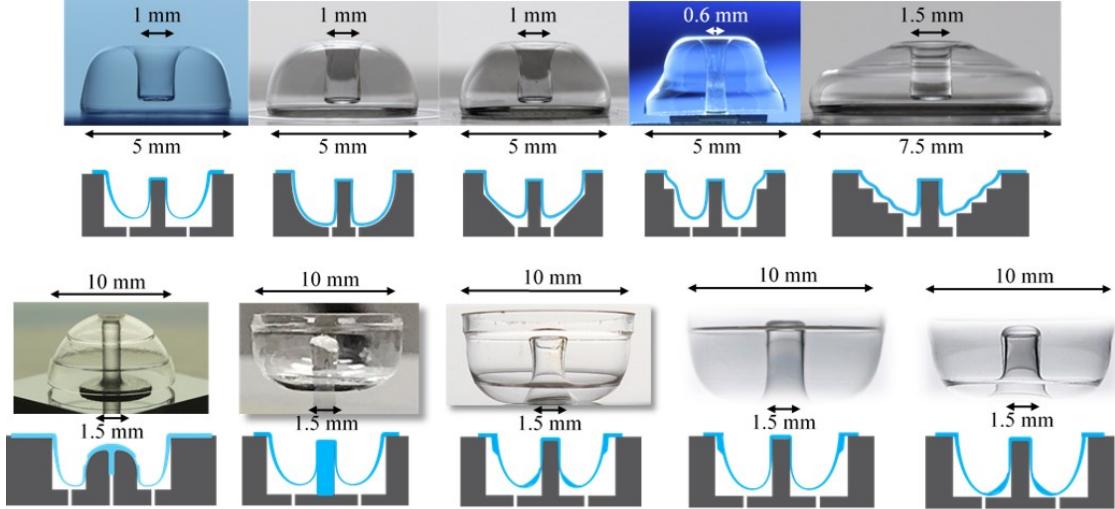


Figure 2.15: Different shapes and aspect ratio shells can be fabricated using different mold and patterned substrates.

which are discussed in this section.

2.8.1 Laser Cutting

Laser cutting of fused silica can be used to singulate the 3D part from a molded structure. Using a laser, regions around the rim can be scanned to ablate FS and singulate the 3D shell. This method has been used in [85] to isolate 3D shells with additional T-shaped masses on the rim. These T-masses are used to tune the frequency mismatch and increase the capacitance for out-of-plane drive and sense. They used a femtosecond laser ablation using ultra-short pulse laser system with UV laser of wavelength 355 nm for 200 fs duration. Laser spot of 10 μm with repetition frequency of 30 kHz is used to scan the perimeter of a shell. Process parameters like laser power, frequency, speed of scanning, and number of scans needs to be optimized to ensure smooth sidewall profile at the ablated regions. At the same time, careful alignment should be done to ensure symmetry of the shells. Using this method, it is possible to fabricate shells with extra masses at the rim for surface electrode transduction, however it is a serial process, needs accurate alignment and sophisticated

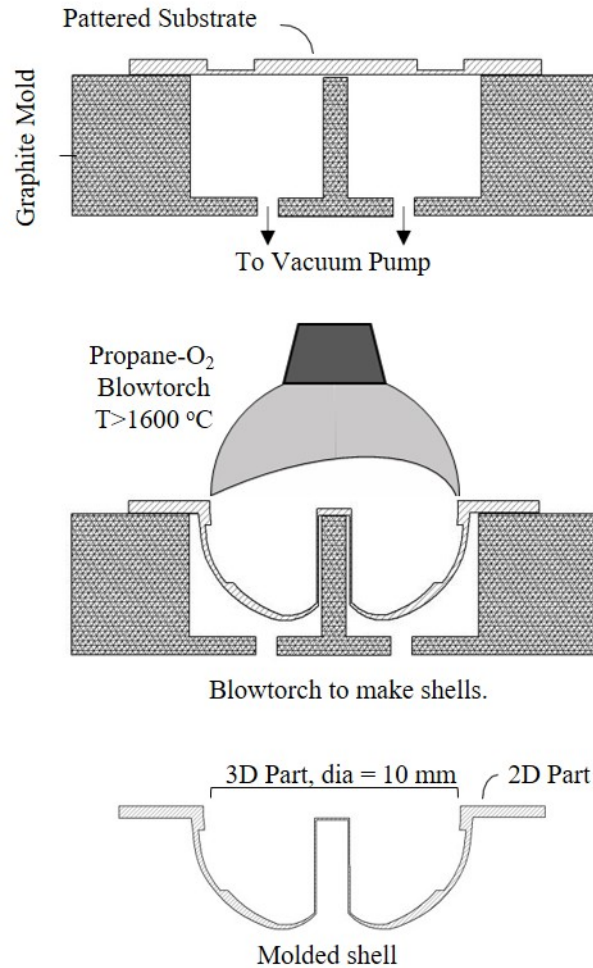


Figure 2.16: After the substrate is blowtorched, the molded structure is taken out of the mold. The molded shell has a desired 3D part and a non-desired 2D part. The 3D part should be singulated from the structure.

tools and rotating fixtures.

2.8.2 Lapping and CMP

Another method to singulate 3D shells from molded structure is by using mechanical lapping followed by chemical mechanical polishing. This method is one of the two methods used in this thesis to singulate shells. Lapping is the method of material removal by mechanically grinding the flat part on an abrasive surface followed by chemical mechanical polishing. Both lapping and polishing requires that the shells are secured with a lapping wax which can later be dissolved. To protect the surface

of the shell from lapping wax, shells are first coated with a sacrificial thin tri-layer of Ti/Au/Ti of thickness 50/1000/50 Å from both sides. Nine metal coated shells are encapsulated in a silicon holder. This holder is made by drilling 9 holes into a 6 mm thick silicon wafer using diamond core drill on a tabletop drilling tool. The height of PSI shells are ~ 5 mm therefore a 6 mm thick holder is chosen to ensure that the shells completely fit inside the holder. Next, nine shells are encapsulated in the holder using a thermally curable lapping wax. Selection of lapping wax is done to ensure easy processing, good adhesion during lapping, and ease of removal after lapping. The holder with shells is then put on a lapping tool to mechanically grind off the flat part.

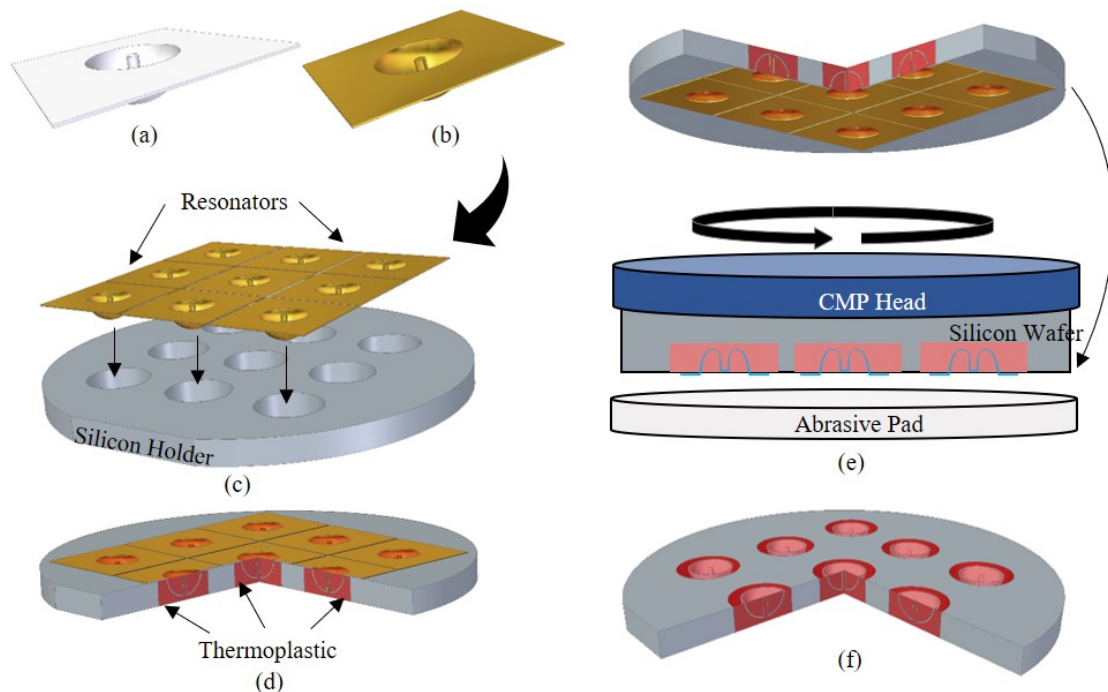


Figure 2.17: The method of singulating shells using lapping/polishing method. (a) A molded is (b) coated with sacrificial protective metal and (c)-(d) set into a thick silicon wafer using thermoplastic. (e)-(f) The flat portion of the shell is lapped, and the rims are polished using CMP. Finally, the thermoplastic is dissolved, and metal is wet etched to release the shells.

The process of lapping is shown in Figure 2.17 [86]. Figure 2.18(a) shows an optical image of the exposed rim after lapping and it can be seen that the rim is rough due

to large grit size on the lapping pad. The rough surface of the rim has shown to degrade Q by an order of magnitude because rough surface increases the surface area (or increases S/V ratio) which increases energy loss. Therefore, it should be polished to make it smooth. The same holder after lapping is subjected to chemical mechanical planarization method using silica-based slurry on a polishing pad. The polishing step smooths the rim as shown in Figure 2.18(b). Lapping is an aggressive material removal method therefore proper bubble free encapsulation is important to avoid damage to the shell. Figure 2.18(c) shows optical photograph of rim damaged during lapping and polishing step probably due to trapped bubble which popped up during lapping compromising encapsulation rigidity.

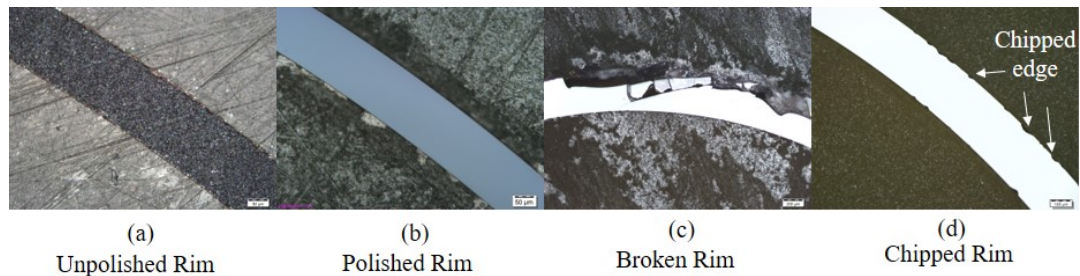


Figure 2.18: Non-idealities during lapping and polishing (a) an unpolished rim has a rugged surface which can be smoothed by (b) polishing after lapping. (c) Due to unoptimized parameter or mounting, the shells can be broken completely or (d) get chipped at the edges. Chipping of rim has not shown to degrade Q significantly.

Therefore, during mounting it should be ensured that there are no trapped bubbles specially around the rim. Even with perfect bubble-free mounting, some chipping as shown in Figure 2.18(d) at the rim edge is inevitable in some devices. It has however been shown that such chips do not significantly affect Q_{TED} [72]. Once polishing is completed, the wax is dissolved, and each shell is transferred to individual pocket of a cleaning jig for batch processing. The shells in the cleaning jig is solvent cleaned in Acetone followed by IPA for 10 minutes each and are then dried on a hotplate. The shells are then cleaned in Piranha solution which removes any trace amount of wax

and etches the top Titanium of the sacrificial tri-layer. Gold is then etched in gold etchant and the last Ti layer is etched in another cleaning in Piranha solution which also dissolves any organic residue which may have been on the surface before coating the sacrificial metal. The shells are thoroughly rinsed in between each etching. The two Piranha clean step while etching Ti also cleans off organic residue. Therefore, Ti is chosen instead of Cr as adhesion layer for sacrificial metals. The lapping and polishing method to singulate shells is a batch process. However, careful mounting to ensure bubble free encapsulation and optimizing lapping conditions like downforce, rotation rate, slurry flow rate etc. are critical for effective and damage free lapping and polishing. This method is an efficient method for singulation however, like laser cutting, this method requires sophisticated tools and expensive consumables.

2.8.3 Hydrofluoric Acid Release

Both laser cutting and lapping/polishing method have their own disadvantages specially on singulation time, cost of singulation, requirement of equipment and being serial or a limited-throughput process. Therefore, a new method was developed to singulate 3D shells by selective etching using Hydrofluoric acid (HFA). HFA is an efficient etchant for FS but to singulate resonators using HFA it must be masked everywhere except in the regions to etch. However, masking against HFA is challenging, especially for long etch times. A combination of metals and photoresist to mask against HFA for etching FS wafer for more than 4 hours is done to prepare patterned substrate. However, lithography on curved surfaces is difficult and complex. To overcome this complexity, Crystalbond 509 [87] is used to mask against HFA for long etch times. Crystalbond 509 is a low cost clear adhesive wax used for temporary bonding for dicing, lapping etc. It adheres readily to a variety of materials including, ceramics, glass, metals, quartz etc. It melts at about 120 °C and hardens as

the temperature is decreased below 70 °C and is soluble in Acetone. In this method of singulation, shell resonators are first adhered on a thick silicon lapping jig with holes using a thin layer of Crystalbond at 120 °C on a hotplate. They are then filled in with Crystalbond 509 from the front side exposing the flat part to be etched and then capped with aluminum foil. The holder is then flipped and Crystalbond is filled in from the back side. It is then cooled to room temperature and the capping foils are peeled off. Extra overflowing Crystalbond, if any, is then wiped off with Acetone using a cleanroom wipe. The holder with encapsulated shells is dipped in HFA at room temperature. HFA etches the exposed flat part of FS shells approximately at the rate of 1 $\mu\text{m}/\text{min}$ singulating them. Once etching is complete, the holder is thoroughly rinsed in DI water and wax is dissolved in Acetone. They are cleaned again in Acetone and IPA followed by Piranha cleaning and annealing. The process step is shown in Figure 2.19 [88].

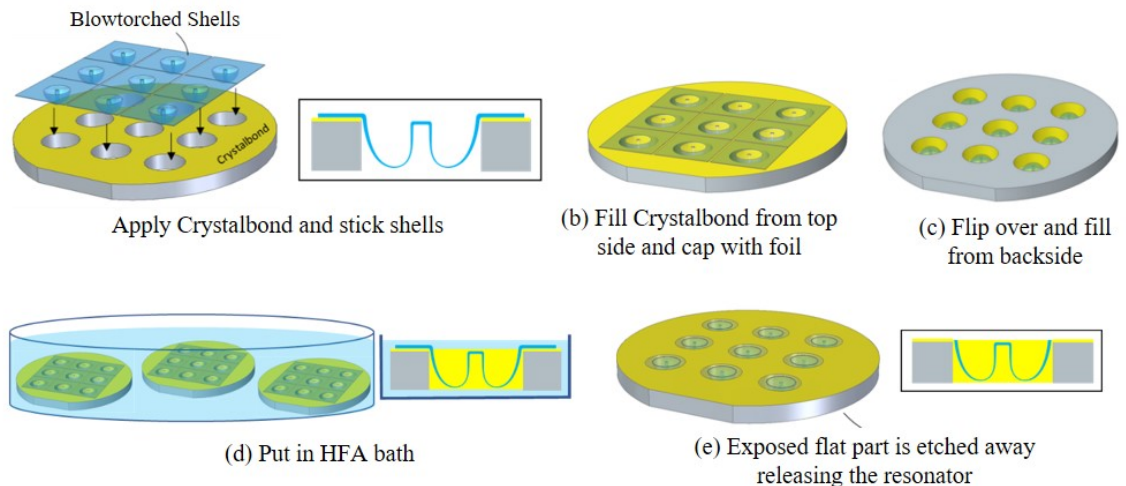


Figure 2.19: Process steps for HFA releasing of shells. (a)-(c) Shells are filled in with Crystalbond and (d) dipped in HFA acid to (e) etch the flat part and release the shell.

Figure 2.20 shows a photograph of shell resonators released using HFA and lap/polish release method. It can be seen that the rim of the resonator released using HFA is rugged and sharp-edged as compared to otherwise flat rim in the case of lapped/polished

devices. The SEM image of the rim in Figure 2.20 shows a closeup of the rugged regions. As would be shown in the next chapter, the rugged rim is not necessarily a problem from performance point of view, but the angled or pointing profile of the rim can be a potential disadvantage for surface electrode transduction [89]-[94] discussed in Chapter IV. To overcome this issue, a combination of HFA and CMP can be used. Unlike laser cutting and lap/polish release method, HFA etch method does not require any sophisticated tools or expensive consumables. Moreover, this process does not require any process optimization or alignment and many devices can be released at a time enabling very high throughput.

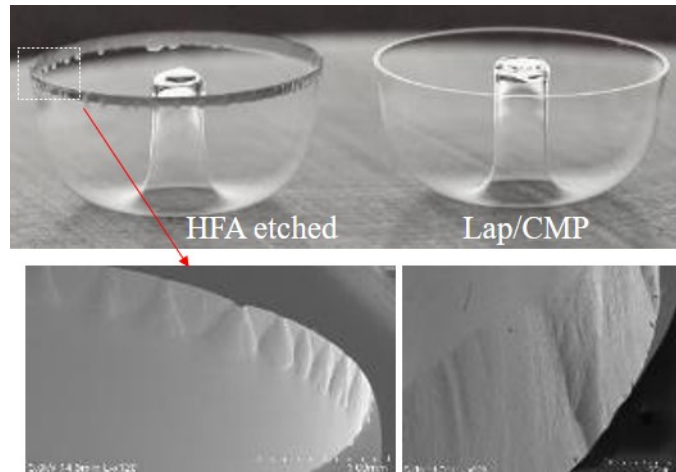


Figure 2.20: Photograph of shells released using lap/CMP and HFA etching. SEM image showing the rough region near the rim.

2.9 PSI Resonators

Different types of PSI resonators can be fabricated using patterned substrate. Figure 2.3 in section 2.1 shows different PSI resonators. In the next sub-sections, three distinct PSI resonators including H-NN, H-TN and S-TT are discussed. This is followed by another class of PSI devices with open or etched-through windows.

2.10 H-NX type PSI

H-NX type PSI resonators is characterized by **H**: Hollow Stem, **N**: Normal thickness shoulder and $X = \text{N/M/T}$: Normal/Medium/Thick thickness rim. PSI structures fabricated using flat unpatterned substrates having hollow stems are also called Birdbath Resonators in published literature. This is because of its resemblance to an invented birdbath. H-NX type PSI resonators are molded using a flat and unpatterned fused silica substrate using a cylindrical mold. A diced and cleaned fused-silica substrate is placed on top of a graphite mold. The thickness of the substrate determines the thickness of the rim which in turn determines the $n=2$ and $n=3$ wineglass frequency and the modal mass.

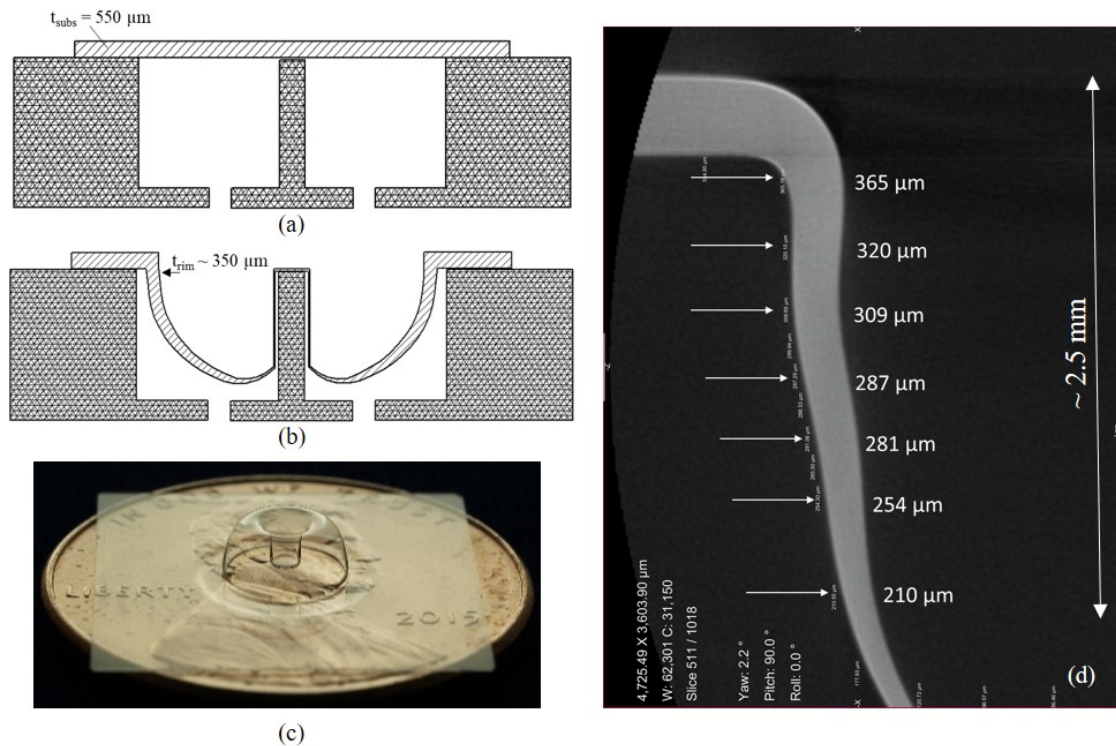


Figure 2.21: 10 kHz H-NT PSI shells are fabricated using (a) 550 μm thick flat FS substrate which when (b) blowtorched gives the (c) 3D shaped resonator. (d) CT scan showing the thickness profile.

The blowtorch flame deforms the substrate into the mold. In this type of struc-

tures, the anchor is self-aligned which imparts excellent symmetry to the shell. Post fabrication, the shells are singulated using either lapping and polishing method or through HFA release method as explained above. Figure 2.21 shows a blowtorched shell and CT scan showing sidewall thickness of H-NT resonator. It is seen that the thickness of such shells gradually reduces from the rim ($>300 \mu\text{m}$ with $n=2$ frequency at ~ 10 kHz) to the shoulder ($\sim 50 \mu\text{m}$) region. If such shells are made from $240 \mu\text{m}$ FS substrate, rim thickness of $\sim 200 \mu\text{m}$ with $n=2$ frequency at ~ 5 kHz is obtained. Testing and characterization results will be discussed in the next chapter.

2.11 H-TN type PSI

As could be seen from the CT scan image of a H-NT resonator, the thickness gradually decreases as one moves away from the rim. The shoulder thickness becomes $10 \mu\text{m}$ for a 5 kHz device. Such thin regions at the shoulder, makes the structure flexible in the vertical direction and in an event of shock, there is large vertical displacement. Therefore, for high shock application, it is desirable to have a thick shoulder. Also, for some applications, it is undesirable to have a gradually thinning profile and a more uniform thickness profile is needed. One such case is to fabricating conformal electrodes which will be discussed in Chapter IV. Therefore, it is important to locally tune the thickness (stiffness and mass). H-TN PSI shells are characterized by H: Hollow Stem, T: Thick shoulder and N: Normal thickness rim. Local tuning of thickness can be done using patterned substrate with etched features instead of a flat substrate. Figure 2.22 shows two approaches to make a H-NT structure. For example. to fabricate H-NT with 5 kHz frequency, the substrate thickness should be $\sim 240 \mu\text{m}$. Now as shown in Figure 2.22(a) a circular trench can be etched on a $240 \mu\text{m}$ substrate so that the thin trench stretches and increase the shoulder thickness.

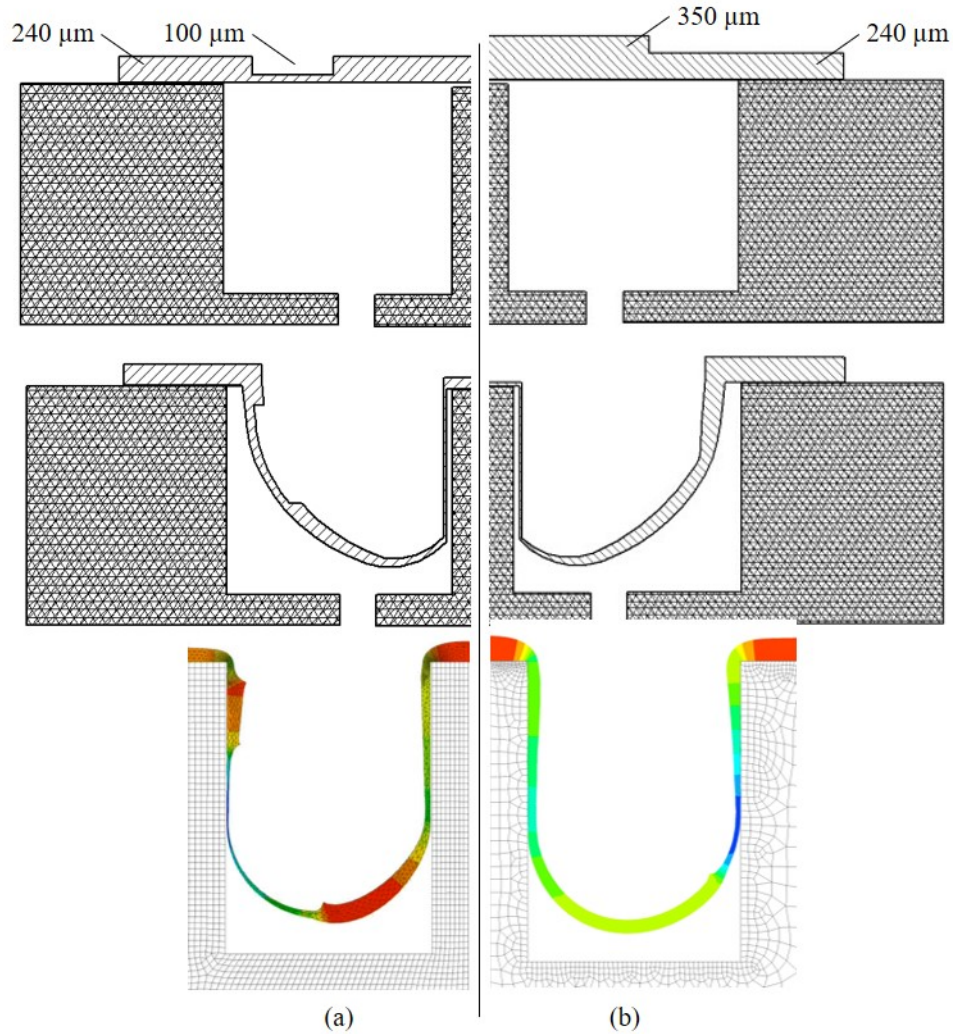


Figure 2.22: Two approaches to fabricate H-TN PSI by (a) etching a thin region and (b) etching to make a thick disc at the center. FEM simulation is used to optimize the dimensions of the patterns to obtain the desired profile and thickness.

The other approach is to start with a thick substrate and etch it down to define a thick $350\ \mu\text{m}$ disc at the center and a thinner $240\ \mu\text{m}$ region at other places as shown in Figure 2.22(b). Both the approaches can yield the desired structure. Figure 2.23 shows photograph of PSI shell fabricated using the two approaches. While both methods of making H-TN yields the desired structure with thick shoulder, however, each one of them is prone to imperfections of different magnitude. In case of misalignment of patterned substrate to the mold, the structure fabricated as

shown in Figure 2.22(a) will inherit mass imbalance at the rim whereas the structure in Figure 2.22(b) will inherit mass imbalance in region away from the rim. Two shell fabricated using each approach is shown in Figure 2.24 and region of mass imbalance can be seen.

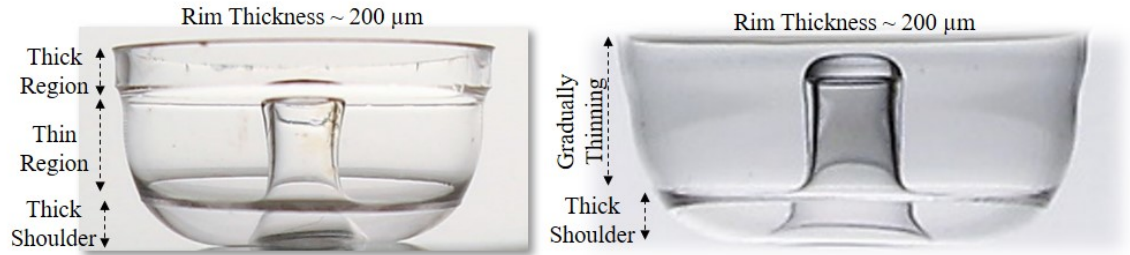


Figure 2.23: Fabricated H-TN shells. Rim thickness in both cases is $200 \mu\text{m}$ and the shoulder thickness is $50 \mu\text{m}$. In the shell on the left, the sidewall thickness is thick and then becomes thin whereas on the right it gradually thins as it reaches the shoulder where it becomes thick.

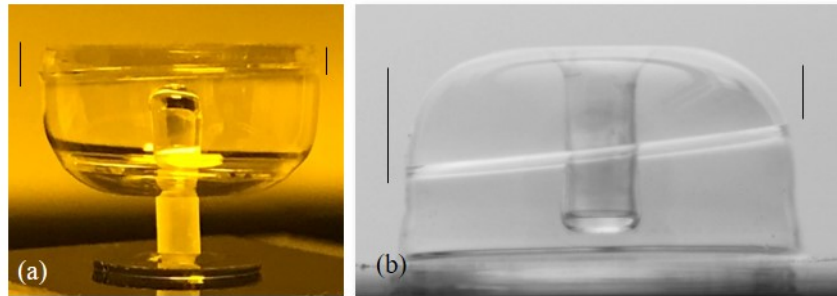


Figure 2.24: PSI resonators with mass imbalance. (a) imbalance is also at the rim while (b) imbalance is mostly away from the rim. Mass imbalance at the rim affects frequency mismatch much more than it being away from the rim.

A finite element model in COMSOL is made to numerically study the effect of mass imbalance at different regions. First a perfect shell is made, and then extra mass is added spanning an angle of 50° . The height of added mass is increased and change in frequency mismatch is analyzed. It is to be noted that the rim thickness is kept constant along the parameter to eliminate any frequency mismatch due to thickness changes. Masses are added at the rim and away from the rim as shown in Figure 2.25 and the frequency mismatch is plotted. Frequency mismatch increases

by a factor of 3 for the same amount of imperfection at the rim than away from rim.

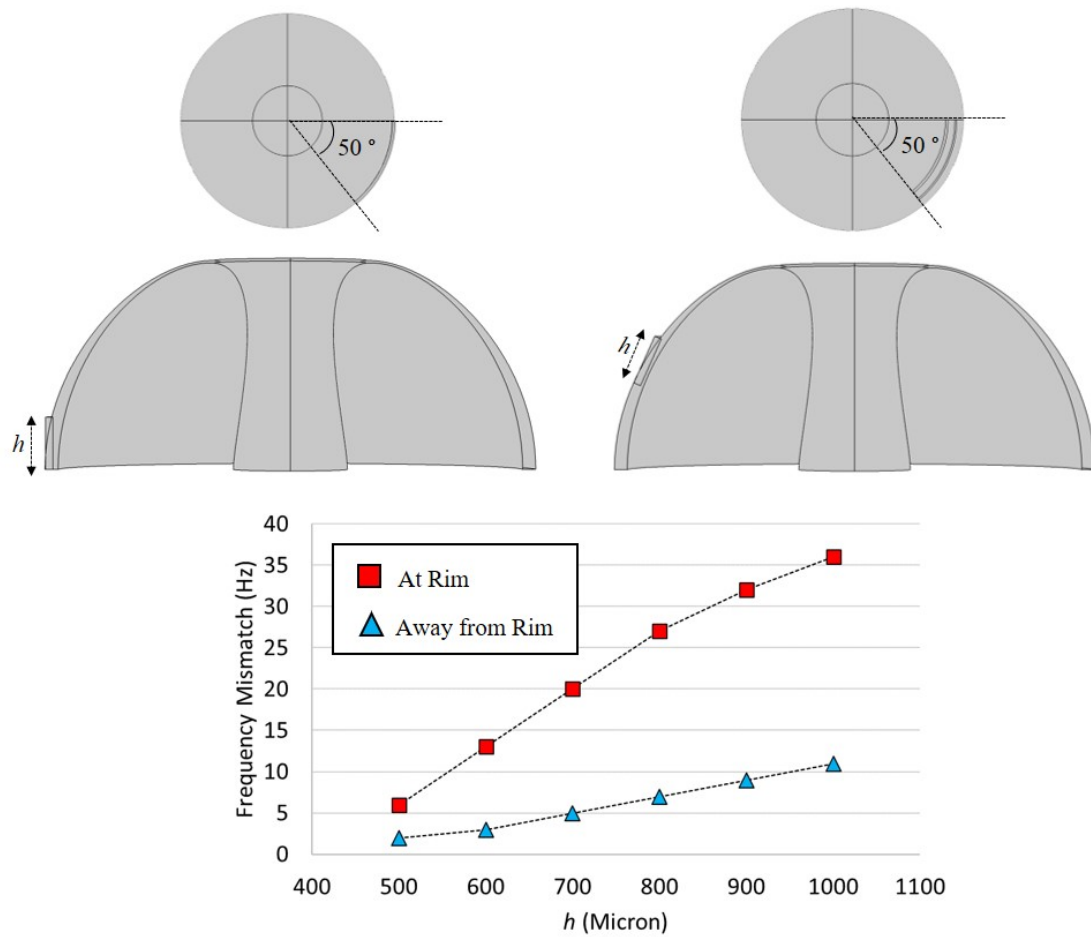


Figure 2.25: Simulation model to calculate $n=2$ frequency mismatch due to imbalanced mass distribution. Mass imbalance at the rim causes 3 times more frequency mismatch as compared to similar mass imbalance away from the rim.

Such mass imbalance also affects Q apart from frequency mismatch. Therefore approach 2 as shown in Figure 2.22(b) is desirable to obtain small frequency mismatch although careful alignment must be done to ensure high symmetry. Effect of other imperfections will be discussed later in this chapter. The dimensions of features on patterned substrate can be used to define the local thickness. Figure 2.26 shows four shells fabricated using substrates with varying radius of the central disc.

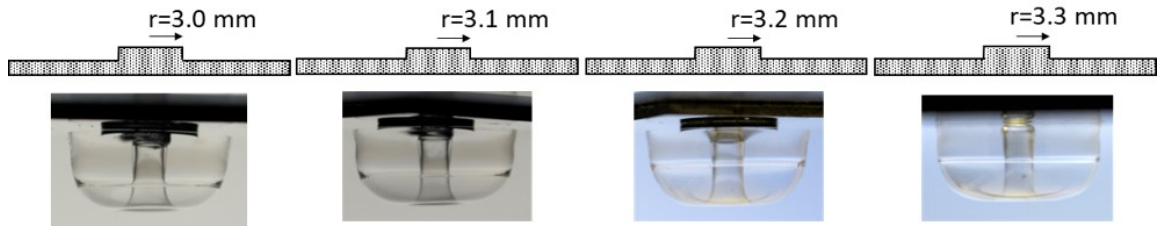


Figure 2.26: By varying the radius of central pattern on patterned substrate the height of the thick shoulder can be controlled.

2.12 S-XX (Solid Stem) type PSI

PSI shells can also be fabricated with a solid stem instead of a hollow stem. Hollow stems in H-XX type PSI is possible due to the mold design which leads to monolithic fabrication of resonator and stem. However, to fabricate solid stem devices monolithic fabrication is not possible and therefore different approach needs to be developed. To fabricate S-XX type PSI devices with solid stem, two approaches has been taken using either an un-patterned or a patterned substrate. In the first approach, a dome-shaped mold is used. The type of substrate whether patterned or unpatterned is determined by the type of PSI device required. For example, to fabricate S-TM type PSI where shoulder or joint is thick, but the rim or hand is medium thickness, a flat substrate is used. Solid FS stem is first inserted in the machined slot of the mold. Next, a flat FS substrate is kept atop the mold and is blowtorch molded. During molding, the substrate deforms and takes the hemispherical shape of the mold while getting micro-welded to the stem on the top. Figure 2.27(a)–(b) shows simulated profile obtained using finite element analysis. Fabrication process is shown in Figure 2.27(c)–(e) and photograph of a fabricated and singulated device is shown in Figure 2.27(f). These devices have a thick shoulder which is largely determined by the thickness of the initial substrate whereas the rim region is medium thickness because as the substrate stretches out-of-plane to form the rim at the bottom, its

thickness gets reduced. Figure 2.28 shows SEM image of a S-TM device where thick shoulder and relatively thinner rim can be seen.

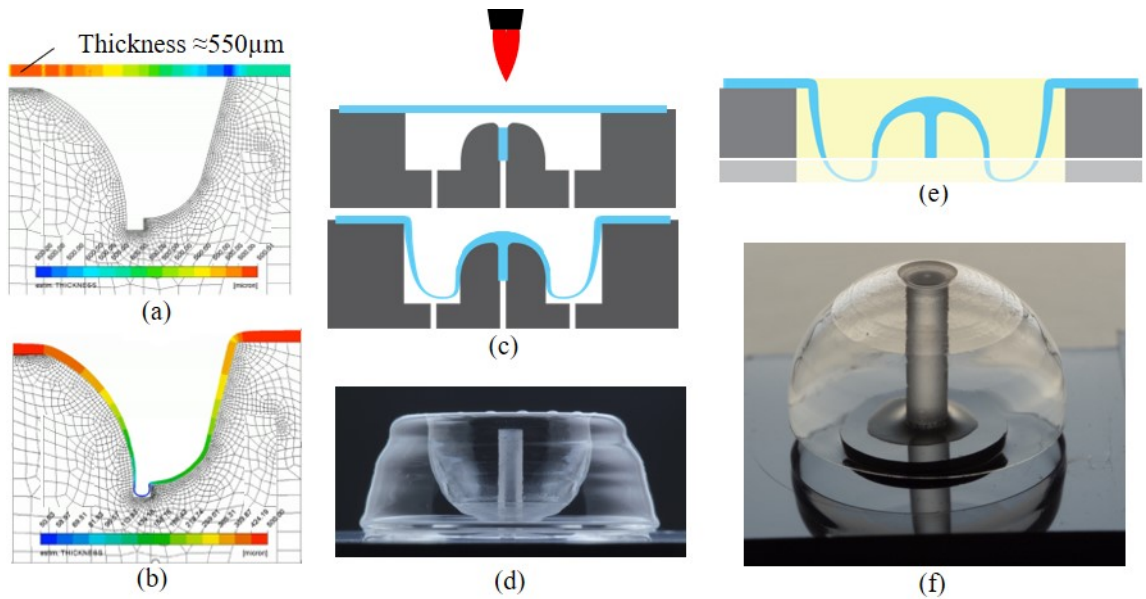


Figure 2.27: Fabrication process of S-TM type PSI structure. (a) Finite element model is used to optimize the dimension of features on patterned substrate. (b) The central disc forms the thick top shoulder, the outer annulus defines the thick rim, (c) photograph of a fabricated patterned substrate atop a dome type mold. To fabricate the shell, (d) first a FS rod is inserted, and the substrate is torched on the mold. (e) Optical photograph of a torched shell. After molding, (f) the shell is singulated and (g) mounted on a silicon substrate for testing.

It can be seen from Figure 2.28 that S-TM devices have a medium thickness rim which is $\sim 175 \mu\text{m}$. This rim thickness is nearly the same as those of 5 kHz hollow PSI devices although here the thickness gradually increases from the rim to joint as compared to reverse case in case of hollow stem PSI. This approach therefore places a limit on thickness of rim. To overcome this challenge, a patterned substrate is used. A FS substrate is etched to define a central disc, a thin trench and an outer annulus. The central disc forms the shoulder region, while the outer annulus defines the thick rim. The dimensions of these patterns are determined by finite element simulations as shown in Figure 2.29(a)-(b) [95, 96]. Here the thick annulus lands at the bottom and forms thick rim making a S-TT PSI device as shown in

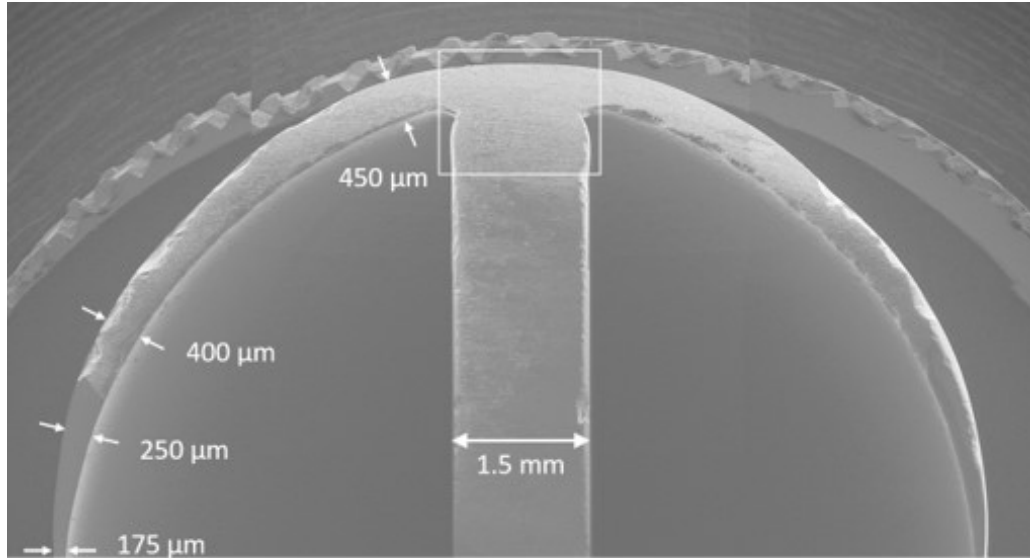


Figure 2.28: SEM image of S-TM PSI resonator. The shoulder region is $450\ \mu\text{m}$ thick and it gradually thins down to nearly $175\ \mu\text{m}$ at the rim. It can be seen that the FS rod gets seamlessly welded to the substrate.

fabrication process in Figure 2.29(c)-(d). Figure 2.29(e) shows optical photo of a fabricated S-TT resonator. After molding the shell is singulated and mounted on a silicon substrate for testing as shown in Figure 2.29(f)-(g). Figure 2.30 shows SEM of shell and the cross-sectional profile with thick rim and seamless welding of the stem. In this approach, the final shape is strongly dependent on the dimensions of etched features.

Another approach to fabricate S-TT is also developed to enable double anchoring scheme. This approach uses a patterned substrate and mold used to make H-TN resonators. However, the mold design is modified to remove the central stem and instead create a slot in its place. A fused silica rod is placed at the center and a patterned substrate is torched. The substrate deforms and 3D shell with thick rim and thick shoulder is formed with a solid stem as shown in Figure 2.31. This approach ensures better thermal uniformity at the rim region and welding with FS stem occurs not only at the top but also from the side of the stem. At the same time,

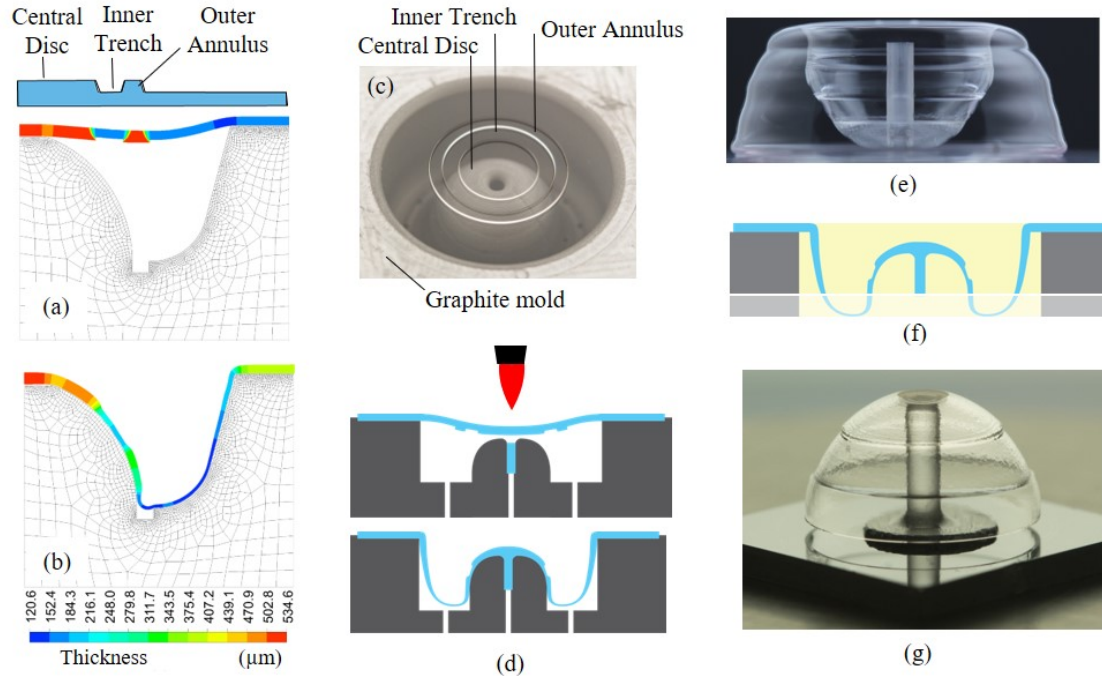


Figure 2.29: Fabrication process of S-TT PSI structure. (a) Finite element model is used to optimize the dimension of features on patterned substrate. (b) The central disc forms the thick top shoulder, the outer annulus defines the thick rim, (c) photograph of a fabricated patterned substrate atop a dome type mold. To fabricate the shell, (d) first a FS rod is inserted, and the substrate is torched on the mold. (e) Optical photograph of a torched shell. After molding, (f) the shell is singulated and (g) mounted on a silicon substrate for testing.

rim thickness can be better controlled. These PSI devices have two stems which can be used for dual anchoring which can further improve shock immunity. Such devices with solid stems however are prone to imbalance due to potential misalignment of stem during torching. Such misalignment could make the device asymmetric which is detrimental for Q . Imperfections and their effects will be discussed later in the chapter.

Although three types of PSI devices are discussed here, however, using the same approach any type of PSI devices can be fabricated.

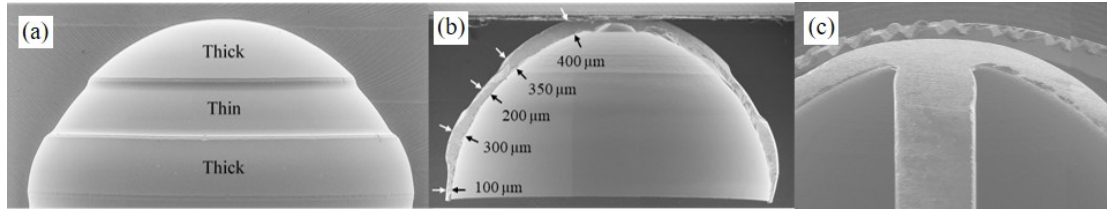


Figure 2.30: SEM image showing (a) a fabricated S-TT PSI resonator showing thick shoulder and thick rim, (b) cross section of the resonator, the rim is $300\ \mu\text{m}$ and shoulder is $400\ \mu\text{m}$ (the stem broke off during cross sectioning). (c) Another resonator showing seamless welding of the substrate to the FS rod.

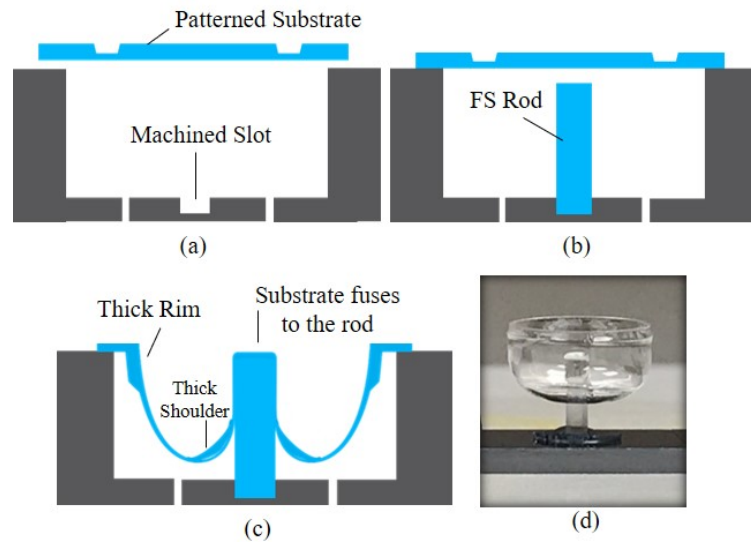


Figure 2.31: Fabrication process of S-TT type PSI structure. (a) Mold like those for H-XX type PSI is used but the stem is removed, and a slot is machined. (b) FS rod is placed in the slot and the patterned substrate is molded. (c) The substrate deforms forming the thick rim and thick shoulder fusing to the solid stem. (d) Photograph of a singulated PSI device.

2.13 Open-PSI Resonators

All 3D shells discussed so far are relatively simple shells with continuous surfaces, meaning the surface does not have any open windows or holes. It is, however, desired for several applications that some predefined regions of these structures have engineered surface topology. That is predefined regions on these shells either have a significantly different thickness or are completely removed to have open windows. Application of such engineered 3D structures with thin/open windows include, 1) as electrode substrate with tailored curvature to be used around a 3D resonator

to define large capacitive overlap, 2) as a shadow mask for pattern formation on curved 3D surfaces, 3) as mechanical resonators with reduced damping, and 4) optomechanical sensors and actuators including lenses, antennas etc. [97, 99]. The technology to fabricate other PSI resonators with thin regions, does not provide the ability to form specific areas where the shells could have selectively opened window. Figure 2.32 shows PSI shells with windows opened at different locations. It also shows photographs of two structures where thin windows are defined on the surface of hemispherical and hemi-toroidal (birdbath) structures.

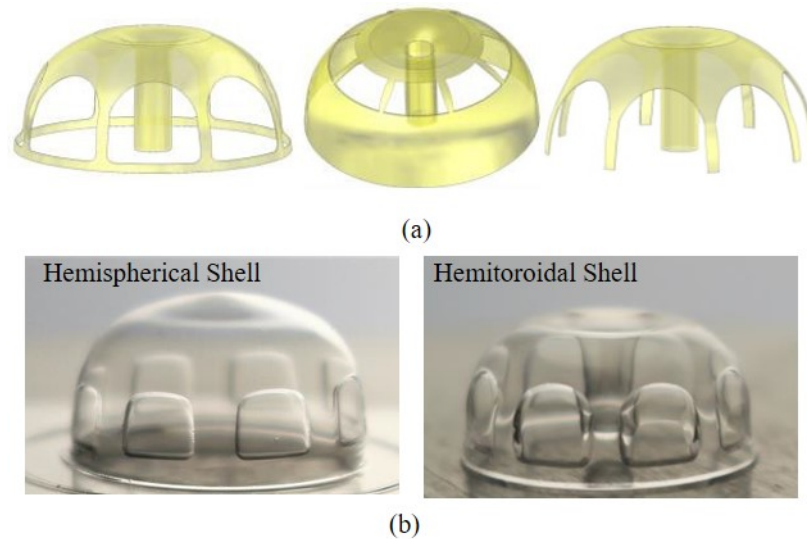


Figure 2.32: (a) Schematic showing shells with open windows at different locations and (b) fabricated shells with discrete thin windows symmetrically defined on the outside of the shell. These thin windows can be through etched to make open windows.

These shells when timed-etch in HF acid etches some thickness of the entire shell, but the thin regions get etched off creating open windows. To fabricate open shell PSI structures, a patterned substrate is fabricated as shown in Figure 2.33 with eight trapezoidal openings which are then etched down. These etched features subsequently define the thin/open windows on the shells and the thick region between the windows define the supporting springs. The dimensions l_w and w_s determine

the shape of thin windows on the final shell and can be tuned to obtain windows of different aspect ratio as will be shown later.

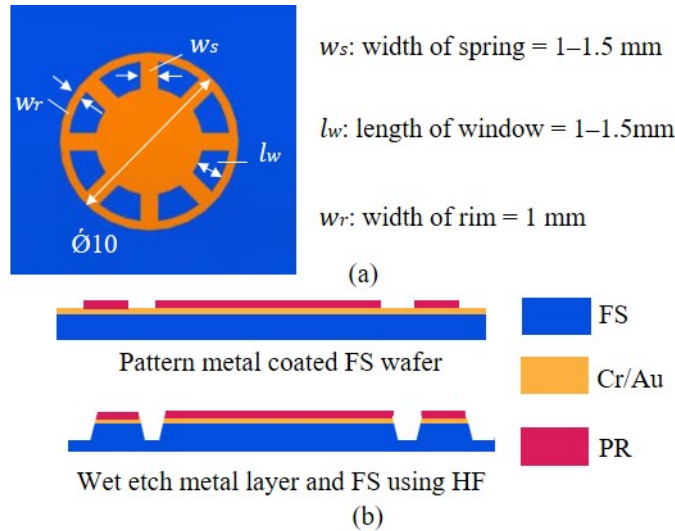


Figure 2.33: (a) Layout of patterned substrate to make 3D shells with eight discrete thin/open regions. The dimensions w_s and l_w can be tuned to obtain desired aspect ratio of windows on the shell. (b) Flat 550 μm FS wafer is patterned and etched in HF to obtain the desired etch depth. The thick and the thin part after etching is 350 μm and 150 μm , respectively.

To fabricate such a shell, a patterned substrate with layout dimension $w_r = 1$ mm, $l_w = 0.5$ mm and $w_s = 1.5$ mm is fabricated. Lateral undercutting is accounted for in the layout design. Patterned substrates are etched for nearly 200 minutes to define 350 μm thick region (shaded) and 150 μm thin regions as shown in Figure 2.33(b). This would add 0.2 mm to each dimension of the window and reduce the same from the spring dimension. After fabricating, cleaning and dicing, a patterned substrate is kept on top of a mold and blowtorched to make 3D structure as shown in Figure 2.34(b)-(c). Figure 2.34(d) shows photograph of a 10 mm diameter hemispherical shell with thin regions symmetrically formed around the outside surface of the shell. SEM image shown in Figure 2.34(e) shows a closeup of the etched window. It is also seen in the same figure that the final dimension of the window on the shell is 1.9x1.8 mm. Extreme stretching occurs in the vertical direction and feature size

increases due to such stretching.

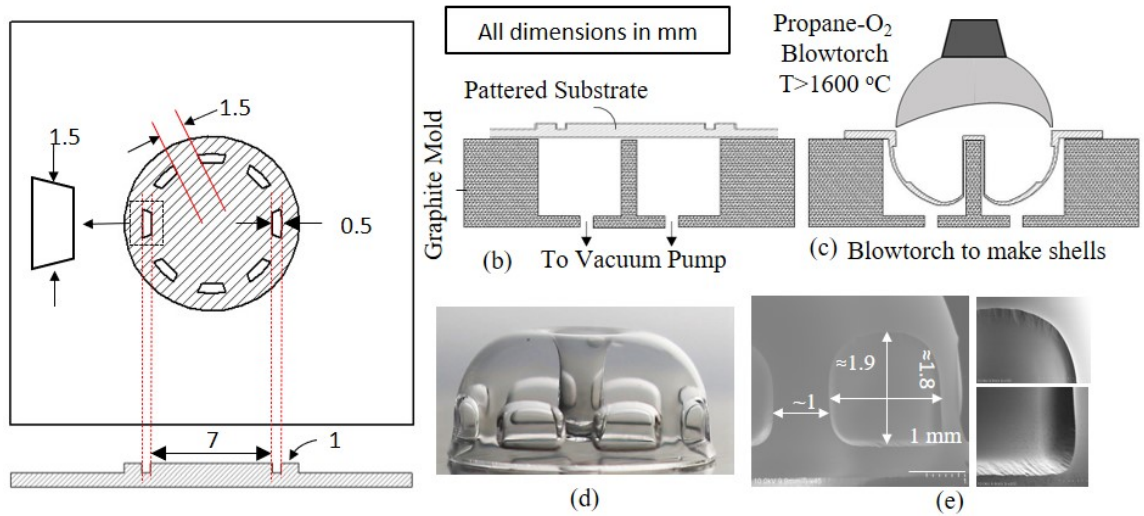


Figure 2.34: Fabrication flow to make shells using (a) patterned substrate which is (b)-(c) blowtorch molded to make shells with thin windows on its surface as shown in (d) photograph of a fabricated and singulated shell. (e) SEM images shows closeup of the etched window on the shell.

Although not evident in this picture, it will be later seen that stretching of thin region occurs in both lateral and vertical direction therefore giving a squared-circle type shape on the shell. Figure 2.35 shows CT scan of one of the shells with key dimensions of both thin windows and thick springs. Figure 2.35(c) shows thickness variation along the height, h , of the shell. The thick part of the initial substrate stretches by $\sim 60\%$ (from $350 \mu\text{m}$ to $\sim 130 \mu\text{m}$) while thin region stretched by $\sim 90\%$ (from $150 \mu\text{m}$ to $\sim 20 \mu\text{m}$) to define the thin windows. There is also a gradual change in thickness at the bottom and top transitional regions. The thickness and shape of windows on the initial substrates can be tuned to obtain windows of different thickness and aspect ratio on the surface of shell. It is to be noted that the flat 2D part of molded structures can be removed through lapping and polishing if needed. Shells with different aspect ratio of thin/open windows can be fabricated by tuning the dimension of etched features on the patterned substrate. Figure 2.36 shows two

other shells fabricated using the same approach as explained above but with different dimensions of patterned features on the substrate.

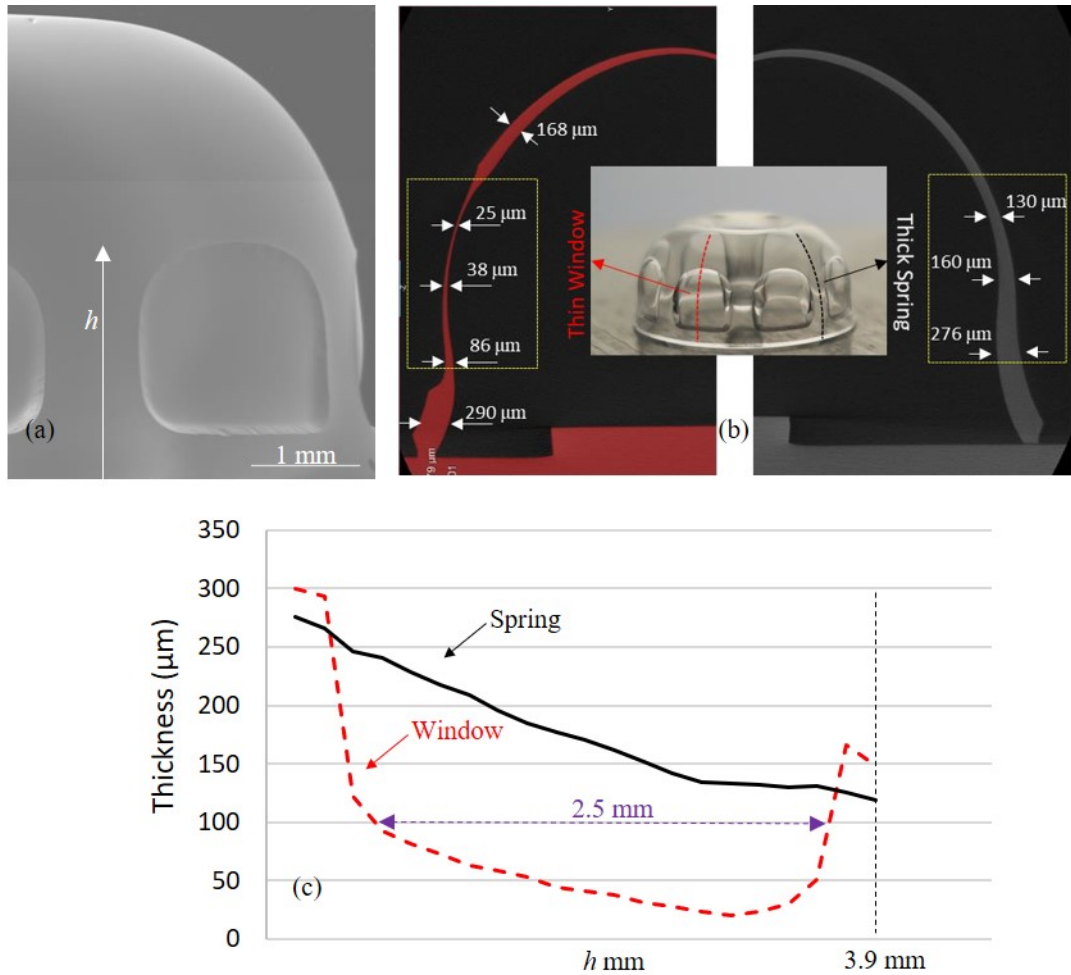


Figure 2.35: (a) SEM of a shell with thinned region, clearly highlighting the region, in the shape of a window, where the flat FS was first thinned, then deformed using blow torching. (b) CT scan image of a shell with thin windows. Cross-sectional view of thin region (shown on left) and thick spring (shown on right) is shown. (c) Variation of thickness along the height, h , of the shell is plotted for both spring and window.

Shell in Figure 2.36(a) is fabricated with layout dimensions of $w_r = 1$ mm, $l_w = 0.8$ mm and $w_s = 1$ mm while that in Figure 2.36(b) is fabricated with $w_r = 1$ mm, $l_w = 1$ mm and $w_s = 1$ mm. These were etched just like previous case to make ~ 350 μm thick and ~ 150 μm thin regions. Springs of these devices are thinner than that of the previous case and the width of the spring gradually reduces along the height of



Figure 2.36: Shells with different aspect ratio of thin windows fabricated by changing dimensions of etched features on the patterned substrate.

the shell. These shells when etched to make open windows would make a continuous cylinder suspended by only a few thin springs. In the next step, these thin regions on the surface of the shells are through-etched. The shells are protected from inside by filling in with Crystalbond 509 using a hotplate at $125\text{ }^{\circ}\text{C}$ and capped with a piece of silicon. It is then dipped in a bath of HFA for ~ 40 minutes. HF acid etches $\sim 40\text{ }\mu\text{m}$ (at the rate of $\sim 1\text{ }\mu\text{m}/\text{min}$) from the shell and regions on the shell with thickness $< 40\text{ }\mu\text{m}$ etches through and becomes open. Figure 2.37 shows the process and photo of a shell where the thinned regions were further etched in HF to create open windows. This etch can be timed to define area of the open window. The device shown in the SEM image shows that the edge regions are not uniformly etched. This is because of thicker transitional regions at the edge. This can be corrected by increasing the etch time to make sure that transition regions are also through-etched. As can be seen from thickness profile of the shell in Figure 2.35(c), etching the shell by $\sim 100\text{ }\mu\text{m}$ (roughly 100 minutes) would create an open window of $\sim 2.5\text{ mm}$ height. Although not shown here, it is also possible to form structures where the original FS substrate is etched to different thicknesses in different regions, enabling the formation of both etched through windows and thin regions in the same structure. This method is an efficient method to fabricate large thin/open windows. Fabrication of extremely

small openings ($< 100 \mu\text{m}$) would however not be possible due to two reasons. First, defining high aspect ratio features (i.e. deep etch to reduce thickness) with small openings using wet etching is not possible due to isotropic nature of HFA.

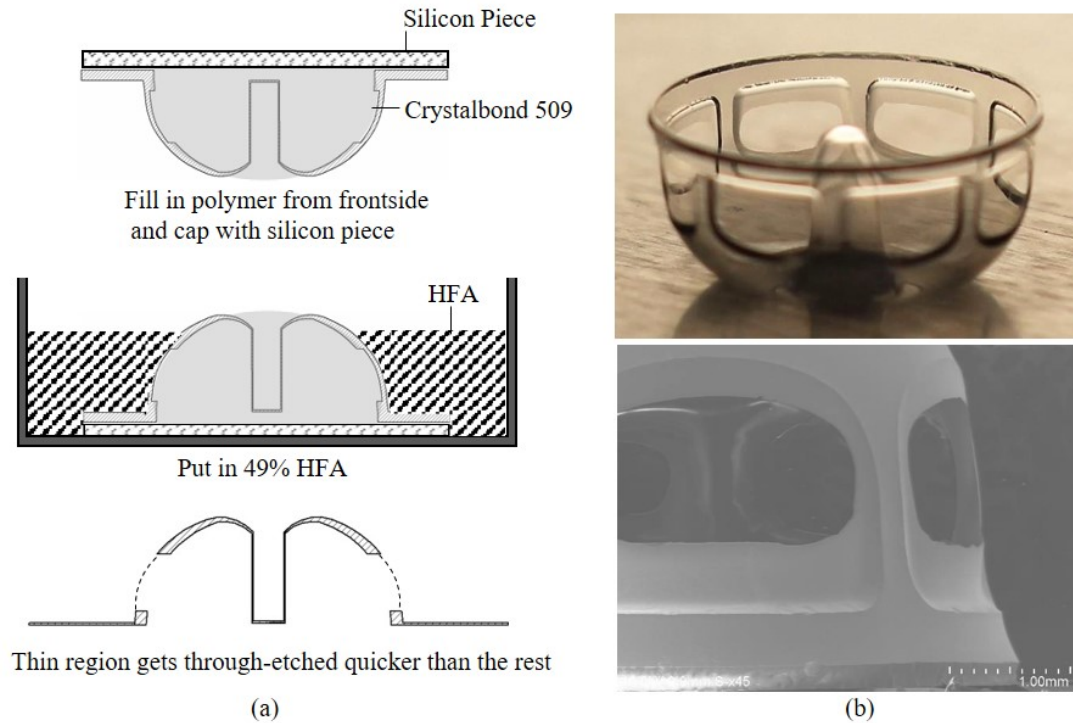


Figure 2.37: (a) Process of through-etching thin windows by protecting the inside with Crystalbond 509 and dipping in HFA bath for timed etching. (b) Photos of a singulated shell where the thinned regions were further etched in HF to create the open windows. This etch can be timed to define the area of the open window.

Second, during molding the substrate stretches by several millimeters therefore very small features would get stretched increasing the dimension. However, this process is efficient to define features $>100 \mu\text{m}$ with low cost and batch-level fabrication. Additionally, the features shown in these devices could be made to have different shapes so that the final shell could have any final shape as desired by a given application. One application of such open shells is as a shadow mask. Stencil masks are routinely used for depositing a variety of regular and sometimes exotic materials on substrates. While shadow masks for flat substrates are commonly used, those for 3D

surfaces are hard to make. Use of shadow masks is quite useful for 3D resonators shells for inertial sensing applications. While fused silica is a favorite material for such resonators due to its low thermoelastic damping (TED) losses, it poses challenges when the structure must be electrostatically sensed or actuated because it is a dielectric. Such shells are often coated with a thin conducting layer. This conductive coating increases damping which reduces quality factor. Therefore, metal should only be deposited on specific regions of interest to reduce energy damping. The best tradeoff is to selectively coat the surface as shown in Figure 2.38(a). The open shell can be used as a shadow mask to deposit metal on a hemispherical shell. Figure 2.38(b) shows a shadow mask shell used to selectively coat a hemispherical shell with metal.

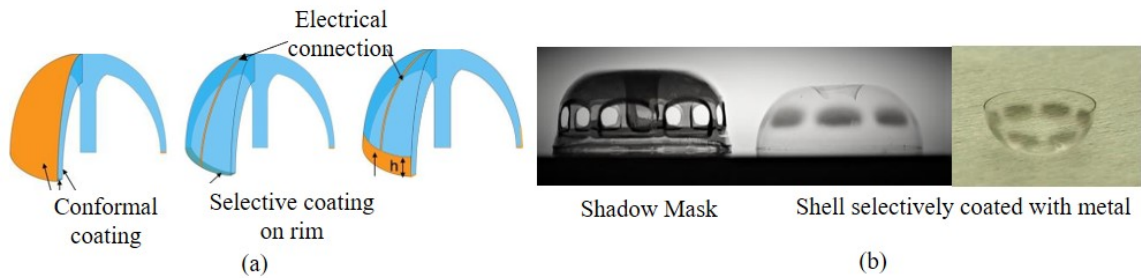


Figure 2.38: (a) Selective conductive coating on shell reduces loss and increases Q . (b) Shell fabricated with open window is used as a stencil mask to selectively coat metal on another shell.

2.14 Imperfections

Fabrication of symmetric resonators is very important to obtain high performance in terms of high Q and low frequency mismatch. To fabricate symmetric resonators, it is important to understand the source and effect of imperfections. Different types of imperfections are shown in Figure 2.39 and some of them are discussed in this section. Guidelines are proposed to fabricate symmetric resonators.

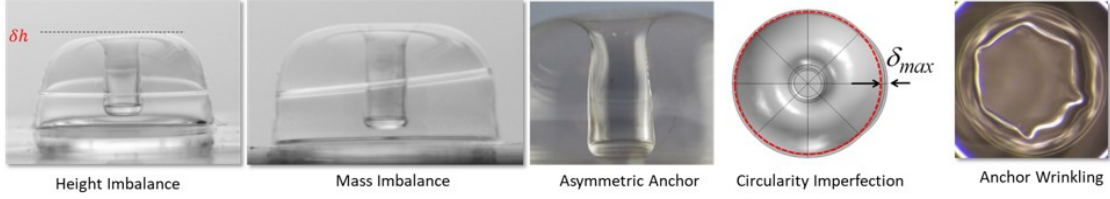


Figure 2.39: Different types of imperfections in shell resonators. These can be mitigated by process optimization.

2.14.1 Height Imperfection

Height imperfection as the name suggests is the mismatch in height of the resonator and is primarily caused by temperature variation during blowtorch molding. Temperature difference causes the shell to deform asymmetrically making one side deform more than the other causing imbalance in height. Other sources which could contribute to height imperfection is the thickness asymmetry on the initial substrate. If the thickness of the initial substrate is not symmetric about the center of mold, thinner regions will deform more than the thick regions causing a mismatch in height. Height imperfection can also be caused from temperature non-uniformity due to misalignment of the flame with the mold. If the flame is precisely aligned with the center of the mold, temperature profile is symmetric about the axis of mold, however, misalignment as small as ten microns is enough to asymmetrically deform the shell. Figure 2.39 shows a shell with height asymmetry. The effect of height asymmetry on Q_{anchor} , Q_{TED} , frequency of $n=2$ mode and frequency mismatch are studied numerically and is presented in the next section.

2.14.2 Circularity Imperfection

Circularity of the resonator also contributes towards the overall symmetry of the resonator. Circularity imperfection can be either in the form of acircular rim or it can be variation in thickness along the circumference. Imperfection in circularity could

be from a non-circular mold or it can be due to asymmetric molding of the substrate. Such imperfection results in non-uniform rim dimension along the circumference and is detrimental to Q as well as to Δf of the resonator. To study the impact of such imperfections, a finite element-based study is presented in [83]. Figure 2.40 presents the numerical results from [83] showing the effect of height and circular asymmetry on Q_{anchor} , Q_{TED} , frequency and frequency mismatch on the two modes.

Results shown in Figure 2.40 are for the case when the shell has imperfections of first harmonics. However, other harmonics imperfections can be also be present. Reference [100] studied such an effect where imperfections in form on higher order harmonics were studied and their effect on Δf was analyzed. They found that 4th harmonic imperfection has the most detrimental effect on $n=2$ wineglass mode frequency mismatch. Circular imperfections can also be caused due to asymmetric thickness along the circumference of the resonator. It can be caused due to temperature non-uniformity as well as thickness variation in the substrate.

2.14.3 Mass Imperfection

PSI structures have tuned stiffness and mass distribution therefore they are also susceptible to imperfection due to mass imperfection besides geometric imperfections. The mass imbalance is caused due to misalignment of patterned substrate with the mold which leads to different masses on either side of the mold. A photo of a shell with mass imbalance is shown in Figure 2.39. It can be seen that the distribution of mass in these shells is not uniform. An unbalanced shell has detrimental effects on Q . They can also have detrimental effect on frequency mismatch depending on where the imbalance lies as analyzed numerically in Figure 2.25.

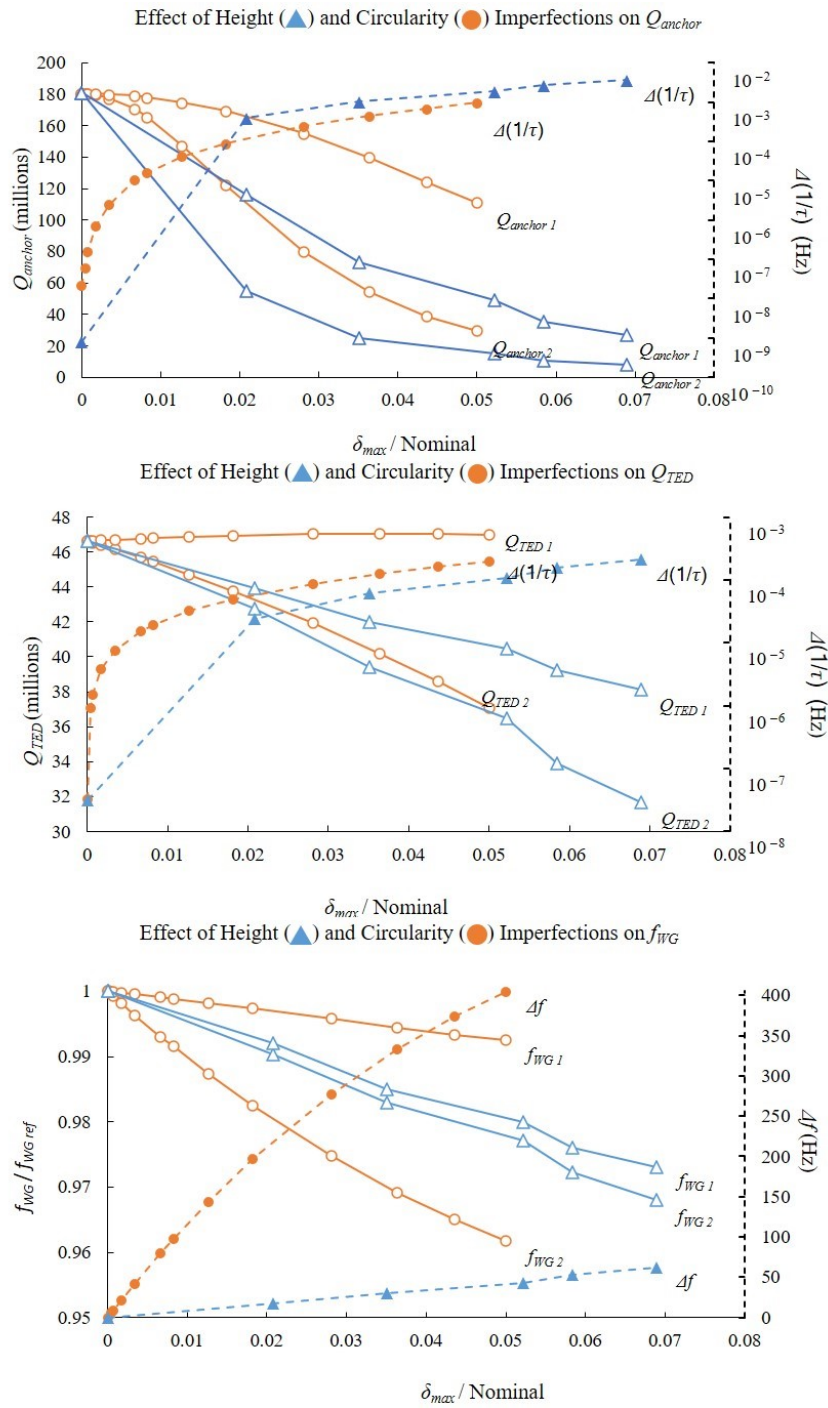


Figure 2.40: Effect of imperfection in height and circularity on Q_{anchor} , Q_{TED} , f and Δf of shell resonator. Figures from Dr. B. Shiari, Univ. of Michigan and reported in [83].

2.14.4 Anchor Misalignment

PSI resonators with hollow stems are less susceptible to anchor misalignment because the anchor is defined and is self-aligned from the mold. Therefore, the alignment of anchor with respect to the shell is solely determined by the precision of mold. Therefore, hollow stems have minimal anchor misalignment imperfection but can suffer from other types of asymmetries like height, circularity imperfection etc. Solid stem PSI resonators on the other hand possess an additional source of asymmetry which is due to misalignment of anchor. Such solid stem PSI devices are not fabricated monolithically instead they are formed by micro-welding of solid FS rod to the substrate during reflow. Therefore, placement of FS rod is a potential source of misalignment. To study the effect of misalignment of anchor on Q_{anchor} , a finite element simulation is done using the method explained in [81]. Figure 2.41 shows the photograph of a S-TT shell from the top with misaligned anchor and numerical results showing effect of anchor misalignment on Q . Q_{anchor} drops by more than three orders of magnitude when anchor is misaligned by $100 \mu\text{m}$.

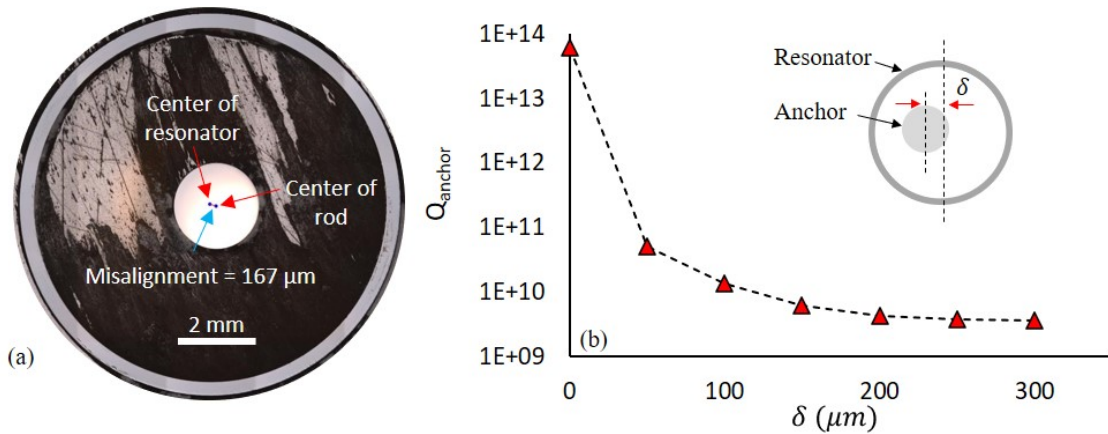


Figure 2.41: (a) Microscope image of a singulated shell taken on Olympus LEXT showing misalignment of anchor wrt shell. (b) Numerical results showing Q_{anchor} with misalignment, δ . Simulation results are from Dr. A. Darvishian.

Even if the slots for placing the rod is machined precisely at the center of mold, the rod is still susceptible to tilting or moving. If the rod tilts by 0.5-degree, misalignment at the top could be $\sim 50 \mu\text{m}$. Such misalignments can be reduced by reducing the tolerance in the machined slots in mold to minimize tilting. Additionally, the rod can also be held in place from top by the substrate during torching.

2.14.5 Surface Imperfection

The surface of the shell is also prone to imperfection. Ideally, a smooth surface is desired to minimize losses from the surface, however, several sources can contribute to surface defects. One of the major causes is deposition/embedment of particle on the surface. Particles can either come from the gas tank during torching or can come from the surrounding. Besides, organic residues on the substrate (example from blue tape during dicing) can also be embedded in the shell during torching if not removed properly. Surface defect can also be induced when the resonator gets overheated during blowtorch molding. To have a defect free shell, high-purity gas cylinders installed with filters are used and blowtorching parameters are optimized to avoid overheating. Additionally, the substrate is thoroughly cleaned after dicing in both solvents and Piranha solution to have a clean surface. Surface imperfections can have detrimental effect on Q of the resonators.

2.15 Conclusion

Fabrication of PSI resonators can be efficiently done using blowtorch molding. This technology allows fabrication of shells with different aspect ratio, shape, dimension and anchor characteristics. Additionally, etching features on initial substrate imparts even greater flexibility and allows better control on selective regions of the shells. This is particularly beneficial for tuning mass and stiffness of localized re-

gions like joint or rim or even making open windows at selected locations. Molds made from an inexpensive and easily machinable material like graphite adds to the simplicity of the process. Besides, mold shapes can be altered to obtain user-defined shape of final structure. All these factors make the proposed technique to make 3D shells an affordable approach. Furthermore, singulation approaches using lap/polish method and HF release method can be used to batch fabricate PSI devices. Study of different imperfections is carried out and factors responsible for each imperfection is identified and mitigated. All these efforts combined have led to record performance even better than our own best results. Test results for different PSI devices will be discussed in the next chapter.

CHAPTER III

Precision Shell Integrating Resonator – Test and Characterization

3.1 Overview

In the last chapter, design and fabrication of resonators are discussed. This chapter will present the test results including resonant behavior as well as material behavior of FS. Most of the test results presented in this chapter are obtained through optical testing method which is first explained. Following this, measured Q , f and Δf from different devices both in $n=2$ and $n=3$ wineglass modes is presented. Chapter II also discussed two methods of singulation, and this chapter will compare performance from each method to evaluate their effectiveness and repeatability. Repeatability and uniformity of devices is also discussed to study effectiveness of methods developed in this thesis to enable volume production for potential commercialization. Some harsh environment testing results like those from shock and fatigue testing is presented. Finally, effect of different metal coating layers to make the resonators conductive for electrostatic testing for gyroscope (discussed in next chapter) is summarized and a systematic study is carried out for four metals and their effect on Q is analyzed. It is shown that the methods developed in this thesis present a robust solution for repeatable, low cost and high-performance resonators with user-defined modal parameters.

3.2 Optical Test Setup

PSI resonators can be tested for their resonant characteristics either optically using a laser Doppler velocimetry (LDV) or electrostatically using a network analyzer. Optical testing relies on the concept of Doppler shift in frequency of an incident light reflected off a moving object. An incident light falling normally on a moving object is scattered from a moving object experiencing a change in frequency which is given by,

$$f_D = 2\frac{\nu}{\lambda} \quad (3.1)$$

Where, ν is the velocity of the moving body and λ is the wavelength of light. This is known as the Doppler Effect. The velocity of the moving body can be determined by measuring the frequency shift experienced by the wave incident at a known wavelength.

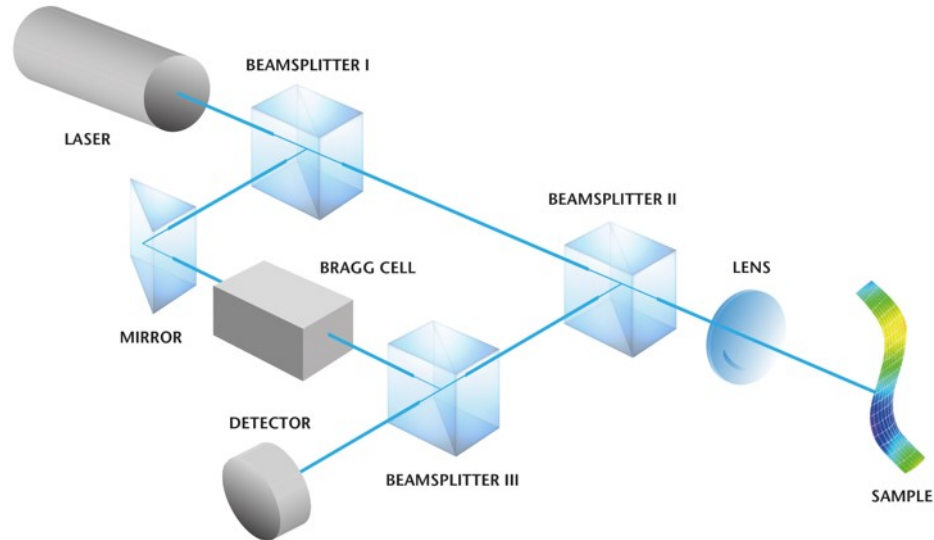


Figure 3.1: Fundamental of laser Doppler velocimetry to measure velocity of moving sample by measuring phase change. Photograph from PolyTec [101].

To do this, laser is first passed through a beam splitter which splits the beam in

two part. One part of the split beam is a reference beam which does not change its frequency with time and the other part is the measurement beam which is allowed to fall on a moving object. The moving object scatters the light back (in all direction) and a part of the reflected beam is allowed to interfere with the reference beam through a set of beam splitters and lenses. The two beams with their corresponding intensities interfere generating a light/dark fringe pattern which gives information of path length difference between two beams. The reference beam does not change its length, but the measurement beam does due to vibration of the object it is incident on. Figure 3.1 shows the fundamental of laser Doppler velocimetry (LDV). To test PSI resonators on an LDV, they are first attached to a silicon test substrate with a pedestal using either glass frit or Crystalbond 509. The test substrates (with attached shells) are then mounted on a thick PZT block and the PZT block is screwed in a vacuum chamber. The chamber is pumped down until the pressure reaches $<10 \mu\text{Torr}$ pressure. Figure 3.2 shows schematic view of the test setup used for testing.

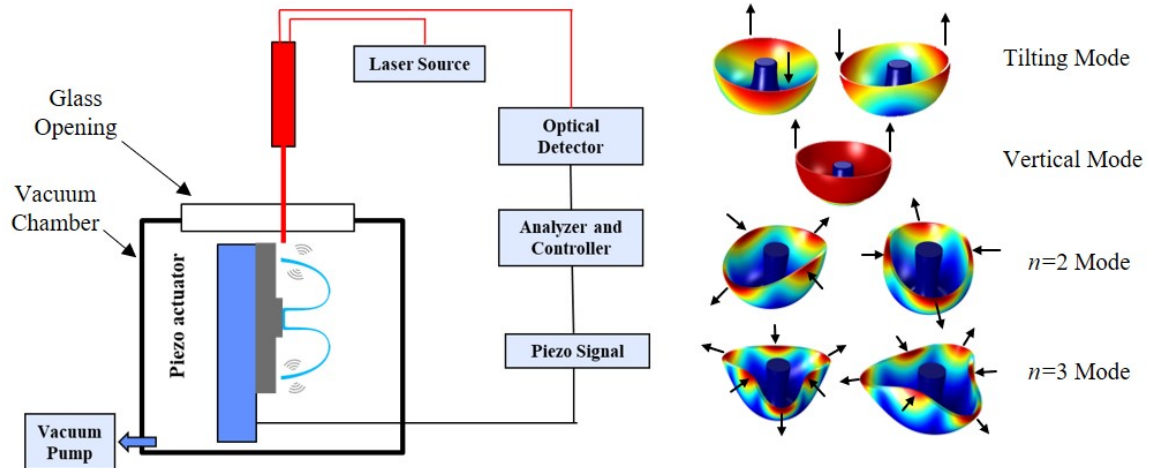


Figure 3.2: Schematic diagram showing the test setup and modeshape of a PSI resonator.

To measure resonance frequency, the PZT is actuated with a periodic chirp signal and the velocity of the rim is measured by reflecting laser off the rim of shells. The

FFT of collected data reveals the mode spectra and the $n=2$ wineglass frequency is measured. The PZT is then driven at the resonance frequency so the velocity of the rim builds up. Once the velocity reaches an appreciable value, the drive excitation is cut off and the vibration is allowed to freely decay. Data is collected for 524 seconds and τ is measured by calculating the time it takes for the amplitude to decay to $1/e$ of its initial value. Quality factor is calculated using the expression $Q = \pi \cdot \tau \cdot f$, where f is the resonant frequency. One device is kept in vacuum and frequency and τ is measured nine times. Frequency varied by a maximum of 0.06 Hz and τ varied by a maximum of 2 second for a device with f 5000 Hz and $\tau=274$ seconds. Therefore, all the results presented in this chapter can be considered within such an error limit which is 0.0001% for f and 0.7% for τ (or Q). Such measurement errors are negligible. The next section discusses test results from different PSI resonators. Mode spectra of a typical PSI resonator fabricated with a rim thickness of $\sim 200 \mu\text{m}$ has the $n=2$ wineglass frequencies at ~ 6 kHz and the $n=3$ wineglass frequencies at $\sim 2.8x$ higher around 17 kHz. Other peaks in the mode spectra corresponds to tilting, vertical and breathing modes. Figure 3.2 shows first four modes and modeshapes of a PSI resonator.

3.3 Test Results of $n=2$ Modes

Several resonance characteristics like Q , τ , f , Δf , $\Delta(1/\tau)$ etc. are important to determine how good a resonator is for its application in a high-performance gyroscope. $\Delta(1/\tau) = |1/\tau_1 - 1/\tau_2|$ is the difference of the inverse of ring-down time constants of the two $n=2$ or $n=3$ modes. As described earlier, desired resonance behavior includes high- Q , long τ , reasonable frequency, low frequency mismatch and low $\Delta(1/\tau)$. Long τ ensures low $\Delta(1/\tau)$ which is desired for low bias instability

[28]. This section will present test results of PSI resonators fabricated over the years and discuss key observations and guidelines for fabricating high-performance resonators. Chapter II discussed two methods employed towards singulating 3D shell from a molded structure. Results from each singulation methods are discussed and comparison is made in terms of performance and cost of each method.

3.3.1 Singulation using Lap/CMP Method

Lap/Polishing method is discussed in Section 2.8.2 This method uses mechanical grinding method to remove the flat part of a molded structure to singulate 3D shell. This section discusses results obtained from resonators singulated using this approach. Figure 3.3 shows the ring-down time plot of three different types of PSI resonators which have been discussed in Section 2.9. For a S-TT PSI resonator, the lowest frequency modes are the tilting and $n=2$ WG modes, with $f_{tilting} \approx 6.5$ kHz and $f_{n=2} \approx 17.1$ kHz. The tilting mode has a very low Q of ≈ 130 , but the $n = 2$ WG mode at 17.126 kHz achieves τ of 25.2 s and a Q of 1.36 million.

The difference in frequency between the WG modes is 25.0Hz. High $n=2$ WG frequency can be attributed to the thick rim (between 200–300 μm) of S-TT resonators as shown in Figure 3.4.

For a H-TN type PSI resonator, maximum Q of 12.5 Million and $\tau = 310$ second is measured at 12.8 kHz. This is the best reported Q for any device ≤ 10 mm. This resonator also had a rim thickness ≈ 300 μm however the thickness gradually decrease and becomes ≈ 50 μm at the shoulder region. As a result, the frequency is lower than that of S-TT PSI. The third plot is from a H-NN PSI resonator operating at $n=2$ wineglass frequency at 6 kHz. Q more than 8.7 Million and $\tau = 470$ s is measured. Such high Qs from PSI resonators are possible because of significant time and effort invested in studying and understanding the impact of design and

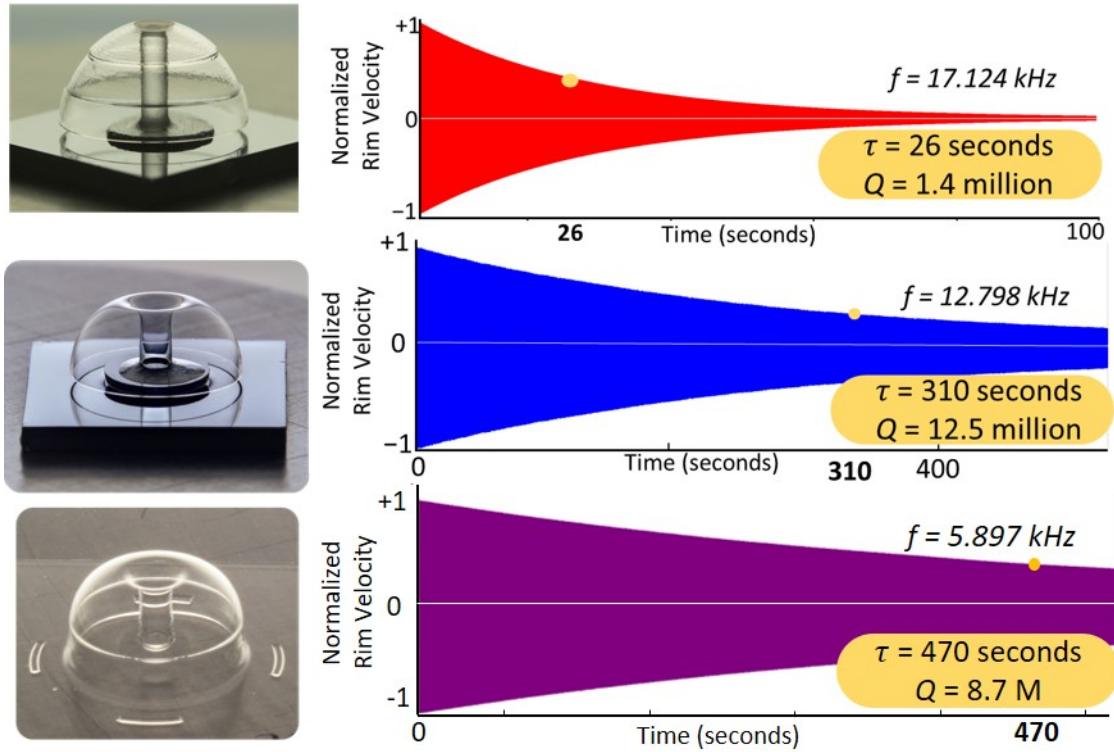


Figure 3.3: Measured ring-down time of three different PSI resonators.

fabrication steps and mitigating them. Although, high Q was measured from different types of PSI resonators however moving forward low frequency (5 kHz) H-TN and H-NN type PSI devices were pursued eventually to make a gyroscope. This is because of the requirement of long τ , better electrostatic tuning capability and large drive amplitude to lower noise which is given by Equation 1.9. Each of these require low frequency $n=2$ mode. Moreover, H-XX PSI resonators are inherently more symmetric

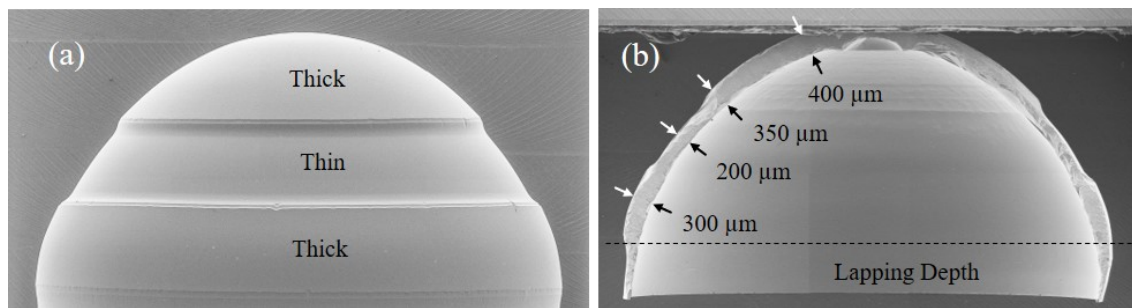


Figure 3.4: SEM image of S-TT PSI resonator showing (a) thick region at the shoulder and rim region. (b) sidewall profile showing thickness variation.

than S-XX type resonators because of monolithic fabrication of anchor. Finally, for gun-launched guided munition, shock survivability of 20,000g is easily met by PSI resonators with hollow stems. More results on shock testing will be discussed later in this chapter. Figure 3.5 shows variation of Q with frequency mismatch.

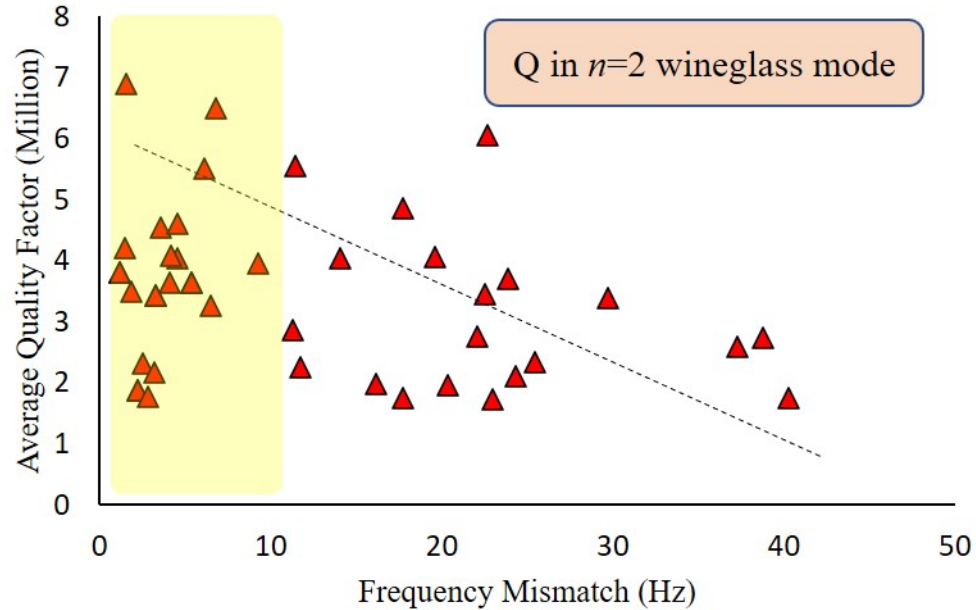


Figure 3.5: Variation of measured Q for several types of PSI resonators. It is seen that as Δf increases, devices's Q decreases.

Two comments can be made based on the results shown in this plot. First, fabrication of high Q and low Δf resonator using methods developed in this thesis is repeatable. Second, in general low Δf devices yield higher Q than those with large Δf . This observation complements the fact that a symmetric and balanced resonator dissipates less energy as compared to an asymmetric resonator. There are however exceptions which is clear from Figure 3.5 as there are cases when low Δf devices have exhibited lower Q than those with relatively higher Δf . This is partially because Δf alone does not determine the symmetry of a resonator. This is also evident from the numerical results in Figure 2.25 where extra mass at regions

near the rim affects Δf more than when it is away from the rim although in both cases, the resonator is asymmetric and imbalanced. The second reason for such behavior is because the resonators in Figure 3.5 were of different designs and were fabricated using different molds in different batches. Although, all of these were processed using the optimized processing conditions of lapping, polishing, cleaning, annealing etc. it is however possible that other factors besides asymmetry like surface cleanliness, adsorbed moisture etc. is dominating Q of some resonators.

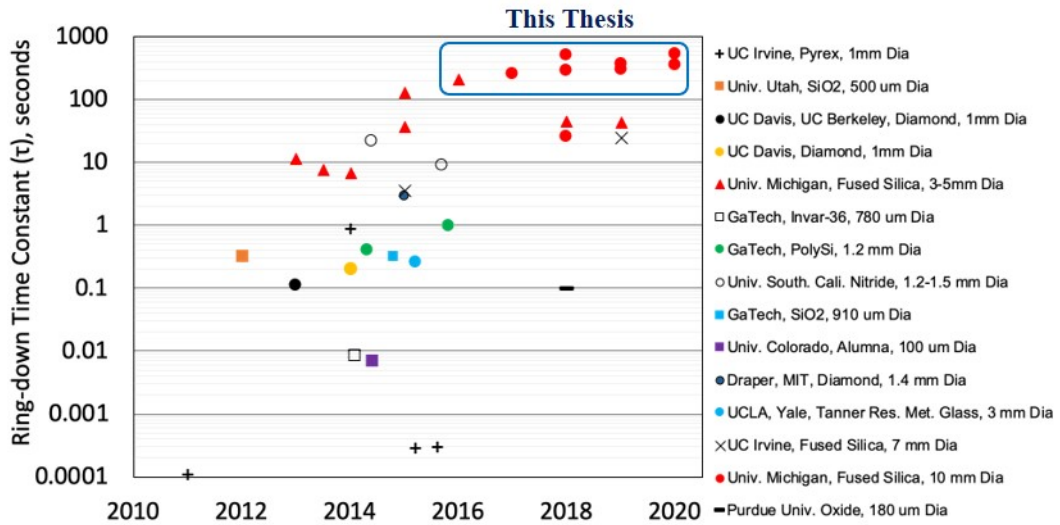


Figure 3.6: Reported ring-down times for 3D shells fabricated using different techniques with different materials and sizes through projects funded by DARPA’s Microscale Rate Integrating Gyroscope (MRIG) program [44]-[56], [13], [63]-[68], [84], [86], [91], [96], [112]-[116].

Figure 3.6 compares τ of resonators fabricated at The University of Michigan with other 3D shell resonators fabricated using different materials and techniques as reported in literature. Figure 3.7 also shows improvements in τ for resonators fabricated at Michigan. These resonators are either uncoated or coated with a thin metal layer to make it conductive. For navigation grade gyroscope, long τ (> 100 second), large driving amplitude ($q > 1 \mu\text{m}$) and large scale-factor ($> 100 \text{ mV/dps}$) are also important alongside high Q [28], [70]. All these parameters depend on operating frequency, f . First, τ and f have inverse relation for constant Q ($Q = \pi \cdot \tau \cdot f$). As a

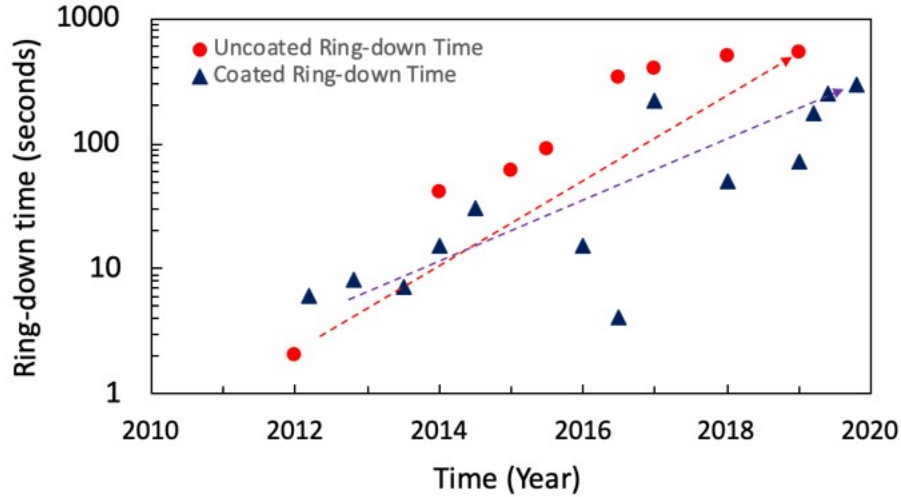


Figure 3.7: Measured ring-down time for Michigan’s fused-silica shell resonators vs. time. The shells are either 5mm or 10mm in diameter operating at 5-10kHz, and are either bare, or coated with a thin metal layer [86], [87]-[89], [109]-[115].

result, high frequency operation would reduce τ . Second, a high frequency device, because of large stiffness would lead to lower drive amplitude, q , at a fixed voltage. Third, scale-factor is proportional to both q and τ for fixed voltage and gap. Finally, $BI \propto f/\tau$. It is therefore clear that although increasing f improves ARW, it is detrimental to the overall sensor performance. Therefore, frequency of operation should be placed between 5–20 kHz—much higher than environmental frequency floor and low enough to ensure large deformation and long τ . As a result, the parameter $Q \cdot \tau$ product is more important than $Q \cdot f$ product for high performance vibratory gyroscopes. For shell resonators in this thesis, $Q \cdot \tau$ product of over 4×10^9 is achieved. Figure 3.8 summarizes $Q \cdot \tau$ product of shell resonators fabricated at the University of Michigan and other places over the past few years [18], [28]-[29], [48], [66], [116].

While obtaining high Q is important, reducing Δf is equally important for application as gyroscopes as can be seen in Figure 1.21. However due to fabrication challenges, often the resonators experiences a finite Δf (>10 Hz) which should be

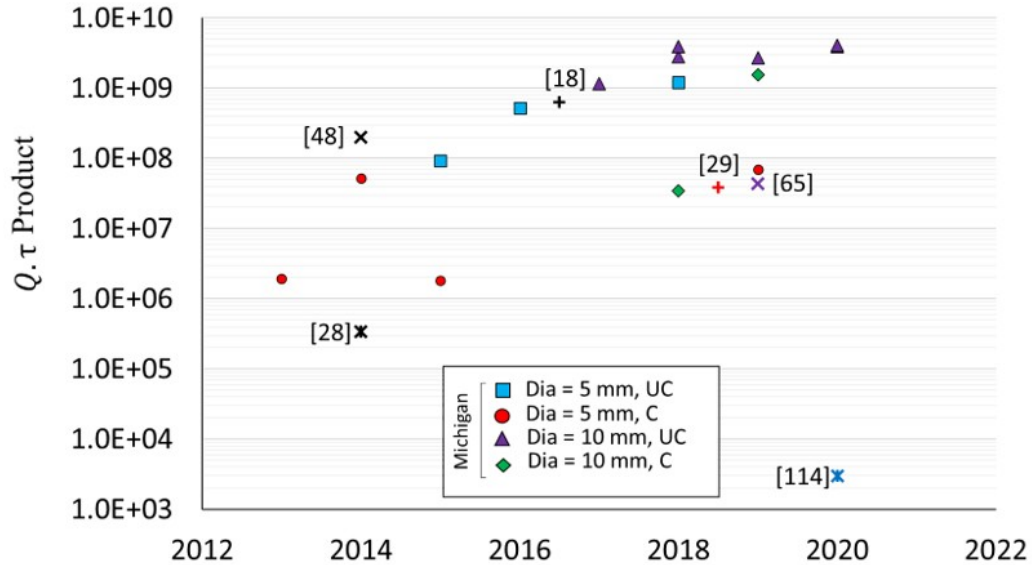


Figure 3.8: $Q \cdot \tau$ product for different micro-resonators reported in literature along with the ones developed at The University of Michigan. C: Coated with metal, UC: Uncoated.

reduced. To mode match, the frequencies can be tuned either by physical trimming or adding mass to tune mass/stiffness or they can be electrostatically tuned by applying voltage causing it to soften. Both these techniques have their own limitations. While physical trimming can match large frequency mismatch but can reliably be done only on large devices like the HRGs. On the other hand, electrostatic tuning cannot match a large frequency split. As a result, at micro scale, the best method is to fabricate an intrinsically low frequency mismatch resonator and tune it electrostatically. There are two main sources of Δf , (i) due to thickness variation along the rim and (ii) due to acircularity of the resonator as shown in Figure 3.9(a). Two main causes of thickness variation are identified, one of them is due to angled lapping. During lapping, the 4" holder experiences TTV nearing hundred microns which causes a concave down profile. Regions near the edge of wafer are thinner than the center of the wafer. Such thickness variation means that lapping would remove material from embedded shells at an angle which can be a potential source of thickness

variation and consequently Δf . Second source of thickness variation could be due to non-uniform temperature distribution around the rim during blowtorch molding. Frequency mismatch can also be caused due to acircularity which could come from acircular mold or acircularity due to blowtorch molding.

It is important to find and mitigate the dominant source of Δf to fabricate resonators with small Δf (<10 Hz) so they can be electrostatically tuned with reasonable voltage. To study the effect of thickness variation on frequency mismatch, 7 shells were blowtorched using a mold. Four shells were blowtorched using the usual setup while 3 of them were blowtorched using a programmable stage which was programmed to move in circles during blowtorching as shown in Figure 3.9(b). This was done to ensure a more uniform temperature uniformity along the rim. The shells were released using lapping/polishing method and the thickness of the rim was measured at four diametrically opposite locations. Figure 3.9(c) shows the thickness deviation and frequency mismatch for each device. It is seen that all the 7 shells have about the same frequency mismatch irrespective of the way they were fabricated. Dithering the mold during blowtorch reduced thickness variation along the rim as compared to other non-dithered shells, however, did not improve Δf . It can therefore be concluded that thickness variation due to temperature non-uniformity is not dominating the mismatch in frequency.

To study the effect of other parameters, several resonators were fabricated using three different molds. These were then singulated using lapping/polishing method in five different batches. Figure 3.10 shows the measured frequency mismatch for resonators fabricated using different molds and processed in different batches. From Figure 3.10, it can be concluded that resonators fabricated using the same mold exhibit similar Δf irrespective of processing batch. For example, resonators made

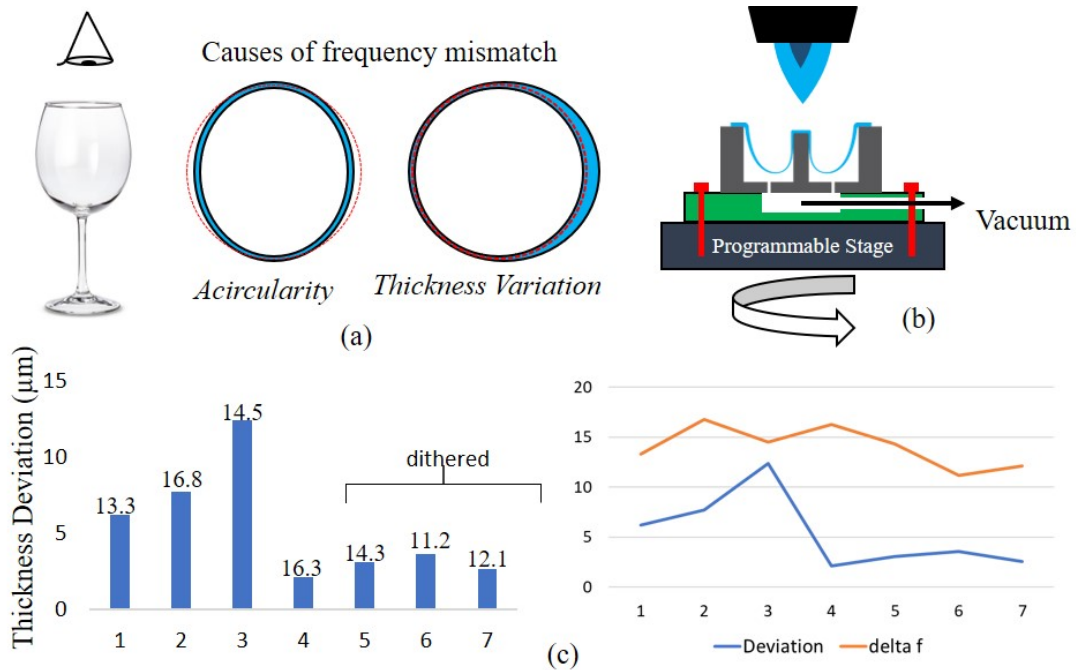


Figure 3.9: (a) Two main causes of Δf includes thickness variation and acircularity. Thickness variation can be reduced by improving temperature distribution around the rim by using (b) a dithering stage which can dither the resonator during torching to improve temperature uniformity. (c) Dithering improved thickness variation however did not affect Δf (shown against each device).

from Mold 1 were singulated in four different batches but all of them exhibited tight Δf . Mold 3 on the other hand did exhibit some variation but they were all between 10–25 Hz. It can therefore be argued that error due to angled lapping is not dominating the frequency mismatch. This claim is further cemented by the fact that resonator placed at the center of the lapping holder exhibited similar frequency mismatch than the rest of the shells although the thickness variation across the central shell is much smaller than those placed at the edges. It is therefore concluded that the acircularity of the resonator due to imperfections in mold is dominating the frequency mismatch. Although other sources discussed above also plays a part in inducing asymmetry.

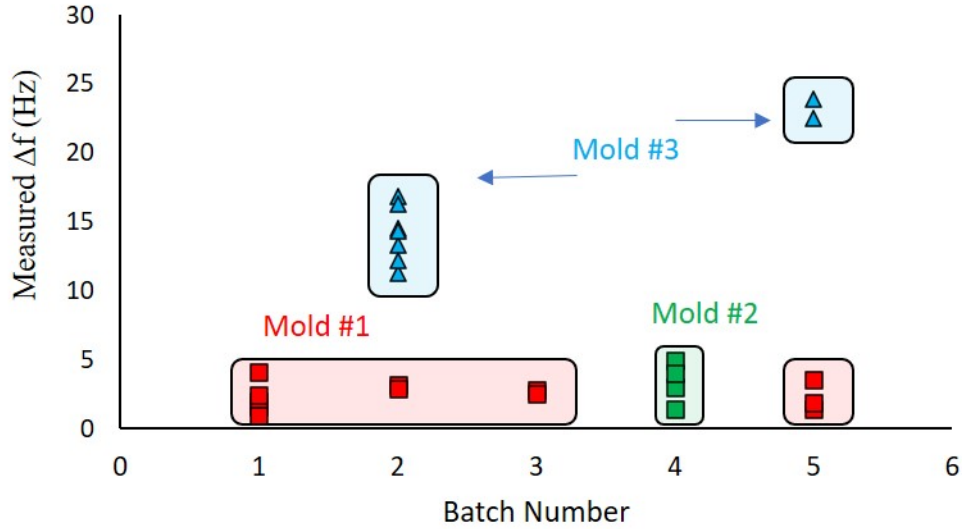


Figure 3.10: Measured Δf from resonators fabricated from three different molds and processed in five different batches. Resonators fabricated from same molds exhibited similar Δf range irrespective of the processing batch.

3.3.2 Singulation using HFA Method

The other method of singulation employs wet-chemical etching using 49% Hydrofluoric acid to selectively etch off the flat part from a molded structure to singulate 3D shells. In this section, measurement results of resonators released using HFA is discussed and compared with lap/CMP method. Figure 3.11 shows shells singulated using the two approaches. Lap/Polish method yields a resonator with sharp and well-defined rim whereas the HFA method yields shells with rugged edges as can be seen in the SEM image. The rugged rim has shown not to impact Q by any dissipation mechanism and Q more than 8 million has been measured from several resonators released using this approach. Figure 3.12 shows the measured ring-down time plot of a shell resonator exhibiting >500 s ring-down time.

To compare HFA and lap/polish method, nine other resonators are released using HFA method and is compared with twenty-two shells released using lap/polish method. Figure 3.13(a) shows a comparison of τ obtained from both the approaches.

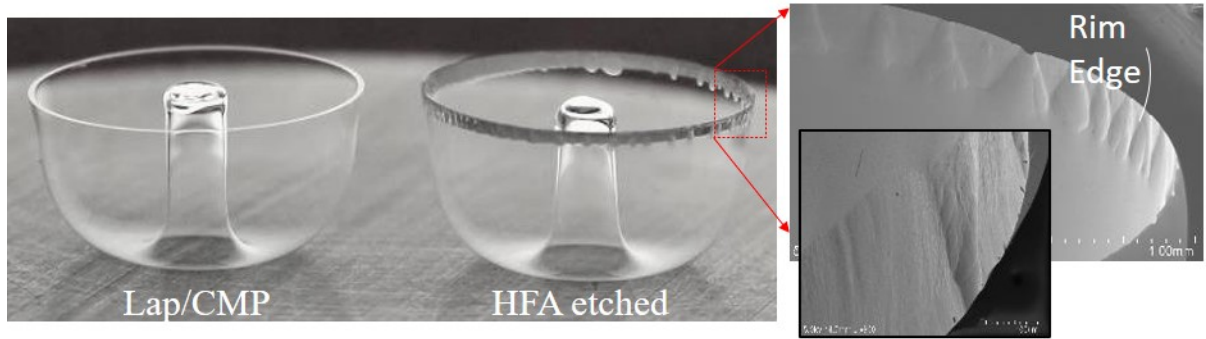


Figure 3.11: Photograph of PSI resonators singulated using lap/polish method and HFA method. SEM image shows the rough region at the rim caused due to HFA penetration through microvoids at the wax-FS junction.

It is clear that the performance of resonators is high irrespective of the method of singulation.

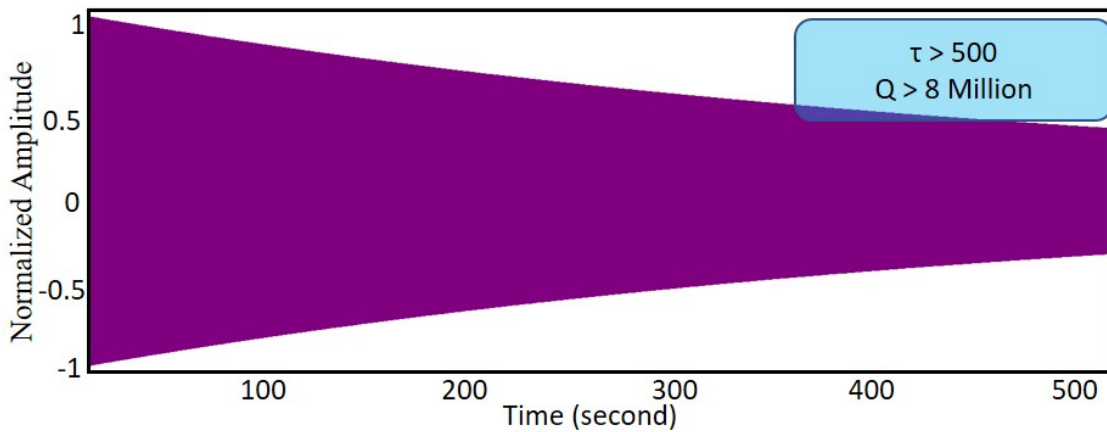


Figure 3.12: Measured ring-down time plot for a H-NN type PSI resonator exhibiting more than 500 seconds ring-down time constant. This resonator is released using HFA method of singulation.

Apart from high-Q, frequency mismatch also determines the effectiveness of a singulation method. While lap/polish method induces angled lapping, HFA method is affected by non-uniform etch rate across the holder. To study the effect of etch rate non-uniformity on Δf , another 8 devices were blowtorched using the same mold. Four were singulated with lap/polish method and 4 were singulated using HFA. Figure 3.13(b) presents the Δf for all 8 shells. The Δf from both techniques is

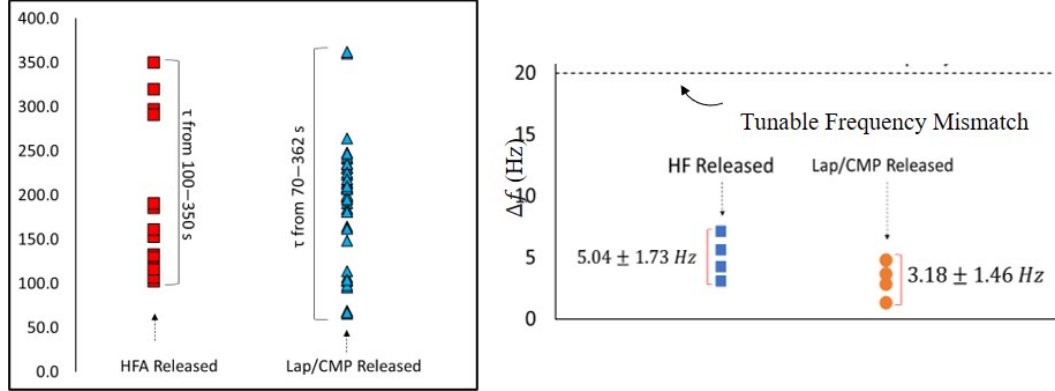


Figure 3.13: (a) Measured ring-down time of nine HF-released devices and comparison with 22 shells released using lap/polish method. (b) To compare Δf , eight shells are blowtorched using the same mold under identical conditions. Four of them are singulated using HFA method and the other four are singulated using lap/polish method. Δf from both the method is comparable indicating that HFA method is not detrimental to Δf .

comparable. Although the average for HFA-released shells (5 Hz) is more than that from lap/CMP-released shells (3.2 Hz), they are well below ≈ 20 Hz which is believed to be tunable using trimming. The HFA release method yields both high-Q and low Δf devices. Additionally, this method is low cost and can enable very high production. This method uses Crystalbond wax and HFA as consumables as compared to sophisticated tools and machinery in other releasing methods as outlined in Table 3.1. Moreover, this technique neither require any alignment nor any careful parameter optimization. Finally, there is no limit on batch-size as several of the resonators can be put in an HF bath. For every batch of 100 resonators, cost of fabrication of each resonator is only 4% of the cost from conventional lap/CMP process. Similarly, time taken to fabricate one device is 43% of the original time. These advantages of being low-cost, fast and high-throughput along with excellently high-Q and low Δf makes this a promising technique to fabricate low cost, high performance micro-gyroscopes.

Table 3.1: Device Performance and Process Parameters of Lap/CMP, Laser and Chemical Singulation Techniques.

	Lap/CMP	Laser Cutting	HFA Release
Q_{Max} (freq. in kHz)	7.9 M (5.1)	153.3k (~7)	5.8 M (5.3)
Lowest Achieved Δf	1.2 Hz	5.1 Hz	3.12 Hz
Alignment	Not Required	Required	Not Required
Throughput	9/ batch	Serial	Many/batch
Machinery/Tool	Lap/CMP	Laser Cutting	-
Consumables	Polishing Slurry	-	HF Acid

3.4 Test Results of $n=3$ Modes

Resonators discussed so far have been operating in the $n=2$ wine-glass mode. However, higher mode operation like the $n=3$ mode can also be used for gyroscope application. Like $n=2$, $n=3$ also has two degenerate modes, however, the anti-nodes are separated at an angle of 30° as compared to 45° separation in the case of $n=2$ mode. This mode of operation has three anti-nodes in each mode. Figure 3.2 shows the mode shapes for a shell resonator in $n=3$ wineglass mode.

Frequency of $n=3$ mode is nearly 2.8 times than that of $n=2$ mode which is advantageous from noise perspective if other parameters either improves or remains same. To compare noise for gyroscope operating in the two modes, a parameter k which considers the geometric parameters of the resonator is defined as $k = A_g \cdot \sqrt{(M_{eff}\omega)}(\sqrt{mg.rad/s})$. A higher value of k will lead to a lower ARW and is therefore desirable. H-NT type PSI resonators (with a rim thickness of $\sim 300 \mu\text{m}$) have simulated value of $k=330.13 \sqrt{mg.rad/s}$ in the $n=2$ wine-glass mode and $k=407.22 \sqrt{mg.rad/s}$ in the $n=3$ wine-glass mode. Table 3.2 tabulates the geometric parameters for the two modes. For a PSI gyroscope with identical drive amplitude and Q of the two modes, operation in the $n=3$ mode would give lower noise as compared to $n=2$ operation.

PSI resonators in their $n=3$ mode is also tolerant towards imperfections. Figure

Table 3.2: Comparison of device parameters affecting noise in the $n=2$ and $n=3$ wineglass modes.

Property	Values	
	$n=2$ Mode	$n=3$ Mode
Frequency (kHz)	11.479	31.949
Angular Gain	0.3039	0.2588
Effective mass (mg)	16.37	12.34
k	330.13	407.22

3.14 shows the frequency mismatch for both $n=2$ and $n=3$ mode for the case discussed in Section 2.11 with mass imbalance at different locations. It is seen that frequency mismatch is $<50\%$ than those of $n=2$ mode. In $n=3$ mode when added mass is at the rim, it is seen that Δf first increases and then continues to decrease as h increase from 0.7 mm to 0.9 mm and then increase again when $h=1$ mm. This is because adding mass at different locations changes the two frequencies by different amount depending on the position of nodal and anti-nodal points which contribute differently towards vibrational velocity of the resonator. Numerical results in Figure 3.14 is specifically for the case discussed in Section 2.11 and other type of imperfections could affect Δf of $n=2$ and $n=3$ modes differently. Measured Δf of $n=2$ and $n=3$ mode of five devices fabricated in a batch is also plotted. It is to be noted that measured devices have not been investigated for any asymmetry and therefore have no correlation with h . Except one device, all of them have low Δf in $n=3$ mode.

These devices have exhibited not only low Δf but also excellent Q in $n=3$ mode. TED and anchor loss simulations have shown their respective Q s to be on the order of tens and hundreds of million. Figure 3.15 shows the comparison of Q in the $n=2$ and $n=3$ mode. Except one, all shells exhibited $Q < 1$ million in $n=2$ mode but Q for the $n=3$ mode was greater than 7 million. One shell, ID 1 exhibited $Q = 10.03$ and 3 Million in the two $n=2$ modes however Q in the two $n=3$ mode was 10.02 and 9.98 Million.

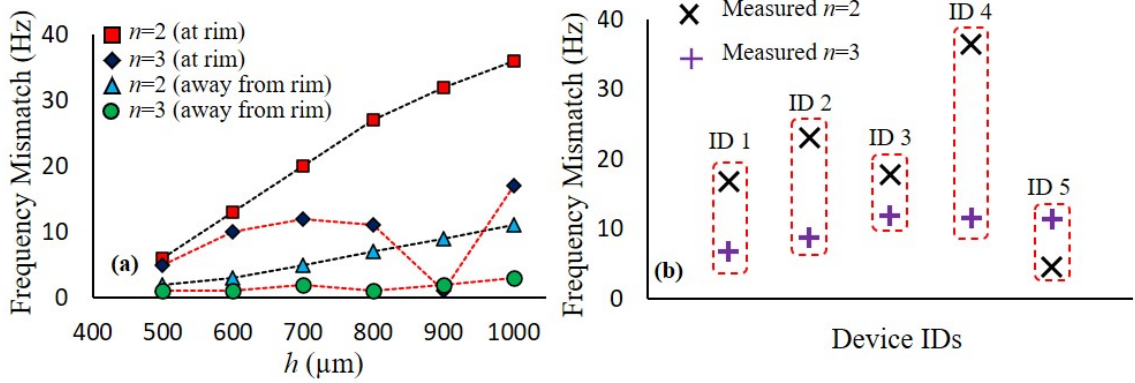


Figure 3.14: (a) Variation of numerically calculated Δf in $n=2$ and $n=3$ wineglass modes for cases where imperfection is near the rim and away from the rim as shown in Figure 2.25. (b) Experimental data for five devices.

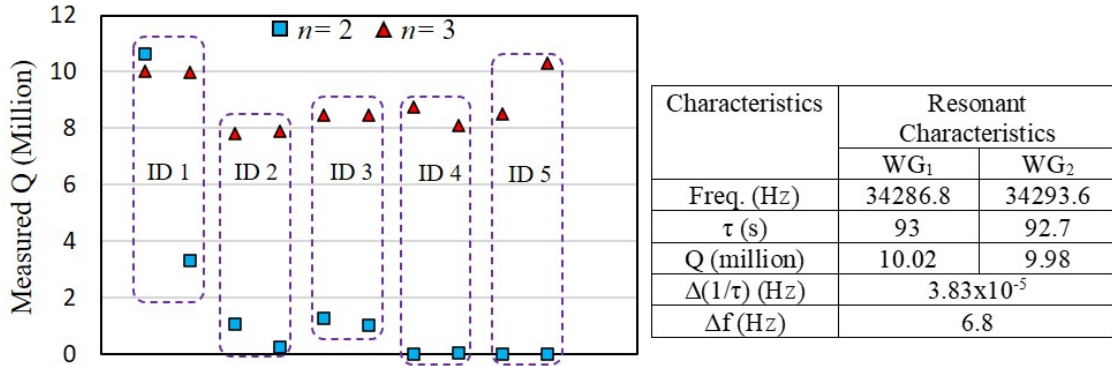


Figure 3.15: Comparison of measured Q in $n=2$ and $n=3$ wineglass modes for five devices. Although high- Q have been measured in $n=2$ mode for other devices, this plot shows that $n=3$ mode exhibits high- Q irrespective of what $n=2$ mode Q is. Measured resonant characteristics are tabulated.

Large Q -mismatch in $n=2$ mode for ID 1 can be attributed to imperfection in the device. This however does not seem to affect $n=3$ mode. High- Q have been measured in $n=2$ mode in other devices like in [86] where $Q \approx 10$ Million have been obtained, however low Q for devices shown in Figure 3.15 may be due to subtle imperfection in the device. It has been investigated that asymmetries can have detrimental effect on Q_{anchor} and is likely dominating Q for devices in Figure 3.15. Material or surface defect if any should equally affect all the modes. Besides, TED simulations for shells with imperfections in the form of chips on rim have shown to have very little effect on

Q_{TED} [72]. Though viscous damping reduces with increasing mode number, but these shells are tested in extremely low vacuum ($<10 \mu\text{Torr}$), therefore viscous damping is not dominating Q . The loss mechanism which is prone to asymmetries is anchor loss. Therefore, anchor loss is likely dominating Q , however more investigation needs to be done to better understand damping mechanisms in $n=3$ mode. Figure 3.15 also tabulates measured resonant characteristics in $n=3$ wineglass mode and indicates their potential for high performance gyro due to their high k , high Q shown in Figure 3.15 and low Δf shown in Figure 3.14. Even higher modes like $n=4$ and $n=5$ have exhibited Q in excess of 4 million and can also be explored for potential gyro or other application. With Q as high as 10 million at $\sim 2.8x$ higher frequency than $n=2$ mode and $\Delta(1/\tau)$ of the order of tens of μHz , PSI resonators can be used in the $n=3$ mode (or higher mode) for obtaining low noise from a gyroscope, potentially better than $n=2$ gyro.

3.5 Test Results for Open Shell Resonators

Application of open shell PSI resonators as a shadow mask has been shown in Chapter II. Another application of open windows on shell is to increase the mechanical quality factor. To obtain high Q , it is necessary to reduce damping due to different sources. It has been shown that making a resonator symmetric increases Q_{anchor} . At the same time decoupling the anchor from rest of the shell also improves Q_{anchor} . This can be done by either reducing the dimension of the anchoring point or by creating a discontinuous path between the region which resonates and the anchor. For the former case, [79],[81] studied the effect of reducing the anchor size on the Q and confirmed the dependence of anchor loss on anchor size. Reference [45] numerically demonstrated an improvement in Q when slots were created

Table 3.3: Measured resonant characteristics of devices before and after opening windows.

ID	Before Opening Windows			After Opening Windows		
	Freq. (Hz)	τ (s)	Q (Million)	Freq. (Hz)	τ (s)	Q (Million)
L1	9138.7	0.2	0.0057	7510.9	20	0.472
(n=2)	9151.3	0.5	0.0143	7524.1	45	1.063
M2	8038.8	1.3	0.033	7357.5	18	0.416
(n=2)	8071.3	4	0.101	7435.3	38	0.887
L1	24556.6	8.9	0.686	20241.2	27	1.716
(n=3)	24582.1	1.7	0.131	20268.1	27	1.718
M2	21746.4	1.2	0.079	20004.1	8.7	0.546
(n=3)	21905.7	1.0	0.069	20055.7	4	0.252

near the anchor. Authors attributed the increase in Q to isolation of anchor from the vibrational stress. Similarly, the work reported in [48] created holes on the top of a dome-type resonator and observed an improvement in Q . This improvement is attributed to reduced thermoelastic damping due to limited flow of heat across the surface during deformation. At the same time, these holes create discontinuity in the path between regions of high vibration energy and the anchor thus reducing losses through the anchor. Both [45],[48] used FIB or laser ablation for creating such discontinuity. This approach limits the size and area of the region, thus limiting the extent to which anchor loss could be modified. In addition, this approach is slow, expensive, and is a serial process. The approach to fabricate open shells employing combination of patterning the initial substrate before reflowing the FS followed by wet etching of thin regions after reflowing, allows for the formation of large open sections in regions of interest. This is a low cost and batch process and allows one to define both small and large discontinuities (open windows and thin sections) in 3D shell resonators.

To study the effect of open windows on Q , two devices with thin windows are tested for their resonant characteristics using LDV. Frequency and ring-down time

is measured in both $n=2$ and $n=3$ wineglass modes. Those shells are then etched in HFA to through etch thin windows to create holes using the process outlined in Section 2.13. The shells are cleaned and resonant characteristics are measured. Table 3.3 tabulates the resonant characteristics including the frequencies and Q for both the shells. Figure 3.16 graphically shows the improvement in Q for each resonator in both $n=2$ and $n=3$ modes. In $n=2$ mode, one device L1 exhibited an improvement as large as 82 times with $Q_{max}=1$ M. Another device M2 showed an improvement of 13 times with Q_{max} of 0.9 M. Both the device also showed an improvement in $n=3$ modes reaching Q_{max} of 1.7 M (14x) and 0.6 M (7x) for L1 and M2 respectively. For both the devices improvement in $Q_{n=3}$ was less than that of $Q_{n=2}$. This can be attributed to inherently lower anchor loss in $n=3$ mode due to the symmetricity of the modeshape. As already discussed, anchor loss is magnified by asymmetry of the anchor and the shell. Both L1 and M2 have some mass imbalance due to etching imperfections and the intrinsic Q is therefore much lower. The same reason can be attributed to the Q mismatch, $\Delta Q = Q_1 - Q_2$ of the two shells. This can be improved by doing a more careful alignment of the patterned substrate over the mold and by minimizing etch non-uniformity making the device more symmetric and balanced. It is believed that the final Q from these open shells can be more than 10 million. The results from two different resonators clearly demonstrates that creating discontinuity leads to an abruption in the path of vibrational energy reaching the anchor and improve Q . For the shell with largest improvement, Q increased from 15,000 to more than 1 million.

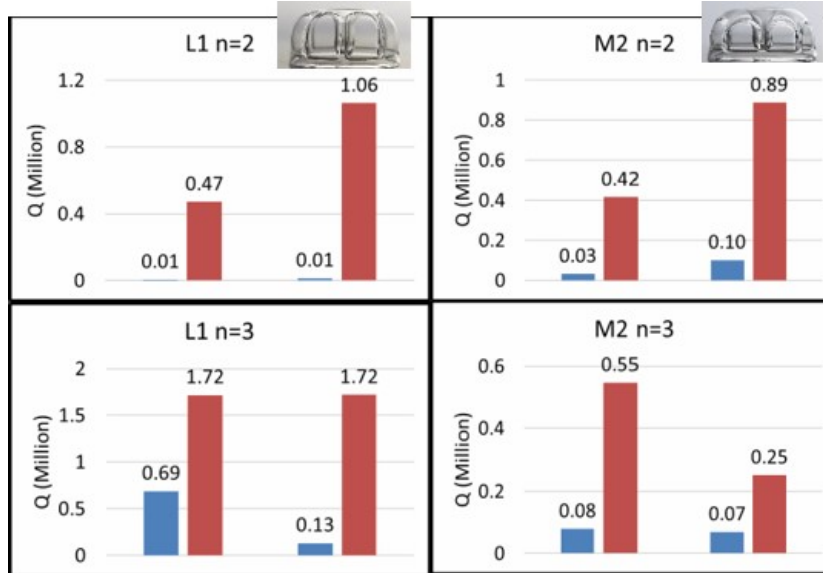


Figure 3.16: Performance improvement in $n=2$ and $n=3$ modes for shells with different sized windows before and after etching off the windows. Bars in blue corresponds to performance before windows are etched and red bars represent Q after etching off the windows.

3.6 Repeatability and Uniformity

For PSI technology to be commercially realized, performance alone is not important but performance repeatability is equally important. Fabrication of PSI device using blowtorch molding technique and other singulation and fabrication technologies developed at University of Michigan has the capability of producing reproducible results. This is evident from results presented until now where repeatable performance have been achieved. In this section, discussion on repeatability and uniformity in performance from devices fabricated in a batch and batch-to-batch is carried out. Frequency and Q from more than 300 devices fabricated in this thesis and previous work from our group is analyzed. These devices include both 10 mm diameter PSI as well as 5 mm diameter Birdbath Resonator Gyroscope (BRG) resonator. To analyze frequency, the measured $n=2$ wineglass frequencies for >200 devices fabricated in different batches is chosen. Each frequency of the two modes is then normalized by the mean frequency of that batch. Figure 3.17 shows the normalized frequency for

all these devices in the two modes. It is seen that barring a few devices, most of the resonators have their frequencies within $\pm 10\%$ of the mean of their batch.

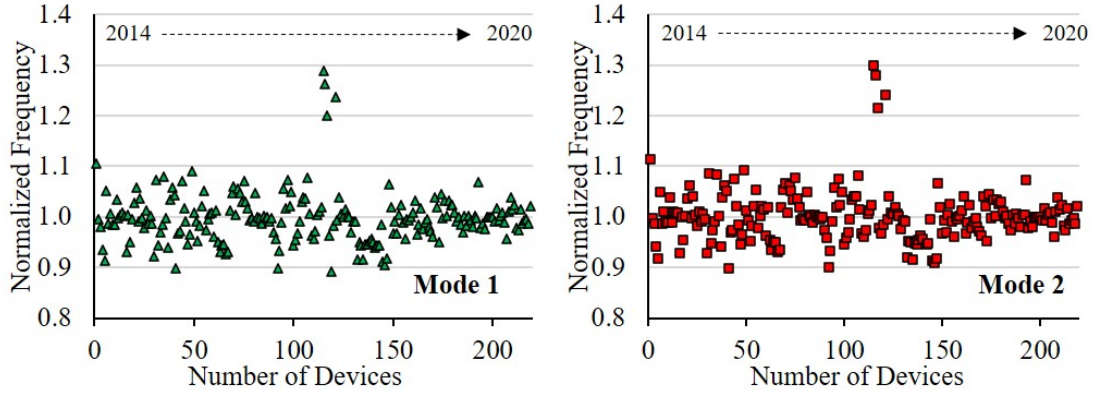


Figure 3.17: Variation of $n=2$ wineglass frequency in the two modes for several shell resonators fabricated at The University of Michigan. Devices are fabricated in several batches over several years and are normalized to the average frequency of the batch. Variation of frequency is within $\pm 10\%$. Some data is from [83].

To analyze batch-to-batch repeatability of Q , Q in each mode is normalized by the maximum Q of that batch and $\frac{Q}{Q_{Max}}$ is obtained. This parameter indicates the value of Q relative to the highest Q from that batch. To study such variation, >150 resonators each with $Q > 1$ Million is chosen. Figure 3.18 shows the variation of $\frac{Q}{Q_{Max}}$ for more than 150 resonators. It is seen that with improvement in molding and processing like improvement in singulation methods, cleaning techniques, annealing etc. tighter spread is obtained meaning the variation of Q is less scattered. At the same time, Q from devices came close to the maximum Q from the batch. Both these means that a typical batch of resonator fabricated with the optimized methods discussed in this thesis would yield devices where most of them will have Q s similar to each other and close to the maximum Q of the batch.

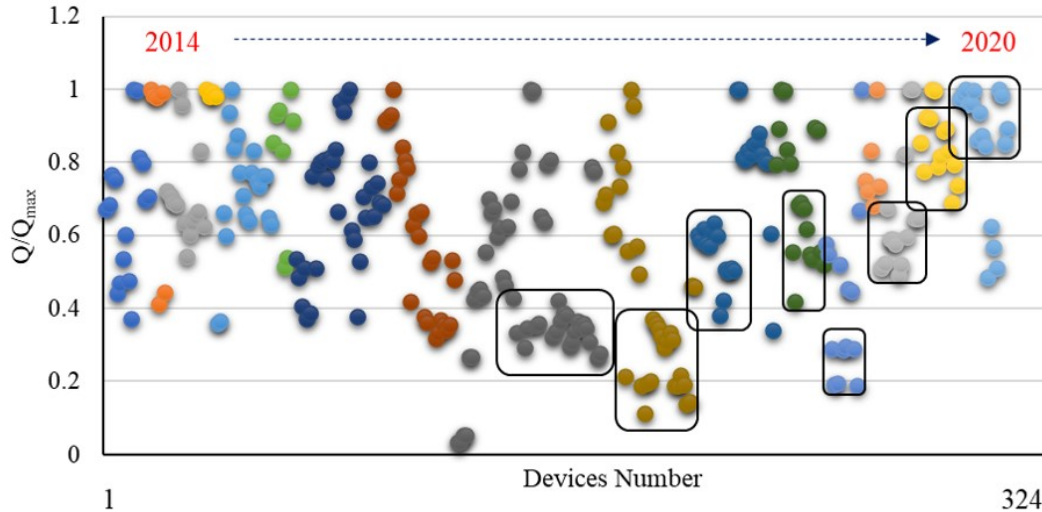


Figure 3.18: Variation of Q from different batches. Each Q is normalized by Q_{max} from that batch. The data presented shows relative values of Q with respect to the highest Q from that batch. It is seen that in initial years, spread of Q was more scattered. However, with improvement in fabrication process, the spread became more tight and closer to the maximum value. This means more devices exhibited Q close to Q_{max} from the batch. For this graph, 150+ devices each with $Q > 1$ Million was chosen.

3.7 Fused Silica Annealing and Material Characterization

Adsorption of water molecules is a source of energy damping in FS resonators. Water molecules can be desorbed by annealing at high temperature. Several groups have studied the effect of annealing on either fiber [117, 118], rod [119, 120], or bulk [121]-[123] FS and have observed improvement in Q . In the fabrication of MEMS sensors and actuators, annealing is not usually the final step and other subsequent processes involving dry and wet chemical exposure are inevitable. Therefore, it becomes necessary to characterize the behavior of FS under these conditions to understand damping characteristics for resonant sensors. In this section, different processing conditions like exposure to atmosphere, Acetone, IPA, Plasma, Piranha Solution ($H_2SO_4 + H_2O_2$), DI Water, are studied and a systematic measurement is done to investigate the effect of each of these on the Q factor of FS shell resonators.

The bulk of FS has four Si atoms bridged with O-atoms. However, the surface of

FS can have several other silanol configurations depending on the number of bridging O atoms, like isolated Geminal, Vicinal or H-bonded [124]. Isolated silanols are not inclined towards adsorbing water whereas other silanols have affinity to adsorb water [125]. Several groups have extensively studied the mechanism and nature of water/substrate interface on FS using sophisticated metrology tools [124]-[133]. Asay and Kim [126] studied the configuration of water molecules on the oxide surface in a humid environment using attenuated total reflection infrared spectroscopy. They studied the molecular configuration of hydrogen-bonding on the Si-OH group on oxide surfaces and concluded that between relative humidity (RH) of 0-60% (typical humidity range), up to 4 layers of hydrogen bonded ice-like structure of water (or liquid water structure in RH range of 30-60%) is grown. Iler [127], Greg and Sing [128] reported that at low temperature (~ 150 °C) in atmosphere, the H-bonded water molecules can be removed. Okkerse [129] further claimed that such low temperature removal of adsorbed water is possible only if the FS structure is free of micropores. Similar studies have also been done by several other groups all claiming that temperature < 200 °C is enough for desorption of water molecules. However, other groups like Fripiat and Uytterhoeven [130] have presented results which suggest that complete desorption does not happen below 300 °C. Furthermore, Kiselev et al. [131] and Chuiko et al. [132] have suggested a temperature range of ~ 400 °C and ~ 650 °C, respectively, for complete desorption of water molecules. Zhuralev's [133] review article is an excellent source with all the compiled results. There have also been several studies pertaining to dehydroxylation of molecules. Dalstein et al. [124] used vibrational sum frequency spectroscopy to measure isolated surface silanol as a function of pH of water on 10-mm fused silica hemispheres. They also investigated the effect when the hemispheres were pre-treated at 1000 °C for 4 hours and Plasma

Table 3.4: Measured resonant characteristics of devices before and after 450 °C annealing.

	Device 1				Device 2			
	<i>Mode 1</i>		<i>Mode 2</i>		<i>Mode 1</i>		<i>Mode 2</i>	
	Q1 (Million)	f1 (Hz)	Q2 (Million)	f2 (Hz)	Q1 (Million)	f1 (Hz)	Q2 (Million)	f2 (Hz)
Before 450 Anneal	4.44	4773.4	4.46	4781.0	4.74	5242.6	4.75	5250.6
After 450 Anneal	6.49	4773.9	6.43	4781.5	6.64	5242.7	6.53	5250.7
Factor Change (After/Before)	1.46	0.99	1.44	1.00	1.40	1.00	1.38	1.00
Change (After-Before)	+2.05	+0.5	+1.97	+0.5	+1.9	+0.1	+1.78	+0.1

cleaned. They concluded through their measurements that thermal treatment resulted in complete dehydroxylation causing complete change of silanol to saturated Si-O-Si. They also witnessed that up to 400 °C, isolated silanol first increased and then completely dehydroxylated at higher temperatures. Similar observation about complete dehydroxylation at high temperature has also been made by Gallas et al. [125]. When the surface is dehydroxylated, it can be rehydroxylated in aqueous environments [133, 134].

3.7.1 Uncoated FS Resonators

The presence of water or other organic molecules on the surface of a resonator causes damping which reduces Q. In this thesis, this has been studied by subjecting shell resonators to annealing at 450 °C and 850 °C. While 450 °C annealing is done at 200 Torr pressure in 5% H₂-95% N₂ gas, 850 °C annealing is done in Argon gas at atmospheric pressure. An improvement in Q is seen in resonators after 450 °C annealing which is mainly due to desorption of molecules from the surface. Because of low temperature, there is no structural or material changes, which is deduced from the fact that there is no change in the resonance frequency. Figure 3.19 and Table 3.4 presents measured frequency and Q for resonators after 450 °C annealing. An improvement of 1.5–2 times is observed.

To study the effect of high temperature annealing, other devices were fabricated,

Table 3.5: Measured resonant characteristics of devices before and after 850 °C annealing.

	Device 1				Device 2			
	Mode 1		Mode 2		Mode 1		Mode 2	
	Q1 (Million)	f1 (Hz)	Q2 (Million)	f2 (Hz)	Q1 (Million)	f1 (Hz)	Q2 (Million)	f2 (Hz)
After 450 Anneal	3.58	6189.3	4.52	6208.9	4.17	6236.1	3.91	6250.2
After 850 Anneal	5.36	6211.1	7.04	6231.7	6.49	6257.5	6.30	6271.5
Factor Change (After- _{850} /After- _{450})	1.50	1.00	1.58	1.00	1.56	1.01	1.61	1.00
Change (After-Before)	+1.78	+21.8	+2.52	+22.8	+2.32	+21.4	+2.39	+21.3

annealed at 450 °C and resonant characteristics were measured. They were then subjected to 850 °C annealing for 7 hours and then tested again. A further improvement of $\sim 1.5x$ in Q was observed.

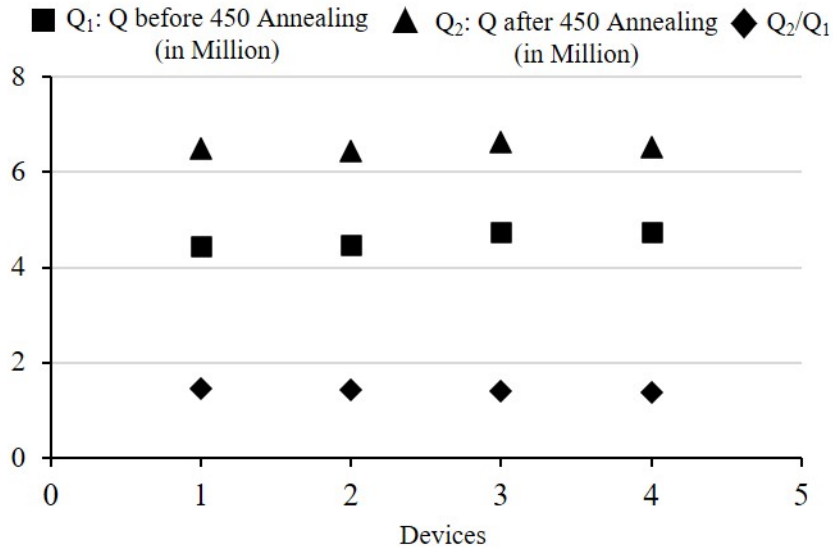


Figure 3.19: Improvement in Q for four modes of two resonators after annealing at 450 °C. More than 1.5 times improvement in Q is measured after subjecting to annealing for 8 hours in forming gas.

Table 3.5 and Figure 3.20 show the measured resonant behavior before and after 850 °C annealing. It is noted that these devices had already undergone a 450 °C anneal before 850 °C annealing. While there was no change in frequency after 450 °C annealing, an increase in frequency of 20-25 Hz occurs for devices after 850 °C anneal as seen in Table 3.5.

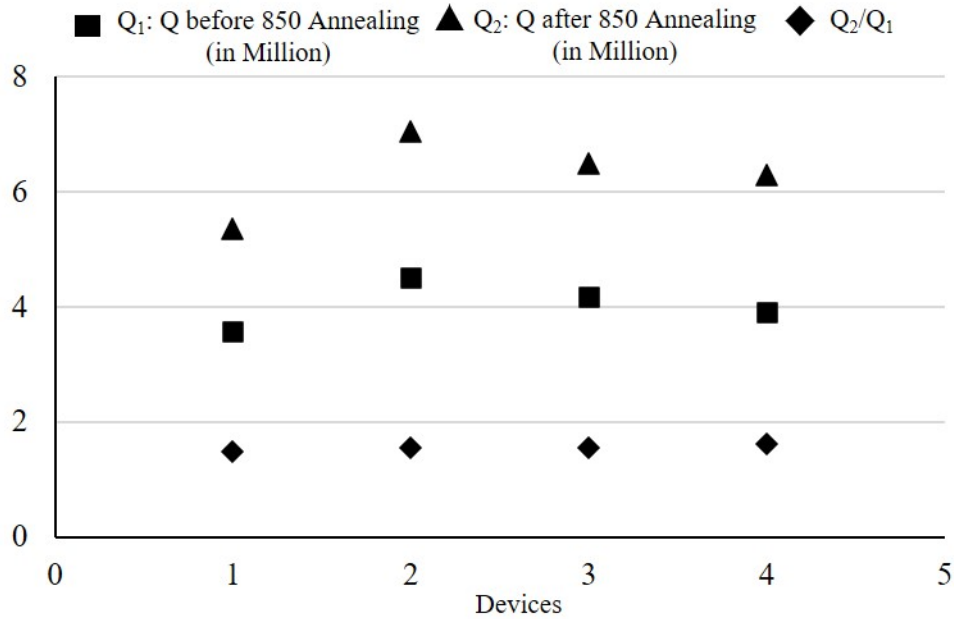


Figure 3.20: Improvement in Q for four modes of two resonators after annealing at 850 °C. More than 1.5 times improvement in Q is measured after subjecting to annealing for 8 hours in Argon gas. This improvement is in addition to 1.5x improvement after 450 °C annealing indicating high temperature annealing improves Q beyond what low temperature does.

This improvement in Q can be attributed to both material relaxation and dehydroxylation of molecules from the surface. To further characterize the resonant behavior of FS resonators, a series of experiments is performed where the resonators are put through several dry (plasma, gas) and wet chemical processes. These chemicals/gases are commonly used in micro/nano fabrication. Q factor is measured after each step as before. To eliminate any uncertainty, each measurement is done using the same substrate at $<10 \mu\text{Torr}$ vacuum. The results of this study are shown in Figure 3.21.

It can be seen that exposure to atmosphere for more than 5 hours reduced Q by around 10%. This reduction in Q can be attributed to weakly-bonded physisorbed molecules from moisture. These physisorbed molecules can be removed from the surface by exposure to vacuum at room temperature. In the second step, same resonators were placed in Acetone followed by IPA for 5 minutes each. They were

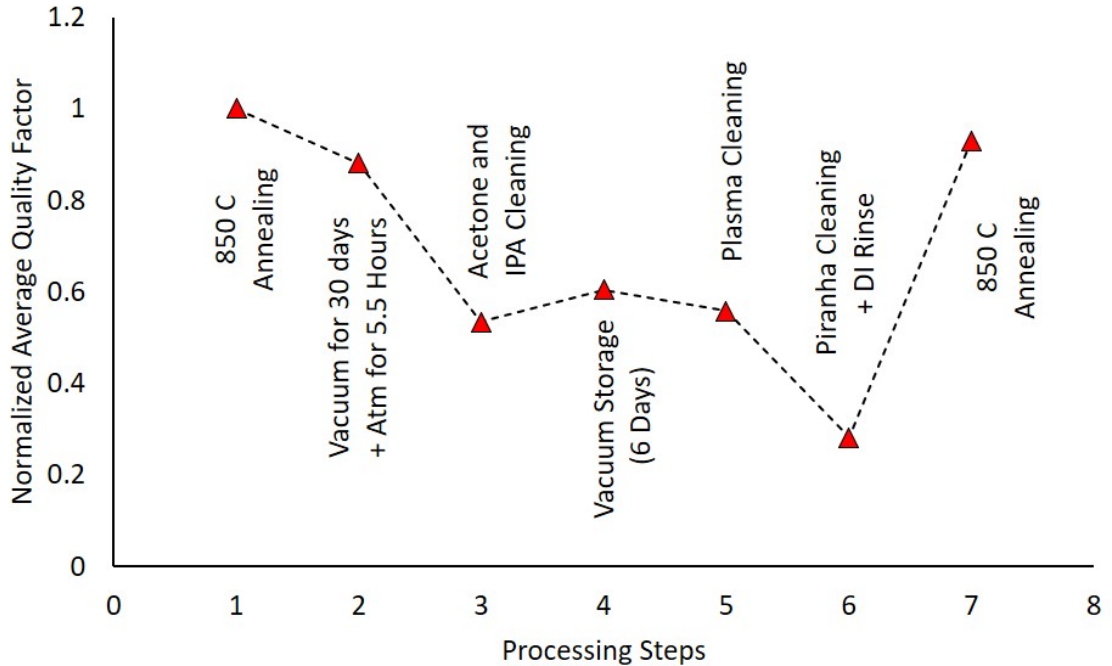


Figure 3.21: Effect of exposure to different environment on quality factor of fused silica resonator. Quality factor is the average of three devices and two modes of each device and is normalized.

then dried at 150 °C for 2 hours on a hotplate in cleanroom before testing. Exposure to solvents led to further reduction in Q resulting in the total drop of ~50%. The resonators were then kept in the test vacuum chamber with pressure $< 10\mu\text{Torr}$ for 6 days at which point the Q was measured and shown to increase by ~10%. Vacuum pumping led to some H-bonded molecules to desorb from the surface as has also been observed by Iler [127]. This observation is in agreement with assumptions made by Kiselev et al. [131] that complete removal of adsorbed molecules occurs only at temperatures $> 400\text{ }^\circ\text{C}$ at low pressure. In the next stage, the resonators were placed in O_2 -plasma for 2 minutes in a vacuum environment. This was to remove any polymer layer formation due to Acetone and IPA. However, no significant change in Q ($< 5\%$) was observed. In the next stage, the shells were cleaned in 3:1 solution of $\text{H}_2\text{SO}_4 : \text{H}_2\text{O}_2$ for 20 minutes and rinsed in DI water for 20 minute. After this the shells were dried on a hotplate at 150 °C for 2 hours and put in the testing

chamber. At this stage, Q dropped significantly by $\sim 70\%$ from its initial value. This is likely due to complete re-hydroxylation of the fused-silica surface in aqueous environment. Heating at $150\text{ }^{\circ}\text{C}$ was not enough to remove the adsorbed water. Finally, the resonators were annealed at $850\text{ }^{\circ}\text{C}$ for 8 hours and put in the test chamber for testing. Q recovered to about 80% of its initial value, validating the fact the quality factor is severely affected by attached $-\text{OH}$ molecules on the surface. It is noted that in all these experiments there was no change in resonance frequency except for the first annealing run where frequency increased by $\sim 20\text{ Hz}$ as shown in Table 3.5. Subsequent water exposure or another annealing run did not cause any change in frequency. This confirms that high temperature annealing did cause some structural or material change, although, Q improvement was mainly due to removal of silanol.

3.7.2 Pt-Coated FS Resonators

To further explore this, two resonators were coated with ALD Platinum to have a conformal thickness of 80 \AA . Q was measured after ALD and then immersed in Acetone followed by IPA each for 5 minutes. The shells were then dried at $150\text{ }^{\circ}\text{C}$ for 2 hours and their Q was measured. It was observed that the drop in Q was $< 20\%$ as compared to $\sim 50\%$ in the case of uncoated resonators when subjected to the same exact conditions. In the next two steps, the shells were first kept in N_2 environment for 2 hours and their Q was measured. Then they were kept in room atmosphere for 10 hours and their Q was measured again.

There were minimal changes in the Q between these two steps, with Q dropping slightly in atmosphere. This is likely because of the inert nature of the Platinum surface. Particularly, N_2 has almost no adsorption affinity towards Pt while O_2 and other atmospheric gases have little adsorption affinity towards Pt surface. Similar

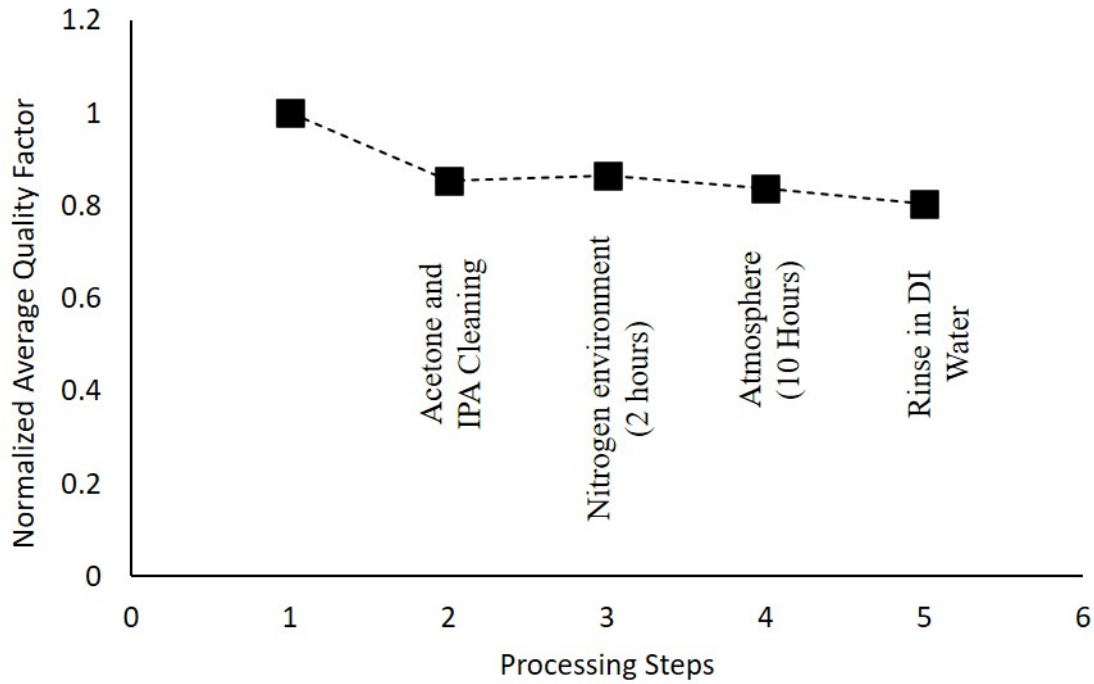


Figure 3.22: Effect of exposure to different environment on quality factor of fused silica resonator coated with ALD Platinum. Quality factor is the average of two devices and two modes of each device and is normalized.

observations have been made by Morgan and Somorjai [136] on Platinum (100) surface. Finally, the shells were rinsed in DI water and dried on a hotplate at 150 °C for 2 hours. The measured Q dropped by $\sim 20\%$ its initial value as compared to $\sim 70\%$ drop in the case of uncoated resonators. These experiments on coated resonators provide further evidence that damping due to adsorbed molecules on the FS resonator surface is a significant source of damping. Additionally, protecting the surface with a metal helps reduce any adsorption of water or gas molecules leading to high quality factor. The result of metal-coated resonators subjected to sequential experiments is shown in Figure 3.22. It is observed that damping due to adsorbed molecules on the fused-silica surface is a major loss mechanism limiting mechanical quality factor. It is experimentally verified that Q drops by as much as 70% after being exposed to aqueous environments. It is hypothesized that at ~ 450 °C, water

molecules desorb from the surface, whereas ~ 850 °C complete dehydroxylation takes place. Another set of experiments with resonators conformally coated with ALD Platinum reveals that exposure to atmosphere and pure N_2 gases does not cause any significant drop in Q , unlike uncoated resonators. It is observed that the Q drop is $\sim 20\%$ when the device exposed to DI water. Therefore, it is concluded that when resonators made from FS are exposed to aqueous and gaseous environments their Q drops by 70%, but when the same resonators are coated with a thin protective metal layer such as Platinum, and then exposed to these same aqueous and gaseous environments, Q does not degrade as much. Consequently, protecting the surface of fused-silica devices is critical to obtaining high- Q resonators.

3.8 Shock Testing

Shock survival is important in harsh-environment applications like gun-launched munition mission which experiences massive shock. The sensors used in such applications should survive these high shocks. Different shock survival mechanisms have been explored in the past. These include using a high frequency operation which reduces deflection. Other methods include using either mechanical or electrical shock-stoppers which basically restricts the motion of resonator under shock. In the event of shock, different regions of the resonator deflect creating regions of stress. This stress when exceeds the maximum tensile stress of material, leads to fracture. PSI resonators are designed to have an inherent feature of shock survival. This is done by selective tuning of stiffness to make the resonator thick at the shoulder region without affecting the operational $n=2$ wineglass frequencies.

To study the effect of high shock ($\sim 20,000g$) on PSI resonators, a finite element model is created in COMSOL where the shell is subjected to horizontal and vertical

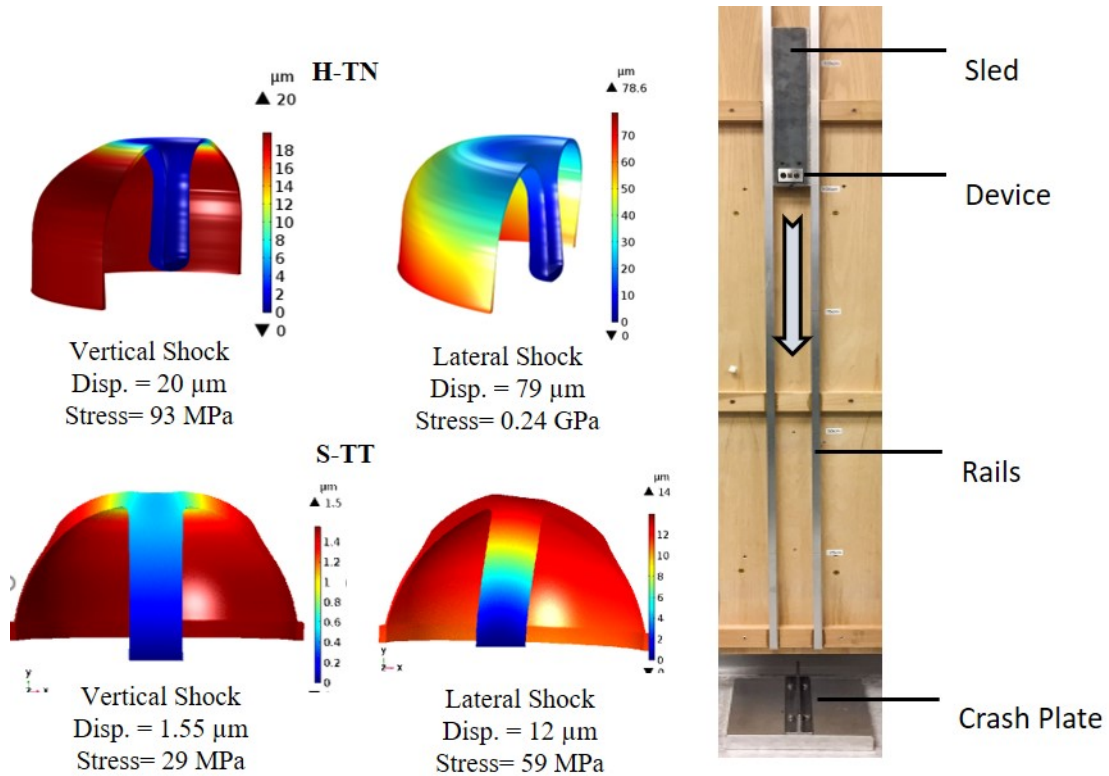


Figure 3.23: Numerical simulation showing displacement of H-TN and S-TT type PSI resonators under 20000g vertical and lateral shock. H-TN PSI experiences larger displacement due to thinner regions at shoulder and rim than S-TT PSI. The maximum stress is 0.24 GPa which is an order of magnitude smaller than the tensile stress of FS. Shock testing setup to impart shock upto 6000g.

shock with profile of half sine for 15 ms with peak amplitude of 20,000g. The movement of the shell as well as the maximum stress is calculated. Figure 3.23 shows the deflections and stresses generated for two PSI resonators. The maximum stress experienced is 0.24 GPa which is an order of magnitude smaller than the tensile strength of FS which is ~ 2 GPa which makes PSI resonators robust to high shock. To experimentally verify the robustness of resonators, a drop-testing setup called **T**unable **H**igh-G **s**hOck-testing **R**esource (**THOR**) was built which could do a drop test from a height of 2 meter limited by the ceiling height of the lab. THOR consists of a sled which slides along rails parallel to the wall as shown in Figure 3.23. The resonator is mounted on the sled using different fixtures to impart either horizontal

or vertical shock to the resonator. When let free, the sled runs along the rails and hits a metallic crash plate. The acceleration is given by,

$$Acceleration = \sqrt{\frac{EAgd}{hm}} \quad (3.2)$$

Where, E is the elastic modulus, A is the impact area, g is acceleration due to gravity, d is the drop distance, h is the height of the object and m is the mass of the object. When a FS resonator is dropped from a height of 2 m, it generated a shock of $\sim 6000g$. PSI resonators and PSI gyroscopes (discussed in next chapter) were drop tested on THOR from a maximum height of 2 m. All the resonator survived multiple shocks in both horizontal and vertical direction without any damage whatsoever to the device or attachment. PSI gyroscopes initially suffered damage to the glass electrode substrate however with design changes the gyro survived 6000g shock.

3.9 Long Term Testing

Long term testing is important to measure reliability and drifts in resonance characteristics of resonators. Three parameters have been chosen for long term study, (i) Q variation with continued resonance (fatigue testing), (ii) frequency drift with time and (iii) frequency mismatch drift with time.

3.9.1 Fatigue Testing

Four PSI resonators with frequencies between 5–6 kHz is chosen for testing their behavior under continuous resonance. Q of all the shells are first measured under vacuum and the PZT is then actuated to continuously sweep from 5 to 6 kHz every 1 second for a period of several hours after which the PZT actuation is stopped and f , Q is measured. Measurements are done using the same technique discussed in

Section 3.2. After measuring resonance characteristics of all the four devices, the PZT is actuated again until next measurement. Continuous excitation is carried out for nearly 30 days and measurement is done in 16 sets. Figure 3.24 shows the variation of Q with number of cycles.

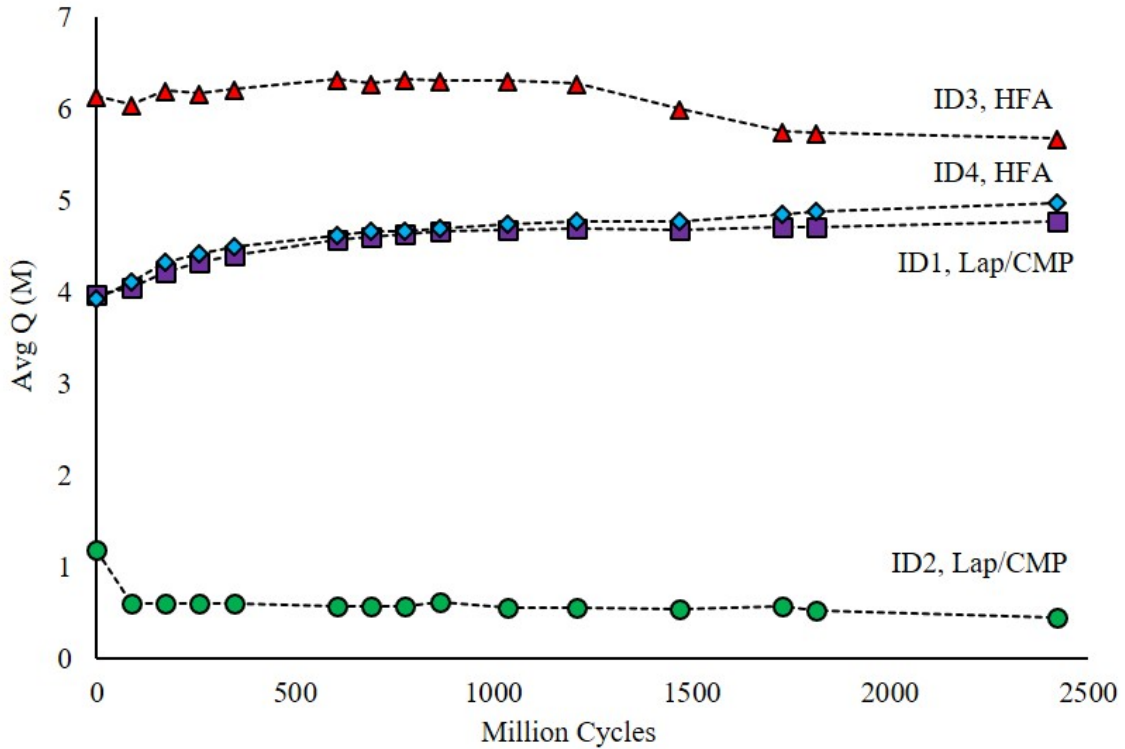


Figure 3.24: Measured Q over a span of one month for four devices under continued resonance. Device 1 and 2 are singulated using lap/CMP method and Device 3 and 4 are singulated using HFA method.

In the first set of measurement, Q dropped for #2 while it remained same for other three devices. In subsequent set of testings, #2 maintained its Q . It is to be noted that #2 had a lower Q than the remaining three devices to begin with which maintained and even improved their Q . The improvement in Q can be attributed to desorption of water molecules under high vacuum as explained in Section 3.7. Q for device 3 reached a peak then started decreasing after around 15 days of resonance. Questions which arises here include why Q dropped initially for Device 2 by $\sim 50\%$

and why Q for device 3 dropped by $\sim 10\%$ after 15 days of resonance. Likely reasons include permanent generation of micro/nano cracks which initiated early in device 2 and much later in device 3, or, a temporary loading of particles on surface of these two devices. To answer these questions, all the four devices were unloaded from the PZT block after all testings were completed and cleaned in Acetone and IPA and dried on hotplate at 150°C . All four devices were then annealed at 450°C in forming gas environment for 16 hours (all annealing run in this thesis is done for 8 hours unless mentioned otherwise but due to fixed-hour access to cleanroom due to COVID-19 pandemic, this run was done for 16 hours). The devices were put back in vacuum chamber and tested when the pressure reached $<10\ \mu\text{Torr}$. The performance for all the four devices increased and became better than their initial performance as is seen in last data set in Figure 3.25. This indicates that Q drop for device 2 and 4 was temporary likely due to loading of particles and the devices could survive more than 2.5 Billion cycles without any degradation in Q .

3.9.2 Frequency and Δf Drift

The drift of frequency is another parameter which is important for long term gyroscope performance. Frequency of the two $n=2$ wineglass modes is monitored for 2500 million cycles of continuous resonance in room temperature without any temperature calibration. Figure 3.26 shows the measured $n=2$ frequencies for all the four devices under testing. It is to be noted that uncertainty in measurements is $<0.06\ \text{Hz}$ as explained in Section 3.2. Very small fluctuations are measured over a span of long testing. Although, all four devices experienced one relatively large dip of $\sim 0.5\ \text{Hz}$. Such fluctuations could be either from device itself by virtue of device damage, mass loading etc. which is however not the case because frequencies recovers in the next measurement cycle. Also, the devices under experiments were

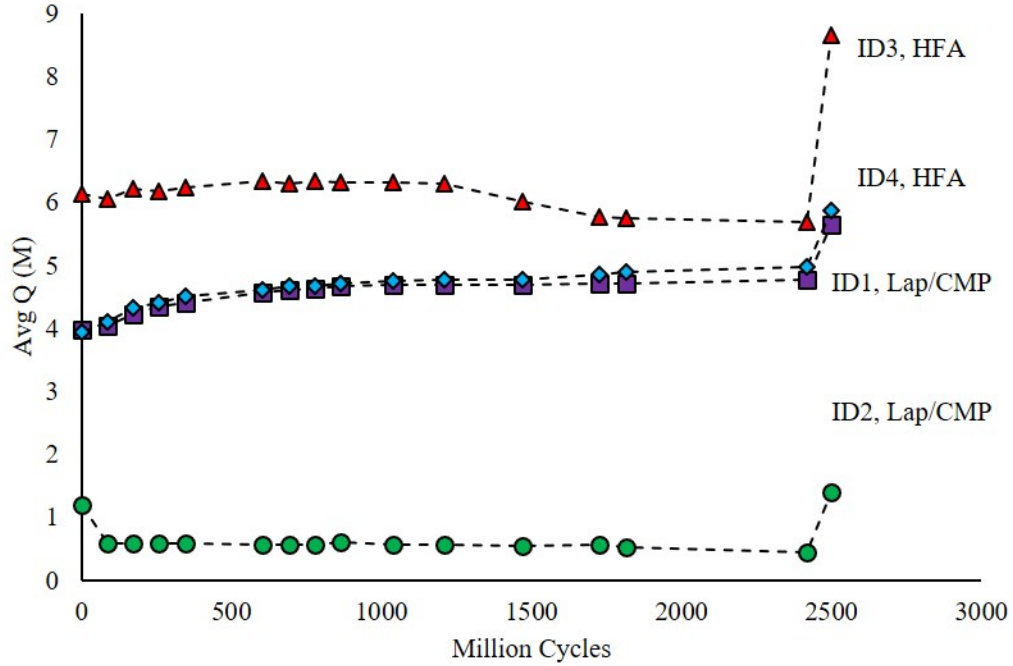


Figure 3.25: Performance of all four devices increased in the last set of measurement after cleaning and annealing. Performance exceeded the initial Q because of longer annealing.

kept in vacuum chamber in ultra-low pressure on a vibration isolation table, therefore it is unlikely that pressure level or disturbance from environment are reasons for frequency drift. It is believed that such frequency changes are due to temperature fluctuations on different days. For FS shell resonators coated with metal, temperature coefficient of $n=2$ wineglass mode frequency is between 75–100 ppm/C. Therefore a 1 °C temperature fluctuation can cause the frequency to drift by $\pm (0.45\text{--}0.55)$ /Hz [137]. Drifts due to temperature related effects can be further minimized by oven control [137]. At the same time, such small changes in frequency can be efficiently tracked by the phase locked loop.

Figure 3.27 shows measurement result of Δf of the four devices under fatigue testing. Δf just like f is measured to be stable with maximum variation of 0.06 Hz over the testing span of one month. Measured variation lies within the measurement error explained in Section 3.2. Δf stability also indicates that the fluctuations in

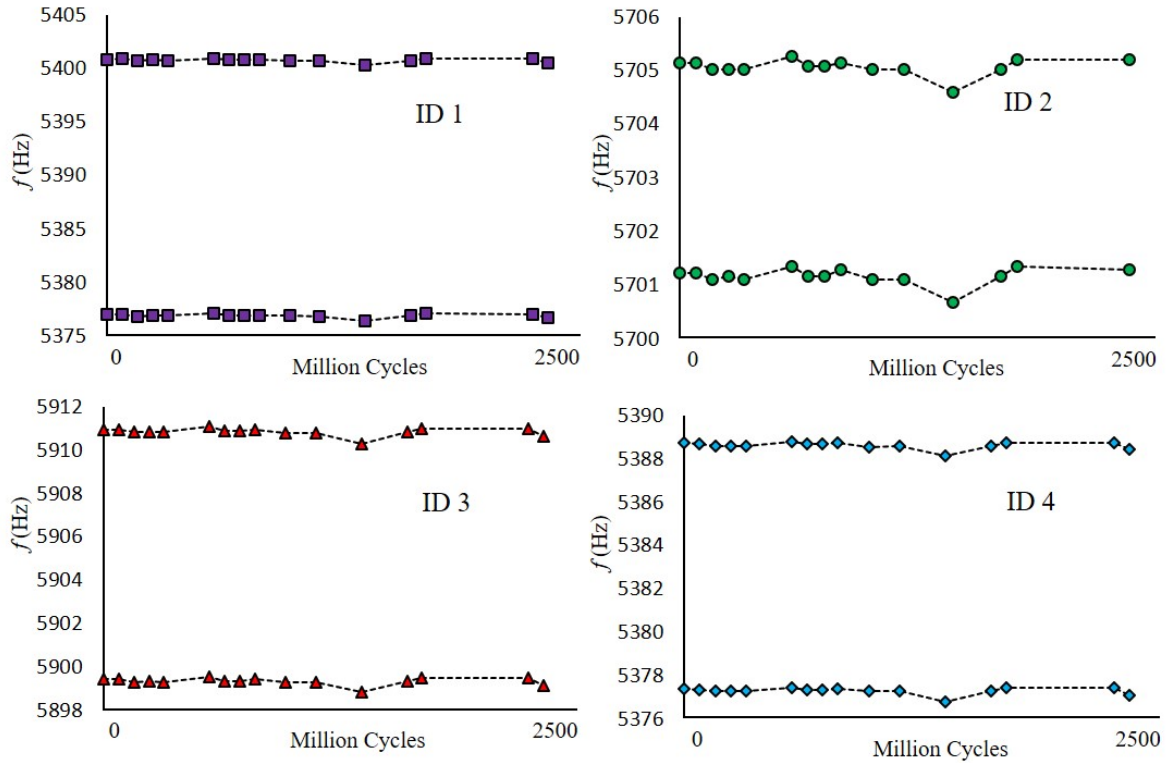


Figure 3.26: Variation of $n=2$ wineglass frequencies measured over 2500 Million cycles of resonance. Maximum frequency drift measured is ~ 0.5 Hz.

f was indeed due to temperature related effects and therefore both modes were uniformly affected (to maintain Δf).

3.10 Metal Coating

For capacitive transduction, the resonator should be conductive. FS, however, is an insulator and therefore should be coated with a conductive layer. This conductive layer should be thick enough to provide a conductive path between the biasing region (at the anchor) and the region of deflection (rim). Coating with metal is however accompanied with loss in energy causing Q drop. This drop is proportional to thickness of metal. Therefore, it is critical to coat the shell with a thin metal layer which can provide a low resistance path for the charge to travel. Another way to reduce the drop in Q is by selective coating of metal only near the rim. Figure

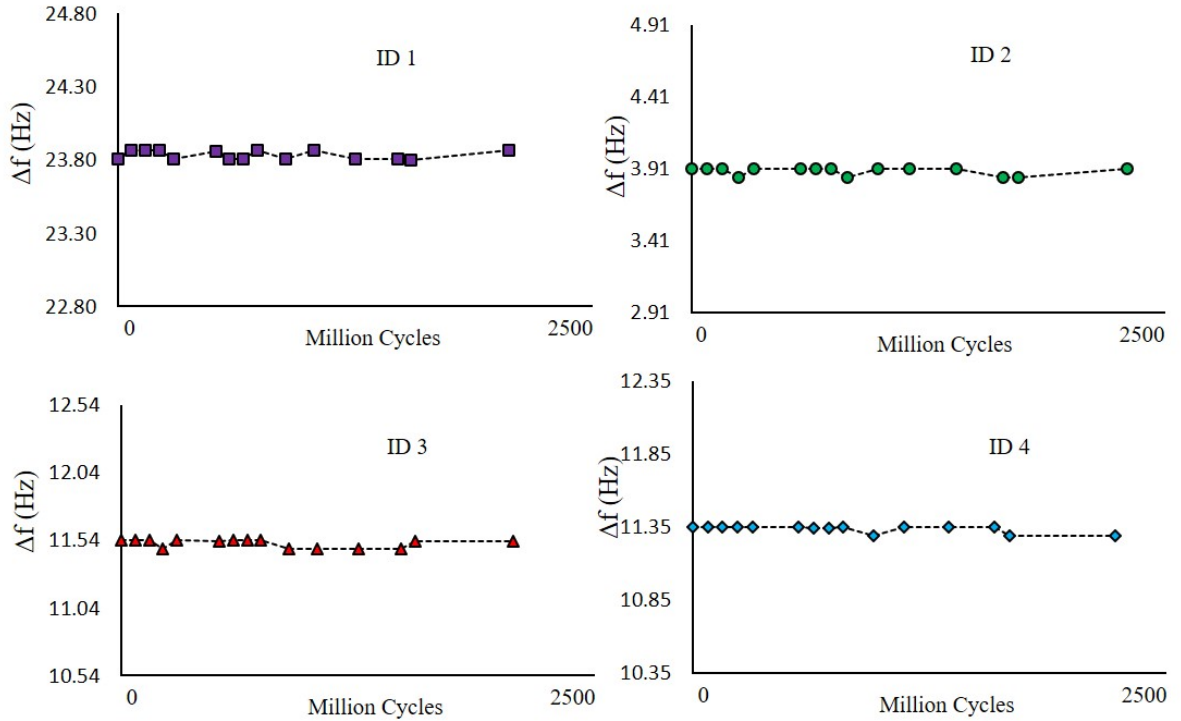


Figure 3.27: Variation of $n=2$ wineglass Δf measured over a month of continued resonance. Δf drifts by ~ 0.06 Hz which is within the measurement uncertainty.

2.35 shows selective coating schemes and a shadow mask discussed in Section 2.13 can be used for such selective coating. Effects of metal coating on Q for different resonators have been explored in the past. These metals/dielectrics include a combination of Cr, Au, Ti, Pt, Al_2O_3 etc. deposited either through metal sputtering or atomic layer deposition technique. There are two key requirements from the material. One is good adhesion on the surface of resonator and other is good electrical conductivity. Therefore, materials which do not easily oxidize in atmosphere are required. Sputtering deposits material by physically removing particles from a source and depositing on the resonator. This process therefore can be applied to only those materials which have good adhesion to the resonator material or another adhesion enhancing layer can be deposited between resonator and target material to promote sticking. In microfabrication, Cr, Ti and Al have shown to have excellent adhesion

on FS substrate and are therefore used as adhesion promoter. These however oxidizes in atmosphere and can therefore not be used as standalone conducting material. Therefore, bilayers like Cr/Au, Ti/Pt, Al₂O₃/Pt etc. is used. While using bilayer of metals it should also be ensured that materials do not diffuse through each other and compromise either adhesion or conductivity. For example, a bilayer of Ti/Au is not the best choice because Ti would easily diffuse through Gold and gets oxidized on the surface. Techniques like ALD are driven by chemical reactions and therefore may not always need an adhesion promoter. For example, Pt can be grown on FS substrate using ALD without any adhesion layer. It is also understood that films grown through ALD due to its amorphous nature do not have large grain boundaries as is the case in physical deposition techniques like sputtering [138]. These grain boundaries are believed to be a potential source of energy dissipation due to slippage between grains. Loss of energy due to metal coating is usually attributed to either TED, material loss or interface loss. Reference [72] numerically studied the effect of metal coating on Q_{TED} and observed as much as three orders of magnitude drop when a thin metal layer (1% of the rim thickness) is added. However, thicknesses as small as 100 Å practically does not affect Q_{TED} . This is however not the case in reality and deposition of even 20–30 Å metal causes Q to drop by a factor of 2 as reported in [123]. Reference [139] observed grain boundaries for their AlN based resonators and modified TED simulation to include effect of such grain boundaries which led to three orders of magnitude reduction in Q_{TED} . Therefore, TED along with losses inside the material and interface is believed to be dominating loss in Q however experiments and modeling needs to be done for complete understanding. Along with method of deposition, selection of metals has also shown to affect Q by different extent. For instance, [138] ALD deposited a bilayer of Al₂O₃/Pt and

observed 20% less reduction in Q as compared to only Pt. This was attributed to reduction of interfacial slippage due to surface passivation from Al_2O_3 . Other studies have also hinted at potential usage of metals with closely matched material property in particular Young's Modulus (E) to those of FS for reducing losses. Reference [140] numerically studied effect of E of material deposited on FS and observed that Q_{TED} is maximum when the added material has E close to that of FS. This can be because of minimal stress gradient between materials when E is closely matched [140]. A similar observation has also been made by [141] for Nb_2O_5 which has E close to that of FS. Reference [83] studied the effect of a variety of metals on Q of FS shell resonators. It was observed that deposition of 15/20 Å of Cr/Au (total thickness = 35 Å) reduced Q by nearly 40% and additional deposition of Au (total thickness = 155 Å) continued to reduce Q but at a slower rate reducing Q by only an additional 30% making the total drop in Q by 70%. It was postulated that the deposition of first metal causes a significant stress gradient which continues to increase as metal thickness is increased although at a reduced rate. Deposition of 10/20 Å of Ti/Pt (total thickness = 30 Å) showed a 45% reduction in Q . Subsequent deposition of Platinum to get 10/60 Å (total thickness = 70 Å) further reduced Q by 15% making the total Q drop by $\sim 52\%$. Other metals like TiN was also explored and it was observed that 65 Å TiN reduced Q by 50–60% of their initial values. Another bilayer of ALD deposited Al_2O_3 and sputtered Gold of thickness 10 Å and 50 Å respectively was also investigated. It was observed that first deposition of ALD alumina reduced Q by around 70% and deposition of sputtered Gold further reduced Q leading to a total drop of 75% which is huge. Finally, Indium Tin Oxide (ITO) was investigated and it was observed that deposition of 500 Å ITO dropped Q by only 30%. Table 3.6 summarizes the metals explored in the past and their effect on Q . While such a

Table 3.6: Summary of metal layers investigate in the past and their effect on Q [83]. Al_2O_3 is deposited through ALD and other metals are sputter coated.

Metal Layer	Thickness Å	% drop in Q
Cr/Au	15/20	40
	15/140	70
Ti/Pt	10/20	45
	10/60	52
TiN	65	50
Al_2O_3	10	70
$\text{Al}_2\text{O}_3/\text{Pt}$	10/50	75
ITO	500	30

study is important to find promising metal layers, it is to be noted that these experiments involved different thickness of deposited metals and on resonators of different diameters. Moreover, some devices were annealed after metal coating. Therefore, a more systematic study needs to be done to truly compare different metals and their effect on Q.

In this section, the effect of a combination of different metals is studied and their effect on drop in Q is investigated. This study is different from the one done in [83] as same thicknesses for different metals are used and extreme care is taken to maintain similar device manufacturing and testing process. This includes annealing all devices right before initial testing and putting for metal coating immediately after taking them out from the vacuum chamber of LDV. It is also ensured that the resonators are exposed to atmosphere for the minimum possible time. Four different metal combinations including Cr/Au, Ti/Pt, Al/Au —all deposited by sputtering and Pt deposited by ALD are explored. In the case of sputtered metals, thickness of 25/80 Å is maintained for all metals and ALD Pt is deposited to a thickness of 80 Å. In the case of sputtered metals, shells are first attached on the silicon pedestal substrate with glass frit and then annealed at 450 °C. Q is measured and the devices are put in the sputter tool. After depositing the metals, they are put back in the vacuum chamber of LDV again ensuring that the resonators are minimally exposed

to atmosphere (only while bringing it back from cleanroom to testing lab).

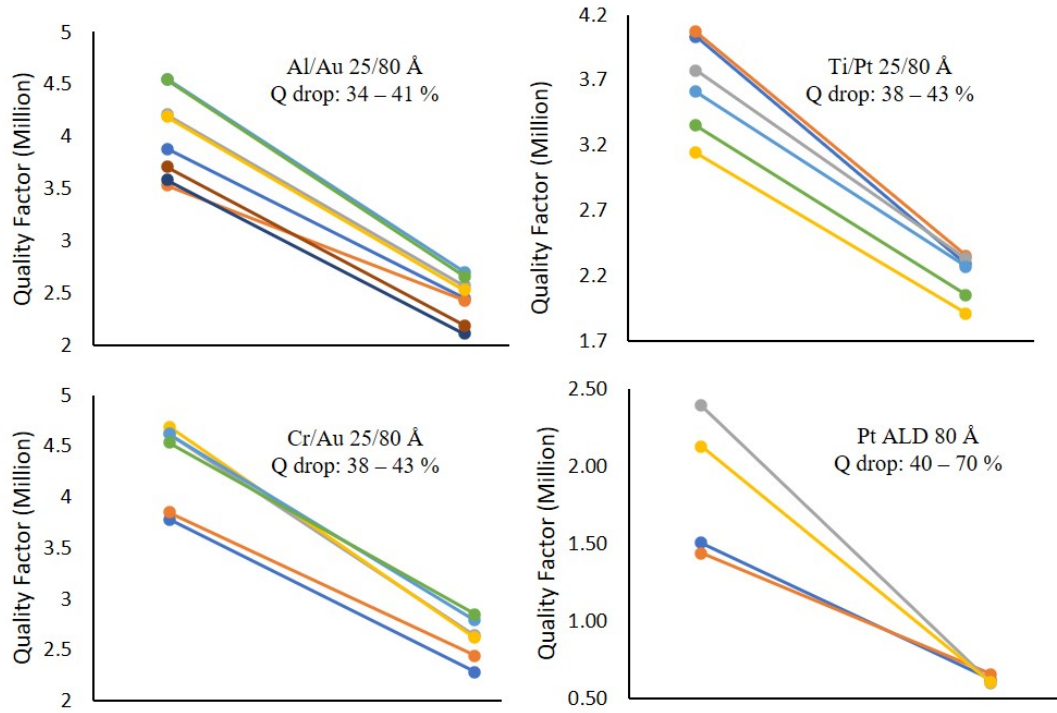


Figure 3.28: Effect of different metals on Q of PSI resonators. Four different combinations of metals are used, and the Q is measured before and after deposition of metal. For sputtered metals, deposition is only on one side but ALD deposition is conformally on both inside and outside of shell.

When the vacuum level reaches $< 10 \mu\text{Torr}$, Q of each devices is measured. In case of Pt deposition by ALD, shells could not be mounted with glass frit due to tool restrictions. Therefore, the shells after annealing (before coating metal) is mounted on silicon pedestal substrate with Crystalbond and Q of uncoated resonator is measured. The shells are then cleaned to remove Crystalbond from anchor area and annealed again and are then put in the ALD tool for Pt deposition of thickness 80 \AA . After deposition, the shells are mounted back on same test substrates using Crystalbond and Q is measured. Figure 3.28 shows the drop in Q due to different metals. While sputtered metals caused the Q to drop by 30–40%, ALD Pt caused it to drop by as much as 70%. It is to be noted that metal sputtering was done only

on one side of the resonator while ALD was done to conformally coat the shell. This may be a reason for relatively larger drop in case of Pt ALD. It is also seen that total thickness of 105 Å reduces Q by similar amount (<50%) irrespective of metals used. At the same time deposition of Al/Au metals whose E is around 70 and 78 GPa respectively and are closest to 72 GPa of FS also reduced Q by similar amount as other metals with relatively higher E. This questions the theory if stress gradient is dominating the drop in Q or is it losses inside the material or at the interface. It is believed that a combination of all these are responsible for Q drop and that innovative experiments needs to be developed to isolate and study the effect of each one of them.

3.11 Conclusion

Test results measured using LDV is presented and $Q > 12.5$ Million, $\tau > 500$ second and $\Delta f < 2$ Hz is obtained. Such high Q and τ are unprecedented at this scale and are record performance reported till date. It is also shown that performance of devices singulated using lap/polish method and HFA method yield comparable Q and Δf . Many devices are fabricated with repeatable high Q and low Δf . Sources of Δf is also investigated and it is found out that Δf of PSI resonators is dominated from acircularity of the mold. It is also believed that even lower Δf is possible by using ultra-precise mold. Both $n=2$ and $n=3$ modes are measured, and high Q have been obtained in both the modes. It is also shown through numerical modeling and experimental results that Δf of $n=3$ mode is likely more tolerant to asymmetries as compared to those of $n=2$ modes. Test results of open shell PSI resonators is also presented which shows that etching open windows on the surface of shell leads to an increase in Q. Fused silica material characterization is studied systematically, and it

is found that damping due to adsorbed water molecules dominates Q and annealing process either desorbs or dehydroxylates water depending on the temperature of annealing. This is further confirmed by observing smaller drop in Q when exposed to aqueous environment after they are coated with thin layer of ALD Pt. PSI devices have also shown to withstand shock $>6000g$. Shock testing is done on multiple devices and no damage is observed. Fatigue characteristics of shells are also studied and no degradation in performance is witnessed after 2500 Million cycles. Repeatable results have been obtained and an analysis of more than 200 resonators is done to show the variation of f and Q fabricated in a batch. With improved fabrication and processing methods, it is shown that variation of Q of devices in a batch is reduced which further indicates that the developed methods are efficient for volume production of PSI devices. Finally, a systematic study is done to quantify effect of sputtered Cr/Au, Ti/Pt, Al/Au and ALD Pt on Q . Metal coating is important to make the devices conductive for electrostatic actuation for gyroscope. It is observed that irrespective of sputtered metal used, drop in Q is 30–45%. However, for ALD Pt, drop is between 40–70%. It is also experimentally observed that even metals with closely matched Young's Modulus with that of FS, reduces Q by similar amount as compared to others with relatively larger mismatch. However, even with a 50% drop, Q is on the order of several million for PSI devices which is sufficient for obtaining navigation-grade performance from gyros as will be seen in the next chapter. Once resonators are fabricated and coated with metal, they are assembled on electrode substrates for capacitive transduction for gyroscope operation. Next chapter will discuss the design, fabrication and testing results from different PSI gyroscopes.

CHAPTER IV

Precision Shell Integrating Gyroscope

4.1 Gyroscope Architectures

Different transduction mechanisms of gyroscope have been discussed in Chapter I. One of the popular method is using capacitive transduction by sensing change in capacitance in response to external rotation. Capacitive transduction is used in this thesis. In this mechanism, 3D resonators are actuated to resonance and their resonance pattern is sensed using electrodes that are located close to and separated from the resonator by a small capacitive gap. For large and symmetric drive/sense signal, it is desirable to have substantially uniform gap dimensions and conformal overlap of the electrode with a substantial portion of the resonator to obtain large capacitance. Similarly, for better tuning capability (matching the drive and sense frequencies), large electrostatic forces are needed which can be obtained by using large voltages or by increasing the overlap area between the electrodes and the vibrating resonator. Two approaches to fabricate 3D shells have been discussed in Chapter II. These are either by depositing a thin film of device material on sacrificial mold or by micro-molding. In each case, electrodes are needed to drive and sense the motion of the shell in resonance. Electrodes for shells made using the thin-film approach can be formed in or on the substrate before the deposition of the device structural layer.

This approach allows for very small and uniform gaps and at the same time leads to conformal overlap between the resonator and the electrodes due to the curved nature of the electrodes. However, gyroscopes fabricated using this approach have failed to achieve high Q ($Q \ll 1$ Million), due to a combination of factors related to increased energy loss due to structure, size, and material quality. Moreover, because of the limited aspect ratio, the intrinsic capacitance is small even though the electrodes are conformal. Gyroscopes fabricated using micro molding approach usually fabricate resonators and electrodes separately and are integrated together. However, a few approaches have been explored to either electroplate metal on resonator with a sacrificial layer [142] or by co-blowing resonator and electrode [143]. These approaches have the advantage of uniform azimuthal gap but suffers from issues due to either process complexity or small capacitive overlap. The approach where both resonator and electrode are fabricated separately and mechanically assembled will be discussed in this chapter. Three different electrode architectures namely ‘Surface Electrodes Architecture’, ‘Side Electrode Architecture’ and ‘SiS Conformal Electrode Architecture’ are discussed. These approaches utilize the deflection of resonator in the out-of-plane or in-plane directions to sense change in capacitance as shown in Figure 4.1. Irrespective of electrode architecture, the focus has been to obtain small and uniform capacitive gaps with large overlap capacitance. Besides, simpler fabrication and assembly process is also required. Figure 4.1 compares key aspects of in-plane and out-of-plane transduction mechanisms. In the next section, measurement technique to evaluate resonant characteristics and gyroscope noise is discussed.

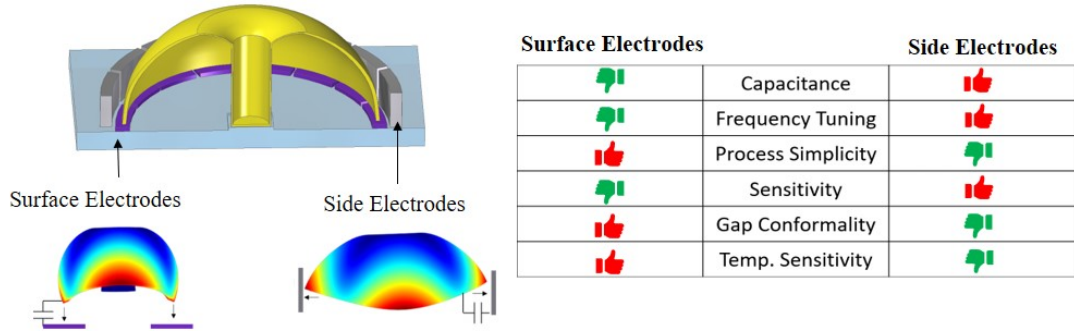


Figure 4.1: Gyroscope architectures showing surface electrodes where electrodes are placed beneath the rim to measure out-of-plane displacement and side electrodes where electrodes are placed beside the rim to measure in-plane displacement. Advantages and disadvantages of each architecture is tabulated.

4.2 Test Setup and Measurement Technique

Resonance characteristics of a resonator integrated on electrode substrates are measured on Lakeshore probe station at $< 1\text{mTorr}$ pressure using Zurich Instruments HF2LI lock-in amplifier. Needle probes are used to probe electrodes. Three electrodes are chosen at a time. Bias voltage is applied to the resonator through one of the four bias electrodes. The remaining two electrodes are used to apply the drive signal and to sense the motion. Figure 4.2 shows the testing setup.

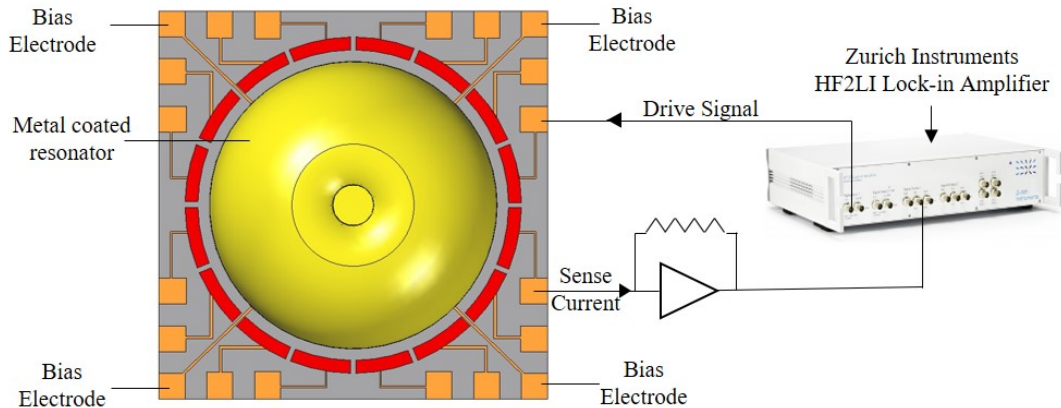


Figure 4.2: Measurement technique to measure resonant characteristics.

Drive signal is applied to one of the electrode and sensed from the other which generates an output current. This is fed to a transimpedance amplifier to convert

to voltage output. Signal processing inside Zurich instrument lock-in amplifier is done and measured information in an easy to understand form is outputted. To test resonance parameters, first, a frequency sweep of sine wave is applied to the electrode. FFT of the output signal is done to measure the wineglass frequencies. Once the frequencies are known, the resonator is driven at its resonance frequency to increase the amplitude of motion. The input signal is then cut-off and the amplitude decay is measured and recorded. A MATLAB script is used to measure τ for each mode.

To test a gyroscope, bonding pads of electrodes are wire bonded to pins of the LTCC package and mounted on a PCB. Zurich Instrument HF2LI Lock-In Amplifier is used to implement the control circuitry in the force re-balance mode. An ultra-low-noise TIA is used. The gyroscope is tested at <1 mTorr at room temperature on a rotation table. Allan Deviation plot is generated from data collected for less than a day at room temperature without any temperature control. In the next couple of sections, gyroscopes fabrication and assembly methodology using each approach will be discussed and test results will be presented. Pros and cons of each architecture will be discussed. Following this, a new architecture to develop gyroscopes with conformal electrodes will be introduced. Design and fabrication method will be discussed, and test results will be presented.

4.3 Surface Electrode Architecture

In surface electrode architecture, electrodes are placed beneath the rim of the resonator. This approach measures change in capacitance by virtue of out-of-plane displacement of rim. In the $n=2$ wine-glass modes, the deformation of resonator in out-of-plane direction is shown in Figure 4.1 where it is sensed by electrodes placed

beneath the rim. Figure 4.3 shows schematic and photograph of PSI gyro with surface electrode configuration. Resonators are fabricated and singulated by processes described in Chapter II and electrode substrates are fabricated using lithography as explained in the next section. They are then assembled with a small capacitive gap. As will be explained in the following sections, fabrication and assembly of surface electrode gyros is very simple and fast. However, due to limited overlap (limited by the rim thickness), such gyros have small capacitance. Besides, due to small deflection in out-of-plane direction (as compared to in-plane motion), these gyros have small sensitivity and frequency tuning capability.

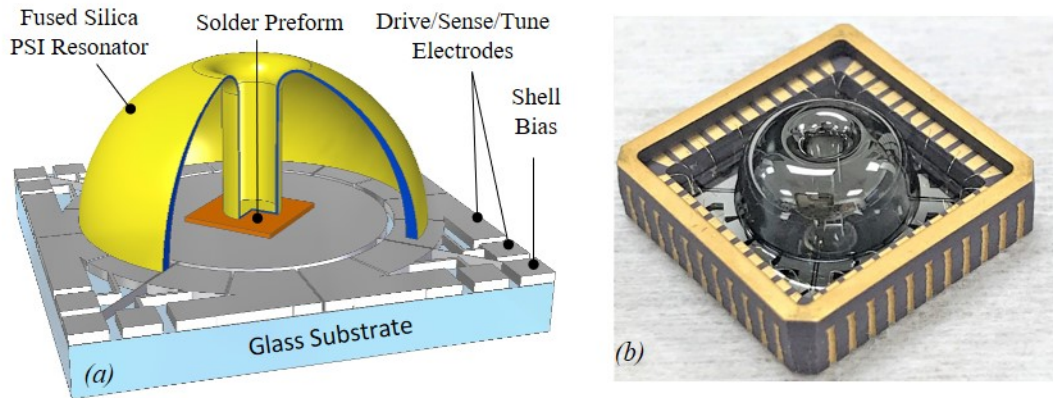


Figure 4.3: PSI Gyroscope with surface electrode architecture. (a) Schematic representation and (b) photograph of a fabricated and assembled PSI gyroscope wire bonded inside LTCC package.

4.3.1 Fabrication of Electrodes

Fabrication of electrode substrate is simple because of its planar nature. A glass wafer is cleaned and coated with $1.6 \mu\text{m}$ Shipley 1813 photoresist. The photoresist is photolithographically patterned to define electrode patterns for lift-off. A tri-layer of $\text{Ti/Pt/Au} = 50/700/3000 \text{ \AA}$ is then deposited using evaporation. The top gold layer is patterned using $6.5 \mu\text{m}$ Shipley 1827 resist and is wet etched to define circular regions near the anchor for eutectic bonding. Then, the wafer is put in Acetone in an ultrasonic bath to define the electrodes by lift-off of the photoresist layer. Finally,

the backside of the wafer is coated with Ti/Pt/Au of thickness 50/700/3000 Å for die attach inside the LTCC package. The wafer is finally solvent cleaned and diced in squares of size 11.5 mm. Figure 4.4 shows fabrication process and photograph of electrode substrates fabricated on a 4-inch glass wafer.

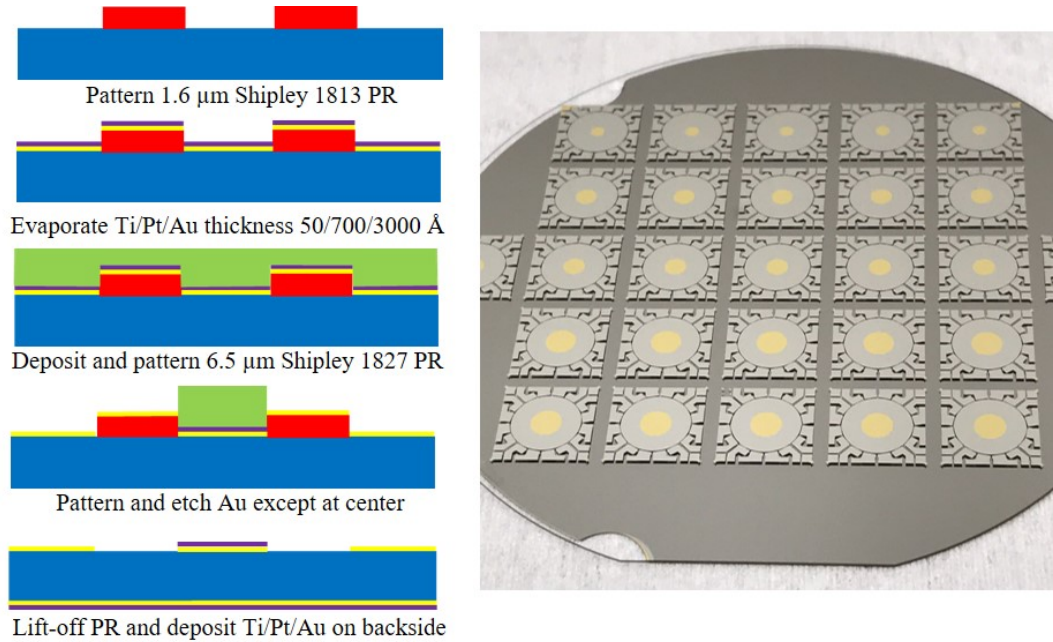


Figure 4.4: Fabrication flow to make surface electrode substrates and photograph of wafer with electrode substrates

4.3.2 Assembly Process

Au-Sn solder preforms are used to attach the shell on the electrode substrate as well as die attach to an LTCC package. First, a 44 pin LTCC package is placed on a hotplate and a solder preform followed by an electrode substrate is placed inside the package. Then another preform is placed at the center on the gold patterned region of the electrode substrate and 12–15 μm thin silicon spacers are placed on the electrode substrate as shown in Figure 4.5(a). Finally, the resonator is placed on the center preform using a semi-automatic arm and aligned using a camera. Once the alignment is complete, a 1 mm fused silica pressing rod is placed inside the hollow

stem as shown in Figure 4.5(b). The hotplate is turned on and the temperature is ramped to 400 °C. As the temperature reaches above the eutectic temperature of Au-Sn (280 °C), a downward force is applied on the pressing rod.

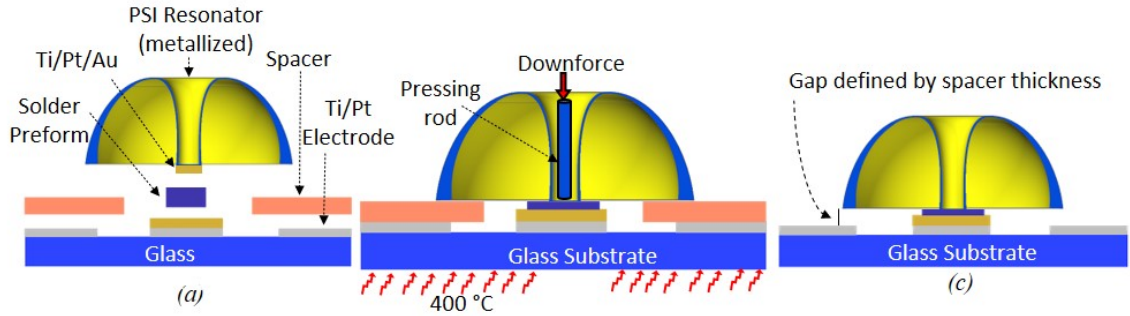


Figure 4.5: Assembly process. (a) Solder preform and spacers are placed beneath the anchor and rim respectively, (b) temperature is ramped up to 400 °C while applying pressure on the shell, (c) temperature is cooled down and the spacers are removed.

This force ensures that the shell is sitting on the mechanical spacers so that the capacitive gap is determined by the spacer thickness. The temperature is dwelled for 10 minutes at 400 °C and then ramped down to 50 °C. The applied force and the pressing rod are removed, and the spacers are slid out leaving a suspended resonator attached at the center as shown in Figure 4.5(c). An SEM image of a PSI gyroscope with narrow capacitive gap is shown in Figure 4.6(a). Figure 4.6(b) shows the measured capacitance values between the rim of the shell and surface electrode. Large and uniform capacitance of 0.2–0.3 pF is measured between the shell and each electrode (parasitic capacitances are zeroed out).

4.3.3 Gyroscope Testing

Three devices are assembled using the approach described above. Table 4.1 lists resonance characteristics for the three devices all using surface electrodes for driving and sensing. Device 1 and 2 exhibited $Q > 1$ Million in both the modes with closely matched Q s while Device 3 exhibited high Q but a larger Q mismatch but had

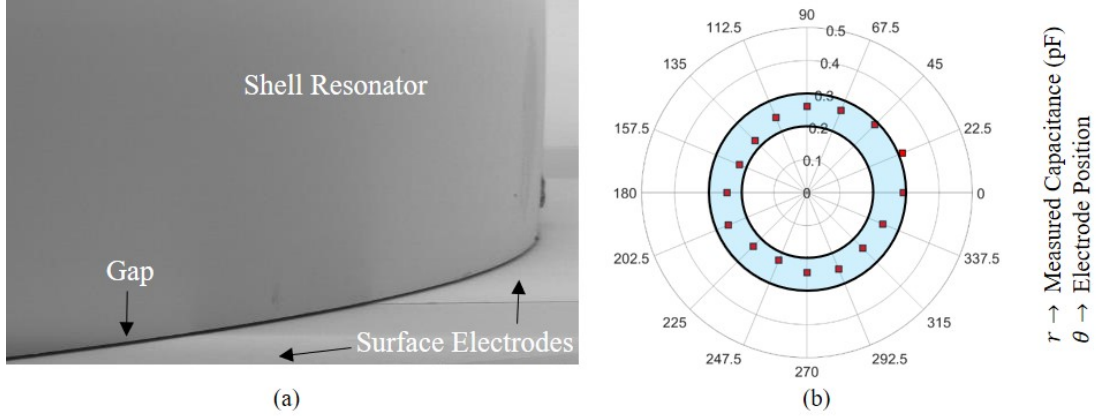


Figure 4.6: (a) SEM image showing resonator, electrode and the capacitive gap. (b) Measured capacitance (in pF) at all sixteen electrodes for a gyroscope with surface electrodes.

Table 4.1: Measured resonant characteristics of three PSI gyros with surface Electrodes.

	Device 1	Device 2	Device 3
Freq. 1 (Hz)	5560.23	7473.00	5801.00
Freq. 2 (Hz)	5543.69	7475.69	5803.10
Q1 (Million)	1.04	1.75	1.27
Q2(Million)	1.02	1.42	0.53
Δf	16.54	2.69	2.1

the lowest frequency mismatch of the three devices. As discussed earlier, frequency tuning is a challenge using surface electrodes and very small gap and large voltage is needed to tune high Δf . Therefore device 3 is chosen for operation as a gyroscope.

Device 3 was then wire bonded to the pins of LTCC package and was tested on a rate table using the method described in Section 4.2. The as-fabricated $n=2$ wine-glass modes are measured at 5,801 and 5,803 Hz. $\Delta f_{n=2} = 2.1$ Hz is electrostatically tuned to ± 100 mHz and a quadrature cancellation loop is applied for further tuning. After mode-matching, Q is measured to be 69.71 seconds ($Q_1 = 1.27$ million) and 29.22 seconds ($Q_2 = 0.53$ million). Figure 4.7 shows PSI gyro on a PC board and the measured ring-down time.

Allan Deviation is computed from data collected for less than a day at room temperature without temperature control. An ARW of 0.0062 deg/rt-hr and an in-

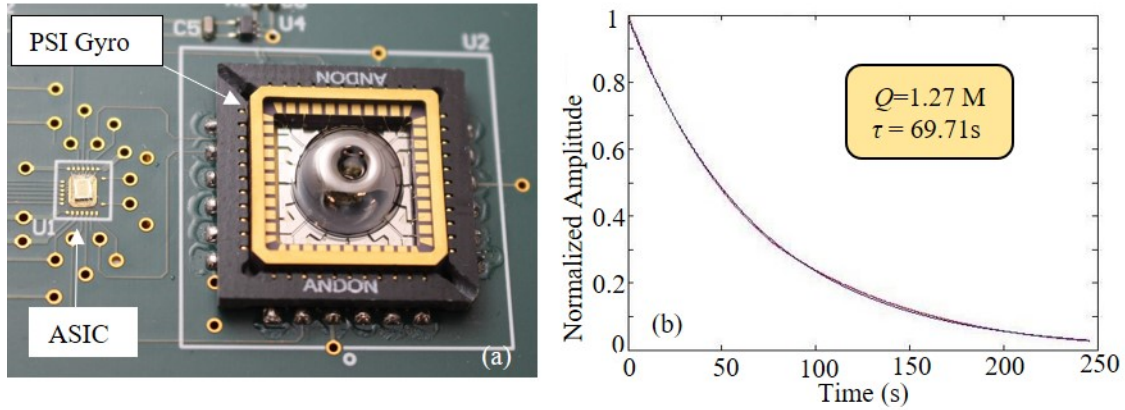


Figure 4.7: (a) The bonding pads are wire bonded to pins of the LTCC package and mounted on a PC Board with an ASIC. (b) Measured ring-down time plot of one mode.

run BI of 0.027 deg/hr are measured as shown in the ADEV plot in Figure 4.8. The testing results are also summarized in Figure 4.8.

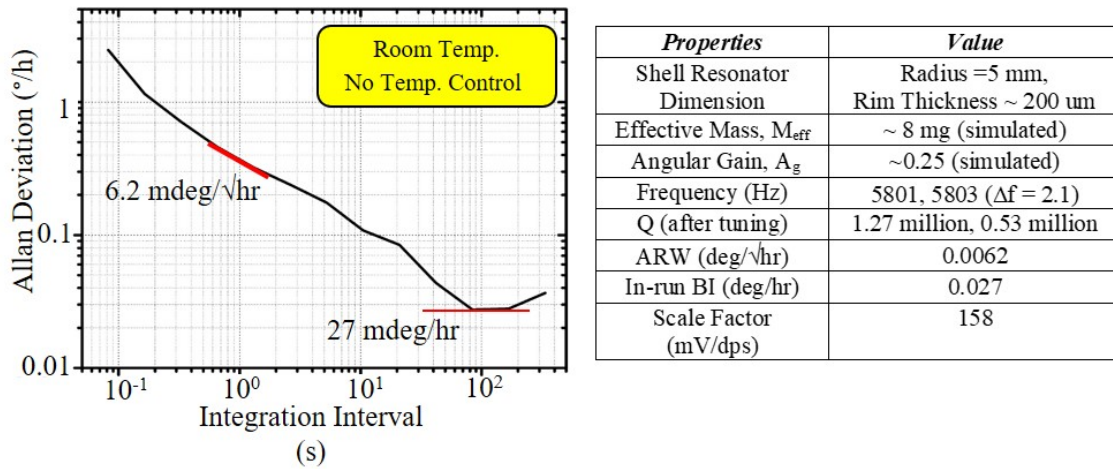


Figure 4.8: ADEV plot exhibiting 0.006 deg/rt-hr ARW and 0.027 deg/hr BI and table containing device characteristics.

A couple of groups have also reported gyroscopes with surface electrode transduction [62, 91]. This is however the best ARW and BI reported using surface electrodes for a shell gyroscope of this size.

4.4 Side Electrode Architecture

Side electrode architecture have electrodes placed around the resonator either inside or outside. These electrodes measures change in capacitance due to in-plane motion of the resonator in its wineglass mode. Figure 4.9 shows schematic and photograph of PSI gyroscopes with side electrodes. In this architecture, tall electrodes are fabricated using a combination of micromachining techniques including DRIE, bonding etc. and therefore makes the approach expensive as compared to surface electrodes. However, due to larger in-plane motion as compared to out-of-plane motion alongside larger overlap area, side electrode gyros have much better capacitance, sensitivity and frequency tuning capability.

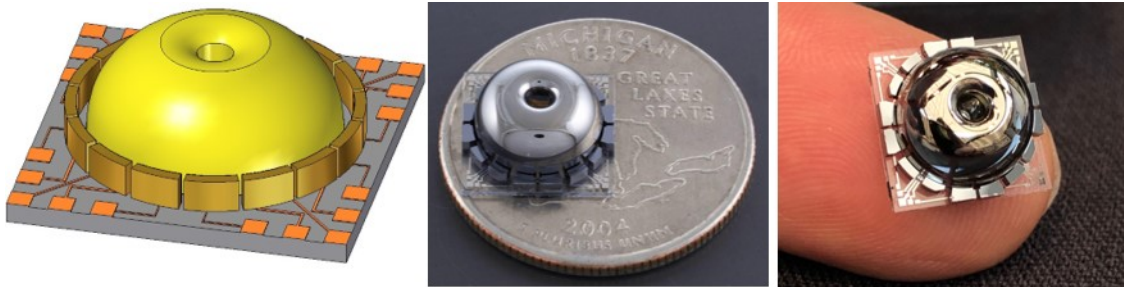


Figure 4.9: Schematic diagram and photographs of PSI gyro on a quarter and finger for scale.

4.4.1 Fabrication of Electrodes

Electrodes are fabricated using Silicon-on-Glass (SoG) process. This process starts with patterning metal connection lines on a glass wafer. In the next step, a 500 μm Boron doped wafer is bonded to the glass substrate. The bonded wafer is then patterned lithographically to define sixteen discrete electrodes. Top silicon is then deep etched to isolate each electrode using Deep Reactive Ion Etching (DRIE). The backside of bonded wafer is then coated with Cr/Au for die attach. The wafer is then diced to singulate each electrode substrate of side 11.2 mm.

4.4.2 Assembly Process

The assembly process starts with placing a metallized resonator facing down on the electrode substrate. The anchor attachment is made conductive to provide a path for bias voltage. The integrated device is then die attached on a 44-pin LTCC package and the electrodes are wire bonded to the pads of the package. To vacuum package the gyro, another LTCC package is flipped and placed on top and vacuum packaged. Figure 4.10 shows schematic diagram of an assembled gyro and photographs of vacuum packaged devices. Details of the assembly process can be found in [93].

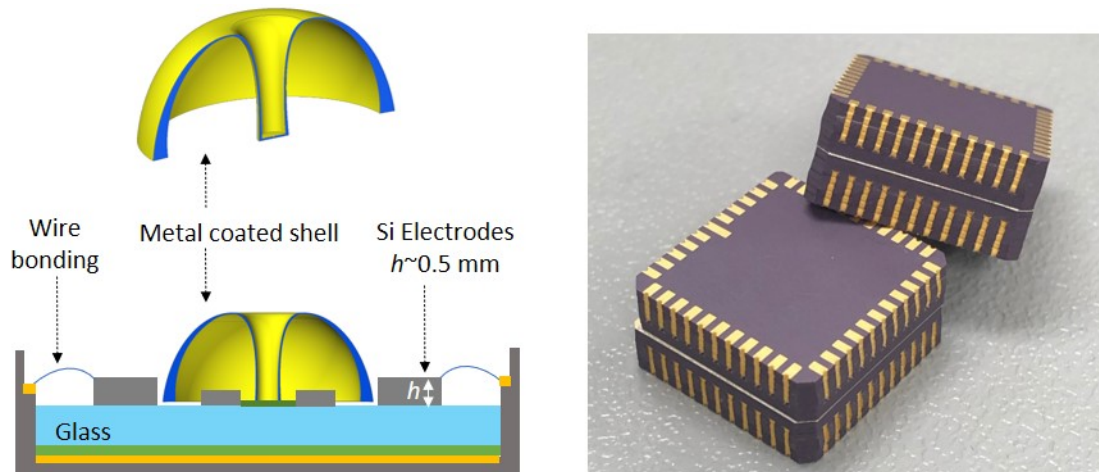


Figure 4.10: Cross sectional view of PSI gyro integrated on electrode substrate and photograph of vacuum packaged PSI gyros.

4.4.3 Gyroscope Testing

The gyroscope is tested at $<1 \text{ mTorr}$ at room temperature on Ideal Aerospace Aero900 rotation table. Zurich Instrument HF2LI FPGA is used to implement the control circuitry in the force re-balance mode. The as-fabricated $n=2$ wine-glass modes are measured at 5,664.9 and 5,668.2 Hz ($\Delta f_{n=2} = 3.3 \text{ Hz}$) and are electrostatically tuned to $< 100 \text{ mHz}$ and a quadrature cancellation loop is applied for

further tuning. After mode-matching, the ring-down time is measured by applying a drive signal at resonance frequency to raise the vibration amplitude. The drive signal is then cut off and the vibration is allowed to freely decay. Ring down time is measured by calculating the time it takes for the amplitude to decay to $1/e$ of its initial value. Ring-down time for the two modes is measured to be 295.53 seconds ($Q_1=5.26$ M) and 290.70 seconds ($Q_2=5.174$ M). Figure 4.11 shows the control and readout circuitry in the force-rebalance mode and ring-down time measurement.

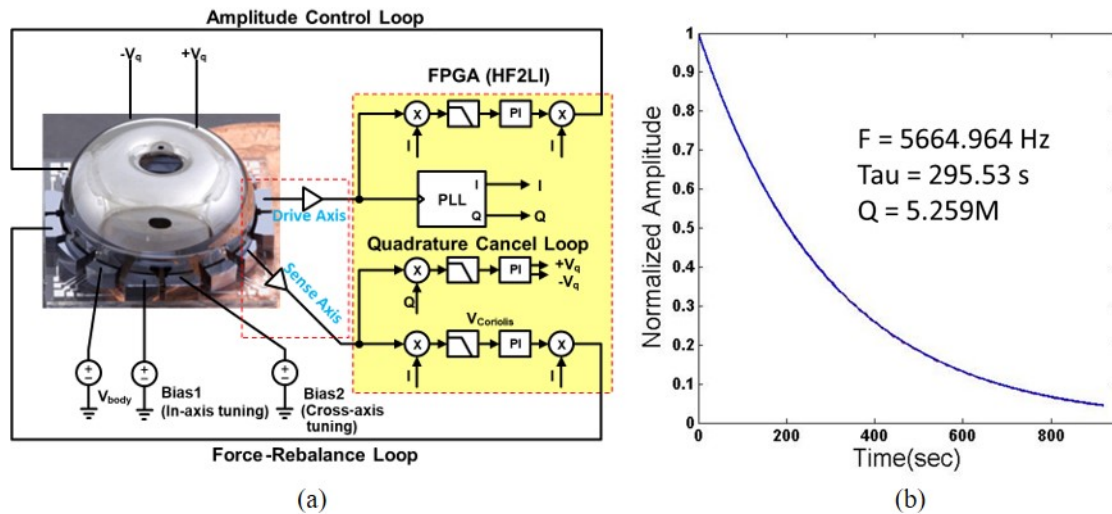


Figure 4.11: (a) Control and readout system for operating PSI gyro in force rebalance mode and (b) measured ring-down time of one of the $n=2$ wineglass modes after reducing frequency split to <100 mHz.

To generate the ADEV plot, signal is collected for less than a day and ADEV graph is plotted. ARW is measured by reading the value corresponding to $\tau=1$ second and BI is measured by reading the lowest point on the plot. ARW is revealed to be 0.00096 deg/rt-hr and in-run bias stability of 0.0014 deg/hr at room temperature. Figure 4.12 shows ADEV plot generated after room temperature measurement without any temperature compensation. With temperature compensation, the performance is likely to improve. The testing results are also summarized in Figure 4.12.

Figure 4.13 compares the reported ARW and BI for different gyroscopes. PSI gyro

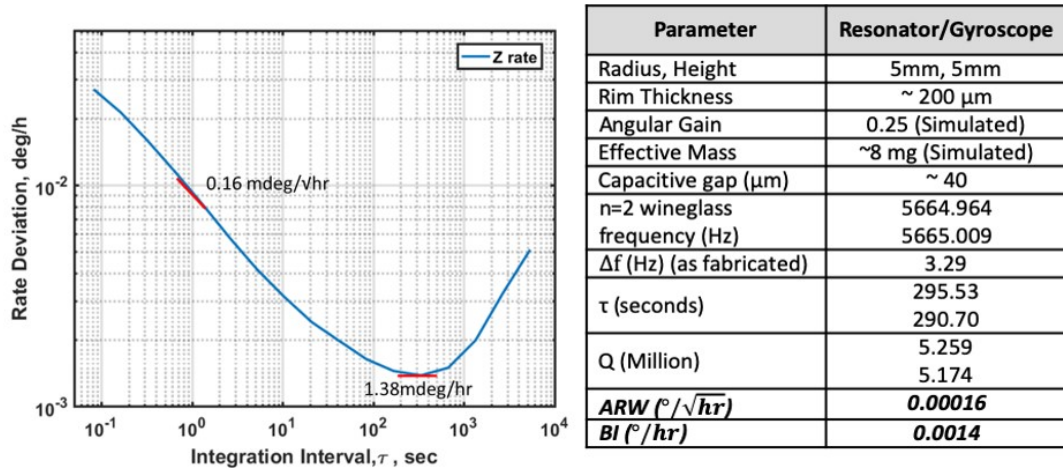


Figure 4.12: Measured ADEV plot generated at room temperature showing navigation-grade ARW and BI. Other resonant characteristics are tabulated.

with side electrode architecture have exhibited unprecedented ARW even better than the larger HRGs from Northrop Grumman and SAFRAN. BI of only SAFRAN's gyro is better than that of PSI gyro.

4.5 Shell-in-Shell (*SiS*) Architecture

As discussed, both side and surface electrode architectures have their own advantages and disadvantages. Ideally one wants a gyroscope with

- Large capacitance for better sensitivity and small operating voltage.
- Large capacitance for good frequency tuning capability.
- In-plane sensing mechanism due to larger deflection in-plane.
- Immunity to temperature variation.

Electrode configurations discussed above possess some of these characteristics but not all. Large capacitance is usually limited due to limited height and lack of geometric conformality with the shell curvature, that they do not maximize shell-electrode capacitance. Temperature variations can be minimized by using same material to


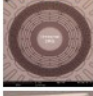
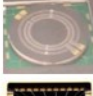




Gyro Design	Dia (mm)	ARW ($^{\circ}/\text{hr}/\text{rt-Hz}$)	BI ($^{\circ}/\text{hr}$)	
MSRG [61]	8	2.1	0.877	
DRG [29]	8	0.6	0.04	
Boeing DRG [28]	8	0.126	0.012	
Michigan BRG [137]	5	0.17	0.01	
Northrop Grumman HRG [38]	30	0.018	0.003	
SAFRAN HRG [39]	20	0.012	0.0001	
Michigan PSI	10	0.0096	0.001	

Figure 4.13: Comparison of ARW and BI of reported gyroscopes.

fabricate resonator and electrodes. To overcome limitations listed above, a new type of gyro device with high aspect-ratio, curved electrodes with nearly conformal profile following the resonator shell called **Shell-in-Shell (SiS)** is developed. SiS as the name suggests consists of two shells of nearly similar curvature. One shell is the freestanding resonator while the other shell is fixed and has electrodes defined on it. They are assembled together with a small capacitive gap. Figure 4.14 shows schematic and photograph of a fabricated SiS device. The capacitive gap can be designed in the range of 10–50 μm . Because the entire SiS device is made from FS, it minimizes gap change due to temperature variations, which is important for bias and scale factor stability.

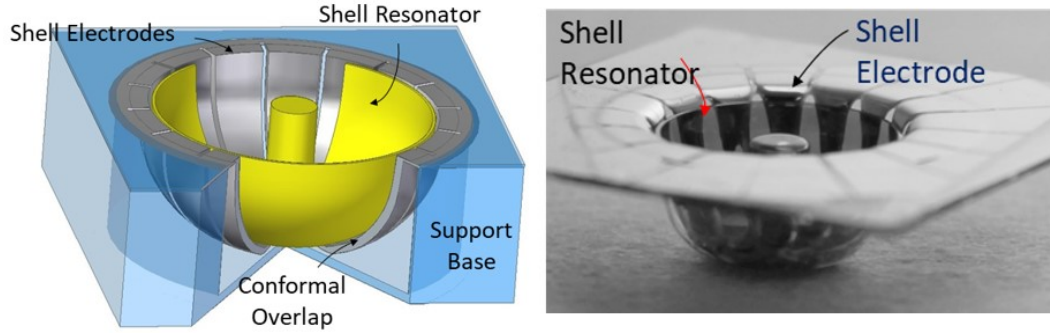


Figure 4.14: Schematic diagram and photograph of fabricated SiS device.

4.5.1 Design and Fabrication

A SiS device consists of a shell resonator and a shell electrode assembled together. Both resonator and electrode shells are fabricated using blowtorch molding technology using two different molds, mold#1 for the resonator and mold#2 for the electrode shell which are of different sizes as shown in Figure 4.15. In the next sections design and fabrication of each component is discussed.

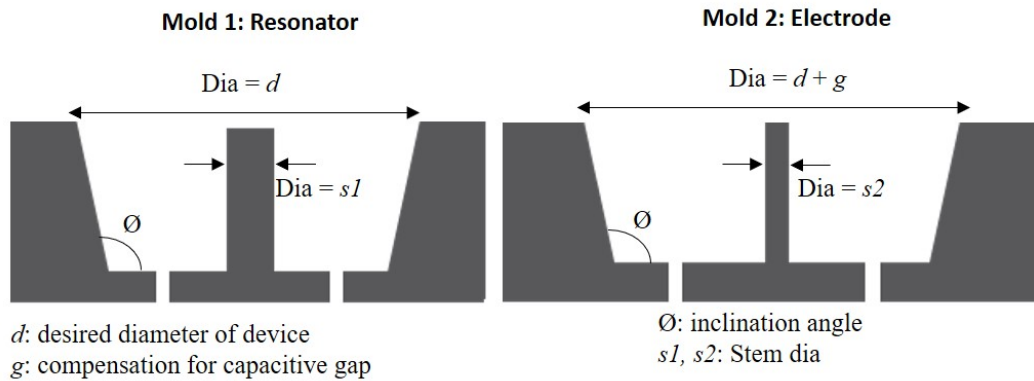


Figure 4.15: Design of molds to make resonator shell and electrode shell.

Resonator Shell

The shell resonator is fabricated by blowtorching a $240 \mu\text{m}$ thick, flat fused-silica substrate using a mold as shown in Figure 4.16(a). This mold (mold#1) is designed to have (a) an angled sidewall, (b) larger anchor diameter, and (c) smaller outer

diameter than the electrode shell mold. The angled sidewall on both molds#1 and #2 ensures that the curvature of both resonator and electrode shells are similar. Additionally, the anchor diameter of mold 1 is designed to be larger than that of mold 2 so that the shell can go inside the electrode shell's anchor. Similarly, the diameter of the mold#1 is smaller than that of mold#2 for the shell to be dropped inside the electrode shell. The outer diameter of mold#2 is dictated by the desired capacitive gap. Resonator shell is molded and singulated using the approach discussed in Chapter II.

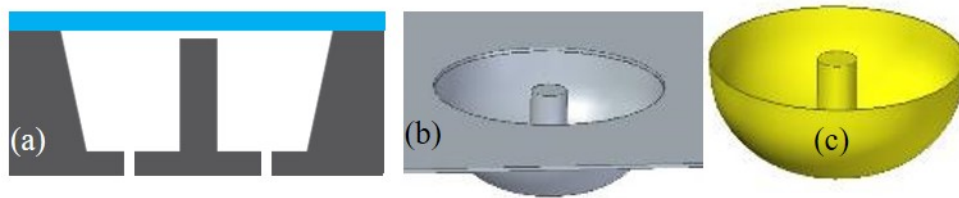


Figure 4.16: (a) A mold with angled sidewall is used to blow a flat fused silica substrate to (b) make the resonator shell which is then (c) lapped/polished to release and cleaned and coated with metal on both sides.

Post singulation, the resonator shell is cleaned and coated with a thin conductive metal on both sides. Figure 4.16 shows the fabrication process of resonator shell.

Electrode Shell

The electrode shell is fabricated by blowing a patterned fused-silica substrate using the approach as outlined in Section 2.10. A fused-silica substrate is etched at sixteen places to define thin trenches. The thin trenches have thickness of $\sim 100 \mu\text{m}$, width $\sim 800 \mu\text{m}$, while the remaining unetched regions are $550 \mu\text{m}$. The etched substrate is then diced in squares of side 23 mm and cleaned. A second mold (mold#2) with same sidewall angle but smaller anchor diameter and larger outer diameter from mold#1 is used to form the electrode shell. During torching, the initially thin regions on the substrate get further thinned. Post fabrication, these shells are protected with

Crystalbond 509 from inside and put in 49% HF acid. This step etches the shell from the outside etching off the thin regions creating open slots forming isolated electrodes. The shell is then cleaned and coated with a thick conductive metal layer to form the electrodes. The open slots naturally isolate the electrodes on the curved part while the bottom and top isolation is done using a shadow mask. Fabrication process of electrode shell is shown in Figure 4.17.

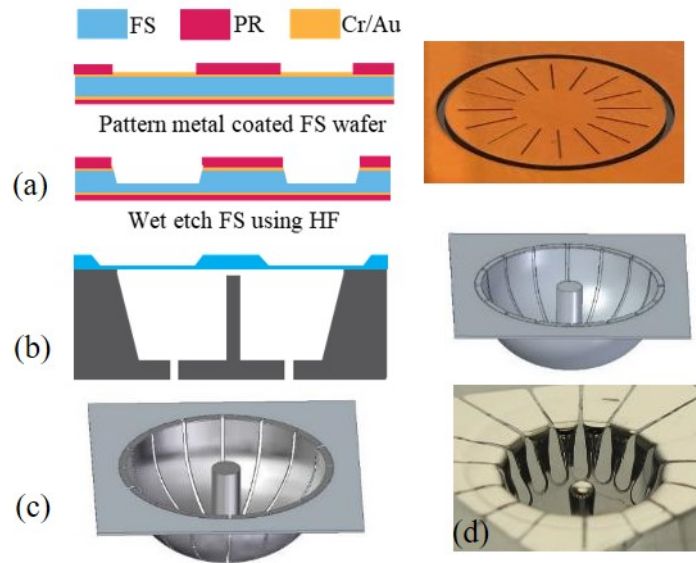


Figure 4.17: (a) Fused silica substrate is patterned to define 16 thin trenches. (b) It is then torched to make electrode shell and (c) filled inside with Crystalbond and etched in HF acid to etch off the thin trenches. (d) The device is then coated with metal.

Assembly

To assemble SiS device, Crystalbond 509 was used for attachment and thin spacers for alignment. First, the electrode shell is attached using Crystalbond to a base support structure and Crystalbond is applied to the anchor at $\sim 120^\circ\text{C}$ on a hotplate. The setup is then pulled off the hotplate and allowed to cool down. Six spacers are then placed at the edge of the electrode shell. The resonator shell is then dropped inside the electrode shell and the assembly is then placed back on the hotplate. A down force is applied on the anchor of the shell to ensure that it is sitting atop the

anchor of the electrode shell. The hotplate is then turned off and the assembly is allowed to cool down. Once it is cooled, spacers are removed. Figure 4.18 summarizes the entire process of fabrication and assembly of SiS device.

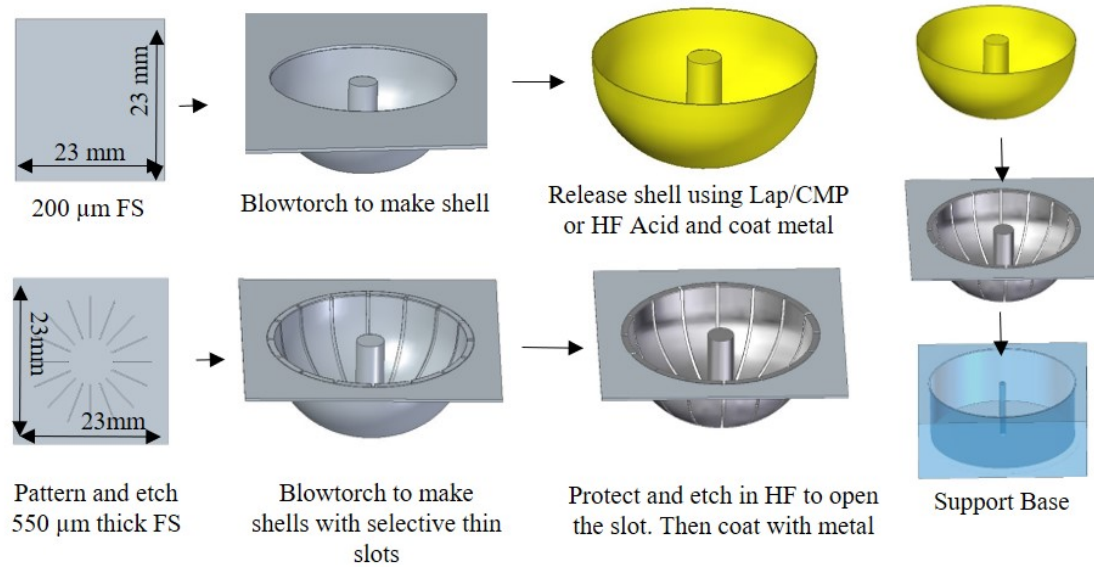


Figure 4.18: Fabrication flow of resonator and electrode shells. They are then integrated together to form SiS device.

In prototype SiS device discussed in this section, $25\ \mu\text{m}$ spacers were used which could cause gap non-uniformity. A tighter spacer on all sides would ensure that the resonator shell is placed symmetrically inside the electrode shell. At the same time, it is important to ensure that the resonator shell is sitting flat on the anchor of the electrode shell which could otherwise lead to tilting of the resonator shell causing gap non-uniformity as well as energy loss. Figures 4.19(a) show photographs of a complete SiS device, showing the resonator shell mounted inside the electrode shell. Figure 4.19(b) shows the side view of a resonator shell inside a partially broken electrode shell.

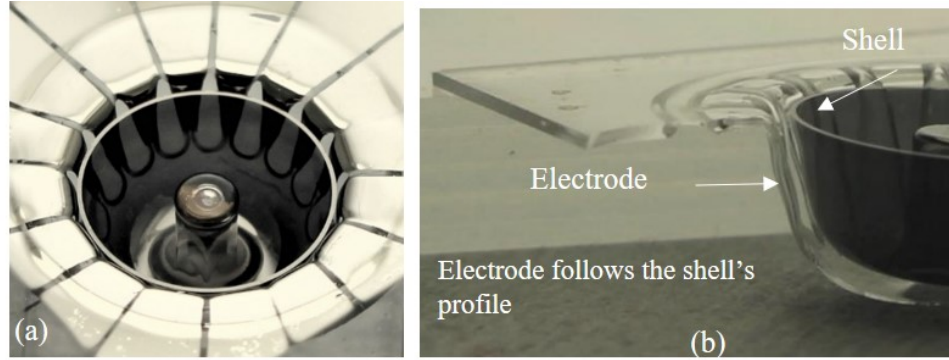


Figure 4.19: (a) Photograph of an assembled SiS device after removing the spacers and (b) photograph of a partially broken SiS device showing the profile of resonator and electrode.

4.5.2 Numerical Analysis

Conform electrodes is a key feature of SiS device. However, due to challenges in fabrication and assembly, it is possible that the electrodes do not conform exactly or only partially conform to the resonator shell. In this section effect of such non-idealities is numerically studied. Finite element analysis using COMSOL Multiphysics is used to develop numerical model. Firstly, capacitance change and frequency tuning using perfectly conformal electrodes is compared to those of conventional side electrodes. Following this, effect of only partially conforming electrodes is analyzed. An electromechanical model coupling solid mechanics and electrostatics is used with moving mesh condition. A 10 mm diameter shell resonator and an electrode separated by a gap of $30\ \mu\text{m}$ is modeled.

Two types of electrodes are used to compare performance, (1) the commonly used straight electrodes, and (2) the proposed conformal electrodes. The model is shown in Figure 4.20(a). First, static capacitance (C_1) is simulated. Next, a constant force is applied on the shell facing the electrode to have a maximum lateral deflection of $13\ \mu\text{m}$ and the capacitance (C_2) is numerically calculated for both electrode configurations. The difference in capacitance ($\Delta C = C_2 - C_1$) is calculated

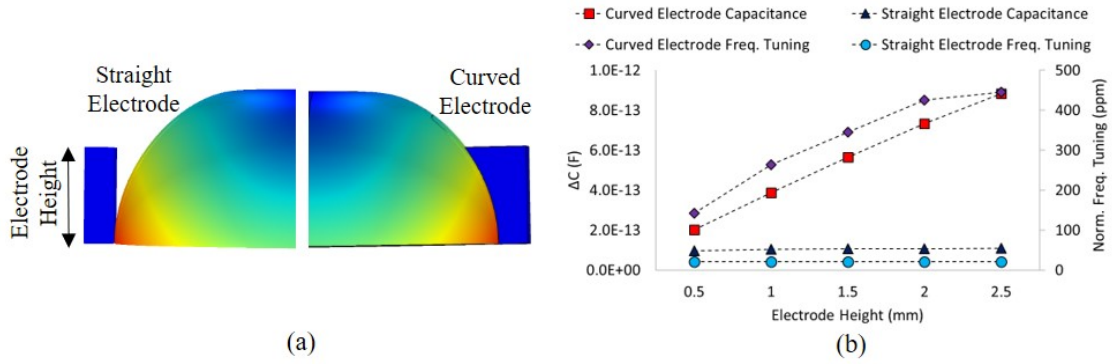


Figure 4.20: (a) Simulation model with straight electrodes and curved electrodes, (b) variation of capacitance change and frequency tuning as a function of electrode height for both electrode configuration.

for different heights of the electrodes for both configurations. To calculate frequency tuning capability, a potential difference is applied between the shell and electrode which changes its resonance frequency through electrostatic softening. First, no bias is applied, and it is confirmed that the two wineglass frequencies have zero frequency mismatch. Then a bias voltage is applied, and the electrode height is varied and the shift in frequency is determined in both electrode configurations. Figure 4.20(b) graphically shows the capacitance change and frequency tuning in both electrode configurations. It can be seen that curved electrodes in SiS are much more efficient in terms of capacitance as well as tuning frequency than side electrodes. Also, tuning capability increases until the electrode height reaches 2 mm and then slowly starts to flatten. Therefore, an electrode height of up 2.5 mm in SiS would lead to excellent tuning capability compared with side electrodes. Results in Figure 4.20(b) are obtained considering the gap is uniform along the electrode height. This however may not be practical due to fabrication challenges. To study the effect of gap non-uniformity along electrode height, another study is done where the gap at the base of the electrode is same as the previous case but it gradually changes towards the top of electrode making the gap non-uniform. A non-uniformity parameter (α)

defined as the ratio of the top to the bottom gap is used to study the effect of such gap variations. $\alpha > 1$ implies $g_2 > g_1$ and $\alpha < 1$ implies the opposite. For instance, $\alpha = 12$ corresponds to $g_2 \sim 350 \mu\text{m}$.

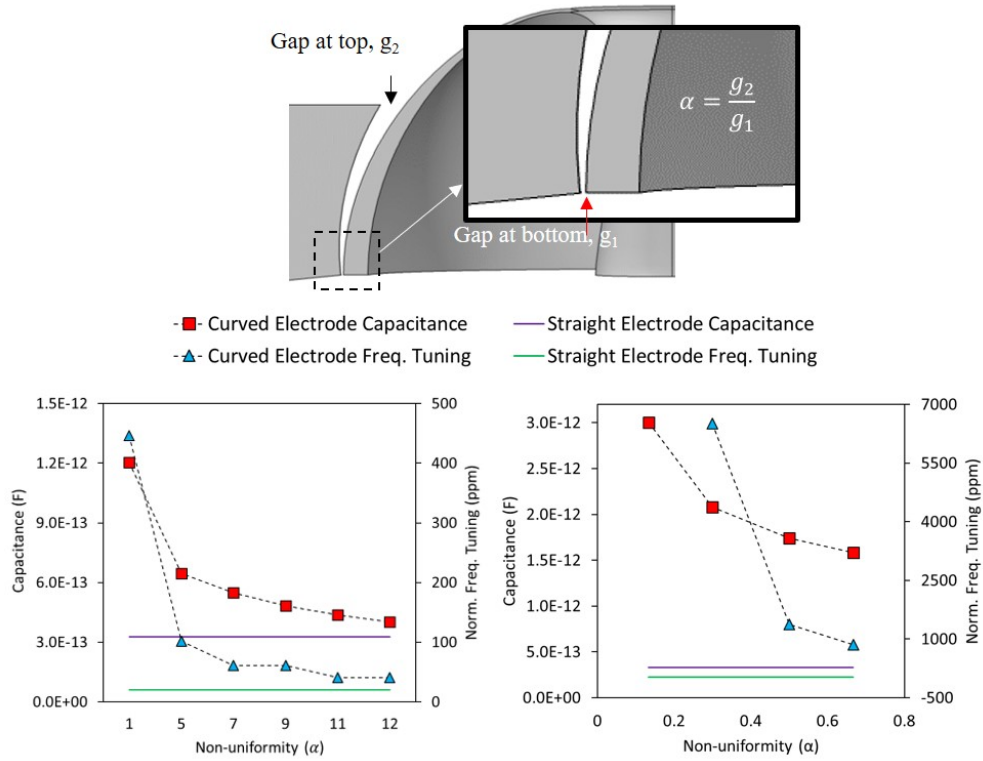


Figure 4.21: Effect of gap non-uniformity on capacitance and frequency tuning for curved electrode. As the non-uniformity increases, capacitance and tuning reduce and becomes comparable to that of straight electrode.

Numerical results are obtained for a range of α . Figure 4.21 shows the cross-section of the model, capacitance and frequency tunability for different α . It can be seen that as the gap non-uniformity, α , increases, capacitance and tuning capability reduces and starts to become comparable to that of straight electrodes. There can be several reasons for such non-idealities. Figure 4.22 shows uniform gap obtained in case of perfectly defined sidewall profile and also cases where sidewall profile is non-ideal due to either thickness or profile variation which leads to non-uniform overlap. Thickness variation is caused due to stretching of FS substrate during torching. This leads to a

gradually thinning profile which causes a non-uniform gap. However, such variations can be minimized by using a patterned substrate to make the electrode shell. As shown in Figure 2.10 and discussed in Section 2.5, patterned substrates can be used to locally tune the thickness of specific regions. Another way of correcting such gap variations can be through changes in mold design to correct for the non-uniform gap. Profile variation can be caused when the shells do not follow the mold's profile. Such variations can be corrected by optimizing parameters of blowtorch molding. In the current SiS devices, maximum estimated total gap variation is $\sim 150 \mu\text{m}$. This corresponds to $\alpha < 5$ which yields at least twice as good capacitance and frequency tuning than side electrodes in addition to reducing temperature effects. Besides, with design changes and optimized assembly methods, such variations can be reduced to be $< 20 \mu\text{m}$ which would further improve performance in terms of capacitance and tuning for a SiS device.

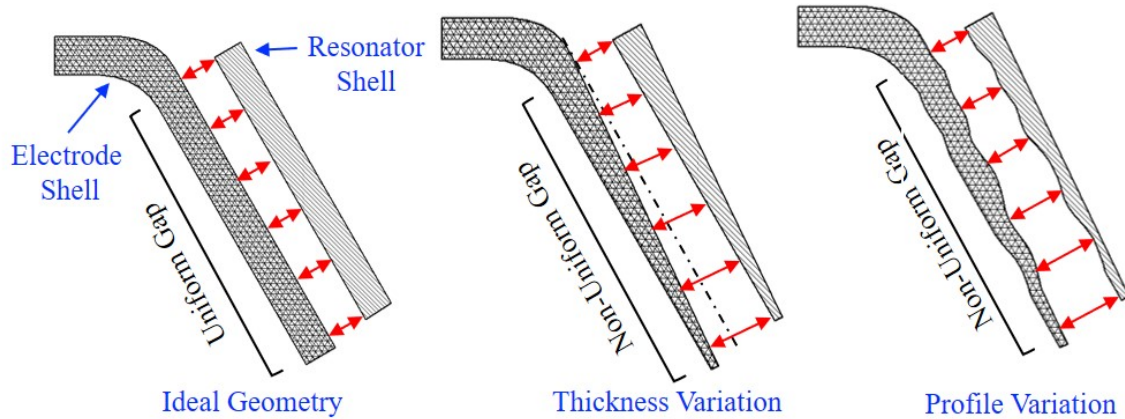


Figure 4.22: Causes of variation in capacitive gap due to thickness or profile variation.

4.5.3 Testing and Evaluation

Two prototype SiS devices are fabricated and tested on the Lakeshore probe station in vacuum. A bias voltage is applied to the anchor of the shell resonator as shown in Figure 4.23. Testing is done using the method explained in Section 4.2.

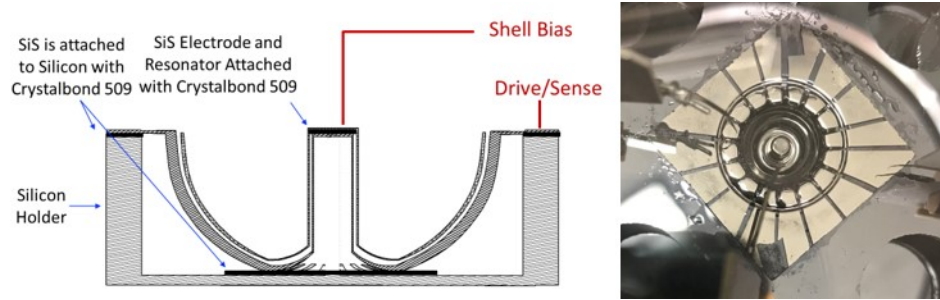


Figure 4.23: Testing method of SiS device. The attachments are done using Crystalbond and shell bias is applied through the anchor.

SiS #1 had its wineglass frequencies at 5904.81 Hz and 5906.11 Hz with a frequency split of 1.3 Hz as shown in Figure 4.24.

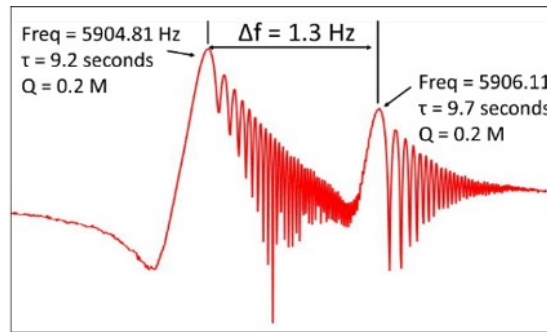


Figure 4.24: Measured FFT of SiS #1 device showing a frequency mismatch of 1.3 Hz and Q of 0.2 Million.

SiS #2 exhibited the two wineglass modes at 5814.55 Hz and 5820.41 Hz with a frequency split of 5.8 Hz. The ring-down time constant was measured to be 23 seconds, $Q = 0.4$ Million and 11 second, $Q = 0.2$ Million in the two wineglass modes. The FFT and ring-down time plot of SiS #2 is shown in Figure 4.25.

To make prototype SiS devices, test resonators were used; as a result, they were not processed using the optimized processing method which is likely the cause of low Q . With improvements in mounting conditions and high- Q from resonator, a high-performance SiS device is possible which could lead to a high-performance SiS Gyroscope. This work can be pursued further to fabricate high performance gyroscopes with large capacitance, better tuning capability and minimized temperature

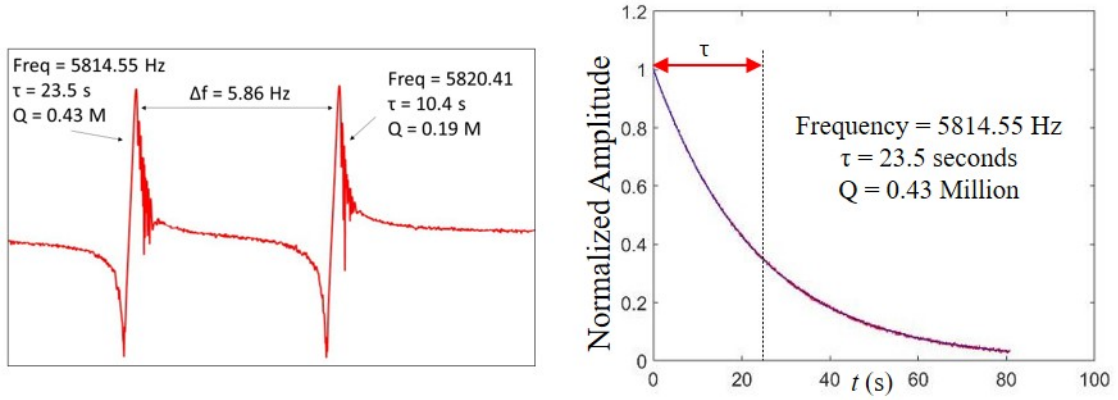


Figure 4.25: Measured FFT and ring-down plot of SiS #2 device showing a frequency mismatch of 5.8 Hz and Q of 0.4 Million.

variations. All these would enable very low ARW, BI and better scale factor stability.

CHAPTER V

Conclusions and Future Work

5.1 Summary

Characteristics like small size, low cost, low power have been the motivations for miniaturizing gyroscopes. These small gyroscopes have provided affordable solution at the small scale where conventional big and costly gyroscopes cannot be used. While miniaturization has solved the problem of cost and size, small gyroscopes have lacked in performance by several orders of magnitude compared to their macro counterparts. At the small scale, sensors face challenges because of their large mechanical losses, large noise, and limited controllability. Challenges have been on all fronts from obtaining high Q, obtaining small capacitive gap, effective vacuum packaging to maintain low pressure inside the package, designing low noise circuitry to ensure maximum signal-to-noise ratio, and many others. Research presented in this thesis solves these challenges and demonstrates that very high performance comparable to larger gyroscopes is possible at orders of magnitude lower cost and significantly smaller size.

5.2 Conclusions

Research in this thesis is aimed at developments in four main fronts, all of which ultimately combine to make low noise and high accuracy small gyroscopes. The

four fronts include, (i) design and fabrication of high-performance resonators with tailored mass and stiffness distribution, (ii) design and fabrication of 3D structures with discrete open windows on the surface, (iii) process development to enable mass production at cost much lower than conventional processes, and finally (iv) integration of resonators with electrode substrates to make gyroscopes with either in-plane or out-of-plane transduction. Besides, development of a new gyro architecture where the resonators are integrated with a custom-designed curved electrodes substrate to enable large overlap capacitance. Following subsections discuss key results on each front.

5.2.1 High-performance Resonators with Tailored Stiffness/Mass

PSI resonators are fabricated by blowtorch molding of fused silica (FS) substrates. These substrates can be patterned and etched to define features in the form of disc, trenches or annulus. Blowtorching of such patterned substrates leads to selective regions being either thicker or thinner than the rest of the shell on the molded structure. This local tuning of thickness can tailor mass and stiffness distribution to modify resonant characteristics. For example, using a patterned substrate, a shell with thick rim ($\sim 350 \mu\text{m}$) and thick shoulder ($\sim 400 \mu\text{m}$) can be fabricated. The thick rim helps increase modal mass which in turns reduces noise. Thick shoulder reduces deformation under an event of shock. Application specific PSI resonators can be fabricated using technologies developed in this thesis. Different types of PSI resonators with varying rim/shoulder thickness and solid/hollow stems are fabricated and it is shown that the thickness of localized regions can be controlled. Imperfections like asymmetry in height or anchor of shell, mass imbalance, acircularity of shell, misalignment of anchor with respect to shells etc. are also studied. It is found that asymmetries in/near rim adversely affect frequency mismatch of $n=2$ wineglass

modes and this can be reduced by designing appropriate patterns on substrates and through careful alignment of substrate on the mold. Different sources of energy dissipation are also investigated. They are identified as structural sources like anchor loss, thermoelastic loss, or material sources like surface loss. Structural sources of energy loss can be minimized by optimizing design of the resonator and making them symmetric and free of any imperfection. These losses are numerically estimated using finite element analysis and are found to be very small for PSI resonators. Energy loss due to material sources can be minimized by ensuring a good surface quality of the resonator that is free of adsorbed moisture. It is experimentally observed that any particles or residue on the shell is detrimental to Q and efficient cleaning should be done to increase Q . It is also found that desorption and dehydroxylation of water molecules by annealing at different temperatures also improves Q . This improvement in Q is however lost by varying amount when resonators are exposed to gaseous or aqueous environment. Therefore, the surface of the shell should be protected to preserve Q . This can be done by keeping the shells in vacuum environment or by coating them with conductive metal immediately after annealing. With the optimized design/fabrication methods developed in this thesis, PSI resonators achieved more than 12.5 Million Q , $\tau > 500$ second, frequency mismatch < 2 Hz at frequency range of 5–13 kHz. It is also shown that fabrication of high-performance resonators is repeatable and uniform across devices fabricated in a batch. An analysis of >200 resonators shows that frequency of devices varies within $\pm 10\%$ in a batch and Q varies by $< 20\%$. Additionally, the least robust design of PSI resonators has shown to withstand 6000g shock applied in both lateral and vertical direction. It is also numerically found that these devices can withstand shock of more than 20,000g.

5.2.2 3D Structures with Discrete Open Windows

Most of the resonators are simple continuous shells which means there are no through-etched features on their surface. It is however desired for some applications where such etched windows are required. A new technology is developed which enables fabrication of these shells with through-etched or open windows on their surface. Shells with selectively thinned regions are formed by thinning regions on the initial flat FS substrate. These substrates are then blowtorch molded to form 3D shells. Thin regions on the substrate get translated to the surface of shell making certain regions thinner than the rest of the shell. To fabricate shells with open windows, shells are protected from inside with Crystalbond 509 and put in Hydrofluoric acid (HFA) for a timed etch. HFA etches the shell and the thin regions etches off creating windows. The protective wax is dissolved, and the shells are cleaned. The thickness and aspect ratio of thin windows can be controlled by modifying the patterning on the initial flat substrate. Also, patterning the substrate along with the mold design can enable the fabrication of many types of structures and not only hemispherical shells. It is shown that through design changes on the patterned substrate, it is possible to form open windows of different aspect ratio and dimensions on the final shell. These shells with open windows can improve Q by reducing thermoelastic and anchor losses. Open features limit the flow of heat across the surface which reduces thermoelastic damping. They also reduce energy path to the anchor reducing anchor loss. Open shells can also be used to define curved electrodes on molded shells or used as a 3D stencil mask to metal coat on curved surfaces. The developed technology would enable design and fabrication of several other MEMS sensors like antennas, lenses, or other opto-MEMS sensors for different emerging applications.

5.2.3 Hydrofluoric Acid Based Singulation Method

Molding to form 3D structures using either blowtorching or glassblowing leads to a structure with a desired 3D part and an undesired flat 2D part which needs to be removed to singulate 3D shells. A new technique which uses HFA to selectively etch the 2D part and singulate FS shell resonators is developed. Commercially available low-cost wax, Crystalbond 509, is used to mask the shell by encapsulating it from both sides and dipping in an HFA bath. Shells singulated using this approach have rugged surface near the rim which does not affect performance. Very high performance in terms of high Q (>8 Million) and low Δf (<3 Hz) is achieved from resonators singulated using this approach. While this technique results in performance comparable to those obtained by singulation through conventionally used lapping method, it dramatically reduces time and cost of fabrication. Because this process uses wet-etchant without any sophisticated equipment or process characterization, it leads to very high throughput and cost reduction by $>25x$ as compared to lapping method. It is shown through measurement results that this process is superior on all fronts and will be instrumental in low-cost batch fabrication of high-performance resonators.

5.2.4 Integration of Resonators to make PSI Gyroscopes

PSI resonators, after they are fabricated and singulated, needs to be coated with metal to make them conductive for capacitive transduction. Different metal combinations have been explored in this work. It is found that sputtered metals irrespective of how close their Young's Modulus is to that of FS, result in similar drop in Q which is $\sim 50\%$. Three metal bilayers Al/Au, Ti/Pt and Cr/Au of thickness 28/80 Å is deposited on one side of resonators and maximum Q drop of 41%, 43% and 43%

is measured. ALD Platinum of conformal thickness 80 Å leads to 40–70% drop in Q. It is believed that a combination of loss mechanisms, including loss due to metal grain boundaries, stress gradient due to Young's Modulus mismatch, and loss at the interface dominate Q. However, due to very high Q from uncoated PSI resonators, a drop of 50% in Q still leads to a final Q on the order of several million. Metal-coated PSI resonators can be integrated with different types of electrode substrates to enable either out-of-plane transduction by placing electrodes beneath the rim or in-plane transduction by placing electrodes on the side of the rim. Both these approaches are investigated, gyros are fabricated, and their pros and cons are discussed. Surface electrode gyros are relatively simpler to assemble but they have small capacitance, limiting frequency tuning as well as scale factor. Side electrodes, though complex in fabrication, can achieve very low noise and very high accuracy. Gyros with side electrode architecture exhibited angle random noise of 160 $\mu\text{deg}/\text{rt-hr}$ and bias instability $<1 \text{ mdeg}/\text{hr}$. Such performance is unheard of at the small scale and compares favorably with some of the commercial state-of-the-art macro-scale gyroscopes. Furthermore, a novel gyroscope architecture which involves integrating PSI resonators with a custom-designed curved electrode substrate is developed. Curved electrodes enable large overlap with the resonator and increase sensitivity and frequency tuning. Moreover, electrodes made of FS also reduce temperature sensitivity. Curved electrodes which nearly follow the resonator's profile are fabricated and integrated with a PSI resonator to make a Shell in Shell (SiS) gyroscope. Numerical analysis is done to compare capacitance and frequency tuning capability of SiS and side electrode gyro architecture. It is found that SiS device can increase both capacitance and frequency tuning capability by $>5x$ due to its conformal overlap. Prototype SiS devices are successfully fabricated and tested. SiS devices with curved electrodes

improve resolution, frequency tuning, and temperature sensitivity.

5.3 Future Works

Very high performance in terms of Q , noise, accuracy have been achieved in this thesis. However even better performance is possible from PSI gyroscopes. This section lists some future directions which can be pursued.

- Q from PSI resonators can be further increased by more research towards improving surface quality and device symmetry. At the same time more investigation needs to be done towards understanding loss mechanisms due to metal coating to reduce Q drop due to the metal layer.
- Research in this thesis has indicated that frequency mismatch of PSI resonators is limited by the precision of the mold. Additionally, as the mold degrades variation in the radius of shells is also observed. These imperfections can be minimized and even lower frequency mismatch (<1 Hz) can be achieved by using an ultra-precise mold.
- PSI devices are made from patterned substrates with two thicknesses. It is also possible to fabricate devices with three thickness by adding a second lithography step. This would enable even greater level of control in controlling thicknesses of different regions. Moreover, this would also enable fabrication of shells where both thin and open windows can be fabricated on the same shell.
- Finally, SiS gyro can be further improved to reduce capacitive gap variation. This can be done by either changing the inclination angle of resonator mold or by molding electrode shell using patterned substrate. This will lead to a uniform thickness electrode shell.

BIBLIOGRAPHY

BIBLIOGRAPHY

- [1] U.S. Air Force, "GPS Applications," 2020. [Online]. Available: <https://www.gps.gov/applications/>. [Accessed: 04-Apr-2020].
- [2] B. W. Parkinson, P. Enge, P. Axelrad, J.J. Spilker (Eds.). Global positioning system: Theory and applications, Volume II. American Institute of Aeronautics and Astronautics.(1996)
- [3] U.S. Air Force, "GPS Accuracy," How accurate is GPS?, 2017. [Online]. Available: http://www.gps.gov/systems/gps/performance/accuracy/#_how-accurate. [Accessed: 04-Apr-2020].
- [4] P.D. Groves, Principles of GNSS, inertial, and multisensor integrated navigation systems. Artech house, (2013)
- [5] N. Yazdi, F. Ayazi, and K. Najafi. "Micromachined inertial sensors." Proceedings of the IEEE 86, no. 8 (1998): 1640-1659.
- [6] L. Wang, R. A. Wolf, Y. Wang, K. K. Deng, L. Zou, R. J. Davis, and S. Trolier-McKinstry. "Design, fabrication, and measurement of high-sensitivity piezoelectric microelectromechanical systems accelerometers." Journal of microelectromechanical systems 12, no. 4 (2003): 433-439.
- [7] D.L. Devoe and A. P. Pisano. "Surface micromachined piezoelectric accelerometers (PiXLs)." Journal of Microelectromechanical Systems 10, no. 2 (2001): 180-186.
- [8] J.P. Lynch, A. Partridge, K. H. Law, T. W. Kenny, A. S. Kiremidjian, and E. Carryer. "Design of piezoresistive MEMS-based accelerometer for integration with wireless sensing unit for structural monitoring." Journal of Aerospace Engineering 16, no. 3 (2003): 108-114.
- [9] J.J. Jency, M. Sekar, and A. Ravi Sankar. "Damping analysis of a quad beam MEMS piezoresistive accelerometer." International Journal of Modelling and Simulation (2020): 1-9.
- [10] J. Chae, H. Kulah, and K. Najafi. "A monolithic three-axis silicon capacitive accelerometer with micro-g resolution." In TRANSDUCERS'03. 12th International Conference on Solid-State Sensors, Actuators and Microsystems. Digest of Technical Papers (Cat. No. 03TH8664), vol. 1, pp. 81-84. IEEE, 2003.
- [11] J. Chae, H. Kulah, and K. Najafi. "A monolithic three-axis micro-g micromachined silicon capacitive accelerometer." Journal of Microelectromechanical systems 14, no. 2 (2005): 235-242.
- [12] S. Zotov, A. Srivastava, K. Kwon, J. Frank, E. Parco, M. Williams, S. Shtigluz et al. "In-Run Navigation Grade Quartz MEMS-Based IMU." In 2020 IEEE International Symposium on Inertial Sensors and Systems (INERTIAL), pp. 1-4. IEEE, 2020.
- [13] T.A. Morris, J. M. Wheeler, M. J. Grant, and M. Digonnet. "Advances in optical gyroscopes." In Seventh European Workshop on Optical Fibre Sensors, vol. 11199, p. 111990T. International Society for Optics and Photonics, 2019.
- [14] J. Lyman, "A new space rate sensing instrument." Aeronautical Engineering Review 12, no. 11 (1953): 24-30

- [15] J.H. Staudte, "Microresonator of tuning fork configuration." U.S. Patent 3,683,213, issued August 8, 1972.
- [16] E.C. Alsenz, W. F. Juptner, and D. F. Macy. "Angular rate sensor system." U.S. Patent 4,654,663, issued March 31, 1987.
- [17] B. Boxenhorn, and P. Greiff. "A vibratory micromechanical gyroscope." In Guidance, Navigation and Control Conference, p. 4177. 1988.
- [18] S. Askari, M. H. Asadian, K. Kakavand, and A. M. Shkel. "Near-navigation grade quad mass gyroscope with Q-factor limited by thermo-elastic damping." In Proc. ENERGY, vol. 44, pp. 124-127. 2016.
- [19] D. Endean, K. Christ, P. Duffy, E. Freeman, M. Glenn, M. Gnerlich, B. Johnson, and J. Weinmann. "Near-Navigation Grade Tuning Fork MEMS Gyroscope." In 2019 IEEE International Symposium on Inertial Sensors and Systems (INERTIAL), pp. 1-4. IEEE, 2019.
- [20] M.W. Putty, "A micromachined vibrating ring gyroscope." PhD diss., 1995.
- [21] G. He and K. Najafi. "A single-crystal silicon vibrating ring gyroscope." In Technical Digest. MEMS 2002 IEEE International Conference. Fifteenth IEEE International Conference on Micro Electro Mechanical Systems (Cat. No. 02CH37266), pp. 718-721. IEEE, 2002.
- [22] F. Ayazi, and K. Najafi. "A HARPSS polysilicon vibrating ring gyroscope." Journal of microelectromechanical systems 10, no. 2 (2001): 169-179.
- [23] D. Senkal, S. Askari, M. J. Ahamed, E. J. Ng, V. Hong, Y. Yang, C. Hyuck Ahn, T. W. Kenny, and A. M. Shkel. "100K Q-factor toroidal ring gyroscope implemented in wafer-level epitaxial silicon encapsulation process." In 2014 IEEE 27th International Conference on Micro Electro Mechanical Systems (MEMS), pp. 24-27. IEEE, 2014.
- [24] B. J. Gallacher, J. Hedley, J. S. Burdess, A.J. Harris, A. Rickard, and D. O. King. "Electrostatic correction of structural imperfections present in a microring gyroscope." Journal of Microelectromechanical Systems 14, no. 2 (2005): 221-234.
- [25] B. J. Gallacher, "Principles of a micro-rate integrating ring gyroscope." IEEE Transactions on Aerospace and Electronic Systems 48, no. 1 (2012): 658-672.
- [26] S. Yoon, U. Park, J. Rhim, and S.S Yang. "Tactical grade MEMS vibrating ring gyroscope with high shock reliability." Microelectronic Engineering 142 (2015): 22-29.
- [27] J. Wang, L. Chen, M. Zhang, and D. Chen. "A micro-machined vibrating ring gyroscope with highly symmetric structure for harsh environment." In 2010 IEEE 5th International Conference on Nano/Micro Engineered and Molecular Systems, pp. 1180-1183. IEEE, 2010.
- [28] A. Challoner, H. G. Howard, and J. Y. Liu. "Boeing disc resonator gyroscope." In 2014 IEEE/ION Position, Location and Navigation Symposium-PLANS 2014, pp. 504-514. IEEE, 2014.
- [29] Q. Li, D. Xiao, X. Zhou, Y. Xu, M. Zhuo, Z. Hou, K. He, Y. Zhang, and X. Wu. "0.04 degree-per-hour MEMS disk resonator gyroscope with high-quality factor (510 k) and long decaying time constant (74.9 s)." Microsystems and nanoengineering 4, no. 1 (2018): 1-11.
- [30] D. Wang, A. Efimovskaya, and A. M. Shkel. "Amplitude Amplified Dual-Mass Gyroscope: Design Architecture and Noise Mitigation Strategies." In 2019 IEEE International Symposium on Inertial Sensors and Systems (INERTIAL), pp. 1-4. IEEE, 2019.
- [31] D. Wang, R. Noor, A.M. Shkel. "Dynamically Amplified Dual-mass Gyroscopes with In-situ Shock Survival Mechanism" In 2020 IEEE International Symposium on Inertial Sensors and Systems (INERTIAL), pp. 1-4. IEEE, 2020.

- [32] H. Wen, A. Daruwalla, C. Liu, F. Ayazi. "A hermitically-sealed 2.9 MHz $n=3$ Disc BAW Gyroscope with sub-degree-per-hour bias instability." In 2020 IEEE 33rd International Conference on Micro Electro Mechanical Systems (MEMS), pp. 741-744. IEEE, 2013.
- [33] S. Nitzan, C. H. Ahn, T-H. Su, M. Li, E. J. Ng, S. Wang, Z. M. Yang et al. "Epitaxially-encapsulated polysilicon disk resonator gyroscope." In 2013 IEEE 26th International Conference on Micro Electro Mechanical Systems (MEMS), pp. 625-628. IEEE, 2013.
- [34] D. M. Rozelle, "The hemispherical resonator gyro: From wineglass to the planets." In Proc. 19th AAS/AIAA Space Flight Mechanics Meeting, pp. 1157-1178. 2009.
- [35] E.J. Loper D. D. Lynch. "Vibratory rotation sensor." U.S. Patent No. 4,951,508. 28 Aug. 1990
- [36] D. M. Rozelle, A. D. Meyer, A. A. Trusov, and D. K. Sakaida. "Milli-HRG inertial sensor assembly—a reality." In 2015 IEEE International Symposium on Inertial Sensors and Systems (ISISS) Proceedings, pp. 1-4. IEEE, 2015.
- [37] A. Trusov, M. R. Phillips, A. Bettadapura, G. Atikyan, G. H. McCammon, J. M. Pavell, Y. A. Choi, D. K. Sakaida, D. M. Rozelle, and A. D. Meyer. "mHRG: Miniature CVG with beyond navigation grade performance and real time self-calibration." In 2016 IEEE International Symposium on Inertial Sensors and Systems, pp. 29-32. IEEE, 2016.
- [38] A. Trusov, M. R. Phillips, G. H. Mccammon, D. M. Rozelle, and A. D. Meyer. "Continuously self-calibrating CVG system using hemispherical resonator gyroscopes." In 2015 IEEE International Symposium on Inertial Sensors and Systems (ISISS) Proceedings, pp. 1-4. IEEE, 2015.
- [39] F. Delhaye. "HRG by SAFRAN: The game-changing technology," IEEE Int. Symp. Inertial Sensors and Systems (INERTIAL), pp. 1-4. IEEE, 2018
- [40] A. Jeanroy, G. Grosset, J. Goudon, and F. Delhaye. "HRG by Sagem from laboratory to mass production." In 2016 IEEE International Symposium on Inertial Sensors and Systems, pp. 1-4. IEEE, 2016.
- [41] F. Delhaye, "HRG by SAFRAN: The game-changing technology." In 2018 IEEE International Symposium on Inertial Sensors and Systems (INERTIAL), pp. 1-4. IEEE, 2018.
- [42] G. Remillieux, and F. Delhaye. "Sagem Coriolis Vibrating Gyros: a vision realized." In 2014 DGON Inertial Sensors and Systems (ISS), pp. 1-13. IEEE, 2014.
- [43] A. Jeanroy, A. Bouvet, and G. Remillieux. "HRG and marine applications." *Gyroscopy and Navigation* 5, no. 2 (2014): 67-74.
- [44] P. Taheri-Tehrani, T. Su, A. Heidari, G. Jaramillo, C. Yang, S. Akhbari, H. Najar et al. "Micro-scale diamond hemispherical resonator gyroscope." In Hilton Head Workshop, pp. 289-292. 2014.
- [45] J.J. Bernstein, M. G. Bancu, J. M. Bauer, E. H. Cook, P. Kumar, E. Newton, T. Nyinjee et al. "High Q diamond hemispherical resonators: fabrication and energy loss mechanisms." *Journal of Micromechanics and Microengineering* 25, no. 8 (2015): 085006.
- [46] N. Mehanathan, V. Tavassoli, P. Shao, L. Sorenson, and F. Ayazi. "Invar-36 micro hemispherical shell resonators." In 2014 IEEE 27th International Conference on Micro Electro Mechanical Systems (MEMS), pp. 40-43. IEEE, 2014.
- [47] M.M. Torunbalci, S. Dai, A. Bhat, and S. A. Bhave. "Acceleration insensitive hemispherical shell resonators using pop-up rings." In 2018 IEEE Micro Electro Mechanical Systems (MEMS), pp. 956-959. IEEE, 2018.
- [48] A. Vafanejad, "Wineglass Mode Resonators, Their Applications and Study of Their Quality Factor." PhD diss., University of Southern California, 2015.

- [49] A. Vafanejad, and E.S. Kim. "Effect of diaphragm perforation on quality factor of hemispherical resonator gyroscope." In 2015 Transducers-2015 18th International Conference on Solid-State Sensors, Actuators and Microsystems (TRANSDUCERS), pp. 27-30. IEEE, 2015.
- [50] A. Heidari, M-L. Chan, H-A. Yang, G. Jaramillo, P. Taheri-Tehrani, P. Fonda, H. Najjar, K. Yamazaki, L. Lin, and D. A. Horsley. "Micromachined polycrystalline diamond hemispherical shell resonators." In 2013 Transducers and Eurosensors XXVII: The 17th International Conference on Solid-State Sensors, Actuators and Microsystems (TRANSDUCERS and EUROSENSORS XXVII), pp. 2415-2418. IEEE, 2013.
- [51] P. Pai, F. K. Chowdhury, C. H. Mastrangelo, and M. Tabib-Azar. "MEMS-based hemispherical resonator gyroscopes." In SENSORS, 2012 IEEE, pp. 1-4. IEEE, 2012.
- [52] P. Shao, C. L. Mayberry, X. Gao, V. Tavassoli, and F. Ayazi. "A polysilicon microhemispherical resonating gyroscope." *Journal of microelectromechanical systems* 23, no. 4 (2014): 762-764.
- [53] P. Shao, V. Tavassoli, C Liu, L. Sorenson, and F. Ayazi. "Electrical characterization of ALD-coated silicon dioxide micro-hemispherical shell resonators." In 2014 IEEE 27th International Conference on Micro Electro Mechanical Systems (MEMS), pp. 612-615. IEEE, 2014.
- [54] J. M. Gray, J. P. Houlton, J. C. Gertsch, J. J. Brown, C. T. Rogers, S. M. George, and V. M. Bright. "Hemispherical micro-resonators from atomic layer deposition." *Journal of Micromechanics and Microengineering* 24, no. 12 (2014): 125028.
- [55] P. Shao, V. Tavassoli, C. L. Mayberry, and F. Ayazi. "A 3D-HARPSS polysilicon microhemispherical shell resonating gyroscope: Design, fabrication, and characterization." *IEEE Sensors Journal* 15, no. 9 (2015): 4974-4985.
- [56] M. Kanik, P. Bordeenithikasem, D. Kim, N. Selden, A. Desai, R. M'Closkey, and J. Schroers. "Metallic glass hemispherical shell resonators." *Journal of Microelectromechanical Systems* 24, no. 1 (2014): 19-28.
- [57] Z. Liu, W. Zhang, F. Cui, and L. Gu. "Micro-manufacturing technology of a three-dimensional curved surface diamond structure for gyroscope applications." *Journal of Micromechanics and Microengineering* 29, no. 12 (2019): 125004.
- [58] J. Y. Cho, S. Singh, J-K. Woo, G. He and K. Najafi. "0.00016 deg/rt-hr Angle Random Walk (ARW) and 0.0014 deg/hr Bias Instability (BI) from 5.2M-Q and 1-cm Precision Shell Integrating (PSI) Gyroscope", In 2020 IEEE International Symposium on Inertial Sensors and Systems (INERTIAL), IEEE, 2020.
- [59] S. Singh, J.K. Woo, G. He, J. Cho and K. Najafi., "0.0062 deg/rt-hr Angle Random Walk and 0.027 deg/hr Bias Instability From a Micro-Shell Resonator Gyroscope With Surface Electrodes", in Proc. IEEE MEMS 2020, Vancouver, BC, Jan. 2020, pp. 737-740.
- [60] S. A. Zotov, A. Alexander, A. Trusov, and A. M. Shkel. "Three-dimensional spherical shell resonator gyroscope fabricated using wafer-scale glassblowing." *Journal of microelectromechanical systems* 21, no. 3 (2012): 509-510.
- [61] D. Senkal, M. J. Ahamed, A. A. Trusov, and A. M. Shkel. "Electrostatic and mechanical characterization of 3-D micro-wineglass resonators." *Sensors and Actuators A: Physical* 215 (2014): 150-154.
- [62] W. Li, X. Xi, K. Lu, Y. Shi, Z. Hou, Y. Wu, X. Wu, and D. Xiao. "A Novel Micro Shell Resonator Gyroscope with Sixteen T-Shape Masses." In 2019 20th International Conference on Solid-State Sensors, Actuators and Microsystems and Eurosensors XXXIII (TRANSDUCERS and EUROSENSORS XXXIII), pp. 434-437. IEEE, 2019.

- [63] J. Giner, and A. M. Shkel. "The concept of "collapsed electrodes" for glassblown spherical resonators demonstrating 200: 1 aspect ratio gap definition." In 2015 IEEE International Symposium on Inertial Sensors and Systems (ISISS) Proceedings, pp. 1-4. IEEE, 2015.
- [64] I. Prikhodko, S. A. Zotov, A. A. Trusov, and A. M. Shkel. "Microscale glass-blown three-dimensional spherical shell resonators." *Journal of Microelectromechanical Systems* 20, no. 3 (2011): 691-701.
- [65] D. Senkal, M. J. Ahamed, A. A. Trusov, and A. M. Shkel. "High temperature micro-glassblowing process demonstrated on fused quartz and ULE TSG." *Sensors and Actuators A: Physical* 201 (2013): 525-531.
- [66] M. H. Asadian, Y. Wang, and A. M. Shkel. "Development of 3D Fused Quartz Hemi-Toroidal Shells for High-Q Resonators and Gyroscopes." *Journal of Microelectromechanical Systems* 28, no. 6 (2019): 954-964.
- [67] B. Luo, J. Shang, Z. Su, J. Zhang, and C.-P. Wong, "Height adjustment of 3-D axisymmetric microumbrella shells for tailoring wineglass frequency," *IEEE T. Compon., Packag. Manuf. Tech.*, vol. 9, no. 3, 2019
- [68] B. Sarac, G. Kumar, T. Hodges, S. Ding, A. Desai, and J. Schroers, "Three-dimensional shell fabrication using blow molding of bulk metallic glass," *J. Micro-Electromech. Syst.*, vol. 20, no. 1, pp. 28–36, 2011
- [69] G. He, R. Gordenker, J. K. Woo, J. A. Nees, B. Shiari, T. Nagourney, J. Y. Cho, and K. Najafi. "Laser self-mixing interferometry for precision displacement measurement in resonant gyroscopes." In 2019 IEEE International Symposium on Inertial Sensors and Systems (INERTIAL), pp. 1-4. IEEE, 2019.
- [70] R. P. Leland, "Mechanical-thermal Noise in MEMS Gyroscopes," *IEEE Sensors Journal*, vol. 5, no. 3, pp. 493-500, June 2005
- [71] A. Darvishian, Design and Analysis of Extremely Low-Noise MEMS Gyroscopes for Navigation. The University of Michigan. Diss. 2018.
- [72] A. Darvishian, Tal Nagourney, Jae Yoong Cho, Behrouz Shiari, and Khalil Najafi. "Thermoelastic dissipation in micromachined birdbath shell resonators." *Journal of Microelectromechanical Systems* 26, no. 4 (2017): 758-772.
- [73] A. H. Nayfeh and M. I. Younis, "Modeling and simulations of thermoelastic damping in microplates," *J. Micromech. Microeng.*, vol. 14, no. 12, pp. 1711–1717, 2004.
- [74] R. N. Candler et al., "Impact of geometry on thermoelastic dissipation in micromechanical resonant beams," *J. Microelectromech. Syst.*, vol. 15, no. 4, pp. 927–934, Aug. 2006.
- [75] A. Hamza, T. Tsukamoto and S. Tanaka, "Quality Factor Trimming Method Using Thermoelastic Dissipation for Ring-Shape MEMS Resonator." In 2020 IEEE International Symposium on Inertial Sensors and Systems (INERTIAL) (pp. 1-4). IEEE.
- [76] C. Zener, "Internal friction in solids. I. Theory of internal friction in reeds," *Phys. Rev.*, vol. 52, pp. 230–235, Aug. 1937.
- [77] C. Zener, "Internal friction in solids II. General theory of thermoelastic internal friction," *Phys. Rev.*, vol. 53, pp. 90–99, Jan. 1938.
- [78] M. Pandey, R. B. Reichenbach, A. T. Zehnder, A. Lal, and H. G. Craighead. "Reducing anchor loss in MEMS resonators using mesa isolation." *Journal of microelectromechanical systems* 18, no. 4 (2009): 836-844.

- [79] J. M. Gray et al., "Hemispherical micro-resonators from atomic layer deposition," *J. Micromech. Microeng.*, vol. 24, no. 12, pp. 125028-1–125028-9, 2014.
- [80] J.J. Bernstein, M. G. Bancu, J. M. Bauer, E. H. Cook, P. Kumar, E. Newton, T. Nyinjee et al. "High Q diamond hemispherical resonators: fabrication and energy loss mechanisms." *Journal of Micromechanics and Microengineering* 25, no. 8 (2015): 085006.
- [81] A. Darvishian, B. Shiari, J.Y. Cho, T. Nagourney, and K. Najafi. "Anchor loss in hemispherical shell resonators." *Journal of Microelectromechanical Systems* 26, no. 1 (2017): 51-66.
- [82] A. Darvishian, "Design and Analysis of Extremely Low-Noise MEMS Gyroscopes for Navigation." PhD diss., 2018.
- [83] T. Nagourney, "High-Q Fused Silica Micro-Shell Resonators for Navigation-Grade MEMS Gyroscopes." The University of Michigan. Diss. 2018.
- [84] T. Nagourney, J. Cho, A. Darvishian, B. Shiari, and K. Najafi. "Micromachined high-Q fused silica bell resonator with complex profile curvature realized using 3D micro blowtorch molding." In 2015 Transducers-2015 18th International Conference on Solid-State Sensors, Actuators and Microsystems (TRANSDUCERS), pp. 1311-1314. IEEE, 2015.
- [85] W. Li, Xiang Xi, Kun Lu, Yan Shi, Zhanqiang Hou, Yulie Wu, Xuezhong Wu, and Dingbang Xiao. "A Novel Micro Shell Resonator Gyroscope with Sixteen T-Shape Masses." In 2019 20th International Conference on Solid-State Sensors, Actuators and Microsystems & Eurosensors XXXIII (TRANSDUCERS & EUROSensors XXXIII), pp. 434-437. IEEE, 2019.
- [86] S. Singh, T. Nagourney, J.Y. Cho, A. Darvishian, B. Shiari, and K. Najafi. "Design and fabrication of high-Q birdbath resonator for MEMS gyroscopes." In 2018 IEEE/ION Position, Location and Navigation Symposium (PLANS), pp. 15-19. IEEE, 2018.
- [87] <https://www.aremco.com/mounting-adhesives/>.
- [88] S. Singh, J. Cho, K. Najafi, "Low-Cost, High-Throughput Process Using HF Acid to Singulate Fused-Silica Shell Resonators with High-Q." In 2020 IEEE International Symposium on Inertial Sensors and Systems (INERTIAL) (pp. 1-4). IEEE.
- [89] S. Singh, JK Woo, G He, JY Cho, K Najafi, "0.0062 deg/rt-hr Angle Random Walk and 0.027 deg/hr Bias Instability From A Micro Shell Resonator Gyroscope Using Surface Electrodes", IEEE 33rd International Conference on Micro Electro Mechanical Systems (MEMS), pp. 737-740
- [90] M. Asadian, Y. Wang, S. Askari, and A. Shkel. "Controlled capacitive gaps for electrostatic actuation and tuning of 3D fused quartz micro wineglass resonator gyroscope." In 2017 IEEE International Symposium on Inertial Sensors and Systems (INERTIAL), pp. 1-4. IEEE, 2017.
- [91] D. Senkal, M. J. Ahamed, M. H. Asadian, S. Askari, and A. M. Shkel. "Demonstration of 1 million Q factor on microglassblown wineglass resonators with out-of-plane electrostatic transduction." *Journal of Microelectromechanical Systems* 24, no. 1 (2014): 29-37.
- [92] J. Alain, and P. Leger. "Gyroscopic sensor and rotation measurement apparatus constituting an application thereof." U.S. Patent 6,474,161, issued November 5, 2002.
- [93] K. Najafi, and J. Y. Cho. "Assembly processes for three-dimensional microstructures." U.S. Patent 10,612,925, issued April 7, 2020.
- [94] F. Delhaye. "HRG by SAFRAN: The game-changing technology." In 2018 IEEE International Symposium on Inertial Sensors and Systems (INERTIAL), pp. 1-4. IEEE, 2018.
- [95] B. Shiari, T. Nagourney, S. Singh, J.Y. Cho, and K. Najafi. "Simulation-based approach for fabrication of micro-shell resonators with controllable stiffness and mass distribution." In 2018 IEEE International Symposium on Inertial Sensors and Systems (INERTIAL), pp. 1-4. IEEE, 2018.

- [96] T. Nagourney, S. Singh, B. Shiari, J.Y. Cho, and K. Najafi. "Fabrication of hemispherical fused silica micro-resonator with tailored stiffness and mass distribution." In 2018 IEEE Micro Electro Mechanical Systems (MEMS), pp. 1000-1003. IEEE, 2018.
- [97] H. Choi, Md Shamim Ahsan, Dongyoon Yoo, Ik-Bu Sohn, Young-Chul Noh, Jin-Tae Kim, Deok Jung, Jin-Hyeok Kim, and Ho-Min Kang. "Formation of cylindrical micro-lens array on fused silica glass surface using CO2 laser assisted reshaping technique." *Optics and Laser Technology* 75 (2015): 63-70.
- [98] C. Pfeiffer, Xin Xu, Stephen R. Forrest, and Anthony Grbic. "Direct transfer patterning of electrically small antennas onto three-dimensionally contoured substrates." *Advanced Materials* 24, no. 9 (2012): 1166-1170.
- [99] C. Pfeiffer, Xin Xu, Stephen R. Forrest, and Anthony Grbic. "A printed spherical helix antenna." In 2010 14th International Symposium on Antenna Technology and Applied Electromagnetics and the American Electromagnetics Conference, pp. 1-4. IEEE, 2010.
- [100] B. Li, X. Xi, K. Lu, Y. Shi, D. Xiao, X. Wu, "Frequency Split Improvement of Fused Silica Micro Shell Resonator Based on Suppression of Geometric Harmonic Error", In 2020 IEEE International Symposium on Inertial Sensors and Systems (INERTIAL), pp. 1-4. IEEE, 2020.
- [101] <https://www.polytec.com/us/vibrometry/technology/>
- [102] Y. Xie, H.-C. Hsieh, P. Pai, H. Kim, M. Tabib-Azar, and C. H. Mastrangelo, "Precision curved micro hemispherical resonator shells fabricated by poached-egg micro-molding," in Proc. IEEE SENSORS, Taipei, Taiwan, Oct. 2012, pp. 1-4.
- [103] D. Saito, C. Yang, A. Heidari, H. Najar, L. Lin, and D. A. Horsley, "Microcrystalline diamond cylindrical resonators with quality-factor up to 0.5 million," *Appl. Phys. Lett.*, vol. 108, no. 5, 2016, Art. no. 051904
- [104] D. Senkal, M. J. Ahamed, A. A. Trusov, and A. M. Shkel, "Achieving Sub-Hz frequency symmetry in micro-glassblown wineglass resonators," *IEEE J. Microelectromech. Syst.*, vol. 23, no. 1, pp. 30-38, Feb. 2014.
- [105] J. Giner, J. M. Gray, J. Gertsch, V. M. Bright, A. M. Shkel, "Design, fabrication, and characterization of a micromachined glassblown spherical resonator with insitu integrated silicon electrodes and ALD tungsten interior coating," *IEEE Int. MEMS Conf.*, 2015
- [106] J.Y. Cho, J. Yan, J. A. Gregory, H. Eberhart, R. L. Peterson, and K. Najafi. "High-Q fused silica birdbath and hemispherical 3-D resonators made by blow torch molding." *Int. IEEE MEMS Conf.*, pp. 177-180, 2013
- [107] J. Y. Cho, J.-K. Woo, J. Yan, R. L. Peterson, and K. Najafi, "Fused-silica micro birdbath resonator gyroscope (μ -BRG)," *IEEE J. Microelectromech. Syst.*, vol. 23, no. 1, pp. 66-77, Feb. 2014
- [108] D. Xiao, W. Li, Z. Hou, K. Lu, Y. Shi, Y. Wu, X. Wu, "Fused silica micro shell resonator with T-shape masses for gyroscopic application." *IEEE J. of Microelectromechanical Systems* 27, no. 1 (2017): 47-58
- [109] J.Y Cho, J-K. Woo, G. He, D. Yang, C. Boyd, S. Singh, A. Darvishian, B. Shiari, and K. Najafi. "1.5-Million Q-factor Vacuum-Packaged Birdbath Resonator Gyroscope (BRG)." 32nd IEEE Int. Conf. on Micro Electro Mechanical Systems (MEMS), pp. 210-213, 2019
- [110] S. Singh, A. Darvishian, J.Y. Cho, B. Shiari, and K. Najafi. "High-Q 3D micro-shell resonator with high shock immunity and low frequency mismatch for MEMS gyroscopes." 32nd IEEE Int. Conf. on Micro Electro Mechanical Systems (MEMS), pp. 668-671. IEEE, 2019

- [111] T. Nagourney, J.Y. Cho, B. Shiari, A. Darvishian, and K. Najafi, "259 second ring-down time and 4.45 million quality factor in 5.5 kHz fused silica birdbath shell resonator." 19th IEEE Int. Conf. Solid-State Sensors, Actuators and Microsystems (TRANSDUCERS), pp. 790-793, 2017
- [112] T. Nagourney, J.Y. Cho, A. Darvishian, B. Shiari, and K. Najafi. "130 second ring-down time and 3.98 million quality factor in 10 kHz fused silica micro birdbath shell resonator." Solid-State Sensors, Actuators, and Microsystems Workshop, Hilton Head Island, SC, USA. 2016
- [113] J. Y. Cho, and K. Najafi, "A high-Q all-fused silica solid-stem wineglass hemispherical resonator formed using micro blow torching and welding," 28th IEEE Int. Conf. Micro Electro Mechanical Systems, p. 821, 2015
- [114] J.Y. Cho, T. Nagourney, A. Darvishian, B. Shiari, J. Woo, and K. Najafi. "Fused silica micro birdbath shell resonators with 1.2 million Q and 43 second decay time constant." Solid-State Sensors, Actuators and Microsystems Workshop, Hilton Head, pp. 103-104. 2014
- [115] J.Y. Cho, S. Singh, J-K. Woo, G. He, K. Najafi. "0.00016 deg/rt-hr Angle Random Walk (ARW) and 0.0014 deg/hr Bias Instability (BI) from 5.2M-Q and 1-cm Precision Shell Integrating (PSI) Gyroscope", IEEE Int. Symposium on Inertial Sensors and Systems (INERTIAL), 2020
- [116] J. Yang, B. Hamelin, F. Ayazi, "Capacitive Lamé mode resonators in 65 mm-thick monocrystalline Silicon Carbide with Q-factors exceeding 20 million" IEEE Micro Electro Mechanical Systems (MEMS), pp. 22-229, 2020.
- [117] V.P. Mitrofanov, and K. V. Tokmakov. "Effect of heating on dissipation of mechanical energy in fused silica fibers." Physics Letters A 308, no. 2-3 (2003): 212-218.
- [118] A. M. Gretarsson, and Gregory M. Harry. "Dissipation of mechanical energy in fused silica fibers." Review of scientific instruments 70, no. 10 (1999): 4081-4087.
- [119] A. Ageev, B.C. Palmer, A.D. Felice, S. D. Penn, and P. R. Saulson. "Very high quality factor measured in annealed fused silica." Classical and Quantum Gravity 21, no. 16 (2004): 3887.
- [120] S. D Penn, G. M. Harry, A. M. Gretarsson, S. E. Kittelberger, P. R. Saulson, J. J. Schiller, J. R. Smith, and S. O. Swords. "High quality factor measured in fused silica." Review of Scientific Instruments 72, no. 9 (2001): 3670-3673.
- [121] S., William, M. A. Beilby, and P. R. Saulson. "Mechanical quality factors of fused silica resonators." Review of scientific instruments 69, no. 10 (1998): 3681-3689.
- [122] M.J. Ahamed, D. Senkal, and A. M. Shkel. "Effect of annealing on mechanical quality factor of fused quartz hemispherical resonator." In 2014 International Symposium on Inertial Sensors and Systems (ISISS), pp. 1-4. IEEE, 2014.
- [123] T. Nagourney, J.Y. Cho, A. Darvishian, B. Shiari, and K. Najafi. "Effect of metal annealing on the Q-factor of metal-coated fused silica micro shell resonators." In 2015 IEEE International Symposium on Inertial Sensors and Systems (ISISS) Proceedings, pp. 1-5. IEEE, 2015.
- [124] L. Dalstein, E. Potapova, and E. Tyrode. "The elusive silica/water interface: Isolated silanols under water as revealed by vibrational sum frequency spectroscopy." Physical Chemistry Chemical Physics 19, no. 16 (2017): 10343-10349.
- [125] J.P. Gallas, J. C. Lavalley, A. Burneau, and O. Barres. "Comparative study of the surface hydroxyl groups of fumed and precipitated silicas. 4. Infrared study of dehydroxylation by thermal treatments." Langmuir 7, no. 6 (1991): 1235-1240.
- [126] D. B. Asay, and S. H. Kim. "Evolution of the adsorbed water layer structure on silicon oxide at room temperature." The Journal of Physical Chemistry B 109, no. 35 (2005): 16760-16763.

- [127] R.K. Iler, and R. Iler. "The chemistry of silica: solubility, polymerization, colloid and surface properties, and biochemistry." (1979).
- [128] S.J. Gregg, and KSW Sing. "Surface Area and Porosity." Academic Press Inc. Ltd., London (1982).
- [129] C. Okkerse, in: B.G. Linsen (Ed.), Physical and Chemical Aspects of Adsorbents and Catalysts (chapter 5), Academic Press, London, 1970, p. 214
- [130] J.J. Fripiat, and J. Uytterhoeven. "Hydroxyl content in silica gel "Aerosil". " The Journal of Physical Chemistry 66, no. 5 (1962): 800-805.
- [131] M.M. Egorov, V.I. Kvlivdze, V.F. Kiselev, K.G. Krasilnikov, Kolloid-Z. Z. Polym. B212 (1966) 126.
- [132] A.A. Chuiko, "Development of Research in The Field of Chemistry Of Solid Bodies Surface." TEORETICHESKAYA I EKSPERIMENTALNAYA KHIMIYA 23, no. 5 (1987): 597-619.
- [133] L.T. Zhuravlev, "The surface chemistry of amorphous silica. Zhuravlev model." Colloids and Surfaces A: Physicochemical and Engineering Aspects 173, no. 1-3 (2000): 1-38.
- [134] E.F. Vansant, P.V.D. Voort, and K. C. Vrancken. Characterization and chemical modification of the silica surface. Elsevier, 1995.
- [135] L.A. Ignat'eva, V.I. Kvlivdze, V.F. Kiselev, in: V.F. Kiselev, V.I. Kvlivdze (Eds.), Bound Water in Dispersed Systems, Issue 1, Moscow State University Press, Moscow, 1970, p. 56.
- [136] Morgan, A. E., and Somorjai, G. A. Low energy electron diffraction studies of gas adsorption on the platinum (100) single crystal surface. Surface Science, 12(3), 405, (1968)
- [137] D. Yang, "Oven-Controlled Inertial Sensors", PhD diss. 2019.
- [138] R. Kubena, D. T. Chang, and R. L. Larson. "Quartz-based disk resonator gyro with ultra-thin conductive outer electrodes and method of making same." U.S. Patent 8,766,745, issued July 1, 2014.
- [139] A. Qamar, S. Sherrit, X. Zheng, J. Lee, P. X-L. Feng, and Mina Rais-Zadeh. "Study of energy loss mechanisms in AlN-based piezoelectric length extensional-mode resonators." Journal of Microelectromechanical Systems 28, no. 4 (2019): 619-627.
- [140] A. Peczalski, "Piezoelectric Fused Silica Resonators for Timing References." PhD diss., 2016.
- [141] R. Flaminio, J. Franc, C. Michel, N. Morgado, L. Pinard, and B. Sassolas. "A study of coating mechanical and optical losses in view of reducing mirror thermal noise in gravitational wave detectors." Classical and Quantum Gravity 27, no. 8 (2010): 084030.
- [142] J.Y. Cho, T. Nagourney, A. Darvishian, and K. Najafi. "Ultra conformal high aspect-ratio small-gap capacitive electrode formation technology for 3D micro shell resonators." In 2017 IEEE 30th International Conference on Micro Electro Mechanical Systems (MEMS), pp. 1169-1172. IEEE, 2017.
- [143] Z. Sergei A., Alexander A. Trusov, and Andrei M. Shkel. "Three-dimensional spherical shell resonator gyroscope fabricated using wafer-scale glassblowing." Journal of microelectromechanical systems 21, no. 3 (2012): 509-510.